COMPUTATION OF UNSTEADY AND NON-EQUILIBRIUM TURBULENT FLOWS USING REYNOLDS STRESS TRANSPORT MODELS

A thesis submitted to the University of Manchester
for the degree of Doctor of Philosophy
in the Faculty of Engineering and Physical Sciences

2010

By
Sharaf F. Al-Sharif
School of Mechanical, Aerospace and Civil Engineering

Contents

List of Tables

List of Figures

Abstract

In this work the predictive capability of a number of Reynolds stress transport (RST) models was first tested in a range of non-equilibrium homogeneous flows, comparisons being drawn with existing direct numerical simulation (DNS) results and physical measurements. The cases considered include both shear and normally strained flows, in some cases with a constant applied strain rate, and in others where this varied with time.

Models were generally found to perform well in homogeneous shear at low shear rates, but their performance increasingly deteriorated at higher shear rates. This was attributed mainly to weaknesses in the pressure–strain rate models, leading to over–prediction of the shear stress component of the stress anisotropy tensor at high shear rates.

Performance in irrotational homogeneous strains was generally good, and was more consistent over a much wider range of strain rates. In the experimental plane strain and axisymmetric contraction cases, with time-varying strain rates, there was evidence of an accelerated dissipation rate generation. Significant improvement was achieved through the use of an alternative dissipation rate generation term, P_ε, in these cases, suggesting a possible route for future modelling investigation.

Subsequently, the models were also tested in the inhomogeneous case of pulsating channel flow over a wide range of frequencies, the reference for these cases being the LES of Scotti and Piomelli (2001). A particularly challenging feature in this problem set was the partial laminarisation and re-transition that occurred cyclically at low and, to a lesser extent, intermediate frequencies. None of the models tested were able to reproduce correctly all of the observed flow features, and none returned consistently superior results in all the cases examined.

Finally, models were tested in the case of a plane jet interacting with a rectangular dead-end enclosure. Two geometric configurations are examined, corresponding a steady regime, and an intrinsically unsteady regime in which periodic flow oscillations are experimentally observed (Mataoui et al., 2003). In the steady case generally similar flow patterns were returned by the models tested, with some differences arising in the degree of downward deflection of the impinging jet, which in turn affected the level of turbulence energy developing in the lower part of the cavity.

In the unsteady case, only two of the models tested, a two-equation $k-\varepsilon$ model and an advanced RST model, correctly returned purely periodic solutions. The other two RST models, based on linear pressure–strain rate terms, returned unsteady flow patterns that exhibited complex oscillations with significant cycle-to-cycle variations. Unfortunately, the limited availability of reliable experimental data did not allow a detailed quantitative examination of model performance.

Declaration

No portion of the work referred to in this thesis has been submitted in support of an application for another degree or qualification of this or any other university or other institute of learning.

Copyright

Acknowledgements

I would like to express my gratitude to my supervisors, Dr. Tim Craft and Dr. Mark Cotton, for their guidance and support throughout the course of this research.

I am also grateful to the Saudi Ministry of Higher Education for the scholarship that has made my PhD research possible.

I would like to thank Dr. Alberto Scotti for providing the LES database for the pulsatile channel flow cases which have been used as a references for model testing in the present work.

My thanks go to all my colleagues in the CFD and Turbulence Mechanics group at the school of MACE, for valuable advice, discussions, support and social activities.

Last but not least, I wish to thank my wife, Amira, and my wonderful children, Hamza, Jumana, Mohammad, and the latest arrival: Faisal! Their love, support and understanding have been a strong driving force throughout my work.

Published Work

Conference papers

Al-Sharif S. F., Cotton M. A., Craft T. J. "Reynolds stress transport models in unsteady and non-equilibrium flows". Proc. 6^{th} Int. Symp. Turbulence and Shear Flow Phenomena (TSFP6), Seoul, S. Korea. 22-24 June 2009.

The above paper was earmarked by a selection committee as one of "approximately twenty of the best papers presented" at TSFP6 for inclusion in a special issue of the International Journal of Heat and Fluid Flow, subject to successful completion of the standard editorial review procedures of the journal.

Refereed journals

Al-Sharif S. F., Cotton M. A., Craft T. J. "Reynolds stress transport models in unsteady and non-equilibrium flows". TSFP-6 special issue of the International Journal of Heat and Fluid Flow. Accepted for publication.

Nomenclature

$\mathbf{A}$ Coefficient matrix resulting from FV discretisation., see equation (3.18), page 56

A Lumley flatness parameter, see equation (2.54), page 41

A_2 Second invariant of the stress anisotropy tensor, see equation (2.53), page 41

A_3 Third invariant of the stress anisotropy tensor, see equation (2.53), page 41

a_E, a_W, a_N, a_S Coefficients of nodes neighbouring node P, see equation (3.16), page 56

a_P Coefficient of scalar ϕ at node P, see equation (3.16), page 56

a_{ij} Reynolds stress anisotropy, see equation (2.11), page 29

c Volumetric flux through a finite volume face, see equation (3.10), page 54

D Half the trace of D_{ij}, see equation (2.23), page 32

D_{ij} Production-like tensor used in certain rapid pressure–strain rate models, see equation (2.23), page 32

$\mathcal{D}$ Diffusion of turbulent kinetic energy, see equation (2.10), page 29

$\mathcal{D}_{ij}$ Diffusion of Reynolds stresses, see equation (2.8), page 29

$\mathcal{D}_\varepsilon$ Diffusion of ε, see equation (2.29), page 35

d_M Dimensionless distance between monitor point M and jet exit, see equation (6.3), page 178

E Flatness parameter based on dissipation rate anisotropy tensor invariants, see equation (2.64), page 43

E_2 Second invariant of the dissipation rate anisotropy tensor, see equation (2.62), page 43

E_3 Third invariant of the dissipation rate anisotropy tensor, see equation (2.62), page 43

e_{ij} Stress dissipation rate anisotropy tensor, see equation (2.63), page 43

H Dimensionless jet exit height, see equation (6.2), page 178

h_M Dimensionless height of monitor point, see equation (6.4), page 179

k Turbulent kinetic energy, see equation (2.9), page 29

$\mathcal{M}_{ijkl}$ Fourth rank tensor arising in the 'exact' rapid pressure–strain rate correlation equation, see equation (2.21), page 32

P_{ij}^a Production of Reynolds stress anisotropy, see equation (4.4), page 77

P_{ij} Production of Reynolds stress, see equation (2.8), page 29

P_κ Production of turbulent kinetic energy, see equation (2.10), page 29

R_{ij} Reynolds stress tensor, see equation (2.8), page 29

$\mathrm{Re}_{\mathrm{jet}}$ Jet Reynolds number, see equation (6.5), page 179

Re_{t} Turbulent Reynolds number, see equation (2.34), page 37

$\mathbf{S}$ Global vector of source terms., see equation (3.18), page 56

S Invariant of mean strain rate tensor, see equation (2.89), page 47

S^* Dimensionless strain rate parameter, see equation (2.88), page 47

S^ϕ Source term for the transported scalar ϕ, see equation (3.1), page 52

S_{ij} Mean strain rate tensor, see equation (2.45), page 39

St Strouhal number, see equation (6.6), page 179

T_{ij} Turbulent diffusion of Reynolds stresses, see equation (2.32), page 36

U_0 Jet exit velocity, see equation (6.5), page 179

V_{ij} Viscous diffusion of Reynolds stresses, see equation (2.31), page 36

X Dimensionless impingement distance, see equation (6.1), page 178

ε Dissipation rate of turbulent kinetic energy, see equation (2.10), page 29

$\tilde{\varepsilon}$ Homogeneous dissipation rate, see equation (2.57), page 41

ε_{ij} Reynolds stress dissipation rate tensor, see equation (2.8), page 29

$\boldsymbol{\phi}$ Global vector of nodal values of variable ϕ., see equation (3.18), page 56

ϕ Generic transported scalar, see equation (3.1), page 52

ϕ_{ij} Pressure–strain rate rate correlation, see equation (2.8), page 29

ϕ_{ij}^{r} Rapid pressure–strain rate rate correlation, see equation (2.14), page 31

ϕ_{ij}^{s} Slow pressure–strain rate correlation, see equation (2.26), page 33

$\phi_{ij}^{r,w}$ Rapid pressure–strain rate wall correction, see equation (2.28), page 34

$\phi_{ij}^{s,w}$ Slow pressure–strain rate wall correction, see equation (2.27), page 34

Ω Invariant of mean vorticity tensor, see equation (2.89), page 47

Ω^{*} Dimensionless vorticity parameter, see equation (2.88), page 47

Ω_{ij} Mean vorticity tensor, see equation (2.60), page 42

Chapter 1

Introduction

1.1 Motivation

Computational fluid dynamics has in many respects matured as a tool in engineering applications. It has become a standard tool in the aerospace, automotive, turbomachinery, chemical process, and several other industries. Its use in engineering, however, has been predominantly in steady-flow, design-point and optimisation type of simulations, where the flow is in a state of equilibrium, and there is no large-scale flow separation. Nevertheless, the need for reliable and accurate simulations of unsteady, non-equilibrium turbulent flows arises in many fields of engineering and scientific studies. Examples include internal combustion engines, aerofoils at high angles of incidence, coastal hydrodynamics, and the flow of blood in veins and arteries, to name but a few.

The requirements of unsteady or largely off-design simulations stretch, and are sometimes beyond, the capabilities of standard eddy-viscosity based Reynolds-averaged treatments of turbulent flows. Nevertheless, typical time and cost limitations make it highly desirable to be able to tackle such problems with an averaged approach that is sensitive to the non-equilibrium effects on the flow quantities of interest, while avoiding the need for high-resolution approaches. Reynolds stress transport (RST) models potentially offer some of this desired sensitivity to unsteadiness and non-equilibrium conditions by allowing for misalignment between mean velocity gradients and turbulent stresses that can affect the rate of production of turbulence. However, other important aspects of flow non-equilibrium, such as delays in the transfer of energy across the turbulence spectrum, are not built-in. Moreover, it is not clear *a priori* how the principal

modelled elements in the stress transport equations, particularly pressure–strain rate redistribution, are themselves affected by non-equilibrium conditions. It is thus desirable to test existing models in a wide range of unsteady non-equilibrium flows to identify the major strengths and weaknesses of the models and main areas requiring improvement.

1.2 Development of RST Modelling

Early work leading to the development of Reynold-stress transport (RST) modelling was mainly theoretical, due to the relative complexity of this level of modelling compared to the available computational capabilities of the time. Chou (1945) constructed a formal solution to the fluctuating pressure Poisson equation that is the basis for current models of the pressure–strain-rate correlation. Later Rotta (1951), laid the foundation for Reynolds stress transport modelling by being the first to develop a closed model of all the terms in the exact equation (Speziale, 1991). Because of limited computational capability at the time, successful computations were not carried out until several decades later (Speziale, 1991). Another important development came when the continuum mechanics community speculated on the potential similarity between turbulent flow and the flow of non-Newtonian fluids (Gatski, 2004). This meant that tensor representation results from the continuum mechanics literature could be used to formulate expressions for the Reynolds-stress tensor, as first proposed by Rivlin (1957). These ideas were then expanded by Crow (1967, 1968), and Lumley (1967, 1970).

Computational work accelerated in the 1970's with the works of Daly and Harlow (1970), Reynolds (1970), Donaldson (1971), Naot et al. (1972), Hanjalić and Launder (1972), and Lumley and Khajeh-Nouri (1974). In a landmark paper, Launder, Reece, and Rodi (1975), developed a hierarchy of Reynolds-stress transport models by consolidating the work of various separate groups into a unified framework. They were able to successfully apply the models to a variety of free-shear and wall-bounded flows of practical interest (Launder et al., 1975). Their model, particularly the simple version (the 'Basic' model), has since been one of the most widely used RST models in engineering applications because of the combined advantage of being simple in form, yet retaining the ability to overcome many of the weaknesses of eddy-viscosity formulations (Hanjalić and Jakirlić, 2002).

Later Schumann (1977) introduced the concept of *realisability* as a constraint to guide model formulation. By this it is meant that models should be designed to prevent certain unphysical solutions, such as negative normal stress components, or a stress tensor that violates the Cauchy-Schwartz inequality. Lumley (1978) extensively discussed the significance and implementation of realisability requirements. He devised and used anisotropy invariant maps, or Lumley triangles, to illustrate the limiting states of turbulence with respect to values of the second and third invariants of the Reynolds-stress anisotropy tensor. Lumley pointed out that to prevent a negative normal stress component from arising during computations, the time derivative of the component must be made to vanish at the instant when the component itself vanishes, thereby preventing a negative value from arising as time progresses. Such a situation can arise near a wall or a free-surface, where the interface-normal component decays much faster than the other components as the interface is approached, thus approaching a *two-component* limit. Shih and Lumley (1985) later used these arguments to devise a realisable model for the pressure–strain-rate correlation. Their model, however, did not perform well in simple shear flows, and higher order corrections were later added to achieve better agreement with these flows (Craft and Launder, 2002). Speziale (1985, 1987) used arguments of material-frame indifference in the limit of two-dimensional turbulence to develop a model for the rapid pressure–strain-rate correlation. Speziale et al. (1991) later considered the simplest topologically equivalent form (returning the same equilibrium states) to that of the Speziale (1987) model, to arrive at a more simplified, similarly performing version (Speziale et al., 1991). This latter model is also in relatively common use in engineering RST computations.

The UMIST group, starting with the work of Fu et al. (1987), Fu (1988), Craft et al. (1989), and Craft (1991) developed a model also based on ensuring realisability in the two-component limit, but using an approach slightly different from that used by Shih & Lumley. This model (the 'TCL' model, in what follows) uses a cubic expansion of the rapid pressure–strain-rate correlation in k and a_{ij}. It was shown to achieve significant improvements over previous models in a wide range of flows.

1.3 The Present work

The present work thus aims to study the performance of a number of existing Reynolds stress transport models in a range of non-equilibrium flows. The models tested include the LRR-IP and LRR-QI models of Launder et al. (1975), the Speziale et al. (1991) model ('SSG'), the Shima (1998) low-Re model, the Jakirlić and Hanjalić (1995) low-Re model ('HJ'), and the TCL model (Craft, 1998; Craft and Launder, 2002). Both homogeneous and inhomogeneous flows are studied.

Chapter 2 presents a theoretical background on Reynolds stress transport modelling rationale and practice. The models used in the present work are also listed in this chapter. This is followed by a description, in Chapter 3, of the numerical solution techniques employed in solving the inhomogeneous turbulence cases studied in later chapters. The performance of RST models in a wide range of homogeneous turbulence cases is the subject of Chapter 4. Results are first reported for homogeneous shear flows, both with constant shear rates and also for a case with a time-varying shear. Some irrotational, plane-strain, cases are then presented, again with both constant and time-varying strain rates.

Chapter 5 considers the problem of turbulent channel flow subject to a pulsatile pressure gradient. Simulations are carried out for three frequencies corresponding to three different regimes identified in the literature. A number of challenging aspects in this set of cases are reported and discussed.

Chapter 6 presents a study of the problem of a plane jet interacting with a dead-end rectangular enclosure. Two configurations are examined, the first corresponding to a steady flow regime, and the second producing intrinsically unsteady flow interactions of a periodic nature.

Finally, conclusions are drawn in Chapter 7, and possible directions for further work are suggested.

Chapter 2

Reynolds Stress Transport Modelling

In this chapter the basic equations for the mean flow of incompressible fluids are presented, along with the equations for the relevant turbulence statistics. At the level of Reynolds stress transport modelling, the Reynolds averaged Navier–Stokes (RANS) equations are solved, along with separate equations for each independent component of the Reynolds stress tensor, as well as a transport equation for the scalar rate of dissipation of turbulent kinetic energy. The modelling approach used for the various terms appearing in the exact Reynolds stress transport equation are briefly reviewed.

2.1 Basic equations of turbulent flow

Turbulent flows are characterised by highly fluctuating velocity, pressure, and other field variables. One approach for dealing with this fluctuating nature of the flow, the one most widely used by engineers, is to work with an averaged form of the basic equations. In *Reynolds averaging* the instantaneous flow variables are decomposed into an average quantity and a fluctuation. Thus,

$$\begin{aligned} \widetilde{U}_i &= U_i + u_i \\ \widetilde{P} &= P + p\,, \end{aligned} \tag{2.1}$$

where capital letters denote averaged quantities, and small letters denote purely fluctuating quantities. The averaging can be either over time or over a repeated

realisation of an experiment with the same nominal conditions. The latter, *ensemble* averaging, will be implied in the following, to allow for temporal variations of mean quantities. When this decomposition is substituted into the Navier Stokes equations for incompressible flow, and the result is ensemble averaged, one obtains the Reynolds-averaged Navier-Stokes (RANS) equations

$$\frac{\partial U_i}{\partial t} + U_j \frac{\partial U_i}{\partial x_j} = -\frac{1}{\rho}\frac{\partial P}{\partial x_i} + \nu \frac{\partial^2 U_i}{\partial x_j^2} - \frac{\partial \overline{u_i u_j}}{\partial x_j}\,. \tag{2.2}$$

When the decomposition is substituted into the continuity equation for incompressible flow, and averaging is applied, one obtains for the mean flow

$$\frac{\partial U_i}{\partial x_i} = 0\,. \tag{2.3}$$

If this is subtracted from the instantaneous continuity equation, the continuity condition for the fluctuating velocity is obtained

$$\frac{\partial u_i}{\partial x_i} = 0\,, \tag{2.4}$$

meaning that both the mean and fluctuating velocity fields are individually divergence free. The last term in the RANS equation (2.2) contains the Reynolds stress tensor $\overline{u_i u_j}$. Thus the averaging process introduced a new unknown tensor term, and the set of equations is no longer closed. This is called the *closure* problem of averaging approaches. The task of turbulence modelling is to construct appropriate models for these stresses that relate them to the mean flow quantities, and thus to construct a closed set of equations allowing numerical solutions to be obtained. An additional implied objective in the engineering context is for the models to be as computationally cheap as possible while being able to reproduce the behaviour and phenomena of relevance to the problem in question, at the required level of accuracy.

A transport equation for the fluctuating velocity can be obtained by subtracting the RANS equation (2.2) from the Navier-Stokes equation. Using the divergence-free property of the fluctuating field, the result can be written as

$$\frac{\overline{D}u_i}{\overline{D}t} = -\frac{1}{\rho}\frac{\partial p}{\partial x_i} - u_j \frac{\partial U_i}{\partial x_j} - \frac{\partial}{\partial x_j}\big[u_i u_j - \overline{u_i u_j} - \nu \frac{\partial u_i}{\partial x_j}\big] \tag{2.5}$$

The operator $\overline{\mathrm{D}}/\overline{D}t$ is used to denote the material derivative following the mean flow

$$\frac{\overline{D}}{\overline{\mathrm{D}}t} = \frac{\partial}{\partial t} + U_j \frac{\partial}{\partial x_j} \,. \tag{2.6}$$

Since this interpretation will be used exclusively here, the over-bar on this mean-flow material derivative will subsequently be dropped. An exact equation for the Reynolds stresses can be obtained by using (2.5) to construct

$$\frac{\mathrm{D}\overline{u_i u_j}}{\mathrm{D}t} = \overline{u_j \frac{\mathrm{D}u_i}{\mathrm{D}t} + u_i \frac{\mathrm{D}u_j}{\mathrm{D}t}} \,.$$

Where it has been assumed that averaging and taking the material derivative (2.6) commute. The result is

$$\begin{aligned} \frac{\mathrm{D}\overline{u_i u_j}}{\mathrm{D}t} = & -\left(\overline{u_i u_k} \frac{\partial U_j}{\partial x_k} + \overline{u_j u_k} \frac{\partial U_i}{\partial x_k} \right) \\ & + \overline{\frac{p}{\rho}\left(\frac{\partial u_i}{\partial x_j} + \frac{\partial u_j}{\partial x_i} \right)} \\ & + \frac{\partial}{\partial x_k}\left[\nu \frac{\partial \overline{u_i u_j}}{\partial x_k} - \overline{u_i u_j u_k} - \overline{\frac{p}{\rho}(u_i \delta_{jk} + u_j \delta_{ik})} \right] \\ & - 2\nu \overline{\frac{\partial u_i}{\partial x_k} \frac{\partial u_j}{\partial x_k}} \end{aligned} \tag{2.7}$$

The first term on the right hand side above is the production rate of Reynolds stress by mean velocity gradients. This term is closed at the RST level since it is given in terms of quantities that are being solved for at this level. All the remaining terms in the equation, except for viscous diffusion, require modelling. The second term is a correlation between the fluctuating pressure and the fluctuating strain rate. From continuity this term is traceless, so it does not contribute directly to the kinetic energy of the turbulence. Its effect is to redistribute the energy between the stress components, so it plays a very important role in determining the degree of anisotropy of the stresses. Accordingly, it has received much attention from researchers, and continues to do so. The third term in (2.7) is a combination of several diffusion terms, all having the effect of spatial redistribution of the Reynolds stresses. Finally, the last term is the dissipation rate of Reynolds stresses by viscous action at the smallest scales of turbulence. Since the smallest scales of motion are assumed to be isotropic, the dissipation rate tensor

is frequently modelled as $\varepsilon_{ij} = \frac{2}{3}\varepsilon\,\delta_{ij}$, where ε is the scalar dissipation rate of turbulent kinetic energy. This approximation is not applicable near walls or free surfaces, where the dissipation tensor becomes markedly anisotropic. Equation (2.7) can be written in short form as

$$\frac{\mathrm{D}\overline{u_i u_j}}{\mathrm{D}t} = P_{ij} + \phi_{ij} + \mathcal{D}_{ij} - \varepsilon_{ij}\ , \tag{2.8}$$

where it is understood that each term above defines the notation for the corresponding term in (2.7).

An equation for the kinetic energy associated with the turbulent fluctuations, $k = \frac{\overline{u_i u_i}}{2}$, can be obtained by taking half the contraction of (2.7). The resulting equation is

$$\frac{\mathrm{D}k}{\mathrm{D}t} = -\overline{u_i u_k}\frac{\partial U_i}{\partial x_k} + \frac{\partial}{\partial x_k}\left[\nu\frac{\partial k}{\partial x_k} - \overline{u_i u_i u_k} - \frac{1}{\rho}\overline{p u_i}\delta_{ik}\right] - \nu\overline{\frac{\partial u_i}{\partial x_k}\frac{\partial u_i}{\partial x_k}}\ . \tag{2.9}$$

In short form, this can be written

$$\frac{\mathrm{D}k}{\mathrm{D}t} = P_\kappa + \mathcal{D} - \varepsilon \tag{2.10}$$

The first term on the right hand side of (2.9) is the production of turbulent kinetic energy by mean velocity gradients. The next term is the diffusion of turbulent kinetic energy by various mechanisms. Finally, the last term is the scalar dissipation rate of turbulent kinetic energy. The short form (2.10) defines the notation that will be used in the following for the respective terms in (2.9). It is often convenient to work with the deviatoric Reynolds stress anisotropy tensor a_{ij} defined as,

$$a_{ij} = \frac{\overline{u_i u_j}}{k} - \frac{2}{3}\,\delta_{ij}\,. \tag{2.11}$$

2.2 Pressure–strain rate correlation

Modelling of the pressure–strain rate correlation is to a large extent guided by consideration of the exact equation for it. An equation for the fluctuating pressure can be obtained by taking the divergence of (2.5), and invoking continuity (2.4).

This gives

$$\frac{1}{\rho}\frac{\partial^2 p}{\partial x_k \partial x_k} = -2\frac{\partial U_i}{\partial x_j}\frac{\partial u_j}{\partial x_i} - \frac{\partial^2}{\partial x_i \partial x_j}(u_i u_j - \overline{u_i u_j}) \tag{2.12}$$

A formal solution to this Poisson equation can be constructed using the method of Green's functions, as first demonstrated by Chou (1945). The Green's function of the Laplacian operator is

$$g(\mathbf{x}|\mathbf{x}') = \frac{-1}{4\pi|\mathbf{x}-\mathbf{x}'|}\,.$$

The fluctuating pressure is thus given by

$$\frac{p}{\rho} = \frac{1}{4\pi}\iiint_V \left[-2\frac{\partial U_i}{\partial x'_j}\frac{\partial u_j}{\partial x'_i} - \frac{\partial^2}{\partial x'_i \partial x'_j}(u_i u_j - \overline{u_i u_j})\right]_{\mathbf{x}',t} \frac{\mathrm{d}\mathbf{x}'}{|\mathbf{x}-\mathbf{x}'|} + \text{Surface integral.} \tag{2.13}$$

It can be seen from this equation that the fluctuating pressure can be decomposed into three components (Pope, 2000), corresponding to the three terms appearing on the right-hand side of (2.13). The first term is linear in the turbulent fluctuations, and responds directly to changes in mean velocity gradient. It is thus called the *rapid* pressure, p^r. The second is a turbulence-turbulence interaction term, that does not respond directly to changes in the mean flow, but through the turbulent cascade process, and is thus called the *slow* pressure, p^s. The last term is the solution to the homogeneous (Laplace) equation and satisfies appropriate boundary conditions that ensure the superposition of the three parts, p, satisfies its own boundary conditions (Pope, 2000). This final term is only significant close to a wall or a free surface, and, since the emphasis here is on modelling regions away from walls, it will be neglected. Wall effects on ϕ_{ij} are considered in Section 2.2.1.

Based on the above decomposition, the pressure–strain rate correlation can similarly be decomposed into rapid, slow, and *wall influence* terms. The rapid part can be constructed as follows

$$\phi^r_{ij} = \overline{\frac{p^r}{\rho}\left(\frac{\partial u_i}{\partial x_j} + \frac{\partial u_j}{\partial x_i}\right)} \tag{2.14}$$

$$\begin{aligned}\frac{p^r}{\rho}\left(\frac{\partial u_i}{\partial x_j}\right) =& \frac{1}{2\pi}\iiint_{-\infty}^{\infty}\left(\frac{\partial U_k}{\partial x'_l}\frac{\partial u_l}{\partial x'_k}\right)_{\mathbf{x}',t}\left(\frac{\partial u_i}{\partial x_j}\right)_{\mathbf{x},t}\frac{\mathrm{d}\mathbf{x}'}{|\mathbf{x}-\mathbf{x}'|} \\ =& \frac{1}{2\pi}\frac{\partial U_k}{\partial x_l}\iiint_{-\infty}^{\infty}\frac{\partial^2}{\partial x_j \partial x'_k}(u_i(\mathbf{x})u_l(\mathbf{x}'))\frac{\mathrm{d}\mathbf{x}'}{|\mathbf{x}-\mathbf{x}'|}.\end{aligned} \tag{2.15}$$

In taking $\frac{\partial U_k}{\partial x'_l}$ outside the integral it is assumed that this term is reasonably constant over the volume integral. In homogeneous flows, that is of course exact, but is an approximation in inhomogeneous ones. One can thus write:

$$\phi^r = \frac{\partial U_k}{\partial x_l}\left(\mathcal{M}_{iljk} + \mathcal{M}_{jlik}\right), \tag{2.16}$$

where the fourth rank tensor $\mathcal{M}_{iljk}$ is given by

$$\mathcal{M}_{iljk} = \frac{-1}{2\pi}\iiint_{\infty}^{\infty}\frac{\partial^2\overline{u_i(\mathbf{x})u_l(\mathbf{x}+\mathbf{r})}}{\partial r_j \partial r_k}\frac{\mathrm{d}\mathbf{r}}{|\mathbf{r}|}, \tag{2.17}$$

using $\mathbf{r} = \mathbf{x}' - \mathbf{x}$ for the separation distance. The $\mathcal{M}_{iljk}$ tensor is symmetric in the first two indices, and in the last two

$$\mathcal{M}_{iljk} = \mathcal{M}_{lijk} = \mathcal{M}_{ilkj}. \tag{2.18}$$

The divergence-free velocity condition means that contraction over the middle indices results in the quantity vanishing:

$$\mathcal{M}_{ijjk} = 0\,, \tag{2.19}$$

and contraction over the last two indices can be shown to yield (twice) the Reynolds stress tensor

$$\mathcal{M}_{ilkk} = 2\,\overline{u_i u_l}\,. \tag{2.20}$$

The last of these kinematic conditions (2.20) suggested to workers that the $\mathcal{M}$ tensor could be modelled as a function of the Reynolds stresses (Launder et al., 1975). The approach taken was to model $\mathcal{M}$ as a polynomial function in the stresses. The most general fourth-rank tensor linear in the Reynolds stresses

satisfying the symmetry conditions (2.18) is

$$\begin{aligned}\mathcal{M}_{ijkl} =&\alpha\delta_{kl}\overline{u_iu_j} + \beta(\delta_{ik}\overline{u_ju_l} + \delta_{il}\overline{u_ju_k} + \delta_{jk}\overline{u_iu_l} + \delta_{jl}\overline{u_iu_k})\\ &+\gamma\delta_{ij}\overline{u_ku_l} + [\eta\delta_{ij}\delta_{kl} + v(\delta_{ik}\delta_{jl} + \delta_{il}\delta_{jk})]k,\end{aligned} \tag{2.21}$$

where the coefficients $\alpha, \beta, \gamma, \eta, v$ are constants (or functions of the invariants of a_{ij}). The continuity condition (2.19), and the normalisation condition (2.20) can be used to reduce the number of undetermined constants to one. When this is done, and the resulting modelled $\mathcal{M}_{ijkl}$ is substituted into (2.16) the resulting linear rapid pressure–strain rate model is

$$\phi^r_{ij} = -\frac{\gamma+8}{11}(P_{ij}-2/3P\delta_{ij}) - \frac{30\gamma-2}{55}k\left(\frac{\partial U_i}{\partial x_j}+\frac{\partial U_j}{\partial x_i}\right) - \frac{(8\gamma-2)}{11}(D_{ij}-2/3D\delta_{ij})\,, \tag{2.22}$$

where D_{ij} is given by

$$D_{ij} = -\overline{u_iu_k}\frac{\partial U_k}{\partial x_j} - \overline{u_ju_k}\frac{\partial U_k}{\partial x_i}\,, \tag{2.23}$$

and $D = D_{ii}/2$. This is the first of the two Launder-Reece-Rodi (LRR) models in Launder et al. (1975), called the *Quasi-Isotropic* model (LRR-QI). A simplified version of (2.22) was also suggested in Launder et al. (1975) by observing that the dominant term in this equation is the first one appearing on the right hand side. The model thus obtained, first proposed by Naot et al. (1972), is sometimes termed the *isotropization of production* model (LRR-IP),

$$\phi^r_{ij} = -c_2(P_{ij} - \tfrac{2}{3}P\,\delta_{ij}). \tag{2.24}$$

Various other models have been proposed following similar lines of reasoning, in which $\mathcal{M}$ is modelled as a tensor-polynomial function of the Reynolds stress tensor or, equivalently, expressed in terms of k and a_{ij}

$$\mathcal{M} = \mathcal{M}(k, \mathbf{a})\,. \tag{2.25}$$

It is worth pointing out at this stage that there is an intrinsic weakness in all such models of the form (2.25). The tensor $\mathcal{M}$, as defined by (2.17), contains two kinds of directional information – the direction of the energetic velocity components, and the direction of variation or dependence of the two-point correlation (Pope,

2000). Only the former type of information is contained in the Reynolds stress tensor, so two fields having the same Reynolds stresses can have different $\mathcal{M}$ tensors. More explicitly put, the evolution of the Reynolds stresses is not uniquely determined by the Reynolds stresses (Pope, 2000). This is an intrinsic limitation in RST modelling, that is difficult to overcome without significantly complicating the modelling approach and/or computational cost (Johansson and Hallbäck, 1994; Kassinos and Reynolds, 1994). This limitation is known to cause poor results in flows where the velocity gradient has a strong rotational component, such as in pure (or dominant) rotation, and in high shear rate flows (Johansson and Hallbäck, 1994). However, in many other flows, including ones with significant rotational effects, RST models have been shown to produce very good results.

As for the slow pressure–strain rate term, ϕ_{ij}^s, it is difficult to extract anything from the exact expression, pertaining to the non-linear turbulence–turbulence interaction part of (2.13). Most early models followed Rotta's (1951) linear return to isotropy model for the slow term

$$\phi_{ij}^s = -C_1 \varepsilon a_{ij} \,. \tag{2.26}$$

This model is motivated by the decay of homogeneous anisotropic turbulence in the absence of mean velocity gradients. It is generally observed that in such cases turbulence progressively tends towards an isotropic state, hence the negative sign in (2.26).

Experimental evidence shows that the return-to-isotropy process is in fact non-linear in a_{ij} (Chung and Kim, 1995). When plotted on anisotropy invariant maps, the paths taken during return-to-isotropy experiments are not straight lines, and have different behaviour depending on the sign of the third invariant (Pope, 2000). It is also found that the rate of return is highly dependent on the Reynolds number. A number of nonlinear models for the slow pressure strain term have been suggested in the literature.

2.2.1 Wall effects on ϕ_{ij}

The presence of a wall alters pressure fluctuations by viscous effect through the no-slip condition, and by inviscid effect through the impermeability condition. DNS results show that the viscous effect is confined to a region within $y^+ \approx 15$ from the wall (Mansour et al., 1988). The inviscid wall-blocking effect on the other hand is

significant where the distance from the wall is of the same order as the turbulent length scale. Wall blocking causes two opposing effects; *wall reflection* of the fluctuating pressure field increases the energy-redistributing pressure fluctuations, which pushes turbulence towards isotropy, while it also causes selective damping of the wall-normal fluctuating velocity component in turbulent eddies, thereby increasing anisotropy. The latter effect dominates, and turbulence anisotropy near a wall is higher than that in a free shear flow at a similar rate of shear. To account for this, Gibson and Launder (1978) proposed two additive corrections to ϕ_{ij} using the unit normal vector to the wall, n_i. The first, based on the proposal of Shir (1973), is an additive correction to the slow part

$$\phi_{ij}^{s,w} = C_1^w \frac{\varepsilon}{k} \left(\overline{u_k u_m} n_k n_m \delta_{ij} - \tfrac{3}{2} \overline{u_i u_k} n_k n_j - \tfrac{3}{2} \overline{u_j u_k} n_k n_i \right) f_w \tag{2.27}$$

and the second, is a correction to the rapid part

$$\phi_{ij}^{r,w} = C_2^w \left(\phi_{km}^r n_k n_m \delta_{ij} - \tfrac{3}{2} \phi_{ik}^r n_k n_j - \tfrac{3}{2} \phi_{jk}^r n_k n_i \right) f_w \tag{2.28}$$

where $C_1^w = 0.5$, $C_2^w = 0.3$, and $f_w = 0.4k^{3/2}/(\varepsilon x_n)$ is a damping function based on the ratio of the turbulence length scale to the normal distance to the wall, x_n.

2.3 Modelling dissipation

While modelling of the turbulent kinetic energy, and of the pressure–strain rate correlation, has been to at least some degree guided by consideration of their exact equations, the same is not true for the standard dissipation rate model (Pope, 2000). Dissipation of turbulent kinetic energy is associated with the smallest scales of the fluctuating field, while the kinetic energy itself is mostly contained in the largest scales of fluctuations. The exact dissipation rate equation is comprised of a large number of terms that are all related to dissipative-scale processes, and all but one of the source-terms require modelling. It is thus not a useful starting point for modelling the dissipation rate. Instead the more empirical approach taken is motivated by the spectral energy transfer view of dissipation. The kinetic energy of the larger energy containing eddies is transferred by vortex-stretching in the presence of mean velocity gradients to smaller eddies, and the same process occurs at the 'next' smaller scales, and so on to the smallest dissipative scales, where kinetic energy is finally converted to heat by viscous (molecular) action. If

the molecular viscosity is somehow changed, all that happens is that the size of the dissipative scales change to accommodate the rate of energy they receive, but the rate itself is not affected. Thus even though the *mechanism* of dissipation is governed by processes that occur at the smallest scales, dissipation can also be viewed as an energy-transfer rate that readjusts itself with the amount of energy it receives. In this sense, the amount (as opposed to the mechanism) of dissipation is in fact determined by the energy in larger scales. Under the assumption of spectral equilibrium, the transfer rate of energy across the spectrum of turbulence scales is constant and determined by the rate of energy input. Based on this assumption, and the preceding arguments, the conventional equation for dissipation is assumed to be of the form

$$\frac{\mathrm{D}\varepsilon}{\mathrm{D}t} = C_{\varepsilon 1}\frac{\varepsilon}{k}P + \mathcal{D}_{\varepsilon} - C_{\varepsilon 2}\frac{\varepsilon^2}{k}\,, \tag{2.29}$$

where $\mathcal{D}_{\varepsilon}$ is the diffusion of ε. The modelled production term above reflects the assumed direct link between a single rate of transfer of energy across the spectrum and production of energy at the large scales. This assumption is an obvious weakness in the model when the turbulence is not in equilibrium, as when unsteady solutions are sought, or where the time-scale of the mean flow is of the same order or smaller than the characteristic time-scale of turbulence. In such cases the small-scale turbulence may not have enough time to adjust to the large-scale scale variations, and the instantaneous link implied by the production term in (2.29) is questionable.

The destruction term in (2.29) is motivated by consideration of the decay of homogeneous isotropic turbulence in the absence of production (Pope, 2000). In such a flow one expects that the turbulence will decay in a self-similar form in which the rates of decay of k and ε are proportional

$$\frac{k/\frac{dk}{dt}}{\varepsilon/\frac{d\varepsilon}{dt}} = \frac{-k/\varepsilon}{\varepsilon/\frac{d\varepsilon}{dt}} = C$$

If this proportionality constant is labelled $C_{\varepsilon 2}$, the following destruction term is implied

$$\frac{d\varepsilon}{dt} = -C_{\varepsilon 2}\frac{\varepsilon^2}{k} \tag{2.30}$$

2.4 Diffusion modelling

There are three diffusive transport terms on the right hand side of (2.7). The first is the viscous diffusion term

$$V_{ij} = \nu \frac{\partial^2 \overline{u_i u_j}}{\partial x_k \partial x_k} \tag{2.31}$$

which is closed and does not require modelling. The following two terms are the pressure diffusion and turbulent convection, respectively. Most commonly these are modelled together as a combined turbulent diffusion term, T_{ij}, using the generalised gradient diffusion hypothesis (GGDH) of Daly and Harlow (1970),

$$T_{ij} = \frac{\partial}{\partial x_l} \left(C_s \frac{\varepsilon}{k} \overline{u_l u_k} \frac{\partial \overline{u_i u_j}}{\partial x_k} \right) \tag{2.32}$$

where C_s is typically 0.22.

A deficiency of this model is that it does not preserve the symmetry under cyclic permutation of indices that is exhibited by the triple velocity moments $\overline{u_i u_j u_k}$. This is only significant when the triple moments and pressure diffusion are modelled separately. In such case an improved model that has been suggested by Hanjalić and Launder (1972) is often used,

$$\overline{u_i u_j u_k} = -C_s \frac{k}{\varepsilon} \left(\overline{u_i u_l} \frac{\partial \overline{u_j u_k}}{\partial x_l} + \overline{u_j u_l} \frac{\partial \overline{u_k u_i}}{\partial x_l} + \overline{u_k u_l} \frac{\partial \overline{u_i u_j}}{\partial x_l} \right). \tag{2.33}$$

More elaborate models exist in the literature, but have not been used in the present work.

2.5 Accounting for low-Re effects

Viscous effects on turbulence properties and their implications on modelling are considered in this section. The absence of viscous terms in the equation for fluctuating pressure (2.12) suggests that viscous effects on the fluctuating pressure will be of secondary importance compared to the inviscid effects due to impermeability, considered in section 2.2.1. The focus of the discussion is thus directed to the dissipation rate tensor, and the transport equation for the scalar dissipation rate. When discussing low-Re effects, reference is frequently made to the

turbulent Reynolds number, $\mathrm{Re_t}$, defined as

$$\mathrm{Re_t} = \frac{k^2}{\nu\varepsilon} \tag{2.34}$$

As previously mentioned, at high Reynolds numbers the dissipation rate tensor is assumed to be isotropic, $\varepsilon_{ij} = \frac{2}{3}\,\varepsilon\,\delta_{ij}$. This, however, will cease to be true near a wall where the high anisotropy of the turbulence is expected to be increasingly felt at the smaller scales as the wall is approached. The simplest model for this effect is that of Rotta (1951), which is based on the idea that the anisotropy of the dissipation rate tensor is similar to the stress anisotropy, thus

$$\varepsilon_{ij} = \frac{\overline{u_i u_j}}{k}\varepsilon \tag{2.35}$$

This model was used by Hanjalić and Launder (1976) to give the following blending approximation for the dissipation rate tensor

$$\varepsilon_{ij} = \frac{2}{3}\,\varepsilon\left[(1-f_s)\,\delta_{ij} + f_s\frac{3}{2}\frac{\overline{u_i u_j}}{k}\right], \tag{2.36}$$

where f_s is a function of $\mathrm{Re_t}$ whose value ranges from 1 to 0 as $\mathrm{Re_t}$ ranges from 0 to ∞, ensuring the desired behaviour of ε_{ij} in these limits. The near-wall model (2.35) is the simplest form accounting for near-wall anisotropy of the dissipation tensor. Launder and Reynolds (1983) have shown that this form does not give the correct near-wall asymptotic behaviour of the individual tensor elements, which are rather given by

$$\begin{aligned}
\frac{\varepsilon_{ij}}{\varepsilon} &= \frac{\overline{u_i u_j}}{k}, \quad i \neq 2, j \neq 2 \\
\frac{\varepsilon_{12}}{\varepsilon} &= 2\frac{\overline{u_i u_2}}{k}, \quad i \neq 2 \\
\frac{\varepsilon_{22}}{\varepsilon} &= 4\frac{\overline{u_2 u_2}}{k}.
\end{aligned} \tag{2.37}$$

What is needed then is a term to replace the Rotta model in (2.36) which yields the correct asymptotic behaviour described by (2.37), and which contracts to 2ε. One possible form that satisfies these requirements is

$$\varepsilon^*_{ij} = \frac{\varepsilon/k\,(\overline{u_i u_j} + \overline{u_i u_k}\,n_j\,n_k + \overline{u_j u_k}\,n_i\,n_k + \overline{u_k u_l}\,n_k\,n_l\,\delta_{ij})}{\left(1 + \frac{5}{2}n_p n_q \overline{u_p u_q}/k\right)}, \tag{2.38}$$

where n_i represents a component of the wall-normal unit vector (Pope, 2000). The use of the wall vector in a model is undesirable because of the ambiguity it introduces in complex geometries. One way to avoid it is based on the observation that the quantity $\nabla k^{1/2}$, evaluated near a wall, is a vector that points in the wall-normal direction. Thus

$$\vec{n} = \frac{\nabla k^{1/2}}{|\nabla k^{1/2}|}, \tag{2.39}$$

and using the value of the dissipation at the wall for a wall with $\vec{n} = (0, 1, 0)$,

$$|\nabla k^{1/2}|_{x_2=0} = \left(\frac{\partial k^{1/2}}{\partial x_2} \frac{\partial k^{1/2}}{\partial x_2} \right)^{1/2}_{x_2=0} = \sqrt{\frac{\varepsilon}{2\nu}}. \tag{2.40}$$

The quantity $n_i n_j$ can therefore be replaced by

$$n_i n_j = \frac{2\nu}{\varepsilon} \frac{\partial k^{1/2}}{\partial x_i} \frac{\partial k^{1/2}}{\partial x_j}. \tag{2.41}$$

Following Hanjalić and Launder (1976), when considering the implications of Low-Re effects on dissipation rate modelling, it is instructive to consider the exact transport equation for the energy dissipation rate. This is given by (Daly and Harlow, 1970)

$$\begin{aligned} \frac{\mathrm{D}\varepsilon}{\mathrm{D}t} = & -2\nu \overline{\frac{\partial u_i}{\partial x_k} \frac{\partial u_i}{\partial x_l} \frac{\partial u_k}{\partial x_l}} - 2\overline{\left(\nu \frac{\partial^2 u_i}{\partial x_k \partial x_l} \right)^2} - \frac{\partial}{\partial x_k} \left[\overline{u_k \varepsilon'} + \frac{2\nu}{\rho} \overline{\frac{\partial u_k}{\partial x_l} \frac{\partial p}{\partial x}} - \nu \frac{\partial \varepsilon}{\partial x_k} \right] \\ & - 2\nu \left(\overline{\frac{\partial u_i}{\partial x_l} \frac{\partial u_l}{\partial x_i}} + \overline{\frac{\partial u_l}{\partial x_i} \frac{\partial u_l}{\partial x_k}} \right) \frac{\partial U_i}{\partial x_k} - 2\nu \overline{u_k \frac{\partial u_i}{\partial x_l}} \frac{\partial^2 U_i}{\partial x_k \partial x_l}. \end{aligned} \tag{2.42}$$

All the terms on the right hand side above are unclosed, with the exception of viscous diffusion. The first two terms on the right hand side of (2.42) are the dominant ones in high Re flows. Respectively they represent generation and destruction of ε. The third term, which represents a combination of diffusive processes, can be of the same order as the difference of the first two, and must therefore be retained. These three terms are modelled by the three terms that typically appear in high-Re ε transport models, as in section 2.3. The fourth and fifth terms are respectively of order ${\mathrm{Re}_\mathrm{t}}^{1/2}$ and Re_t smaller than the other terms (Hanjalić and Launder, 1976), and are thus neglected in high-Re model versions. In low-Re models these terms need to be reconsidered and accounted

for if necessary. The last term is often modelled as

$$-2\nu\overline{u_k\frac{\partial u_i}{\partial x_l}}\frac{\partial^2 U_i}{\partial x_k \partial x_l} = C_{\varepsilon 3}\nu\frac{k\overline{u_j u_k}}{\varepsilon}\left(\frac{\partial^2 U_i}{\partial x_j \partial x_l}\right)\left(\frac{\partial^2 U_i}{\partial x_k \partial x_l}\right). \tag{2.43}$$

This term is present in several Low-Re models developed by the Manchester group. As for the fourth term, initial proposals meant to account for it by allowing the coefficient of the production and destruction terms, $C_{\varepsilon 1}$and $C_{\varepsilon 2}$, to be functions of $\mathrm{Re_t}$. Similarly, possible viscous effects on the diffusion terms were to be accounted for by allowing the term C_ε to depend on $\mathrm{Re_t}$ (Hanjalić and Launder, 1976). However, computations revealed that adding the term in (2.43) alone was sufficient in producing good agreement between computed energy profiles and available data to within experimental accuracy. Thus dependence of the coefficients $C_{\varepsilon 1}$, $C_{\varepsilon 2}$, C_ε on the turbulence Reynolds number is often (not always) abandoned. Finally the viscous diffusion term, neglected in high-Re models, is retained in its exact form.

2.6 The Launder–Reece–Rodi models

In their seminal 1975 paper, Launder, Reece, and Rodi laid out a hierarchy of RST models based on arguments presented in section 2.2. Two rapid pressure-strain rate models were proposed. The first is the quasi-isotropic model (LRR-QI), which has the most general linear tensorial form satisfying the required symmetry conditions, and is given by

$$\phi^r_{ij} = -C_2(P_{ij} - \tfrac{2}{3}\delta_{ij}\,P_\kappa) - C_3(D_{ij} - \tfrac{2}{3}\delta_{ij}\,P_\kappa) - 2C_4 k\,S_{ij}, \tag{2.44}$$

where S_{ij} is the mean strain rate tensor, defined as:

$$S_{ij} = \frac{1}{2}\left(\frac{\partial U_i}{\partial x_j} + \frac{\partial U_j}{\partial x_i}\right) \tag{2.45}$$

and the coefficients have the following values

$$C_2 = 0.764, \quad C_3 = 0.182, \quad C_4 = 0.109 \tag{2.46}$$

The second rapid pressure-strain rate model is the isotropization of production model (LRR-IP), which is also referred to as the 'Basic' model, and simply retains

the first term of the QI model and neglects the other two. Thus,

$$\phi_{ij}^r = -C_2(P_{ij} - \tfrac{2}{3}\delta_{ij}\, P_\kappa), \tag{2.47}$$

where the coefficient C_2 is now set at 0.6. Both models use the Rotta return-to-isotropy model for the slow pressure-strain rate term,

$$\phi_{ij}^s = -C_1\varepsilon a_{ij}\,, \tag{2.48}$$

but the coefficient C_1 is 1.5 for the QI model and 1.8 for the IP model.

In the original proposal turbulent diffusion T_{ij} is modelled using (2.33) for the triple velocity moments (pressure diffusion is usually neglected). In many later implementations, as is in the present work, this is replaced by the simpler GGDH. Thus the models can be written as

$$\frac{\mathrm{D}\overline{u_iu_j}}{\mathrm{D}t} = P_{ij} - C_1\varepsilon a_{ij} + \phi_{ij}^r + \phi_{ij}^{s,w} + \phi_{ij}^{r,w} + \frac{\partial}{\partial x_l}\left(C_s\frac{\varepsilon}{k}\overline{u_lu_k}\frac{\partial\overline{u_iu_j}}{\partial x_k}\right) - \tfrac{2}{3}\delta_{ij}\varepsilon \tag{2.49}$$

where ϕ_{ij}^r is replaced by either the QI or IP models, and the wall-reflection terms $\phi_{ij}^{s,w}, \phi_{ij}^{r,w}$ are given by (2.27) and (2.28), respectively. Since these models are intended as high Re models, the viscous diffusion term is neglected and an isotropic dissipation rate tensor is assumed.

Finally, closure is completed with the standard high-Re dissipation rate equation, given by

$$\frac{\mathrm{D}\varepsilon}{\mathrm{D}t} = C_{\varepsilon1}\frac{\varepsilon}{k}P_\kappa - C_{\varepsilon2}\frac{\varepsilon^2}{k} + \frac{\partial}{\partial x_k}\left(C_\varepsilon\frac{k}{\varepsilon}\overline{u_ku_l}\frac{\partial\varepsilon}{\partial x_l}\right), \tag{2.50}$$

where

$$C_{\varepsilon1} = 1.44, \quad C_{\varepsilon2} = 1.92, \quad C_\varepsilon = 0.15. \tag{2.51}$$

2.7 The Shima low-Re model

In its original form the Launder and Shima (1989) model is a low-Re version of the Basic model that uses wall reflection terms and includes $\mathrm{Re_t}$-based damping coefficients to return the correct near-wall behaviour. Shima (1998) later proposed a low-Re model based on the QI pressure-strain rate model that does away with the wall reflection terms in the interest of more general applicability

to complex geometries. The model admittedly gives stress anisotropy results in steady channel flow that are inferior to his previous low-Re formulation, but this is a compromise made in order to discard the wall reflection terms with their associated difficulties related to complex geometries. The pressure-strain rate coefficients are no longer constant, and are given by the following expressions:

$$C_1 = 1 + 2.45A_2^{0.25}A^{0.75}[1 - \exp(-49A^2)] \times \{1 - \exp[-(Re_t/60)^2]\} \tag{2.52a}$$

$$C_2 = 0.7A \tag{2.52b}$$

$$C_3 = 0.3A^{0.5} \tag{2.52c}$$

$$C_4 = 0.65A(0.23C_1 + C_2 - 1) + 1.3A_2^{0.25}C_3 \tag{2.52d}$$

where A_2, A_3 are the second and third invariants of the stress anisotropy tensor:

$$A_2 = a_{ij}a_{ji} \quad A_3 = a_{ij}a_{jk}a_{ki}\,. \tag{2.53}$$

and A is the 'flatness' parameter first defined by Lumley (1978),

$$A = 1 - \tfrac{9}{8}(A_2 - A_3). \tag{2.54}$$

Turbulent diffusion, comprising the triple velocity correlation and the pressure velocity correlation, is modelled using the simple gradient diffusion of Daly and Harlow (1970)

$$T_{ij} = \frac{\partial}{\partial x_k}\left(C_s\frac{k}{\varepsilon}\overline{u_k u_l}\frac{\partial \overline{u_i u_j}}{\partial x_l}\right) \tag{2.55}$$

where $C_s = 0.22$.

The dissipation equation is given by

$$\frac{\mathrm{D}\varepsilon}{\mathrm{D}t} = C_{\varepsilon 1}\frac{\varepsilon}{k}P - C_{\varepsilon 2}\frac{\varepsilon\tilde{\varepsilon}}{k} + \frac{\partial}{\partial x_k}\left(C_\varepsilon\frac{k}{\varepsilon}\overline{u_k u_l}\frac{\partial\varepsilon}{\partial x_l} + \nu\frac{\partial\varepsilon}{\partial x_k}\right). \tag{2.56}$$

where $\tilde{\varepsilon}$ is the homogeneous dissipation rate, defined as:

$$\tilde{\varepsilon} = \varepsilon - 2\nu\left(\frac{\partial k^{1/2}}{\partial x_i}\right)^2. \tag{2.57}$$

The coefficients $C_{\varepsilon 2}$,C_ε retain their typical values 1.92, 0.15 respectively, but $C_{\varepsilon 1}$

is prescribed as:

$$C_{\varepsilon 1} = 1.44 + \beta_1 + \beta_2\,, \tag{2.58a}$$
$$\beta_1 = 0.25A\min(\lambda/2.5 - 1,\, 0) - 1.4A\min(P/\varepsilon - 1,\, 0)\,, \tag{2.58b}$$
$$\beta_2 = 1.0A\lambda^2\max(\lambda/2.5 - 1,\, 0)\,, \tag{2.58c}$$
$$\lambda = \min(\lambda^*,\, 4)\,, \tag{2.58d}$$
$$\lambda^* = \left[\frac{\partial}{\partial x_i}\left(\frac{k^{1.5}}{\varepsilon}\right)\frac{\partial}{\partial x_i}\left(\frac{k^{1.5}}{\varepsilon}\right)\right] \tag{2.58e}$$

2.8 The Speziale–Sarkar–Gatski model

Speziale et al. (1991) developed a pressure-strain rate model that is quadratic in a_{ij} by first considering the most general form for ϕ_{ij} (slow and rapid) that is linear in the mean strain and rotation tensors and quadratic in a_{ij}. Then they obtained their model by considering the simplest subset of that general form that has an equivalent structural equilibrium in plane homogeneous flows. The resulting model has a rapid part that is linear in a_{ij}, and a quadratic slow part, given by

$$\begin{aligned}\phi_{ij} =& -(2d_1\varepsilon + d_1^* P_\kappa)\frac{a_{ij}}{2} + \frac{d_2}{4}\varepsilon(a_{ik}a_{kj} - \tfrac{1}{3}a_{kl}a_{kl}\delta_{ij}) \\ &+ \left(d_3 - d_3^*\frac{\sqrt{A_2}}{2}\right)kS_{ij} + \frac{d_4}{2}k(a_{ik}S_{jk} + a_{jk}S_{ik} - \tfrac{2}{3}a_{kl}S_{kl}\delta_{ij}) \\ &+ \frac{d_5}{2}k(a_{ik}\Omega_{jk} + a_{jk}\Omega_{ik})\,,\end{aligned} \tag{2.59}$$

where Ω_{ij} is the mean vorticity tensor defined as:

$$\Omega_{ij} = \frac{1}{2}\left(\frac{\partial U_i}{\partial x_j} - \frac{\partial U_j}{\partial x_i}\right), \tag{2.60}$$

and the coefficients have the following values

$$d_1 = 1.7, \quad d_1^* = 1.8, \quad d_2 = 4.2, \quad d_3 = \tfrac{4}{5}, \quad d_3^* = 1.3, \quad d_4 = 1.25, \quad d_5 = 0.4\,. \tag{2.61}$$

The rapid part of the SSG model, aside from the nonlinear dependence on A_2 in third term of (2.59), is tensorially equivalent to the QI model.

Diffusion is modelled using the GGDH, and the standard high-Re version of

the ε equation (2.50) is used, but the coefficient $C_{\varepsilon 2}$ is assigned the slightly lower value of 1.83.

2.9 The Hanjalić–Jakirlić low-Re model

Jakirlić and Hanjalić (1995) developed a low-Re RSTM that is based on the LRR-IP model, and the Gibson and Launder (1978) wall corrections (2.27) and (2.28), making modifications to handle Low-Re and near-wall effects. The modifications are expressed in terms of $\mathrm{Re_t}$, the stress anisotropy invariants, A_2, A_3, in addition to invariants of the stress dissipation rate anisotropy tensor, E_2, E_3, defined as:

$$E_2 = e_{ij}e_{ji} \quad E_3 = e_{ij}e_{jk}e_{ki}\,, \tag{2.62}$$

$$e_{ij} = \frac{\varepsilon_{ij}}{\varepsilon} - \frac{2}{3}\delta_{ij}\,. \tag{2.63}$$

A 'flatness' parameter based on the stress dissipation rate anisotropy invariants is also used:

$$E = 1 - \frac{9}{8}(E_2 - E_3) \tag{2.64}$$

The modelled RST equation is given by:

$$\begin{aligned}\frac{\mathrm{D}\overline{u_iu_j}}{\mathrm{D}t} =& P_{ij} - C_1\varepsilon a_{ij} - C_2\left(P_{ij} - \frac{2}{3}\delta_{ij}P_\kappa\right) + \phi_{ij}^{s,w} + \phi_{ij}^{r,w} \\ &+ \frac{\partial}{\partial x_l}\left(C_s\frac{\varepsilon}{k}\overline{u_lu_k}\frac{\partial\overline{u_iu_j}}{\partial x_k}\right) - \varepsilon_{ij}\,.\end{aligned} \tag{2.65}$$

The coefficients are specified by:

$$C_1 = C + \sqrt{A}E^2, \quad C = 2.5AF^{1/4}f, \quad F = \min(0.6, A_2) \tag{2.66}$$

$$C_2 = 0.8\sqrt{A} \tag{2.67}$$

$$f = \min\left[\left(\frac{\mathrm{Re_t}}{150}\right)^{3/2}, 1\right], \tag{2.68}$$

$$C_2^w = \max(1 - 0.7C, 0.3), \quad C_2^w = \min(A, 0.3) \tag{2.69}$$

The damping coefficient appearing in the wall correction terms (2.27) and (2.28)

is given by:

$$f_w = \min\left[\frac{k^{3/2}}{2.5\varepsilon x_n}, 1.4\right] \tag{2.70}$$

The modelled dissipation rate transport equation is given by:

$$\begin{aligned}\frac{\mathrm{D}\varepsilon}{\mathrm{D}t} &= C_{\varepsilon 1}\frac{\varepsilon}{k}P_\kappa - C_{\varepsilon 2}f_\varepsilon\frac{\varepsilon\tilde{\varepsilon}}{k} + \frac{\partial}{\partial x_k}\left(C_\varepsilon\frac{k}{\varepsilon}\overline{u_k u_l}\frac{\partial\varepsilon}{\partial x_l} + \nu\frac{\partial\tilde{\varepsilon}}{\partial x_k}\right)\\ &\quad + C_{\varepsilon 3}\,\nu\frac{k}{\varepsilon}\,\overline{u_i u_j}\,\frac{\partial^2 U_k}{\partial x_i\partial x_l}\frac{\partial^2 U_k}{\partial x_j\partial x_l} - C_{\varepsilon 4}f_4 k\,\Omega_k\,\Omega_k + S_l.\end{aligned} \tag{2.71}$$

The coefficients have the following specified values:

$$C_{\varepsilon 1} = 2.6 \quad C_{\varepsilon 2} = 1.92 \quad C_{\varepsilon 3} = 0.25 \quad C_{\varepsilon 4} = 0.1 \quad C_\varepsilon = 0.18\,, \tag{2.72}$$

and

$$f_\varepsilon = 1 - \frac{C_{\varepsilon 2} - 1.4}{C_{\varepsilon 2}}\exp\left[-\left(\frac{\mathrm{Re_t}}{6}\right)^2\right]. \tag{2.73}$$

The length-scale growth correction, S_l, is given by:

$$S_l = \max\left\{\left[\left(\frac{1}{C_l}\frac{\partial l}{\partial x_n}\right)^2 - 1\right]\left(\frac{1}{C_l}\frac{\partial l}{\partial x_n}\right)^2, 0\right\}\frac{\tilde{\varepsilon}\varepsilon}{k}A \tag{2.74}$$

where $l = k^{3/2}/\varepsilon$, and $C_l = 2.5$.

The anisotropic stress dissipation rate tensor is modelled as:

$$\varepsilon_{ij} = f_s\varepsilon^*_{ij} + (1 - f_s)\frac{2}{3}\delta_{ij}\varepsilon, \tag{2.75}$$

where ε^*_{ij} is given by:

$$\varepsilon^*_{ij} = \frac{\varepsilon}{k}\frac{\overline{u_i u_j} + (\overline{u_i u_k}\,n_j\,n_k + \overline{u_j u_k}\,n_i\,n_k + \overline{u_k u_l}\,n_k\,n_l\,n_i\,n_j)f_d}{1 + \frac{3}{2}n_p n_q\frac{\overline{u_p u_q}}{k}f_d}, \tag{2.76}$$

$$f_s = 1 - \sqrt{A}E^2, \quad f_d = (1 + 0.1\mathrm{Re_t})^{-1}. \tag{2.77}$$

2.10 The Two-Component-Limit model

Workers at UMIST, starting with the work of Fu et al. (1987), and Craft et al. (1989), used realisability in the limit of two component turbulence to obtain a

cubic model for the rapid term. Using similar arguments as in (2.21), but retaining up to cubic terms in a_{ij}, and using the additional constraint of realisability in the two component limit (TCL), the following model for ϕ^r_{ij} was obtained

$$\begin{aligned}
\phi^r_{ij} = & -0.6\,(P_{ij} - 2/3\delta_{ij}P) + 0.6a_{ij}P \\
& - 0.2\left\{ \frac{\overline{u_k u_j}\;\overline{u_l u_i}}{k}\left[\frac{\partial U_k}{\partial x_l} + \frac{\partial U_l}{\partial x_k}\right] - \frac{\overline{u_l u_k}}{k}\left[\overline{u_i u_k}\frac{\partial U_j}{\partial x_l} + \overline{u_j u_k}\frac{\partial U_i}{\partial x_l}\right]\right\} \\
& - c_2\left\{ A_2(P_{ij} - D_{ij}) + 3a_{mi}a_{nj}(P_{mn} - D_{mn})\right\} \\
& + c_2'\left\{ \left(\frac{7}{15} - \frac{A_2}{4}\right)(P_{ij} - 2/3\delta_{ij}P)\right. \\
& + 0.2[a_{ij} - 1/2(a_{ik}a_{kj} - 1/3\delta_{ij}A_2]P - 0.05a_{ij}a_{lk}P_{kl} \\
& + 0.1\left[\frac{\overline{u_i u_m}}{k}P_{mj} + \frac{\overline{u_j u_m}}{k}P_{mi} - 2/3\,\delta_{ij}\frac{\overline{u_l u_m}}{k}P_{ml}\right] \\
& + 0.1\left[\frac{\overline{u_l u_i}\;\overline{u_k u_j}}{k^2} - 1/3\,\delta_{ij}\frac{\overline{u_l u_m}\;\overline{u_k u_m}}{k^2}\right]\cdot\left[6D_{lk} + 13k\left(\frac{\partial U_l}{\partial x_k} + \frac{\partial U_k}{\partial x_l}\right)\right] \\
& \left. + 0.2\frac{\overline{u_l u_i}\;\overline{u_k u_j}}{k^2}(D_{lk} - P_{lk})\right\}
\end{aligned} \tag{2.78}$$

where A_2 is the second invariant of the stress anisotropy tensor

$$A_2 = a_{ij}a_{ji}\,, \tag{2.79}$$

and the recommended values of the coefficients, in the earliest, high-Re version of the model are

$$C_2 = 0.55, \quad C_2' = 0.6\,.$$

In the TCL modelling framework (in its high Reynolds number formulation) a second-order expression for ϕ^s_{ij} is used, where the coefficients are allowed to depend on the invariants in such a way as to satisfy realisability in the two-component limit (Craft and Launder, 2002). Dependency on the third invariant

$$A_3 = a_{ij}a_{jk}a_{ki}\,,$$

is introduced through the flatness parameter,

$$A = 1 - \tfrac{9}{8}(A_2 - A_3). \tag{2.80}$$

This flatness parameter becomes zero when one component vanishes. Thus using

$$\phi^s_{ij} = -C_1\varepsilon[a_{ij} + c'_1(a_{ij}a_{jk} - \tfrac{1}{3}A_2\delta_{ij})] - f'_A\varepsilon a_{ij}\,, \tag{2.81}$$

where the coefficients are given by

$$C_1 = 3.1(A_2A)^{1/2} \quad C'_1 = 1.1 \quad f'_A = A^{1/2}\,,$$

ensures that ϕ^s_{ij} drops to zero when the turbulence is two-component.

2.10.1 Low-Re TCL model

A low-Re version of the TCL model was presented by Craft (1998). This version adopts a slightly different decomposition of the velocity-pressure gradient correlation Π_{ij} that was found to be more appropriate when modelling inhomogeneous flows. Where this correlation is typically decomposed into the pressure strain rate correlation and pressure diffusion, an alternative decomposition is obtained be defining:

$$\phi^*_{ij} = \Pi_{ij} - \tfrac{1}{3}\delta_{ij}\Pi_{kk} \tag{2.82}$$

Constructing ϕ^*_{ij}in this way ensures that it is redistributive in nature, since it is traceless and thus cannot contribute to the level of kinetic energy. This redistributive quantity is modelled as

$$\phi^*_{ij} = \phi^{*,s}_{ij} + \phi^{*,r}_{ij} + \phi^{\mathrm{inh},s}_{ij} + \phi^{\mathrm{inh},r}_{ij} \tag{2.83}$$

The quantities $\phi^{*,s}_{ij}, \phi^{*,r}_{ij}$ have the same form as their homogeneous counterparts (2.81) and (2.78), respectively, but the coefficients C_1, C_2 and C'_2 are prescribed

by

$$C_1 = 3.1 f_A f_{\mathrm{Re_t}} A_2^{1/2} \tag{2.84a}$$

$$C_2 = \min\left\{0.55\left[1-\exp\left(\frac{-A^{1.5}\mathrm{Re_t}}{100}\right)\right],\ \frac{3.2A}{1+S^*}\right\} \tag{2.84b}$$

$$C_2' = \min(0.6, A) + \frac{3.5(S^*-\Omega^*)}{3+S^*+\Omega^*} - 2S_I \tag{2.84c}$$

where

$$f_A' = \sqrt{A} f_{\mathrm{Re_t}} + A(1-f_{\mathrm{Re_t}}) \tag{2.85}$$

$$f_{\mathrm{Re_t}} = \min[(\mathrm{Re_t}/160)^2, 1] \tag{2.86}$$

$$f_A == \begin{cases} (A/14)^{1/2} & A < 0.05 \\ A/0.8367 & 0.05 < A < 0.7 \\ A^{1/2} & A > 0.7 \end{cases} \tag{2.87}$$

$$S^* = Sk/\varepsilon, \quad \Omega^* = \Omega k/\varepsilon, \tag{2.88}$$

$$S = (2S_{ij}S_{ji})^{1/2}, \quad \Omega = (2\Omega_{ij}\Omega_{ji})^{1/2}, \tag{2.89}$$

$$S_I = \frac{2\sqrt{2}S_{ij}S_{jk}S_{ki}}{(S_{lm}S_{ml})^{3/2}}, \tag{2.90}$$

and

$$S_{ij} = \frac{1}{2}\left(\frac{\partial U_i}{\partial x_j} + \frac{\partial U_j}{\partial x_i}\right),\ \Omega_{ij} = \frac{1}{2}\left(\frac{\partial U_i}{\partial x_j} - \frac{\partial U_j}{\partial x_i}\right). \tag{2.91}$$

The inhomogeneous corrections are independent of the wall-normal vector, and are given by

$$\begin{aligned}
\phi_{ij}^{\mathrm{inh},s} =& f_{w1}\frac{\varepsilon}{k}(\overline{u_l u_k}d_l^A\delta_{ij} - \tfrac{3}{2}\overline{u_i u_k}d_j^A - \tfrac{3}{2}\overline{u_j u_k}d_i^A)d_k^A \\
&+ f_{w2}\frac{\varepsilon}{k^2}\overline{u_l u_n}(\overline{u_n u_k}d_k^A\delta_{ij} - \tfrac{3}{2}\overline{u_i u_n}d_j^A - \tfrac{3}{2}\overline{u_j u_n}d_i^A)d_l^A \\
&+ f_{w3}\nu\left(a_{il}\frac{\partial\sqrt{k}}{\partial x_l}\frac{\partial\sqrt{k}}{\partial x_j} + a_{jl}\frac{\partial\sqrt{k}}{\partial x_l}\frac{\partial\sqrt{k}}{\partial x_i} - \frac{2}{3}a_{nl}\frac{\partial\sqrt{k}}{\partial x_l}\frac{\partial\sqrt{k}}{\partial x_n}\delta_{ij} - \frac{4}{3}a_{ij}\frac{\partial\sqrt{k}}{\partial x_l}\frac{\partial\sqrt{k}}{\partial x_l}\right) \\
&+ f_{w1}'\frac{k^2}{\varepsilon}\left(\overline{u_k u_l}\frac{\partial\sqrt{A}}{\partial x_k}\frac{\partial\sqrt{A}}{\partial x_l}\delta_{ij} - \frac{3}{2}\overline{u_i u_k}\frac{\partial\sqrt{A}}{\partial x_k}\frac{\partial\sqrt{A}}{\partial x_j} - \frac{3}{2}\overline{u_j u_k}\frac{\partial\sqrt{A}}{\partial x_k}\frac{\partial\sqrt{A}}{\partial x_i}\right)
\end{aligned} \tag{2.92}$$

$$\phi_{ij}^{\mathrm{inh,r}} = f_I k \frac{\partial U_l}{\partial x_n} d_l d_n (d_i d_j - \tfrac{1}{3} d_k d_k \delta_{ij}) \tag{2.93}$$

where the 'normalised length-scale gradients' d_i, d_i^A, introduced by Craft and Launder (1996), are used indicate the direction of strong inhomogeneity, when present, without the use of a wall-normal vector. These are defined by

$$d_i = \frac{N_i}{0.5 + (N_k N_k)^{0.5}}, \quad \text{where} \quad N_i = \frac{\partial (k^{1.5}/\varepsilon)}{\partial x_i}, \tag{2.94a}$$

$$d_i^A = \frac{N_i^A}{0.5 + (N_k^A N_k^A)^{0.5}}, \quad \text{where} \quad N_i^A = \frac{\partial (k^{1.5} A^{0.5}/\varepsilon)}{\partial x_i}. \tag{2.94b}$$

The coefficients appearing in the inhomogeneous corrections are given by:

$$f_{w1} = 0.4 + 1.6 \min[1, \max(0, 1 - (\mathrm{Re_t} - 55)/20)] \tag{2.95}$$

$$f_{w2} = 0.1 + 0.8 A_2 \min[1, \max(0, 1 - (\mathrm{Re_t} - 50)/85)] \tag{2.96}$$

$$f_{w3} = 2.5\sqrt{A} \tag{2.97}$$

$$f'_{w1} = 0.22 \tag{2.98}$$

$$f_I = 2.5\, f_A \tag{2.99}$$

As discussed in Section 2.5, the dissipation tensor near a wall or free surface is anisotropic, and the low-Re TCL accordingly prescribes the following anisotropic model for the dissipation rate tensor,

$$\varepsilon_{ij} = (1 - f_\varepsilon) \frac{\varepsilon'_{ij} + \varepsilon''_{ij} + \varepsilon'''_{ij}}{D} + \tfrac{2}{3} f_\varepsilon \varepsilon \delta_{ij} \tag{2.100}$$

where

$$\begin{aligned}
\varepsilon'_{ij} =& \varepsilon \frac{\overline{u_i u_j}}{k} + 2\nu \frac{\overline{u_l u_n}}{k} \frac{\partial \sqrt{k}}{\partial x_l} \frac{\partial \sqrt{k}}{\partial x_n} \delta_{ij} \\
&+ 2\nu \frac{\overline{u_l u_i}}{k} \frac{\partial \sqrt{k}}{\partial x_j} \frac{\partial \sqrt{k}}{\partial x_l} + 2\nu \frac{\overline{u_l u_j}}{k} \frac{\partial \sqrt{k}}{\partial x_i} \frac{\partial \sqrt{k}}{\partial x_l}, \\
\varepsilon''_{ij} =& \varepsilon \left(2 \frac{\overline{u_l u_k}}{k} d_l^A d_k^A \delta_{ij} - \frac{\overline{u_l u_i}}{k} d_l^A d_j^A - \frac{\overline{u_l u_j}}{k} d_l^A d_i^A \right), \\
\varepsilon'''_{ij} =& C_{\varepsilon s} \nu k \left(\frac{\partial \sqrt{A}}{\partial x_k} \frac{\partial \sqrt{A}}{\partial x_k} \delta_{ij} + 2 \frac{\partial \sqrt{A}}{\partial x_i} \frac{\partial \sqrt{A}}{\partial x_j} \right), \\
D =& \frac{\varepsilon'_{kk} + \varepsilon''_{kk} + \varepsilon'''_{kk}}{2\varepsilon},
\end{aligned} \tag{2.101}$$

and the coefficients are taken as $f_\varepsilon = A^{3/2}$, $C_{\varepsilon s} = 0.2$. The term ε'_{ij} is similar in nature to the model in (2.38), and its purpose is to ensure the correct wall-limiting behaviour of ε_{ij}, as discussed in Section 2.5. The term ε''_{ij} serves the specific purpose of producing the dip in ε_{12} near $y/\delta = 0.1$ observed in DNS studies of plane channel flow, and finally the term ε'''_{ij} improves the behaviour of ε_{ij} at a free surface where there is strong inhomogeneity even without significant viscous effects (Craft and Launder, 1996).

2.10.2 Dissipation rate equation

Early high-Re implementations of the TCL model used the same transport equation for the scalar dissipation rate (2.50) as in the LRR models. In later versions of the TCL model (Craft, 1998; Batten et al., 1999), an equation for the homogeneous dissipation rate,

$$\tilde{\varepsilon} = \varepsilon - 2\nu \left(\frac{\partial k^{1/2}}{\partial x_i} \right)^2 , \tag{2.102}$$

is solved, which takes the form

$$\begin{aligned} \frac{\mathrm{D}\tilde{\varepsilon}}{\mathrm{D}t} = {} & C_{\varepsilon 1} \frac{\tilde{\varepsilon}}{k} P_\kappa - C_{\varepsilon 2} \frac{\tilde{\varepsilon}^2}{k} - C'_{\varepsilon 2} \frac{(\varepsilon - \tilde{\varepsilon})\tilde{\varepsilon}}{k} + \frac{\partial}{\partial x_k} \left(C_\varepsilon \frac{k}{\varepsilon} \overline{u_k u_l} \frac{\partial \tilde{\varepsilon}}{\partial x_l} + \nu \frac{\partial \tilde{\varepsilon}}{\partial x_k} \right) \\ & + C_{\varepsilon 3}\, \nu \frac{k}{\varepsilon} \overline{u_i u_j} \frac{\partial^2 U_k}{\partial x_i \partial x_l} \frac{\partial^2 U_k}{\partial x_j \partial x_l} + Y_E . \end{aligned} \tag{2.103}$$

The term Y_E is a length-scale correction based on the proposal of Iacovides and Raisee (1997), and is given by

$$Y_E = C_{\varepsilon l} \frac{\tilde{\varepsilon}^2}{k} \max[F(F+1)^2, 0], \tag{2.104}$$

and F in turn is given by

$$F = \left(\frac{\partial l}{\partial x_j} \frac{\partial l}{\partial x_j} \right) - C_l \{ [1 - \exp(-B_\varepsilon \mathrm{Re_t})] + B_\varepsilon C_l \mathrm{Re_t} \exp(-B_\varepsilon \mathrm{Re_t}) \} , \tag{2.105}$$

$$l = k^{3/2}/\varepsilon, \quad B_\varepsilon = 0.1069, \quad C_l = 2.55 . \tag{2.106}$$

The remaining coefficients are given by

$$\begin{aligned} &C_{\varepsilon 1} = 1.0, \quad C_{\varepsilon 2} = \frac{1.92}{1 + 0.7 A_d \sqrt{A_2}}, \quad A_d = \max(A, 0.25), \\ &C'_{\varepsilon 2} = 1.0, \quad C_{\varepsilon 3} = 0.875, \\ &C_{\varepsilon l} = 0.5, \quad C_{\varepsilon} = 0.15. \end{aligned} \tag{2.107}$$

Chapter 3

Numerical Solution Techniques

This chapter presents the numerical solution techniques used to solve the governing equations presented in Chapter 2, for inhomogeneous turbulence cases. Numerical solution of the governing equations in these inhomogeneous turbulence cases, which are examined in Chapters 5 and 6, was carried out using the in-house code STREAM. The code is based on the finite volume method for structured grids, which can be body-fitted non-orthogonal, using Rhie–Chow interpolation (Rhie and Chow, 1983) to allow a collocated velocity and pressure storage arrangement. It uses the SIMPLE algorithm for pressure-velocity coupling, and a number of possible interpolation schemes for the convective terms. The main features of this code, relevant to the present work, will be presented briefly.

Presentation in this chapter will focus on the numerical features of the code that are relevant to the problems examined in this work. Thus generalisation to 3 dimensions, non-orthogonal grids, variable density or compressibility effects, etc. which the STREAM code is capable of handling, but were not used, will not be described here. Further details of numerical implementation and the above generalisations are available in Lien and Leschziner (1994).

3.1 The Finite volume method

In the finite volume method one works with the integral form of the relevant governing equations. Thus the transport equation for the generic scalar ϕ in differential form

$$\frac{\partial(U_j\phi)}{\partial x_j} = \frac{\partial}{\partial x_j}\left(\gamma\frac{\partial\phi}{\partial x_j}\right) + S^{\phi}, \tag{3.1}$$

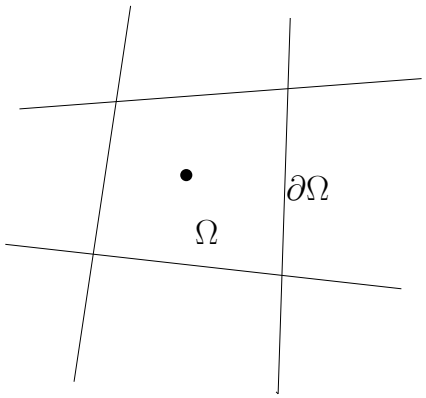

Figure 3.1: 2-D Finite volume cell

where S^ϕ is a point source, is integrated over a control volume Ω having a surface denoted $\partial\Omega$, as depicted in Figure 3.1, to give

$$\int_\Omega \frac{\partial}{\partial x_j}\left(U_j\phi - \gamma\frac{\partial\phi}{\partial x_j}\right)\mathrm{d}\mathcal{V} = \int_\Omega S^\phi \mathrm{d}\mathcal{V}. \tag{3.2}$$

It is more convenient to work with surface integrals, thus using the Gauss divergence theorem to transform the integral on the left hand side to a surface integral, the equation becomes

$$\int_{\partial\Omega}\left(U_j\phi - \gamma\frac{\partial\phi}{\partial x_j}\right)n_j\mathrm{d}\mathcal{S} = \int_\Omega S^\phi \mathrm{d}\mathcal{V}, \tag{3.3}$$

where n_j represents an element of the unit vector normal to the differential element of surface area $\mathrm{d}\mathcal{S}$. The domain is discretised by a set of control volumes, cells, and variables are stored at the cell centres. The surface integral is thus discretised as

$$\int_{\partial\Omega}\left(U_j\phi - \gamma\frac{\partial\phi}{\partial x_j}\right)n_j\mathrm{d}\mathcal{S} \approx \sum_k\left[\left(U_j\phi - \gamma\frac{\partial\phi}{\partial x_j}\right)n_j\Delta\mathcal{S}\right]_k, \tag{3.4}$$

where values in the square brackets are evaluated at the centre of the edge segment k. The source term on the right hand side of (3.3) is discretised using the following approximation

$$\int_\Omega S^\phi \mathrm{d}\mathcal{V} \approx \overline{S^\phi}\Delta\mathcal{V} \approx S^\phi|_P\,\Delta\mathcal{V}, \tag{3.5}$$

where the subscript P denotes the quantity evaluated at the storage node located at the cell centre.

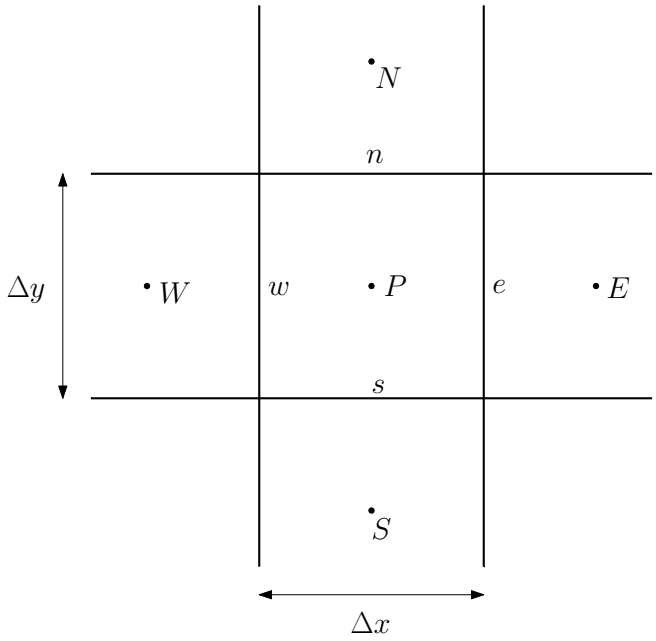

Figure 3.2: 2-D Finite volume computational stencil

Using the preceding approximations to integrate (3.3) over the 2-D finite volume cell in Figure 3.2 leads to

$$[U\phi\Delta y]_w^e + [V\phi\Delta x]_s^n = \left[\gamma\frac{\partial\phi}{\partial x}\Delta y\right]_w^e + \left[\gamma\frac{\partial\phi}{\partial y}\Delta x\right]_s^n + S^\phi\Delta x\Delta y. \tag{3.6}$$

All variables appearing above, except for the source term S^ϕ are to be evaluated at the cell faces e, w, n, s, while values are stored at cell centres, and interpolation is therefore required. The diffusive terms are discretised using central differencing,

$$\begin{aligned}\left[\gamma\frac{\partial\phi}{\partial x}\Delta y\right]_w^e + \left[\gamma\frac{\partial\phi}{\partial y}\Delta x\right]_s^n = \\ \left[\gamma\frac{\partial\phi}{\partial x}\Delta y\right]_e - \left[\gamma\frac{\partial\phi}{\partial x}\Delta y\right]_w + \left[\gamma\frac{\partial\phi}{\partial x}\Delta y\right]_n - \left[\gamma\frac{\partial\phi}{\partial x}\Delta y\right]_s \approx \\ (\phi_E-\phi_P)\left[\gamma\frac{\Delta y}{\Delta x}\right]_e - (\phi_P-\phi_W)\left[\gamma\frac{\Delta y}{\Delta x}\right]_w + (\phi_N-\phi_P)\left[\gamma\frac{\Delta x}{\Delta y}\right]_n - (\phi_P-\phi_S)\left[\gamma\frac{\Delta x}{\Delta y}\right]_s.\end{aligned} \tag{3.7}$$

The above diffusive contribution can be rearranged in the form

$$a_E^d\phi_E + a_W^d\phi_W + a_N^d\phi_N + a_S^d\phi_S - a_P^d\phi_P, \tag{3.8}$$

where the coefficients associated with the neighbouring nodal values are given by

$$\begin{aligned} a_E^d &= \left(\gamma\frac{\Delta y}{\Delta x}\right)_e, \quad a_W^d = \left(\gamma\frac{\Delta y}{\Delta x}\right)_w, \\ a_N^d &= \left(\gamma\frac{\Delta x}{\Delta y}\right)_n, \quad a_S^d = \left(\gamma\frac{\Delta x}{\Delta y}\right)_s, \\ a_P^d &= a_E^d + a_W^d + a_N^d + a_S^d. \end{aligned} \tag{3.9}$$

Expanding the convective terms in (3.6) leads to

$$\begin{aligned} [U\phi\Delta y]_w^e + [V\phi\Delta x]_s^n = \\ (U\Delta y)_e\,\phi_e - (U\Delta y)_w\,\phi_w + (V\Delta x)_n\,\phi_n - (V\Delta x)_s\,\phi_s = \\ c_e\phi_e - c_w\phi_w + c_n\phi_n - c_s\phi_s \end{aligned} \tag{3.10}$$

where the coefficients c_e, c_w, c_n, c_s are the volumetric fluxes through the subscripted faces.

As in the case of the diffusive terms, variable values (U, V, ϕ) are required at cell faces while they are stored at cell centres, and interpolation is thus required. Interpolation schemes suitable for convective fluxes are briefly outlined in the next section.

3.2 Convective differencing schemes

The directional nature of convection means that special treatment is required in the discretisation of convective terms. The use of central differencing leads to un-physical wiggles in the solution, since this scheme is neither directional nor bounded. A number of convective schemes are available for use in STREAM. These include upwind differencing, QUICK and UMIST. The simplest method is upwind differencing where, as the name suggests, the value of ϕ_{face} is taken simply as the value of ϕ at the upwind node. For example,

$$\phi_e = \begin{cases} \phi_P & \text{if } c_e > 0 \\ \phi_E & \text{if } c_e < 0 \end{cases}$$

Using this approximation, the discretised convective terms can be written

$$-a_E^c\phi_E - a_W^c\phi_W - a_N^c\phi_N - a_S^c\phi_S + a_P^c\phi_P, \tag{3.11}$$

where

$$\begin{aligned} a_E^c &= \max(-c_e, 0) \qquad a_W^c = \max(c_w, 0) \\ a_N^c &= \max(-c_n, 0) \qquad a_S^c = \max(c_s, 0) \\ a_P^c &= a_E^c + a_W^c + a_N^c + a_S^c \end{aligned} \tag{3.12}$$

The upwind differencing scheme is unconditionally bounded, but is only first order accurate. Accuracy can be increased by using a higher order interpolation. This is the approach taken in the QUICK scheme, where a quadratic polynomial is fitted through three nodes with an upwind bias, to achieve the desired property of directionality (transportiveness). Using the subscripts U, D, UU to denote the upwind, downwind, and upwind-upwind nodes, the value of ϕ at a face can be interpolated by

$$\phi_{face} = -\tfrac{1}{8}\phi_{UU} + \tfrac{3}{4}\phi_U + \tfrac{3}{8}\phi_D. \tag{3.13}$$

This scheme is third order accurate and is transportive, but is not bounded, which can cause serious problems when solving for non-negative turbulent quantities such as k, ε and the normal Reynolds stresses. One solution to this problem is to use flux-limiting, or total variation diminishing (TVD) schemes. In such schemes, a higher order interpolant is fitted through the nodes only if the variable is monotonically increasing or decreasing over these nodes. If not, they switch to first order upwind to maintain boundedness. The variable is monotonic if

$$(\phi_D - \phi_U)(\phi_U - \phi_{UU}) > 0$$

The following auxiliary quantity representing a ratio of successive gradients is used in formulating TVD schemes,

$$r = \frac{\phi_U - \phi_{UU}}{\phi_D - \phi_U} \tag{3.14}$$

There are two TVD schemes available in STREAM, the Upstream Monotonic Interpolation for Scalar Transport (UMIST) scheme Lien and Leschziner (1994), and van Leer's harmonic scheme (1974). Only the UMIST scheme has been used

in the present work, and it is given by

$$\phi_{face} = \begin{cases} \phi_U + (\phi_D - \phi_U)\max[0, \min(1, r, \frac{1}{8} + \frac{3}{8}r, \frac{3}{8} + \frac{1}{8}r)] & \text{if monotonic,} \\ \phi_U & \text{otherwise.} \end{cases} \tag{3.15}$$

The UMIST scheme is a flux-limited variant of the QUICK scheme, and is third order accurate where the solution is monotonic.

3.3 Algebraic system of equations

Substituting the diffusive contributions (3.8), and the convective contributions as outlined in Section 3.2 back into (3.6), a linear equation of the following form is obtained for each node:

$$a_P\phi_P = a_E\phi_E + a_W\phi_W + a_N\phi_N + a_S\phi_S + S\,, \tag{3.16}$$

where $a_E = a_E^d + a_E^c$, and similarly for the other faces, and $a_P = a_E + a_W + a_N + a_S$. This can also be written as

$$a_P\phi_P - \sum_i a_i\phi_i = S\,, \tag{3.17}$$

where the index i runs over the neighbouring nodes. When such an equation is written for each cell in the finite volume grid, an algebraic system of equation is constructed

$$\mathbf{A}\boldsymbol{\phi} = \mathbf{S} \tag{3.18}$$

where $\boldsymbol{\phi}$ is the global vector of nodal values of variable ϕ, $\mathbf{A}$ is the coefficient matrix of the algebraic equations system, and $\mathbf{S}$ is the global vector of source terms. Since the STREAM code uses structured grids exclusively, the coefficient matrix has a pre-defined sparse structure (5 non-zero diagonals in 2D). This allows the use of the highly efficient tridiagonal matrix algorithm (TDMA), within a line iteration method, where the solution is updated in sweeps along the rows and columns in an alternating fashion. This involves temporarily treating adjacent lines during a sweep as having known values, so that only three variables are treated as unknown, and the matrix becomes tridiagonal. The process must

therefore be done iteratively until a converged solution is obtained. Further details of this method are available in textbooks such as Versteeg and Malalasekera (2007).

3.3.1 Source–term linearisation

Numerical stability of the solution algorithm is enhanced by increasing the diagonal dominance of the coefficient matrix. To this end, source-term linearisation is performed provided the source term can be re-written as

$$S = S_P \phi_P + S_U \tag{3.19}$$

with the solution dependent part having an unconditionally negative slope (i.e. $S_P < 0$). This allows part of the source term to be treated implicitly by absorbing the coefficient S_P into a_P

$$a_P \leftarrow a_P + S_P \tag{3.20}$$

For a non-negative quantity ϕ, such as, for example, a normal Reynolds stress component, if form of the source term admits negative values, the source term is treated

$$S_U = \max[S, 0], \quad S_P = \frac{\min[S, 0]}{\phi_P} \tag{3.21}$$

This also helps to prevent negative values of the variable from arising in a computation.

3.4 Pressure–velocity coupling

There is no explicit equation for pressure among the governing equations for mean turbulent flow. Since the momentum equations provide a link between velocity fields and pressure gradients, requiring velocity fields that satisfy the momentum equations to simultaneously satisfy the continuity equation provides a route to obtaining an equation for pressure. This is the idea behind pressure-velocity coupling algorithms. The algorithm used in STREAM is the Semi-Implicit Method for Pressure-Linked Equations (SIMPLE) of Patankar and Spalding (1972). This involves solving the momentum equations using an initial guess for the pressure field, then using the thus obtained velocity field to solve an equation for a continuity-based pressure correction equation. The pressure correction is then

used to 'nudge' the pressure field in the correct direction, and use this improved pressure estimate in the momentum equation. The process is repeated iteratively until a converged solution for velocity and pressure satisfying both momentum and continuity equations within a specified tolerance is obtained.

The solution starts by solving the discretised momentum equations with the current pressure field, which might be an initial guess.

$$a_P^U U_P = \sum_i a_i^U U_i + \frac{\Delta y}{a_P^U}(P_w - P_e) + S^U \qquad a_P^V V_P = \sum_i a_i^V V_i + \frac{\Delta x}{a_P^V}(P_s - P_n) + S^V \tag{3.22}$$

$$U_P = \sum_i \frac{a_i^U U_i}{a_P^U} + D^U(P_w - P_e) + s^U \qquad V_P = \sum_i \frac{a_i^V V_i}{a_P^V} + D^V(P_s - P_n) + s^V \tag{3.23}$$

where

$$D^U = \frac{\Delta y}{a_P^U}, \quad D^V = \frac{\Delta x}{a_P^V}, \quad s^U = \frac{S^U}{a_P^U}, \quad s^V = \frac{S^V}{a_P^V}.$$

The resulting velocity field generally will not satisfy continuity. We thus wish to find corrections U', V', P' such that the corrected variables

$$U^* = U + U', \quad V^* = V + V', \quad P^* = P + P', \tag{3.24}$$

satisfy both momentum and continuity. If these are substituted into the discretised momentum equations, and (3.22) is subtracted, the following equations for the velocity corrections are obtained

$$U'_P = \sum_i \frac{a_i^U U'_i}{a_P^U} + D^U(P'_w - P'_e) \qquad V'_P = \sum_i \frac{a_i^V V'_i}{a_P^V} + D^V(P'_s - P'_n) \tag{3.25}$$

The discretised continuity equation is

$$(U_e^* - U_w^*)\Delta y + (V_n^* - V_s^*)\Delta x = 0 \tag{3.26}$$

Or,

$$(U'_e - U'_w)\Delta y + (V'_n - V'_s)\Delta x = \\ -((U_e - U_w)\Delta y + (V_n - V_s)\Delta x) = -S^m \tag{3.27}$$

The current mass imbalance (S^m) thus represents a source term for this form of the continuity equation. At this point expressions equivalent to (3.25) for the

velocity corrections at cell faces are substituted in the above expression, bearing in mind that the SIMPLE scheme neglects the first term on the RHS of equations (3.25) (which go to zero as the solution converges). Thus,

$$(D^U \Delta y)_e(P'_P - P'_E) - (D^U \Delta y)_w(P'_W - P'_P) + (D^V \Delta x)_n(P'_P - P'_N) - (D^V \Delta x)_s(P'_S - P'_P) = -S^m \quad (3.28)$$

This can be re-arranged into a set of equations of the form

$$a_P P'_P = \sum_i a_i P'_i - S^m \,, \quad (3.29)$$

which are then solved using the same methods described in Section 3.3.

3.4.1 Rhie–Chow velocity interpolation

It is well known that the use of a collocated grid where all variable are stored at the same node locations, in conjunction with straightforward linear interpolation for the velocity at cell faces when calculating mass fluxes, leads to 'checker-boarding' of the pressure field. This results from odd-even decoupling between the velocity and pressure fields, where node velocities are dependent on the pressure at adjacent nodes but not at the node itself. One possible remedy for this problem is to use a staggered grid where the pressure and all other variables aside from velocities are stored at cell centres, while velocities are stored at cell faces. This provides a stronger coupling between local velocities and pressures and solves the problem of checker-boarding. Staggered grids present some difficulties, however, in non-Cartesian grids, and in the interest of geometrical flexibility the STREAM code uses a collocated grid arrangement. This necessitates special treatment in velocity interpolation that avoids odd-even decoupling. The STREAM code uses the technique proposed by Rhie and Chow (1983), which provides a means for using a collocated velocity and pressure storage while retaining the necessary local coupling between these variables.

The method can be outlined as follows. The x-momentum equation for the

cell centred at node P, as shown in Figure 3.2, yields an equation for U_P

$$U_P = \underbrace{\sum_i \frac{a_i^U U_i}{a_P^U} + s^U}_{H_P} + (D^U)_P(P_w - P_e), \tag{3.30}$$

or,

$$U_P = H_P + (D^U)_P(P_w - P_e)_P. \tag{3.31}$$

Similarly for the neighbouring node to the east:

$$U_E = H_E + (D^U)_E(P_w - P_e)_E \tag{3.32}$$

To obtain the velocity at the cell face e, the idea of Rhie-Chow interpolation is to interpolate the two parts of the velocity source terms differently. Thus

$$\begin{aligned} U_e &= H_e + (D^U)_e(P_w - P_e)_e \\ &= \tfrac{1}{2}(H_P + H_E) + \tfrac{1}{2}\big[(D^U)_P + (D^U)_E\big](P_P - P_E) \end{aligned} \tag{3.33}$$

Bearing in mind that

$$H_P = U_P - (D^U)_P(P_w - P_e)_P \qquad H_E = U_E - (D^U)_E(P_w - P_e)_E \tag{3.34}$$

We have

$$\begin{aligned} U_e = \tfrac{1}{2}\big[U_P - (D^U)_P(P_w - P_e)_P + U_E - (D^U)_E(P_w - P_e)_E\big] \\ + \tfrac{1}{2}\big[(D^U)_P + (D^U)_E\big](P_P - P_E) \end{aligned} \tag{3.35}$$

This expression may be viewed as a linear interpolation and a pressure smoothing term by rewriting in the form (Leschziner and Lien, 2002)

$$\begin{aligned} U_e = {} & \underbrace{\tfrac{1}{2}(U_P + U_E)}_{\text{linear interpolation}} \\ & + \underbrace{\frac{1}{2}\Big\{\big[(D^U)_P + (D^U)_E\big](P_P - P_E) - (D^U)_P(P_w - P_e)_P - (D^U)_E(P_w - P_e)_E\Big\}}_{\text{pressure smoothing}}. \end{aligned} \tag{3.36}$$

Rhie-Chow interpolation is applied to calculate mass fluxes through cell faces

before solving the pressure-correction equations, exemplified by (3.28).

3.5 Time-stepping

Integration in time for time-dependent problems which have the (semi) discretised form

$$\frac{\partial(\Delta\mathcal{V}\phi)}{\partial t} + \sum_k \left[\left(U_j\phi - \gamma\frac{\partial\phi}{\partial x_j}\right) n_j \Delta\mathcal{S}\right]_k = S^\phi \Delta\mathcal{V} \tag{3.37}$$

can be achieved by a simple extension of the FV method for steady state problems. The default method for time-stepping in STREAM is the backward differencing scheme, which may be written as

$$\frac{(\Delta\mathcal{V}\phi)^{\text{new}} - (\Delta\mathcal{V}\phi)^{\text{old}}}{\Delta t} + \left[a_P^\phi\phi_P - \sum a_i^\phi\phi_i - S^\phi\right]^{\text{new}} = 0 \tag{3.38}$$

This can be rearranged to write

$$\left(a_P^\phi + \frac{\Delta\mathcal{V}}{\Delta t}\right)\phi_P - \sum a_i^\phi\phi_i = S^\phi + \left(\frac{\Delta\mathcal{V}\phi_P}{\Delta t}\right)^{\text{old}} \tag{3.39}$$

It can be seen that this method is implemented by a change of coefficients and the source term:

$$a_P^\phi \leftarrow a_P^\phi + \frac{\Delta\mathcal{V}}{\Delta t} \qquad S^\phi \leftarrow S^\phi + \left(\frac{\Delta\mathcal{V}\phi_P}{\Delta t}\right)^{\text{old}} \tag{3.40}$$

This method has the advantage that there are no time-step restrictions dictated by stability, but it is only first order accurate. The second order Crank-Nicolson scheme is also available in STREAM. This is defined by

$$\frac{(\Delta\mathcal{V}\phi)^{\text{new}} - (\Delta\mathcal{V}\phi)^{\text{old}}}{\Delta t} + \frac{1}{2}\left[a_P^\phi\phi_P - \sum a_i^\phi\phi_i - S^\phi\right]^{\text{old}} + \frac{1}{2}\left[a_P^\phi\phi_P - \sum a_i^\phi\phi_i - S^\phi\right]^{\text{new}} = 0. \tag{3.41}$$

Upon rearrangement,

$$\left(a_P^\phi + 2\frac{\Delta\mathcal{V}}{\Delta t}\right)\phi_P - \sum a_i^\phi \phi_i = S^\phi + \left[\left(2\frac{\Delta\mathcal{V}\phi_P}{\Delta t} - a_P^\phi\right)\phi_P + \left(S^\phi + \sum a_i^\phi \phi_i\right)\right]^{\text{old}} \quad (3.42)$$

This is implemented by applying the following change of coefficients and source term:

$$\begin{aligned} a_P^\phi &\leftarrow a_P^\phi + 2\frac{\Delta\mathcal{V}}{\Delta t} \\ S^\phi &\leftarrow S^\phi + \left[\left(2\frac{\Delta\mathcal{V}\phi_P}{\Delta t} - a_P^\phi\right)\phi_P + \left(S^\phi + \sum a_i^\phi \phi_i\right)\right]^{\text{old}} . \end{aligned} \quad (3.43)$$

3.6 Numerical issues specific to RST modelling

There are a number of difficulties associated with the use of RST models that are not present when using eddy viscosity formulations. In particular, the use of RST models results in relatively large source terms that increase the stiffness of the algebraic equation system, in addition to the fact that the equation set becomes highly non-linear and strongly coupled (Lien and Leschziner, 1994; Leschziner and Lien, 2002). When using a collocated grid, there is also the issue of odd-even decoupling of the velocities and the Reynolds stresses.

The use of an eddy-viscosity approach adds to the momentum equations a momentum diffusion term that can be treated implicitly, thus enhancing stability. Since no such term is present in RST model equations, one approach to improve stability when applying RST models, the approach used in STREAM, is to add and subtract a gradient-diffusion term based on an effective viscosity, ν_{eff}. Considering $\overline{u^2}$ for example, one may write

$$\overline{u^2} = \left(\overline{u^2} + \nu_{\text{eff}}\frac{\partial U}{\partial x}\right) - \nu_{\text{eff}}\frac{\partial U}{\partial x}$$

allowing the unbracketed term to be treated implicitly in the U-momentum equation.

Since the effective viscosity does not affect the final converged solution, it is not uniquely specified, and one would, in general, simply be trying to significantly reduce the residual stress term that must be treated explicitly in the source term.

One way to specify the effective viscosity is by reference to a simplified form of the Basic Reynolds stress model equations. What is needed is to construct a relation between $\overline{u^2}$ and $\frac{\partial U}{\partial x}$, between $\overline{v^2}$ and $\frac{\partial V}{\partial x}$, and so on. Take $\overline{u^2}$ for example, and start by assuming its transport equation is source dominated:

$$P_{11} + \phi_{11} - \frac{2}{3}\varepsilon\delta_{ij} = 0 \tag{3.44}$$

Substituting for ϕ_{11} from the Basic model,

$$P_{11} - C_1\varepsilon\Big(\frac{u^2}{k} - \frac{2}{3}\Big) - C_2\big[P_{11} - \frac{1}{3}(P_{11} + P_{22} + P_{33})\big] - \frac{2}{3}\varepsilon\delta_{ij} = 0 \tag{3.45}$$

This leads to

$$-2\overline{u^2}\frac{\partial U}{\partial x}\Big(1 - \frac{2}{3}C_2\Big) - C_1\frac{\varepsilon}{k}\overline{u^2} + \Big(\text{other terms not containing } \overline{u^2} \text{ or } \frac{\partial U}{\partial x}\Big) = 0 \tag{3.46}$$

or

$$\overline{u^2} = \frac{(2 - \frac{4}{3}C_2)\overline{u^2}}{C_1}\frac{k}{\varepsilon}\frac{\partial U}{\partial x} + \text{O.T.} \tag{3.47}$$

Thus a suitable choice for ν_{11} is

$$\nu_{11} = \frac{2 - \frac{4}{3}C_2}{C_1}\frac{\varepsilon}{k}\overline{u^2} \tag{3.48}$$

Similar consideration of the $\overline{v^2}$ transport equation leads to the specification

$$\nu_{22} = \frac{2 - \frac{4}{3}C_2}{C_1}\frac{\varepsilon}{k}\overline{v^2}, \tag{3.49}$$

and finally relating the shear stress $\overline{uv}$ to $\frac{\partial U}{\partial y}$ leads to the following specification for ν_{12}

$$\nu_{12} = \frac{1 - C_2}{C_1}\frac{\varepsilon}{k}\overline{v^2}, \tag{3.50}$$

Maintaining the required coupling between the velocity and Reynolds stress components is accomplished through a Rhie-Chow-type interpolation (Leschziner and

Lien, 2002):

$$\overline{u_P^2} = \underbrace{\frac{1}{a_P}\Big(\sum_i a_i \overline{u_i^2} + S_u\Big) + \frac{S_u}{a_P}}_{H_P/a_p} + \nu_{11}^P \frac{(U_w - U_e)_P}{\Delta x}. \tag{3.51}$$

Similarly,

$$\overline{u_E^2} = \frac{H_E}{a_E} + \nu_{11}^E \frac{(U_w - U_e)_E}{\Delta x}, \qquad \overline{u_e^2} = \frac{H_e}{a_e} + \nu_{11}^e \frac{(U_P - U_E)}{\Delta x}$$

Using linear interpolation for ν_{11}^e and H_e/a_e, one obtains for the value at face e:

$$\begin{aligned}\overline{u_e^2} = & \underbrace{\tfrac{1}{2}(\overline{u_P^2} + \overline{u_E^2})}_{\text{linear interpolation}} \\ & + \underbrace{\frac{1}{2\Delta x}\Big\{\big[\nu_{11}^P + \nu_{11}^E\big](U_P - U_E) - \nu_{11}^P (U_w - U_e)_P - \nu_{11}^E (U_w - U_e)_E\Big\}}_{\text{velocity smoothing}}\end{aligned} \tag{3.52}$$

3.7 Wall functions

Wall functions are used in the jet-cavity interaction problem examined in Chapter 6. The form used is a simplified version of the Chieng and Launder (1980) formulation based on the modified Log-law

$$U^* = \frac{U}{u^*} = \frac{1}{\kappa}\log(E^* y^*) \tag{3.53}$$

where

$$u^* = C_\mu^{1/4} k_v^{1/2}, \quad y^* = \frac{y k_v^{1/2}}{\nu}, \tag{3.54}$$

and k_v denotes the value of k at the edge of the viscous sub-layer, which is assumed to lie at $y^* = 20$. In practice, k is assumed to be constant over the fully turbulent region, so that k_v is assumed to be the same as the value k_P, at the wall-adjacent node. The nominal friction velocity u^* is based on the eddy viscosity specification of $\overline{uv}$

$$-\overline{uv} = \frac{\tau_w}{\rho} = u_\tau^2 = C_\mu^{1/2}\frac{P_\kappa}{\varepsilon}k. \tag{3.55}$$

Under equilibrium conditions $P_\kappa/\varepsilon = 1$, and the quantity on the right hand side is used to provide an alternative estimate of u_τ that does not vanish at separation and reattachment points. Using the form of the log law above the value of wall shear stress is set as:

$$\tau_w = \begin{cases} \mu \frac{U_P}{y_P} & \text{if } y_P < y_v, \\ \frac{\rho \kappa^* u^* y_P}{\log(E^* y_P^*)} \frac{U_P}{y_P} & \text{otherwise.} \end{cases} \tag{3.56}$$

If the wall is assumed to lie on the south face of cell P, the above is implemented by modifying the coefficients of the wall parallel velocity at the wall adjacent node, U_P, as:

$$\begin{aligned} a_S &= 0 \\ S_P &= -\frac{\tau_w A}{U_P}, \end{aligned} \tag{3.57}$$

where A is the area of the wall segment. Setting $a_S = 0$ is to suppress the link with the south face, which would erroneously imply a linear velocity variation if the node lies outside the viscous sub-layer.

Because of the large variation of the production and dissipation rates over the wall adjacent cell, cell-averaged values of these quantities are used in the source terms of the k equation. These are obtained by integration,

$$\overline{P_\kappa} = \frac{1}{y_n} \int_0^{y_n} P_\kappa \, \mathrm{d}y \,, \qquad \overline{\varepsilon} = \frac{1}{y_n} \int_0^{y_n} \varepsilon \, \mathrm{d}y \tag{3.58}$$

The integrals are evaluated by employing simplified assumptions regarding the variations of the integrands over the wall adjacent cell. In this case, the assumptions are:

- The Reynolds shear stress is zero across the viscous sub-layer, and is constant and equal to the wall shear stress over the fully turbulent region.
- The dissipation rate is uniformly equal to its wall value, assumed to be:

$$\varepsilon_w = \frac{2\nu k_P}{y_v^2}, \tag{3.59}$$

  over the viscous sub-layer. In the fully turbulent region, the length scale is assumed to vary linearly with the distance from the wall $k^{3/2}/\varepsilon = c_l y$.

- k varies quadratically in the viscous sub-layer, and is constant in the fully turbulent region.

These assumptions lead to the following cell-averaged P_κ and ε:

$$\overline{P_\kappa} = \begin{cases} 0 & \text{if } y_n < y_v \\ \frac{\tau_w^2}{\rho^2 \kappa^* u^* y_n,} \log\left(\frac{y_n}{y_v}\right) & \text{otherwise,} \end{cases} \tag{3.60}$$

and

$$\overline{\varepsilon} = \begin{cases} \varepsilon_w & \text{if } y_n < y_v \\ \varepsilon_w \frac{y_v}{y_n} + \frac{u^{*3}}{\kappa^* y_n,} \log\left(\frac{y_n}{y_v}\right) & \text{otherwise.} \end{cases} \tag{3.61}$$

The above cell-averaged production and dissipation are then used to over-write the corresponding previously set local values in the source terms of the k equation (where one is solved) in all wall adjacent nodes.

The boundary condition for ε is applied at the wall-adjacent nodes, where it set by assuming equilibrium of production and dissipation, and using the scale u^* instead of the typical u_τ, to be:

$$\varepsilon_P = \frac{u^{*3}}{\kappa^* y_P} = \frac{k_P^{3/2}}{2.55 y_P} \tag{3.62}$$

Similarly, the boundary conditions for the Reynolds stress components are applied at the wall-adjacent nodes. The Reynolds stresses are derived by assuming local equilibrium and applying the Basic model with wall reflection terms, which leads to:

$$(\overline{u^2})_P = 1.098 k_P, \quad (\overline{v^2})_P = 0.248 k_P, \quad (\overline{w^2})_P = 0.654 k_P, \quad (\overline{uv})_P = -0.255 k_P. \tag{3.63}$$

In the above equations y_P is used to represent the wall distance, implying a Cartesian coordinate system with the wall coinciding with the south face of the cell. The STREAM code is able to handle more general cases than that, but for present purposes the only other possibility is for the wall to coincide with another single face or, if the cell is a corner of the geometry, two faces coincide with that wall. All these possibilities are handled by using a distance variable that is half the volume of the cell divided by the area of the face tagged as a wall. In the latter case, when the cell is at a corner, only one of the two wall distance variables will be used (the one appearing later in a loop over all wall segments).

3.8 Convergence criteria

The root-mean-square of the normalised residual error is used as the convergence measure in the present work. The normalised residual error at each node is defined as

$$\epsilon_r = \frac{a_P \phi_P - \sum_i \phi_i - S}{a_P}, \tag{3.64}$$

and the rms residual error is

$$\epsilon_{\text{rms}} = \sqrt{\frac{1}{N} \sum \epsilon_r^2} \tag{3.65}$$

where N is the total number of nodes.

Chapter 4

Homogeneous Turbulence

This chapter deals with the performance of Reynolds Stress Transport models in various types of homogeneous turbulent flow. The concept of homogeneous turbulence is introduced in Section 4.1. Next, a review of experiments and numerical simulations in homogeneous turbulence is provided in section 4.2. Section 4.3 presents the governing equations for homogeneous turbulent flows in the RST modelling framework. Numerical results arising from the application of the models to reference cases identified from the literature are presented and discussed in section 4.4. Finally, the chapter is ended with some concluding remarks in section 4.5.

4.1 Introduction

Considerable simplification of the governing equations is obtained if the turbulence can be said to be homogeneous. By this it is meant that all spatial gradients of statistical moments are negligibly small. The mean velocity gradients, if present, must be constant in space for this to be true, implying that there can be no boundaries in such a flow. This can be approximated experimentally in a duct by considering a 'turbulent box' convected with the mean flow, and having dimensions larger than the integral length scales of the turbulence, and smaller than those of the duct. The time dependence can then be related to the spatial dependence for a flow with mean velocity U_1 along the axial direction of the duct x_1 by

$$t \sim x_1/U_1$$

In such a case turbulence cannot strictly be homogeneous along the axial direction, but it can be treated as such if

$$\frac{\mathrm{d}L}{\mathrm{d}x_1} \ll 1 \quad \text{and} \quad \frac{\mathrm{d}Q}{\mathrm{d}x_1} \ll \frac{Q}{L}\,, \tag{4.1}$$

where L is an integral length scale, and Q represents a turbulent statistic (Gence, 1983). Numerically, homogeneous turbulence is in principle more straight-forward to produce, but other limitations apply. In direct numerical simulation (DNS) of homogeneous turbulence, the Navier-Stokes equations are solved using a pseudo-spectral method on a periodic box of side $\mathcal{L}$, larger than the integral length scales. The number of grid-points, N, determines the largest wavenumber κ_{max} (smallest length-scale) that can resolved by

$$\kappa_{max} = \frac{\pi N}{\mathcal{L}}\,.$$

As the Reynolds number increases, the disparity of scales increases, thus demanding a larger number of nodes for adequate resolution. This, along with stringent requirements on the time step required for accuracy and stability, which must decrease as the number of nodes increases, means that a very large computational cost is associated with the DNS approach. One implication of the high cost of direct numerical simulations is that ensemble averaging is often not feasible, and volume averaging is used to take advantage of homogeneity. The results are thus often single realisations of a random process (Tavoularis et al., 1997). In addition to that, the number of large eddies in a computational box is limited. When the length of the computational box is 3 times the integral length scale, as is typically the case, one can expect the uncertainty of large scale properties, such as the Reynolds stresses, to be of the order of 10% (Tavoularis et al., 1997). When the turbulence is strained the turbulent length scales grow, so the simulation must eventually be stopped, as the length-scales begin to outgrow the computational box. If the box size is too small, this may happen before the effects of the initial conditions are lost and self-similar evolution of the flow is attained. Despite these difficulties, high quality DNS results, when available, provide far more detailed information than experiments possibly can, since all turbulent statistics can be calculated.

Because there can be no gradients of Reynolds stresses in homogeneous turbulence, the turbulence can have no effect on the mean flow. The mean flow

gradients can thus be prescribed independently, and their effect on the turbulence evolution can be studied. The governing equations reduce to ordinary differential equations to be solved with appropriate initial conditions. Thus the effects of convection and diffusion, in addition to near–wall effects, with all their modelling and numerical burden, can be temporarily eliminated from the analysis, allowing other important effects to be studied more closely. Specifically, the redistributive effects due to pressure–strain-rate interaction, and the dissipation rate are the only unclosed source terms that remain in the Reynolds-stress equations.

4.2 Homogeneous turbulence data

Homogeneous shear

Simulations of homogeneous simple shear have been carried out by several researchers. Rogers and Moin (1987) generated a database of homogeneous turbulence fields by direct numerical simulation of the unsteady, incompressible Navier-Stokes equations on a domain of up to 128^3 grid points. The purpose of their study was to examine the structure and development of the vorticity field under various mean strain configurations. They were interested in particular in the conditions under which 'hairpin' vortices develop. They found that such vortices require a nonzero mean shear to develop, and thus are not found in purely irrotational strain fields. Of relevance to the current work are the results for the evolution of turbulent kinetic energy, its dissipation rate, and the Reynolds stresses obtained from their simulations. Three simulations are available, for which the initial shear parameter was kept constant at $S_0^* = 2.365$ and the initial turbulence Reynolds number was varied in the range $Re_{t0} = 33 - 530$. A *random* initial velocity field satisfying continuity, and having a prescribed three dimensional energy spectrum was specified in each case. The initial stage of evolution might thus be of less value for comparison in these simulations since a realistic turbulence field might not have fully developed. A deforming computational grid that followed the mean flow was used, and the grid was re-meshed at regular intervals as it became skewed following the deforming flow. The data were saved at time steps when the mesh was orthogonal. The length scale was found to grow more slowly as the turbulence Reynolds number was increased.

Jakobitz et al. (1997) performed DNS of homogeneous, uniformly sheared, and stably stratified flow. They considered the effects of varying the gradient Richardson number, the initial micro-scale Reynolds number, $Re_{\lambda 0} = (\sqrt{2k}\lambda/\nu)_0$, and the initial shear number on turbulence evolution. A base case in their study was one having a zero Richardson number, and the results of that case are relevant to the current study since stratification is not considered here. A spectral collocation method on a 128^3 grid was used in the simulations. A deforming grid with regular re-meshing was also used in this study. Aliasing errors which arise from re-meshing were handled by truncation of the modes corresponding to the highest third of the wavenumber spectrum, before and after re-meshing. This translates to a loss in energy and dissipation rate, of the order of 1-5% when the shear is 'weak' (Lee et al., 1990), as it is here. The researchers demonstrated the effect of the assumed initial velocity spectrum (energy spectrum) on the evolution of turbulence statistics. Their concern was that, in order for a parametrisation based on initial values of the statistics to be meaningful, these initial values must be characteristic of the evolution to follow. They demonstrated that using a random field with a prescribed energy spectrum (usually top hat or exponential) results in an initial transient in which there is a large drop in Re_λ and S^*. This drop is due to to the energy redistributing into the high wavenumber portion of the spectrum, whose energy the initial conditions largely underestimate, thus sharply increasing the viscous dissipation. The result is a large unrealistic drop in Re_λ and S^* (Jakobitz et al., 1997). To avoid this, an initialization simulation was carried out for a time interval larger than the initial transient, and the field thus obtained was used as an initialization for the subsequent study cases.

Matsumoto et al. (1991) ran two simulations at an intermediate and high initial strain parameter. They used a Fourier spectral method on a 64^3 grid for the lower shear case, and a $256 \times 64 \times 64$ grid for the higher shear case. A deforming grid, with re-meshing and aliasing treatment similar to the previously mentioned workers was used. An isotropic velocity field satisfying continuity, with a specified energy spectrum, was used to initialise the simulation.

Lee et al. (1987, 1990) used DNS to study the structure of turbulence at high shear rate. They report the results of simulation cases having S_0^* of 17 (Lee et al., 1990) and 50 (Lee et al., 1987). The numerical scheme used in these cases is similar to the previous ones, except that re-meshing was not used because the anti-aliasing measure it requires would introduce too large an error (energy loss).

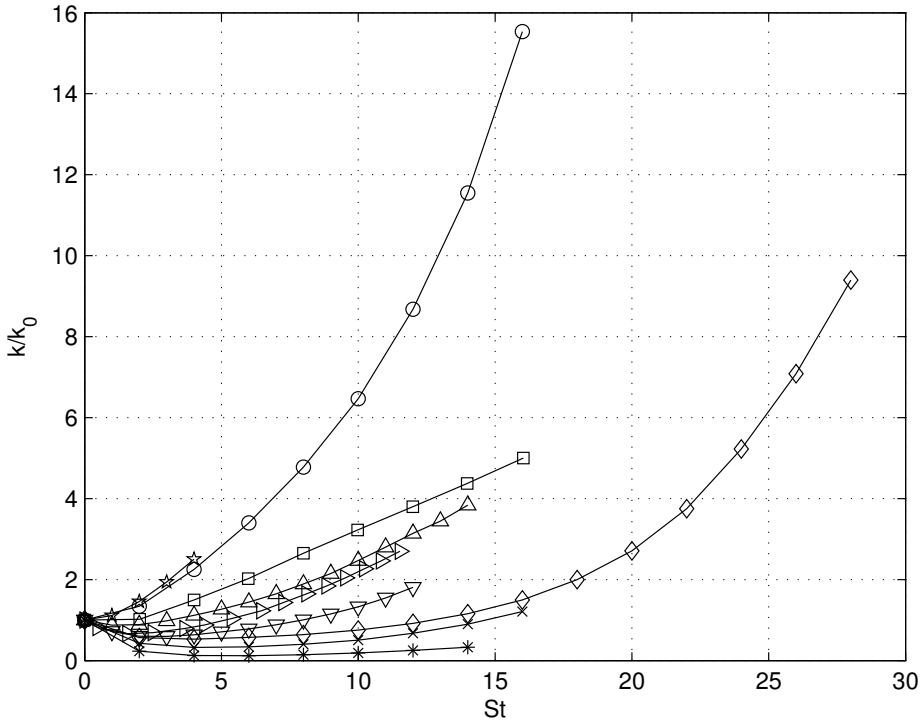

(a) Turbulent kinetic energy

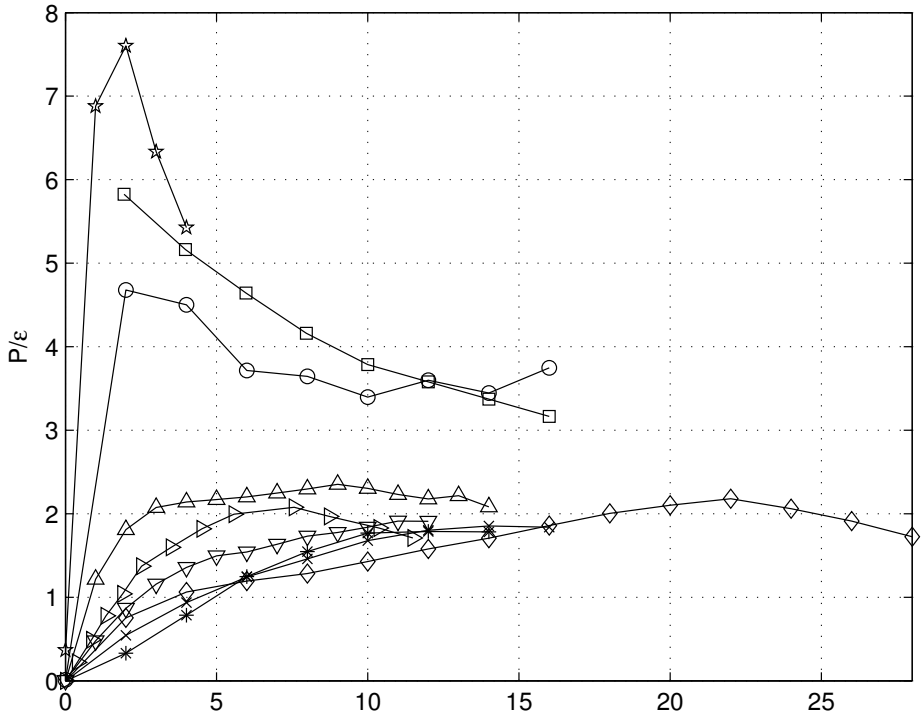

(b) Production-to-dissipation ratio

Figure 4.1: Evolution of turbulent kinetic energy and the ratio of the production to dissipation rates in homogeneous shear DNS cases. Symbols are defined in Table 4.1.

	$\mathrm{Re}_{\lambda 0} = (\sqrt{2k}\lambda/\nu)_0$	Re_{t0}	S_0^*	Symbol
Jakobitz et al. (1997)	44.72		2.0	$\triangleright$
Rogers and Moin (1987) 1	~ 70	33.4	2.365	$\diamond$
Rogers and Moin (1987) 2		133.6	2.365	$\times$
Rogers and Moin (1987) 3		534.25	2.365	$*$
Sarkar (1995)	24.3		2.6	$\triangledown$
Matsumoto et al. (1991) 1	55.24	152.5	4.715	$\triangle$
Matsumoto et al. (1991) 2	19.24	18.1	30.65	$\star$
Lee et al. (1990) 1	~ 40	75	16.75	$\circ$
Lee et al. (1987) 2	~ 20	10	50	$\square$

Table 4.1: Summary of initial data of simple shear DNS cases, and symbols used in Figures 4.1 and 4.2

Their argument was that, because of the high shear involved, the turbulence scales grow rapidly so the skewed mesh is still able to resolve the fine scales. The grid used in these cases is also larger than the previous studies with $512 \times 128 \times 128$ nodes in the stream-wise, normal and span-wise directions respectively. This is necessary to resolve properly the elongated eddies that form due to the high shear rate (Lee et al., 1990).

The relevant initial data for the above DNS cases are summarised in table 4.1. The evolutions of turbulent kinetic energy and the production-to-dissipation ratio are shown in figure 4.1, and evolution of the anisotropy components is shown in figure 4.2. The three lowest curves in figure 4.1a are for the Rogers and Moin (1987) cases with $S_0^* = 2.37$, followed by that from Sarkar (1995) with $S_0^* = 2.6$, then Jakobitz et al. (1997) with $S_0^* = 2.0$. The significant variation in this set of curves with similar initial shear rate parameter reflects the strong effect that the choice of initial spectrum has on the evolution of the level of turbulence, something that conventional RANS models cannot replicate. While there seems to be a large degree of variation in kinetic energy evolution for the different DNS cases, a clear pattern can be observed in the evolutions of the production-to-dissipation ratio and stress anisotropy. The anisotropy is independent of the level of turbulence, but rather depends on the turbulence time scale k/ε, so it is not strongly affected by the choice of initial velocity field. Similarly, at the smaller shear rates P_κ/ε seems to be affected only slightly in the initial stages, but later on, curves with similar initial shear rates tend to converge to a similar equilibrium level. The two general patterns of P_κ/ε and a_{ij} are reflected in the

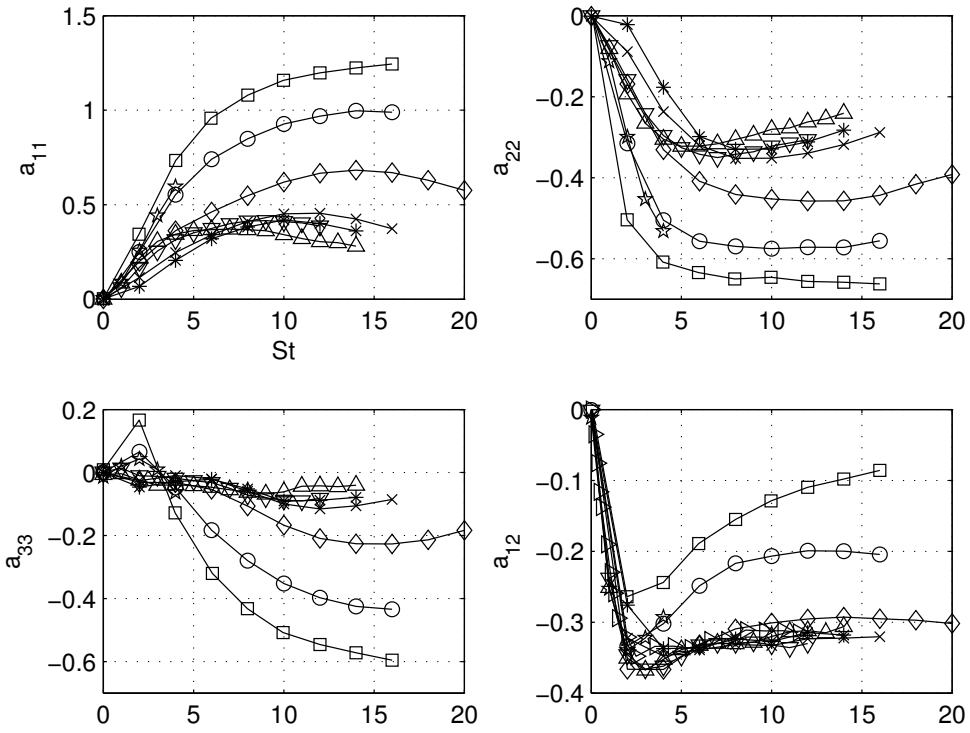

Figure 4.2: Evolution of Reynolds stress anisotropy in homogeneous shear DNS cases. Symbols are defined in Table 4.1.

clustering of the lower-shear rate data, and the departing higher shear rate data observable in figures 4.1b and 4.2 (if the lowest $\mathrm{Re_t}$ case of Rogers and Moin is excluded).

Yu and Girimaji (2006) carried out a DNS study of homogeneous turbulence subjected to a sinusoidally oscillating shear, given by

$$\frac{\partial U}{\partial y} = S_{\max} \sin \omega t, \tag{4.2}$$

where $S_{\max}$ is the amplitude of the shear, and ω is the angular frequency. The periodic shear was imposed on the flow through the addition of a body force to the governing equations. Their numerical simulations were based on the Lattice-Boltzmann method which, rather than solving the Navier–Stokes equations, solves the discrete Boltzmann equation for a function describing the statistical distribution of single particles. The macroscopic phenomena of viscous fluid flow emerge when simulating the interactions between a sufficiently large number of particles. Yu and Girimaji performed validations of this method by comparing with other

Case	S_0^*	Re_{t0}
LRPS1	1.0	9.8
LRPS2	8.0	11
LRPS3	154	9.8
LRAC1	0.965	12
LRAC2	9.65	14
LRAC3	96.5	12
LRAE1	0.707	11
LRAE2	7.07	14
LRAE3	70.7	14

Table 4.2: Summary of initial data in DNS cases of Lee and Reynolds (1985), and symbols used in corresponding figures

well-established DNS results, such as those of Rogers and Moin (1987) and Jakobitz et al. (1997), and obtained good agreement. The initial shear parameter, in this case defined as $S_0^* = S_{\max} k_0/\varepsilon_0$, was fixed at 3.3 for all their simulations, and the initial Taylor-micro-scale Reynolds number was $\mathrm{Re}_\lambda = 33$. Simulations were carried out for a range of frequencies $0.125 < \omega/S_{\max} < 10$.

Irrotational strains

Lee and Reynolds (1985) carried out simulations of homogeneous turbulence subjected to three classes of irrotational strains: plane strain, axisymmetric contraction, and axisymmetric expansion. Each type of strain was run at several different strain rates. Three strain-rates are selected for study here for each type of strain, each separated from the next by an order of magnitude, as summarised in table 4.2. The numerical solutions of Lee and Reynolds were obtained on grids of 128^3 points, using a procedure very similar to those mentioned above for homogeneous shear. Regarding the specification of initial conditions, Lee and Reynolds devised and used a rational method for specifying the initial energy spectrum and micro-scale Reynolds number in their simulations based on specifying the required resolutions of the energy-containing eddies, and the smallest dissipative eddies (Lee and Reynolds, 1985).

Sjögren and Johansson (1998) carried out an axisymmetric contraction experiment with the purpose of demonstrating the application of new theoretical results

that allow the pressure–strain-rate correlation to be measured directly in axisymmetric turbulence without having to infer it from a balance of the Reynolds-stresses. The method, due to Lindborg (1995), is based on evaluating integrals of measurable second and third order two-point velocity correlations. The duct had a contraction ratio of 9, and a relaxation section of constant area. Measurements of k, ε, and the normal stress anisotropy a_{11}, as well as the slow and rapid pressure–strain-rate correlations, among other statistics, are reported at a turbulence Reynolds number of 1250.

Chen et al. (2006) used an experimental setup to study the response of turbulence to a sequence of straining-relaxation-destraining. The experimental apparatus consisted of a water tank having dimensions $325\,(\mathrm{L}) \times 125\,(\mathrm{H}) \times 20\,(\mathrm{W})$ cm, active grids for generation of turbulence, and a piston used to effect plane straining and destraining. The test section was at the bottom centre of the tank, and two active grids were located a distance away on each side of it. Particle image velocimetry (PIV) measurements were made through windows located below and on both sides of the test section. The turbulent field generated by the active grids was strained by the descending piston, creating a plane strain field. This was followed by a relaxation period during which the piston was stationary, then a period of plane destraining as the piston ascended to its starting position. The measurements were repeated 1000 times at each recording time step, and the data was ensemble-averaged. The researchers report the strain history, and the Reynolds stresses in the strained directions only. Unfortunately, the $\overline{w^2}$ component, and therefore the total turbulent kinetic energy, was not measured.

4.3 Governing equations

In homogeneous turbulence the mean velocity gradients, and all turbulent statistics, are constant in space. The exact turbulent kinetic energy equation (2.10) in this case reduces to

$$\frac{\mathrm{d}k}{\mathrm{d}t} = P_\kappa - \varepsilon \tag{4.3}$$

It is convenient under such situations to consider separately the evolutions of the level of turbulence, represented by k (4.3), and the degree of anisotropy of the

stresses, given by a_{ij}. Using the definition (2.11), one can write

$$\begin{aligned}\frac{\mathrm{d}a_{ij}}{\mathrm{d}t} &= \frac{1}{k}\frac{\mathrm{d}R_{ij}}{\mathrm{d}t} - \frac{R_{ij}}{k}\frac{P_\kappa - \varepsilon}{k} \\ &= \frac{1}{k}(P_{ij} + \phi_{ij} - \varepsilon_{ij}) - (a_{ij} + \frac{2}{3}\delta_{ij})\frac{P_\kappa - \varepsilon}{k}\,,\end{aligned}$$

or

$$\frac{\mathrm{d}a_{ij}}{\mathrm{d}t} = P^a_{ij} + \frac{1}{k}\phi_{ij} - \frac{\varepsilon}{k}\left(e_{ij} - a_{ij}\right)\,, \tag{4.4}$$

where P^a_{ij} is the production of stress anisotropy,

$$P^a_{ij} = \frac{1}{k}(P_{ij} - (a_{ij} + \frac{2}{3}\delta_{ij})P_\kappa)\,, \tag{4.5}$$

and e_{ij} is the anisotropy of dissipation,

$$e_{ij} = \frac{\varepsilon_{ij}}{\varepsilon} - \frac{2}{3}\delta_{ij} \tag{4.6}$$

The mean strain rate and vorticity tensors are defined as

$$S_{ij} = \frac{1}{2}\left(\frac{\partial U_i}{\partial x_j} + \frac{\partial U_j}{\partial x_i}\right), \quad \Omega_{ij} = \frac{1}{2}\left(\frac{\partial U_i}{\partial x_j} - \frac{\partial U_j}{\partial x_i}\right) \tag{4.7}$$

respectively, and

$$S = \sqrt{2S_{ij}S_{ji}}\,, \tag{4.8}$$

is an invariant of the mean strain, which can be interpreted as a modulus of the mean strain rate.

For a constant strain rate modulus, as in the cases to be considered shortly, the parameter $S^* = \frac{Sk}{\varepsilon}$ has the interpretation of a dimensionless turbulent time-scale. Evolution of this time-scale, or more conveniently its inverse $\psi = \frac{1}{S^*}$, with respect to the dimensionless time $t^* = St$ is given by

$$\frac{\mathrm{d}}{\mathrm{d}t^*}\left(\frac{\varepsilon}{Sk}\right) = \frac{1}{S^2 k}\frac{\mathrm{d}\varepsilon}{\mathrm{d}t} - \frac{\varepsilon}{S^2k^2}(P_\kappa - \varepsilon) \tag{4.9}$$

If the modelled dissipation equation (2.29) is substituted, one obtains

$$\frac{\mathrm{d}\psi}{\mathrm{d}t^*} = \left[(C_{\varepsilon 1} - 1)\frac{P_\kappa}{\varepsilon} - (C_{\varepsilon 2} - 1)\right]\psi^2 \tag{4.10}$$

This result is significant because it states that, regardless of the type of homogeneous flow (provided S is constant), using (2.29) will always produce the same equilibrium value of the production-to-dissipation ratio at which the time-scale becomes constant

$$\left(\frac{P_\kappa}{\varepsilon}\right)_\infty = \frac{C_{\varepsilon 2} - 1}{C_{\varepsilon 1} - 1}\,. \tag{4.11}$$

Whether this is realistic or not will be considered in relation to the available data.

4.3.1 Simple shear

In simple shear the velocity gradient tensor is given by

$$\frac{\partial U_i}{\partial x_j} = \frac{\mathrm{d}U}{\mathrm{d}y}\begin{pmatrix} 0 & 1 & 0 \\ 0 & 0 & 0 \\ 0 & 0 & 0 \end{pmatrix} \tag{4.12}$$

The Reynolds stress production tensor is thus

$$P_{ij} = -\frac{\mathrm{d}U}{\mathrm{d}y}\begin{pmatrix} 2\overline{uv} & \overline{v^2} & 0 \\ \overline{v^2} & 0 & 0 \\ 0 & 0 & 0 \end{pmatrix} \tag{4.13}$$

The production of turbulent kinetic energy is

$$P_\kappa = -\overline{uv}\frac{\mathrm{d}U}{\mathrm{d}y} = -ka_{12}\frac{\mathrm{d}U}{\mathrm{d}y} \tag{4.14}$$

Thus, the production of stress anisotropy is

$$P^a_{ij} = \frac{\mathrm{d}U}{\mathrm{d}y}\begin{pmatrix} -\frac{4}{3}a_{12} + a_{12}a_{11} & -\frac{2}{3} - a_{22} + a_{12}^2 & 0 \\ -\frac{2}{3} - a_{22} + a_{12}^2 & \frac{2}{3}a_{12} + a_{12}a_{22} & 0 \\ 0 & 0 & \frac{2}{3}a_{12} + a_{12}a_{33} \end{pmatrix} \tag{4.15}$$

The above expressions are the exact terms in the transport equations. In order to get complete evolution equations for k and a_{ij}, modelled redistributive and dissipative parts need to be included. Using the Basic model, evolutions of $k^* = \frac{k}{k_0}$, a_{ij} and $\psi = \frac{1}{S^*} = \frac{\varepsilon}{Sk}$ are given by

$$\frac{\mathrm{d}k^*}{\mathrm{d}t^*} = -k^*(a_{12} + \psi) \tag{4.16}$$

$$\frac{\mathrm{d}a_{11}}{\mathrm{d}t^*} = -\tfrac{4}{3}(1-c_2)a_{12} + a_{12}a_{11} - (c_1-1)\psi a_{11} \tag{4.17}$$

$$\frac{\mathrm{d}a_{22}}{\mathrm{d}t^*} = \tfrac{2}{3}(1-c_2)a_{12} + a_{12}a_{22} - (c_1-1)\psi a_{22} \tag{4.18}$$

$$\frac{\mathrm{d}a_{12}}{\mathrm{d}t^*} = -(1-c_2)(a_{22}+\tfrac{2}{3}) + a_{12}^2 - (c_1-1)\psi a_{22} \tag{4.19}$$

$$\frac{\mathrm{d}\psi}{\mathrm{d}t^*} = -(c_{\varepsilon 1}-1)\psi a_{12} - (c_{\varepsilon 2}-1)\psi^2 \tag{4.20}$$

4.3.2 Plane strain

The velocity gradient tensor in homogeneous plane strain is

$$G_{ij} = \frac{\partial U_i}{\partial x_j} = \frac{\mathrm{d}U}{\mathrm{d}x}\begin{pmatrix} 1 & 0 & 0 \\ 0 & -1 & 0 \\ 0 & 0 & 0 \end{pmatrix} \tag{4.21}$$

The Reynolds stress production tensor is

$$P_{ij} = -\frac{\mathrm{d}U}{\mathrm{d}x}\begin{pmatrix} 2\overline{u^2} & 0 & 0 \\ 0 & -2\overline{v^2} & 0 \\ 0 & 0 & 0 \end{pmatrix} \tag{4.22}$$

The production of turbulent kinetic energy is now

$$P_\kappa = -\frac{\mathrm{d}U}{\mathrm{d}x}(\overline{u^2} - \overline{v^2}) = -\frac{\mathrm{d}U}{\mathrm{d}x}\,k\,(a_{11}-a_{22}) \tag{4.23}$$

We then have, for the evolution of the anisotropy using the Basic model:

$$\frac{\mathrm{d}a_{11}}{\mathrm{d}t^*} = -\frac{4}{3}(1-c_2)a_{11} - \frac{2}{3}(1-c_2)a_{22} - a_{11}(a_{22}-a_{11}) - (c_1-1)\psi a_{11} - \frac{4}{3}(1-c_2), \tag{4.24}$$

$$\frac{\mathrm{d}a_{22}}{\mathrm{d}t^*} = \frac{4}{3}(1-c_2)a_{22} + \frac{2}{3}(1-c_2)a_{11} - a_{22}(a_{22}-a_{11}) - (c_1-1)\psi a_{22} + \frac{4}{3}(1-c_2), \tag{4.25}$$

$$\frac{\mathrm{d}a_{33}}{\mathrm{d}t^*} = -a_{33}(a_{22}-a_{11}) - \frac{2}{3}(1-c_2)(a_{22}-a_{11}) - (c_1-1)\psi a_{33}, \tag{4.26}$$

$$\frac{\mathrm{d}\psi}{\mathrm{d}t^*} = (c_{\varepsilon 1} - 1)(a_{22} - a_{11})\psi - (c_{\varepsilon 2} - 1)\psi^2. \tag{4.27}$$

4.3.3 Axisymmetric contraction

In this class of flow the velocity gradient tensor is

$$G_{ij} = \frac{\partial U_i}{\partial x_j} = \frac{\mathrm{d}U}{\mathrm{d}x}\begin{pmatrix} 1 & 0 & 0 \\ 0 & -1/2 & 0 \\ 0 & 0 & -1/2 \end{pmatrix} \tag{4.28}$$

The Reynolds stress production tensor is

$$P_{ij} = -\frac{\mathrm{d}U}{\mathrm{d}x}\begin{pmatrix} 2\overline{u^2} & 0 & 0 \\ 0 & -\overline{v^2} & 0 \\ 0 & 0 & -\overline{w^2} \end{pmatrix} \tag{4.29}$$

The production of k in homogeneous axisymmetric contraction flow is given by

$$P_\kappa = -\frac{1}{2}(2\overline{u^2} - \overline{v^2} - \overline{w^2})\frac{\mathrm{d}U}{\mathrm{d}x} = -\Big(\frac{3}{2}\overline{u_1^2} - k\Big)\frac{\mathrm{d}U}{\mathrm{d}x} = -\frac{3}{2}a_{11}k\frac{\mathrm{d}U}{\mathrm{d}x} \tag{4.30}$$

Using the Basic model, the evolution of the stress anisotropy and ψ are given by (note that, because of symmetry, $a_{33} = a_{22}$):

$$\frac{\mathrm{d}a_{11}}{\mathrm{d}t^*} = \frac{3}{2}a_{11}^2 - (1 - c_2)a_{11} - (c_1 - 1)\psi\, a_{11} - \frac{4}{3}(1 - c_2), \tag{4.31}$$

$$\frac{\mathrm{d}a_{22}}{\mathrm{d}t^*} = \frac{3}{2}a_{11}a_{22} + (1 - c_2)a_{11} + (1 - c_2)a_{22} - (c_1 - 1)\psi\, a_{22} + \frac{2}{3}(1 - c_2), \tag{4.32}$$

$$\frac{\mathrm{d}\psi}{\mathrm{d}t^*} = -\frac{3}{2}(c_{\varepsilon 1} - 1)a_{11}\,\psi - (c_{\varepsilon 2} - 1)\,\psi^2. \tag{4.33}$$

4.3.4 Axisymmetric expansion

In this type of strain the velocity gradient tensor is given by:

$$G_{ij} = \frac{\partial U_i}{\partial x_j} = \left|\frac{\mathrm{d}U}{\mathrm{d}x}\right|\begin{pmatrix} -1 & 0 & 0 \\ 0 & 1/2 & 0 \\ 0 & 0 & 1/2 \end{pmatrix} \tag{4.34}$$

The Reynolds stress production tensor is

$$P_{ij} = \left|\frac{\mathrm{d}U}{\mathrm{d}x}\right| \begin{pmatrix} 2\overline{u^2} & 0 & 0 \\ 0 & -\overline{v^2} & 0 \\ 0 & 0 & -\overline{w^2} \end{pmatrix} \tag{4.35}$$

The production of k in homogeneous axisymmetric expansion flow is given by

$$P_\kappa = \frac{1}{2}(2\overline{u^2} - \overline{v^2} - \overline{w^2}) \left|\frac{\mathrm{d}U}{\mathrm{d}x}\right| = \frac{3}{2} a_{11} k \left|\frac{\mathrm{d}U}{\mathrm{d}x}\right| \tag{4.36}$$

and the anisotropy evolution, using the Basic model, is obtained from

$$\frac{\mathrm{d}a_{11}}{\mathrm{d}t^*} = -\frac{3}{2}a_{11}^2 + (1-c_2)a_{11} - (c_1 - 1)\,\psi\, a_{11} + \frac{4}{3}(1-c_2), \tag{4.37}$$

$$\frac{\mathrm{d}a_{22}}{\mathrm{d}t^*} = -\frac{3}{2}a_{11}a_{22} - (1-c_2)a_{11} - (1-c_2)a_{22} - (c_1 - 1)\,\psi\, a_{22} - \frac{2}{3}(1-c_2), \tag{4.38}$$

$$\frac{\mathrm{d}\psi}{\mathrm{d}t^*} = \frac{3}{2}(c_{\varepsilon 1} - 1)\,\psi\, a_{11} - (c_{\varepsilon 2} - 1)\,\psi^2. \tag{4.39}$$

4.4 Results

4.4.1 Simple shear

The evolution of turbulent kinetic energy and the a_{11} and a_{12} components of stress anisotropy as predicted by four different models are shown in Figure 4.3, along with reference DNS data, for a range of values of the initial dimensionless shear parameter S_0^*. The models used are the Basic, LRR-QI, SSG, and TCL models. The reference DNS data used for these cases are listed in Table 4.3. At the lowest initial shear rate $S_0^* = 1.2$, both k and the two anisotropy components are well predicted by all the models. At the next level of dimensionless shear, the SSG model slightly under-predicts the rate of k^* evolution. In simple shear the evolution of k^* is given exactly by

$$\frac{\mathrm{d}k^*}{\mathrm{d}t^*} = \frac{P_k - \varepsilon}{S k_0} = -a_{12}k^* - \frac{\varepsilon^*}{S_0^*}\,. \tag{4.40}$$

Thus, given the initial value S_0^*, any error in the predicted k^* evolution must originate from errors in the shear stress anisotropy or dissipation rate predictions.

Table 4.3: DNS data used as reference for homogeneous shear cases. t_0^* is the dimensionless time taken as the starting point for the models, and to which S_0^* corresponds, and t_{end}^* is the end point of the available DNS data.

S_0^*	t_0^*	t_{end}^*	Reference
1.2	2	14	Rogers and Moin (1987) Case 3
2.0	1	12	Sarkar (1995)
5.16	2	14	Matsumoto et al. (1991) Case 1
16.75	0	16	Lee et al. (1990)
50	0	16	Lee et al. (1987)

Figure 4.4 shows the terms appearing on the right hand side of (4.40). It can be seen in this figure that the SSG model more closely reproduces both production and dissipation rates of k^* at $S_0^* = 1.2$, while it slightly under-predicts these rates (particularly the production) at $S_0^* = 2.0$. The opposite is true for the other three models. These trends are reflected in the k^* evolutions as seen in the top two rows of Figure 4.3. Considering that the value of a_{12} at t_{end}^* that is returned by the SSG model is closer to those of the DNS than the other models, the under-predicted level of k^* and production rate must be due to the slight under-prediction of a_{12} in the initial stage of development, as can be seen by inspection of Figure 4.3. This leads to less energy being accumulated from the initial stage in the integration of (4.40).

These discrepancies notwithstanding, it can generally be said that at these two rates of shear both turbulence energy and the a_{11}, a_{12} components of the anisotropy tensor are reasonably reproduced by the models.

It should be noted here that the TCL results presented in Figures 4.3 and 4.4 were obtained using $C_{\varepsilon 1} = 1.44$ and $C_{\varepsilon 2} = 1.92$. Although later references on the TCL model, such as Craft (1998) and Craft and Launder (2002), recommend the alternative prescription, listed previously in Equations (2.107):

$$C_{\varepsilon 1} = 1.0, \qquad C_{\varepsilon 2} = \frac{1.92}{1 + 0.7 A_d \sqrt{A_2}}, \tag{4.41}$$

the former more conventional values were used here because, as (4.11) suggests, the use of $C_{\varepsilon 1} = 1$ (in conjunction with the standard ε equation) in homogeneous turbulence leads to an unbounded 'equilibrium' level of P_κ/ε. It was found, for instance, that the use of (4.41) leads to odd behaviour in a_{ij}. The prescription in (4.41) is retained, however, in later chapters where inhomogeneous flows are

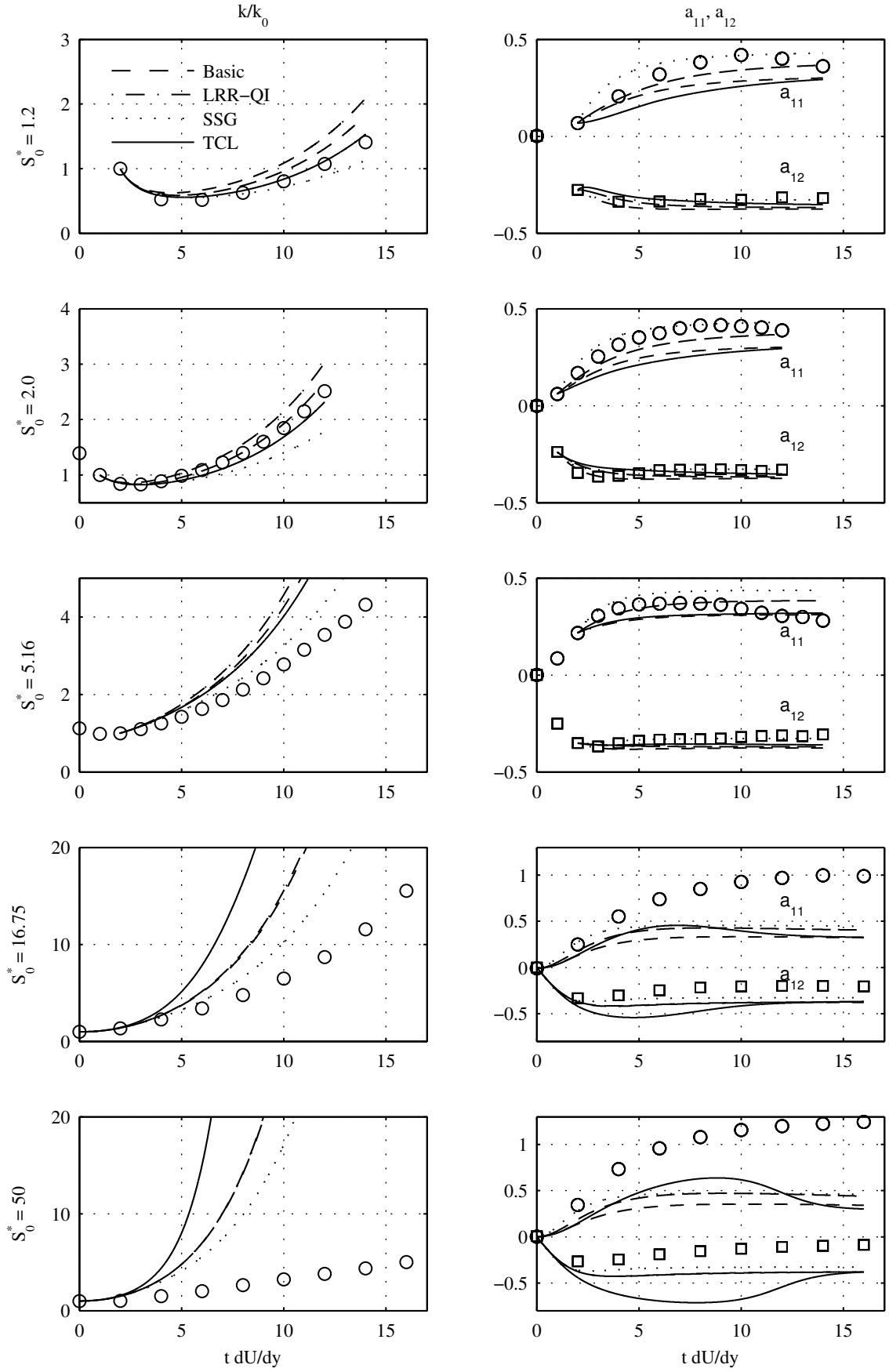

Figure 4.3: Evolution of turbulent kinetic energy (left) and a_{11},a_{12} components of anisotropy (right) in simple homogeneous shear at various shear rates.

examined.

At the intermediate level of shear, $S_0^* = 5.16$, the Basic, LRR-QI and TCL models significantly over-predict k^*, this is due to over-predicting the magnitude of a_{12} (21, 23%, and 18% higher than the DNS value, respectively, compared to 7% higher for the SSG model). It can still be said, however, that at this level of shear the anisotropy prediction is qualitatively correct.

At the higher shear levels, $S_0^* = 16.75$ and 50, there is a marked qualitative change in the behaviour exhibited by the DNS turbulence statistics. Due to the high shear rate in these cases, the DNS results resemble the Rapid Distortion Theory (RDT) solution for simple shear, as confirmed by Lee et al. (1990). In the rapid distortion limit, simply-sheared homogeneous turbulence tends towards a one-component limit, where all of the energy is contained in the $\overline{u^2}$ component, the $\overline{uv}$ component is suppressed, and the asymptotic growth of k is linear rather than exponential (Pope, 2000). These trends are seen in the bottom two rows of Figure 4.3. Specifically, the normal anisotropy a_{11} is markedly higher than in the previous cases, and is largely under-predicted by the models, and the magnitude of the turbulence energy-producing a_{12} is lower than in previous cases, and over-predicted by all the models. The over-prediction of a_{12} leads to an exaggerated rate of growth of k. The reduction in the magnitude to which a_{12} falls with increasing S_0^* is also highlighted in Table 4.4, showing the value of a_{12} at the end of each simulation. The table reveals that, in the DNS results, there is a definite decreasing trend in the long-time shear stress anisotropy.

4.4.2 Modelling explorations

Constant ϕ_{ij}^r model coefficients

The simplest variation applied to the TCL model that was surprisingly found to yield significant improvements in all the homogeneous shear cases (including the unsteady cases to follow shortly), was to use constant values for the rapid pressure-strain rate model, using the values $C_2 = 0.55$, $C_2' = 0.6$, as originally recommended by Fu (1988).

The currently used variable prescription of these coefficients in the Low-Re TCL model was found by Craft (1998) to improve the model's performance in near-wall shear flows and the backward facing step problem, where it was noted that a higher C_2 contributed an excessively large sink for the shear stress (Craft,

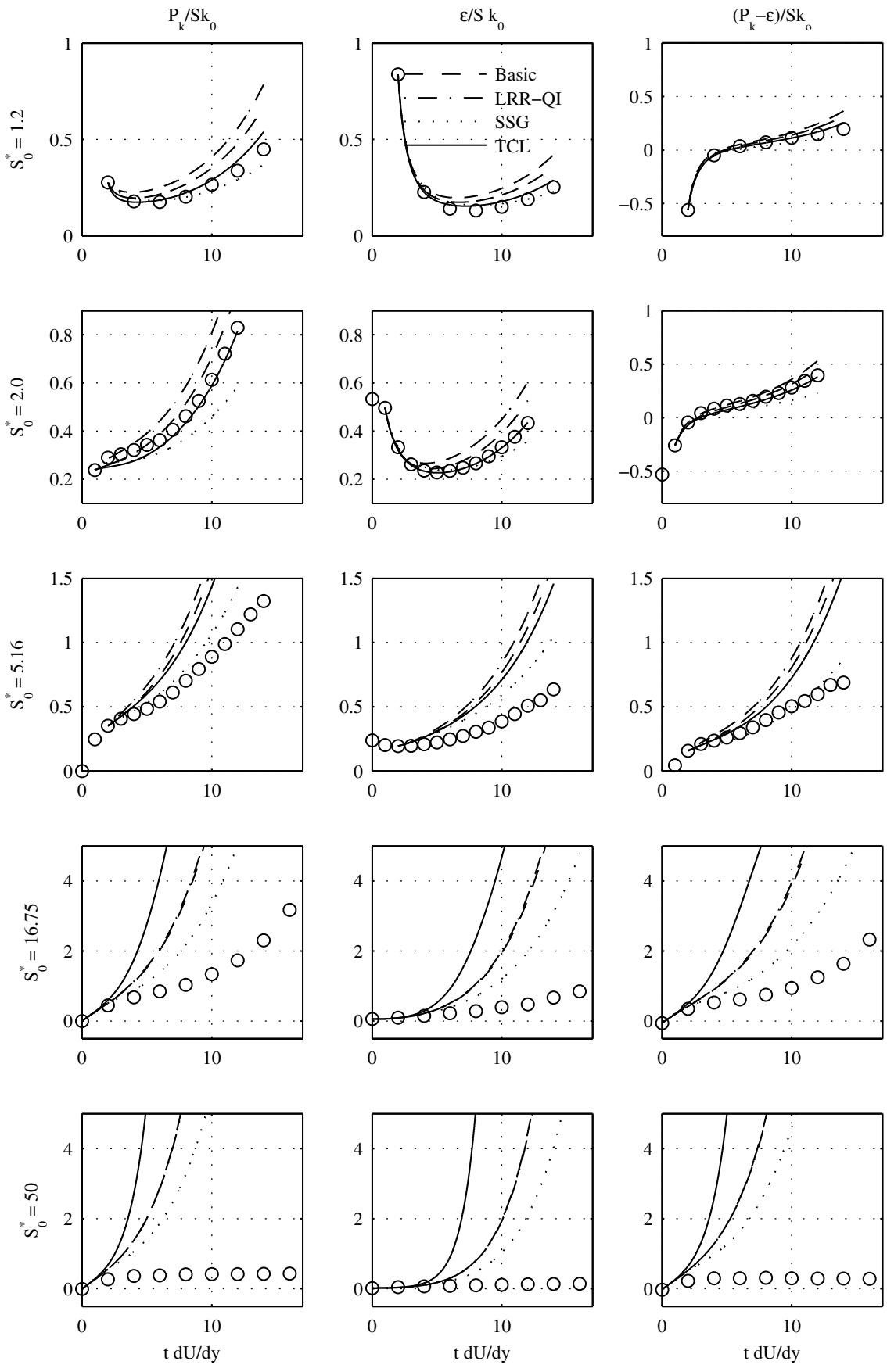

Figure 4.4: Evolution of the quantity $(P_\kappa - \varepsilon)/Sk_0$, representing the right-hand side of k/k_0 evolution equation.

1998), it was therefore desirable to reduce the C_2 coefficient in regions of high shear rate. In the present homogeneous shear cases, the former effect (C_2 contributing a large sink for the shear stress) is precisely what is desired, as the RDT solution predicts that a_{12} decays. Inspection of Table 4.4, shows that only the TCL model with constant coefficients (denoted TCL cc) displays a decreasing trend of a_{12} with increasing S_0^*. The low-Re TCL exhibits an opposite trend.

The improvement brought about by using constant C_2 and C_2' coefficients was not found to extend to irrotational strains where, as will be seen later, the more recent version of the TCL, with variable C_2, C_2' coefficients, gives superior results.

The preceding observations therefore suggest that the modelled term should be reformulated in order to only bring about the reduction of the C_2 coefficient with strain rate in near-wall, or strongly inhomogeneous, flow regions.

Modifications to P_ε

Another modification that was also tested is to use an alternative form for P_ε borrowed from the eddy-viscosity formulation. In eddy viscosity models P_κ is given by

$$P_\kappa = 2C_\mu \frac{k^2}{\varepsilon} S_{ij} S_{ji}. \tag{4.42}$$

If this is used in the modelled dissipation rate production term, one obtains the following,

$$P_\varepsilon = C_{\varepsilon 1} \frac{\varepsilon}{k} P_\kappa = 2\, C_{\varepsilon 1}\, C_\mu k\, S_{ij} S_{ji}. \tag{4.43}$$

This modification has the effect of increasing the sensitivity of the model, through the dissipation rate production rate, to the strength of the mean strain. It is denoted TCL mod P_ε in Table 4.4 and upcoming figures.

The effect of the previous two modifications, compared to the Craft (1998) version of the TCL model, is shown in Figures 4.5 and 4.6, where they are applied to the same cases presented previously in Figures 4.3 and 4.4. The effect of both modifications at low S_0^* is small. Starting from the intermediate dimensionless shear level $S_0^* = 5.56$ onwards, the TCL model, as was previously seen, over-predicts the rate of growth of k/k_0. Both modifications bring down this growth rate at intermediate to high S_0^*. In the case of the TCL model with the modified P_ε, the growth rate of k/k_0 is brought down excessively at $S_0^* = 5.56$ and 16.75, but is in good agreement with the DNS results at $S_0^* = 50$. The constant coefficient version does relatively well over the whole range of S_0^*, but exhibits some

Table 4.4: Magnitude of a_{12} from DNS and models at t^*_{end} at various levels of dimensionless shear. Values in brackets are the percentage difference between the model and DNS values.

	a_{12}	% difference in a_{12} at t^*_{end} between models and DNS					
S^*_0	DNS	Basic	LRR-QI	SSG	TCL	TCL cc	TCL mod P_ε
1.2	0.318	15.6%	18%	2.97%	10.7%	-2.97%	3.03%
2.0	0.330	11.5%	13.8%	-0.773%	6.73%	-6.68%	-0.734%
5.56	0.306	20.9%	22.8%	7.03%	17.6%	-4.55%	6.91%
16.75	0.204	83.1%	84.9%	60.6%	80.6%	21.9%	60.44%
50	0.086	342%	342.5%	281%	342%	66.2%	281%

oscillatory behaviour, not seen in the reference DNS data, at the highest shear rate.

The impact of the dissipation rate on the observed behaviour at high shear rates can be assessed by using pressure–strain rate data from DNS results, which leaves the dissipation rate as the only remaining modelled element in the evolution equations. This is done in Figures 4.7 and 4.8, using data from the Lee et al. (1990) DNS at $S^*_0 = 16.75$. As can be seen in Figure 4.8, the rate of growth of k/k_0 is substantially improved when the correct level of a_{12} is achieved. This indicates that the standard dissipation model does give roughly the correct balance between generation and distruction processes in this case. Further improvement is achieved in Figure 4.9 when a smaller value 1.25 is used for $C_{\varepsilon 1}$ instead of 1.44, which means that the actual rate of production of ε appears to be lower, in this case, than the widely–accepted equilibrium rate implied by $C_{\varepsilon 1} = 1.44$.

4.4.3 Oscillating homogeneous shear

The case of homogeneous turbulence subjected to an oscillating shear is considered next. The DNS and modelled evolution of k/k_0 at different forcing frequencies (up to $\omega/S_{\max} = 1.0$) are shown in Figure 4.10. It can be seen that turbulence energy grows (on average) at the lower frequencies of the applied shear, and decays at high frequencies. Yu and Girimaji identified the frequency at which this change in behaviour occurs to be around $\omega/S_{max} \sim 0.5$. The critical mechanism determining whether k grows or decays is the phase shift between the shear stress $\overline{uv}$ and the applied rate of shear $\frac{\partial U}{\partial y}$. The models correctly reproduce this qualitative change of behaviour between low and high frequencies, due to the intrinsic quality of RST models, where the Reynolds stresses are obtained from individual transport equations, and thus need not be in phase with the mean strain. The

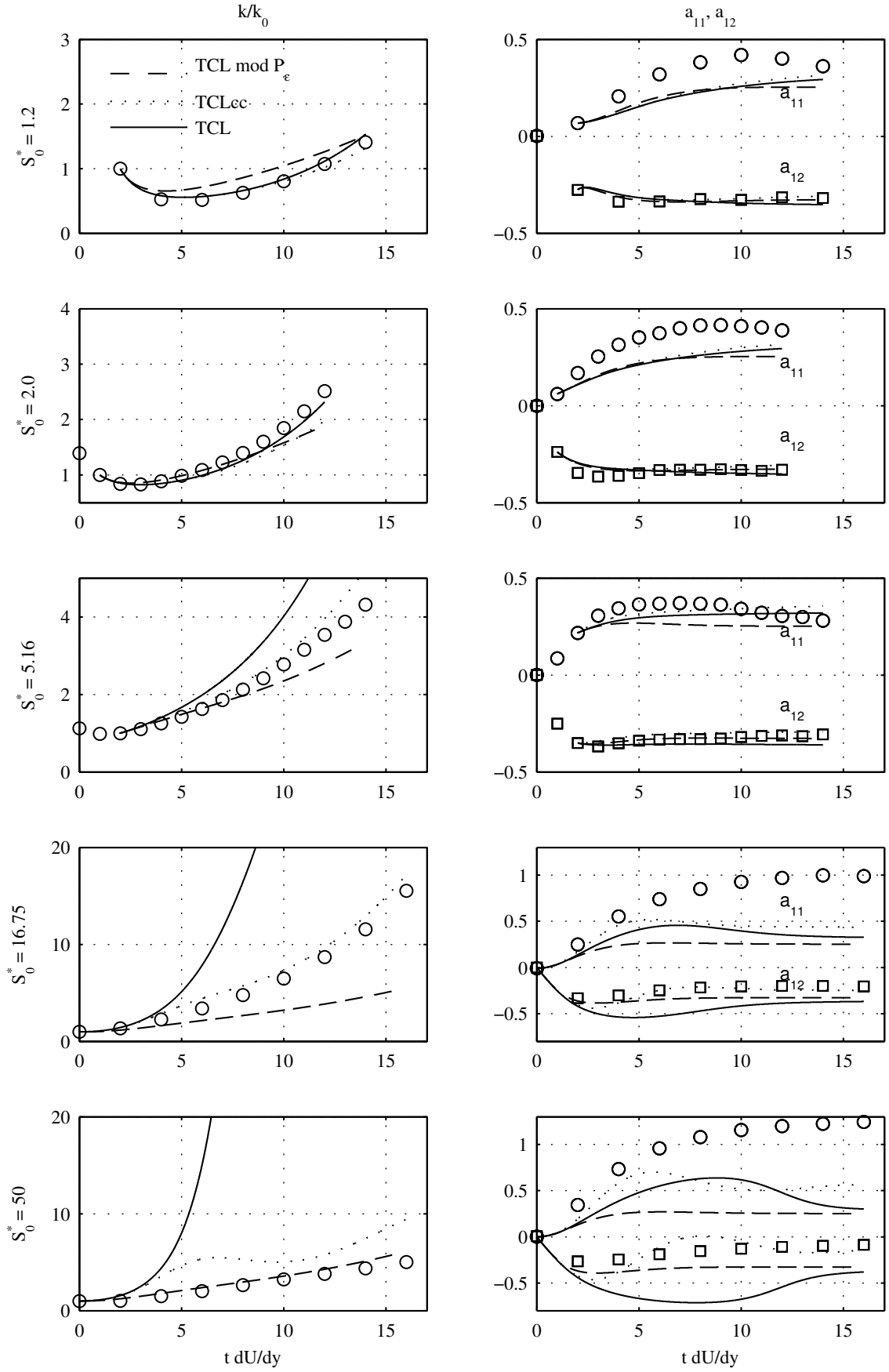

Figure 4.5: Evolution of turbulent kinetic energy (left) and a_{11},a_{12} components of anisotropy (right) in simple homogeneous shear at various shear rates.

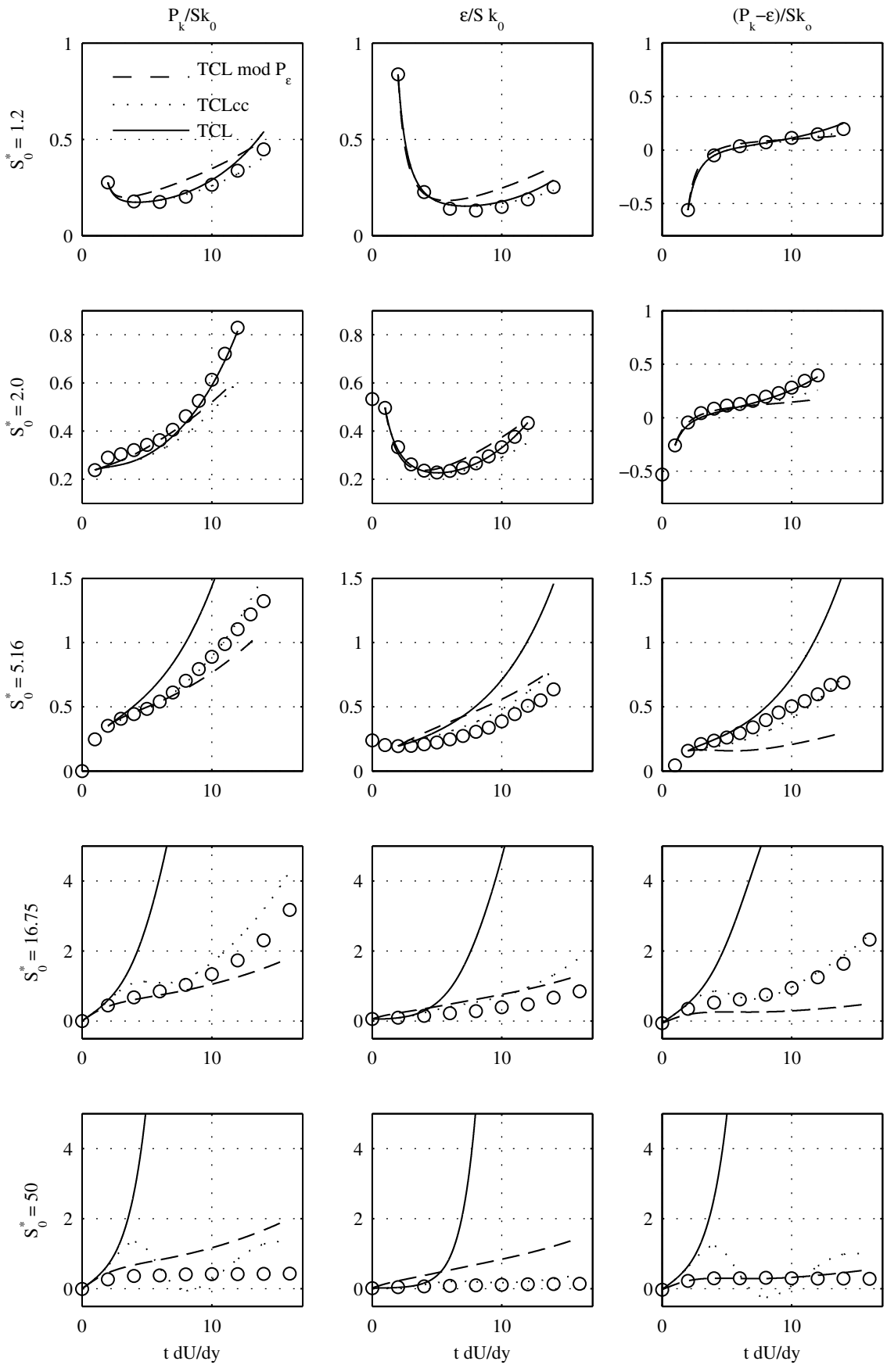

Figure 4.6: Evolution of the quantity $(P_\kappa - \varepsilon)/Sk_0$, representing the right-hand side of k/k_0 evolution equation.

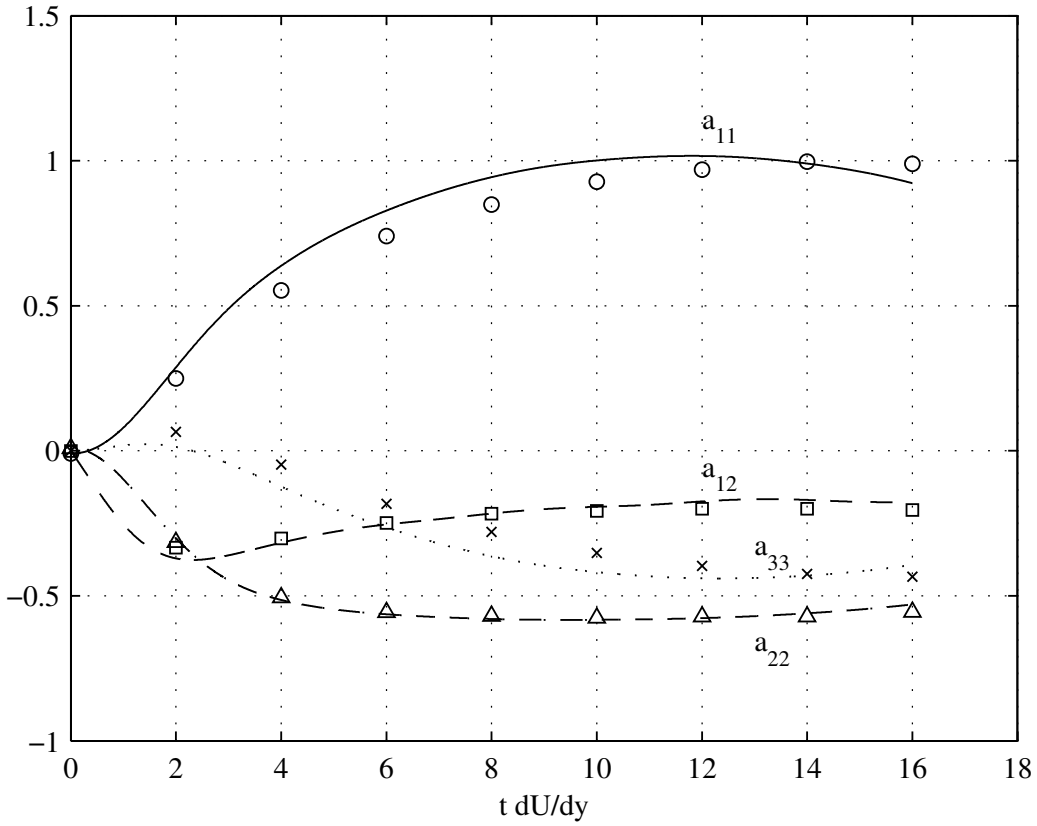

Figure 4.7: Anisotropy evolution using pressure–strain rate data from DNS and the standrad dissipation rate model, for the case $S_0^* = 16.75$.

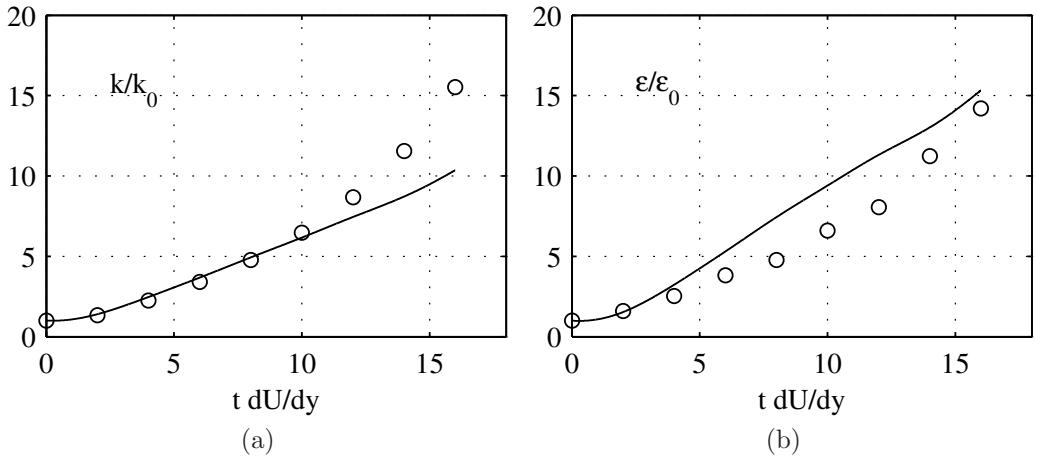

Figure 4.8: Evolution of k/k_0 and $\varepsilon/\varepsilon_0$ using pressure–strain rate data from DNS and the standard dissipation rate model, for the case $S_0^* = 16.75$.

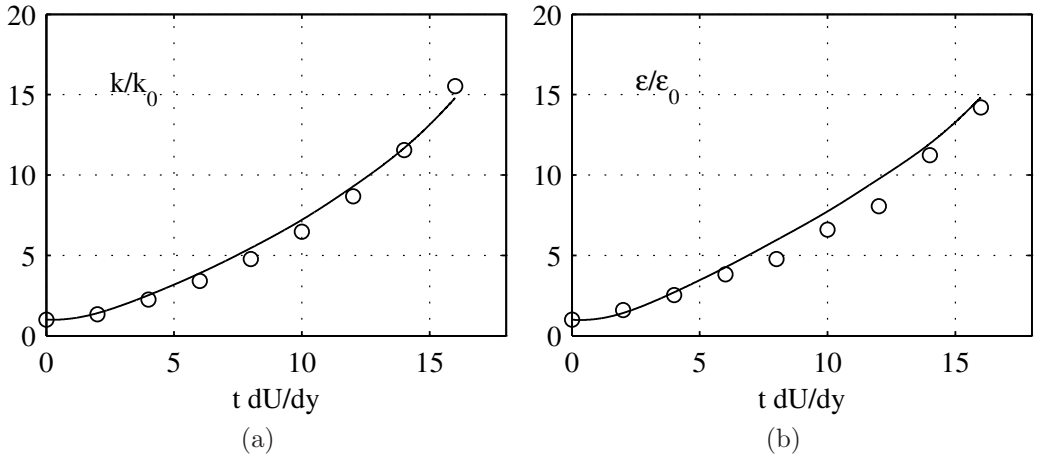

Figure 4.9: Evolution of k/k_0 and $\varepsilon/\varepsilon_0$ using pressure–strain rate data from DNS and the standard dissipation rate model, for the case $S_0^* = 16.75$, showing the effect of using $C_{\varepsilon 1} = 1.25$.

observed critical frequency at which the growth behaviour changes appears to be picked up most closely by both versions of the TCL model. Although they do not capture the entire temporal variation, at $\omega/S_{max} = 0.5$ they both return solutions oscillating with approximately the same amplitude as the DNS data, with a mean that is almost constant. The DNS shows a very slow long-term increase at this frequency, whilst both Basic and SSG models return a mean that is already decreasing at this frequency. When considering the performance over the whole range of frequencies, the TCL model with constant C_2 and C_2' coefficients appears to most closely follow the trend of the DNS data over the considered range, while the version with variable coefficients significantly over-predicts the rate of growth of k at the lower frequencies.

Figure 4.11 shows the Reynolds shear stress anisotropy evolution at $\omega/S_{\max} = 0.5$ for the Basic and TCL models. It is clearly seen in this figure that the Reynolds stress and the applied strain are not in phase. The lag between these two quantities determines the intervals where they have opposite signs, leading to a positive turbulence energy production, and where they have the same sign, leading to negative production. This can be seen in Figure 4.12, which shows the ratio of production to dissipation rates, for the same models and frequency as the previous figure. A difficult feature of this problem is made clear by the last two figures, where it can be seen that, even with reasonably good prediction of a_{12}, and a stress–strain lag that is not much different from the reference data,

over the whole simulation interval, small differences in production (between the models and the data, mostly over-prediction) accumulate in k with integration. This in turn feeds back into $P_\kappa = -a_{12}k\frac{\partial U}{\partial y}$, and, in the low frequency cases where k grows, initially small differences quickly grow. This helps explain the increasing deviation between the models and the reference data as the frequency decreases, as seen in Figure 4.10.

4.4.4 Irrotational strains

The performance of the models in various irrotational strain fields is considered next. Figure 4.13 shows the evolution of turbulent kinetic energy and Reynolds stress anisotropy components, as well as the rate of production of turbulence energy, in plane strain at three dimensionless strain rates. The reference data for these cases are from the DNS results of Lee and Reynolds (1985). In plane strain the production of turbulent kinetic energy is given by $P_\kappa = -S_{11}k(a_{11}-a_{22})$. The dimensionless strain parameter in this case is defined as $S^* = \sqrt{2S_{ij}S_{ji}}\,k/\varepsilon = 2\frac{\mathrm{d}U}{\mathrm{d}x}\,k/\varepsilon$. One immediately notices in Figure 4.13 that, in contrast to the homogeneous shear cases, the evolution of k is quite well predicted over a much larger range of S^* by all the models tested. This is true even though in all the models, with the exception of the Low-Re TCL, the anisotropy evolution tends to deviate from the reference data. Evidently, in the two higher strain rate cases, $S_0^* = 8$ and 154, both a_{11} and a_{22} deviate in the same direction and, since it is the difference $(a_{11} - a_{22})$ that determines P_κ, the errors tend to cancel and the turbulent kinetic energy evolution is well predicted. This is not true at the lowest strain rate, $S_0^* = 1$, where the magnitude of both a_{11} and a_{22} is under-predicted, leading to under-prediction of P_κ and thus also of k. It is also notable that all the models, except for the low-Re TCL, predict the wrong sign for the third normal stress anisotropy component a_{33} (unstrained direction) particularly at the higher strain rates, predicting negative a_{33} where the reference data shows it to be positive. Since $a_{33} = -(a_{11} + a_{22})$, the error cancellation that is favourable for P_κ does not apply for a_{33}. Given that a_{22} is positive and a_{11} is negative, it is seen that

$$a_{33} = -(a_{11} + a_{22}) = -(a_{22} - |a_{11}|)\,.$$

Thus, if $a_{22} > |a_{11}|$, a_{33} will (erroneously) be negative. This is clearly observable in Figure 4.13. The low-Re TCL model (with coefficients C_2 and C_2' dependent on

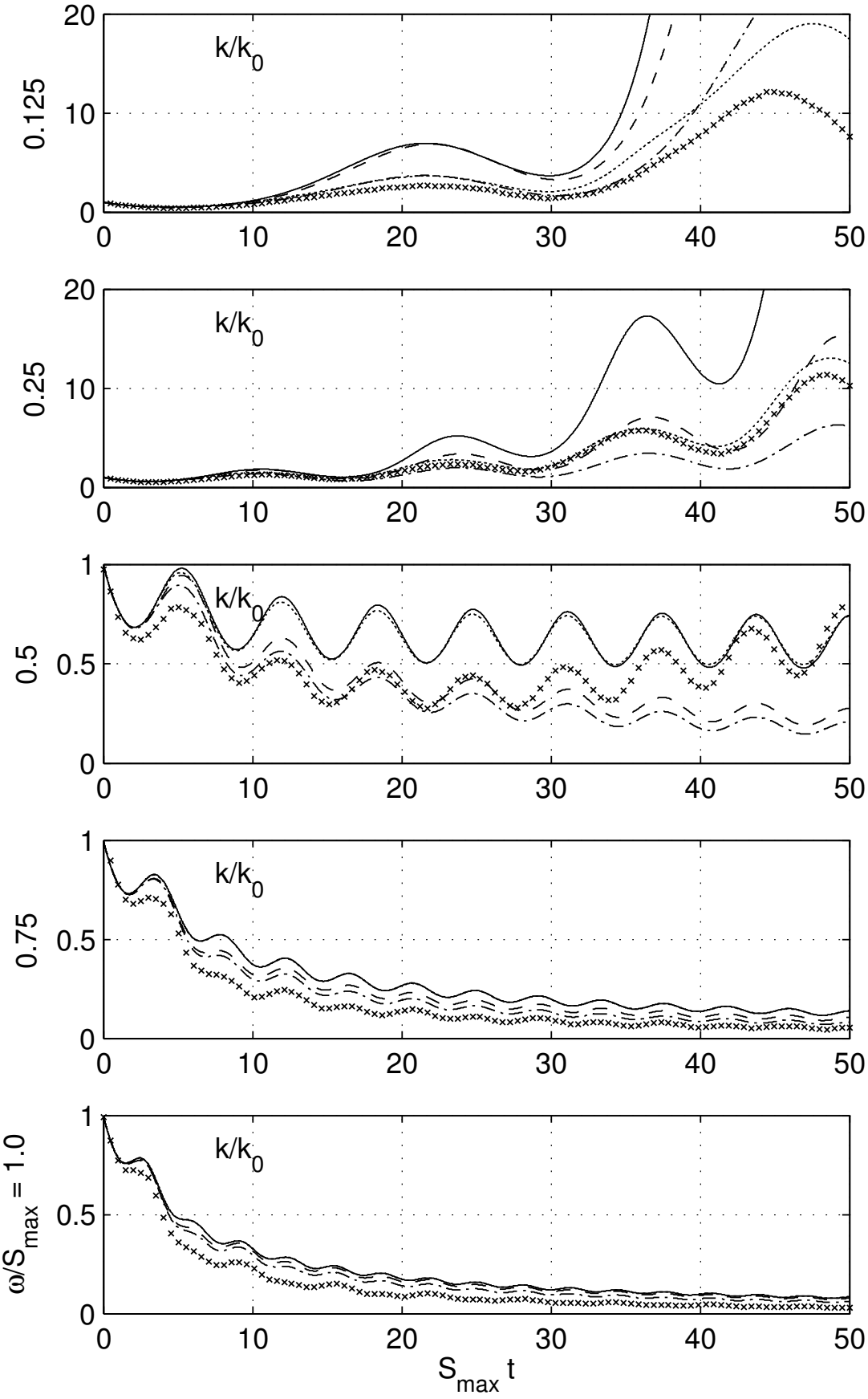

Figure 4.10: Evolution of k/k_0 in oscillating homogeneous shear. Lines: computations; '– –': Basic model; '– - –': SSG; '—': TCL; '· · ·': TCL cc. Symbols: DNS, Yu and Girimaji (2006).

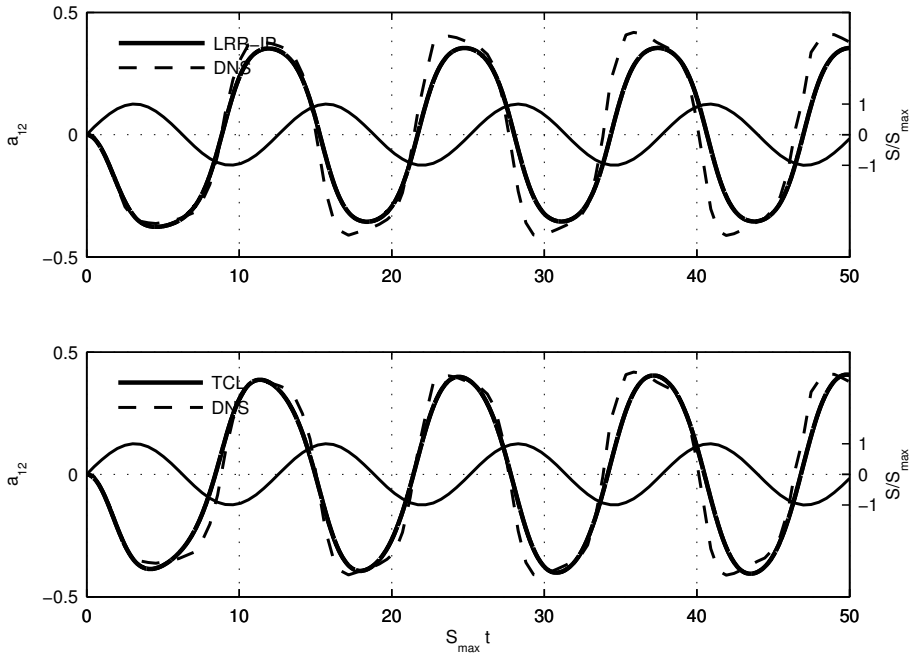

Figure 4.11: Evolution of Reynolds shear stress anisotropy a_{12} (thick lines) in oscillating homogeneous shear at $\omega/S_{\max} = 0.5$, and the applied shear (thin line).

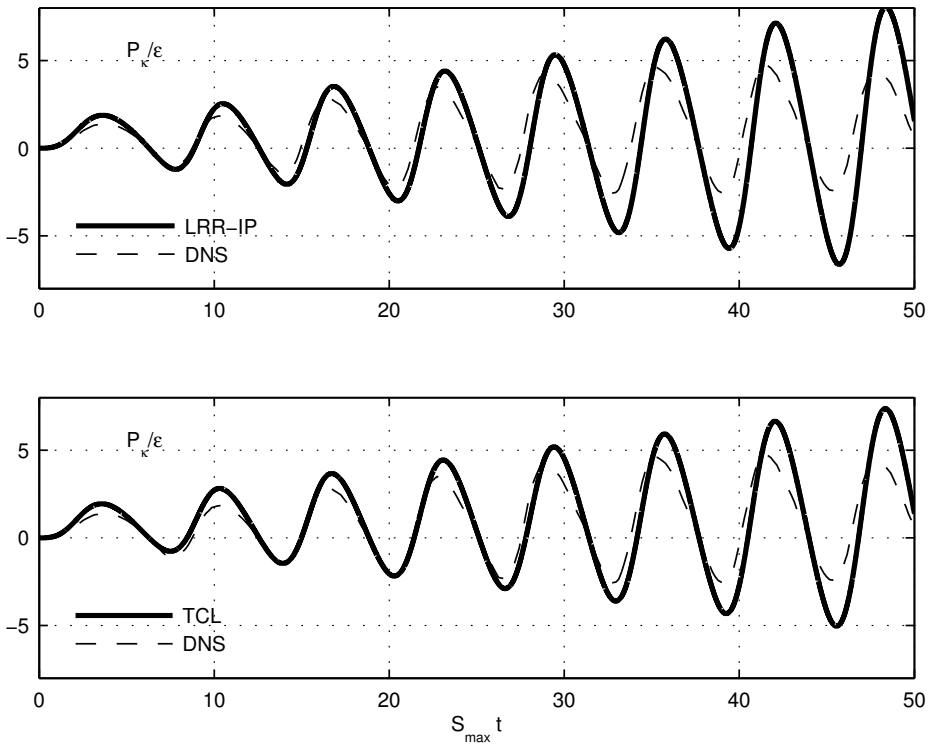

Figure 4.12: Evolution of P_κ/ε in oscillating homogeneous shear at $\omega/S_{\max} = 0.5$.

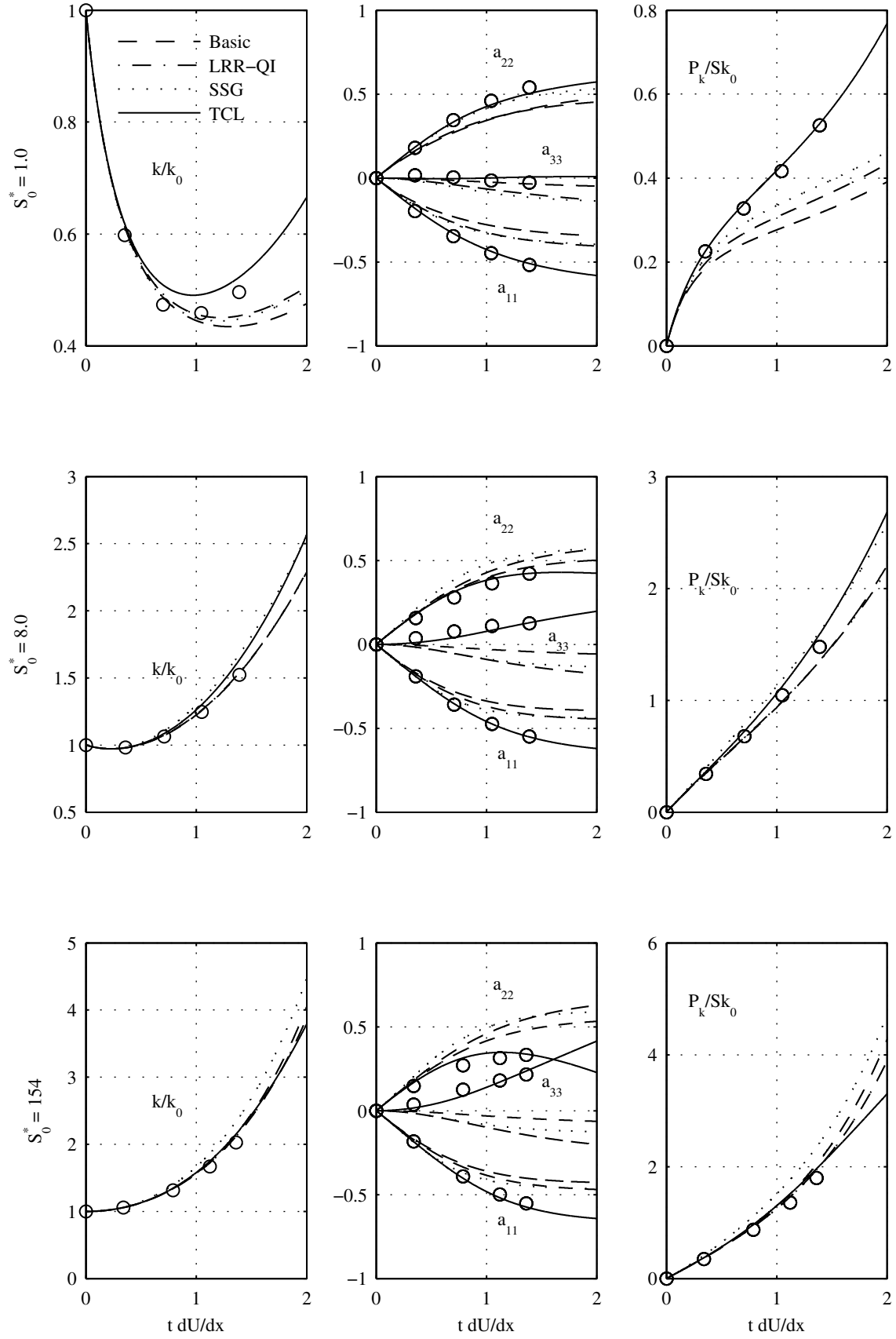

Figure 4.13: Evolution of k/k_0, anisotropy components and turbulence production rate in plane strain at various rates. Symbols: DNS, Lee and Reynolds (1985). Lines: solid: TCL; dashed: Basic model; dash-dot: LRR-QI; dotted: SSG.

strain rates) in these cases predicts the correct production and stress anisotropy levels, as well as turbulence energy evolution, over the range of strain rates considered. Figure 4.14 compares the results obtained using the TCL model with constant coefficients (TCL cc), with those obtained with the Low-Re, variable coefficient version (TCL) for the same plane strain cases as in the previous figure. It can be seen that the constant-coefficient version is significantly worse in predicting anisotropy and P_κ for this set of cases. Similar comments can be made regarding the performance of the constant coefficient version in the remaining irrotational strain cases, and results using this version will therefore not be presented.

Next, attention is turned to the axisymmetric contraction cases from Lee and Reynolds (1985). Similar to the previous figure, Figure 4.15 shows the evolution of turbulence energy, stress anisotropy and the rate of turbulence production at three strain rates. In axisymmetric contraction flow the evolution of stress anisotropy of homogeneous turbulence depends only on the total strain (time), and is independent of the rate of strain (Lee and Reynolds, 1985). This is evident in the DNS data from the second column of plots in Figure 4.15, where it is seen that the anisotropy levels are practically constant over two orders of magnitude of the strain rate. Further, due to symmetry, only one anisotropy component is independent. Written in terms of a_{11}, the production rate of k in this case is $P_\kappa = -\frac{3}{2}S_{11}ka_{11}$. As in the previous set of cases, evolution of turbulence kinetic energy seems to be fairly well predicted over a wide range of strain rates. In these cases however, there is no favourable error cancellation in the production in the Basic and SSG models, since the clearly under-estimated anisotropy levels by these models can be seen to lead to under-estimated P_κ. The fact that these models nevertheless give reasonable predictions of the evolution of k must mean that the dissipation rate (data not available) is also under-estimated, which is understandable because of the link between P_κ and P_ε. The low-Re TCL returns the correct anisotropy levels over the range of strain rates considered. At the lowest stain rate, however, the level of k is slightly over-predicted by this model towards the end of the integration time, and P_κ is slightly over-predicted. Considering that the model gives the correct anisotropy level, the over-estimated P_κ must be a result of the over-estimated k, which, in turn, must be due to an under-estimation of ε.

Figure 4.16 shows the evolution of k, a_{ij} and P_κ in the axisymmetric expansion

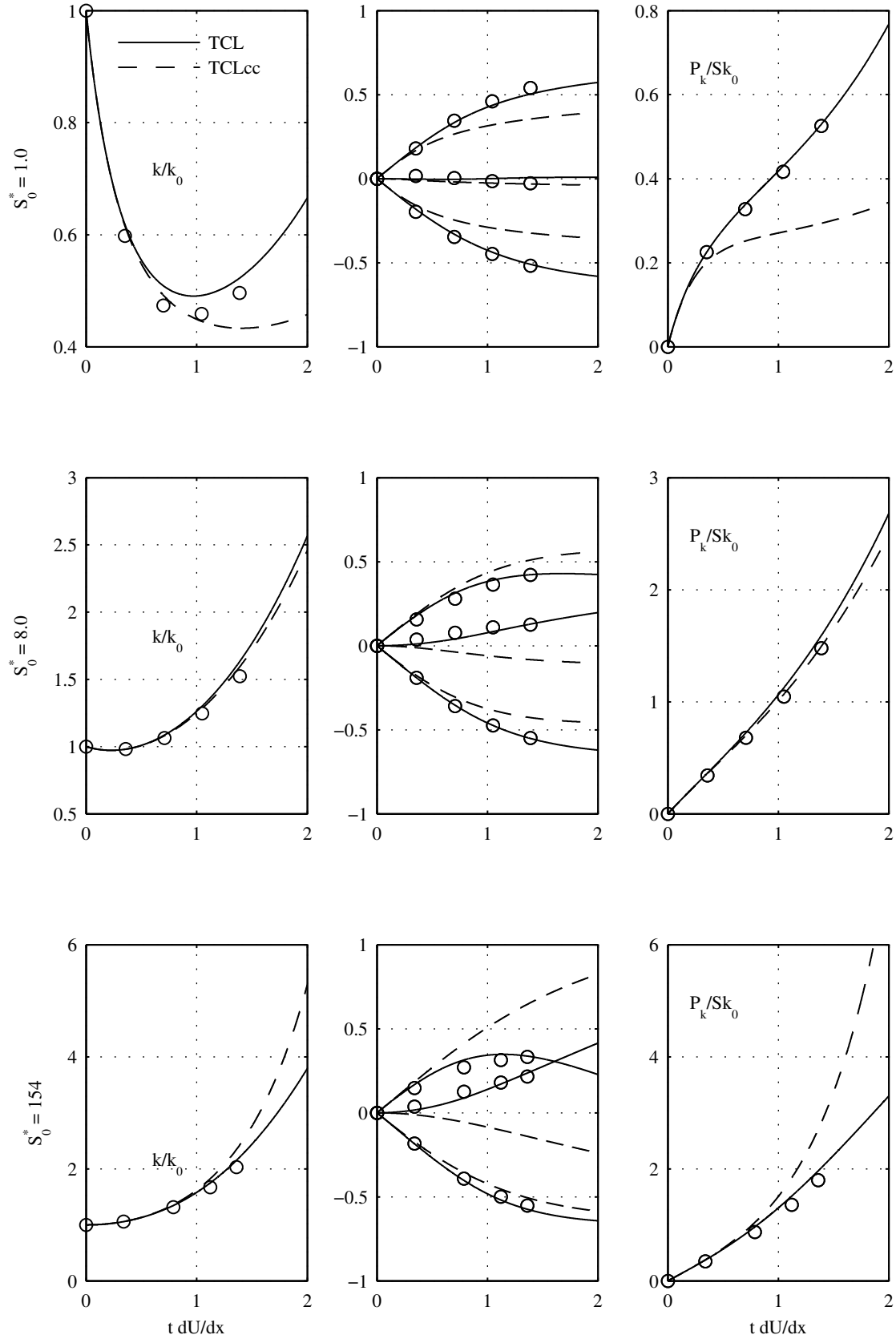

Figure 4.14: Evolution of k/k_0, anisotropy components and turbulence production rate in plane strain at various rates using two versions of the TCL model. Symbols: DNS, Lee and Reynolds (1985). Solid lines: variable-coefficient TCL; dashed lines: constant-coefficient TCL (TCL cc).

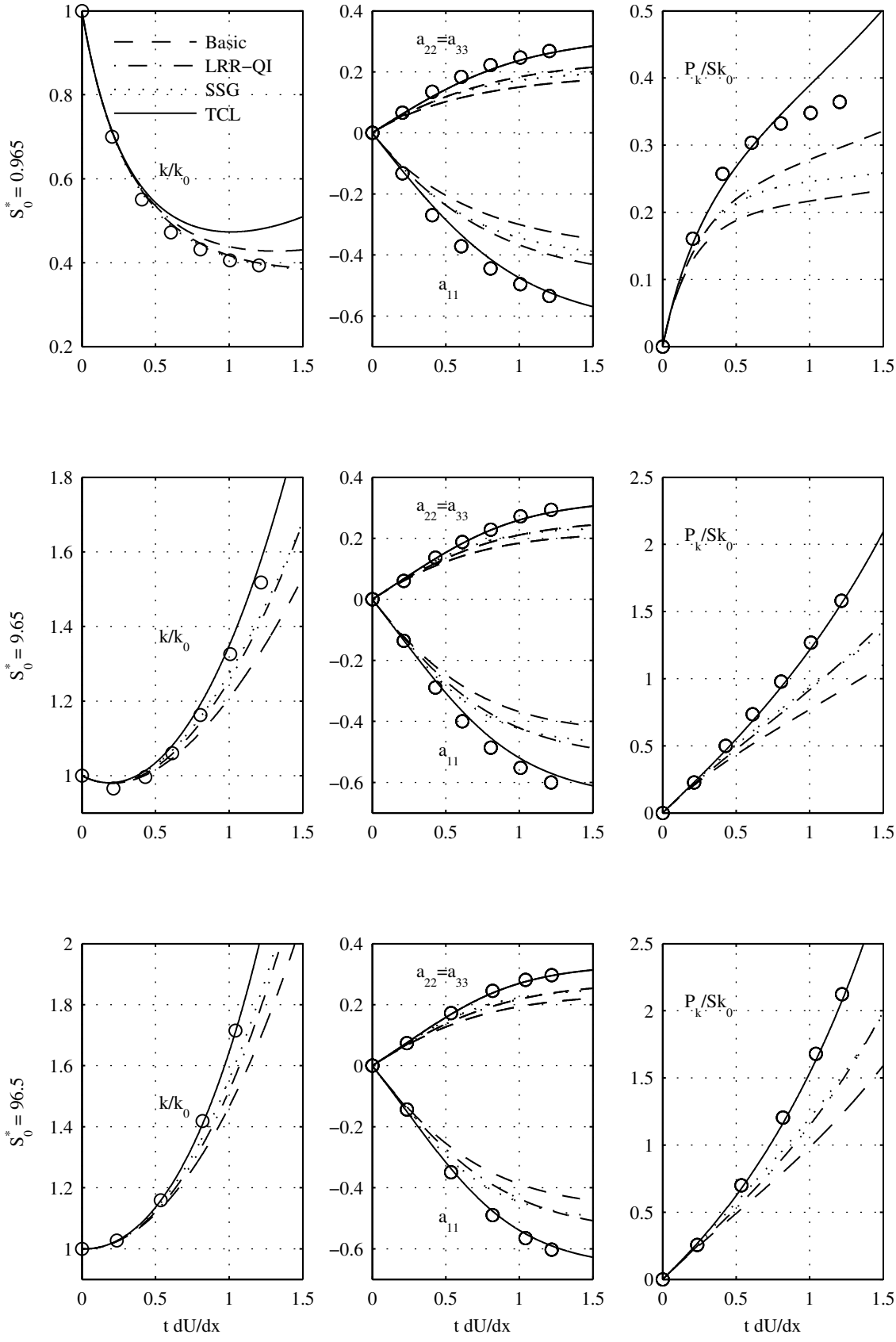

Figure 4.15: Evolution of k/k_0 and anisotropy components in axisymmetric contraction flow at various rates. Symbols: DNS, Lee and Reynolds (1985). Lines: solid: TCL; dashed: Basic model; dash-dot: LRR-QI; dotted: SSG.

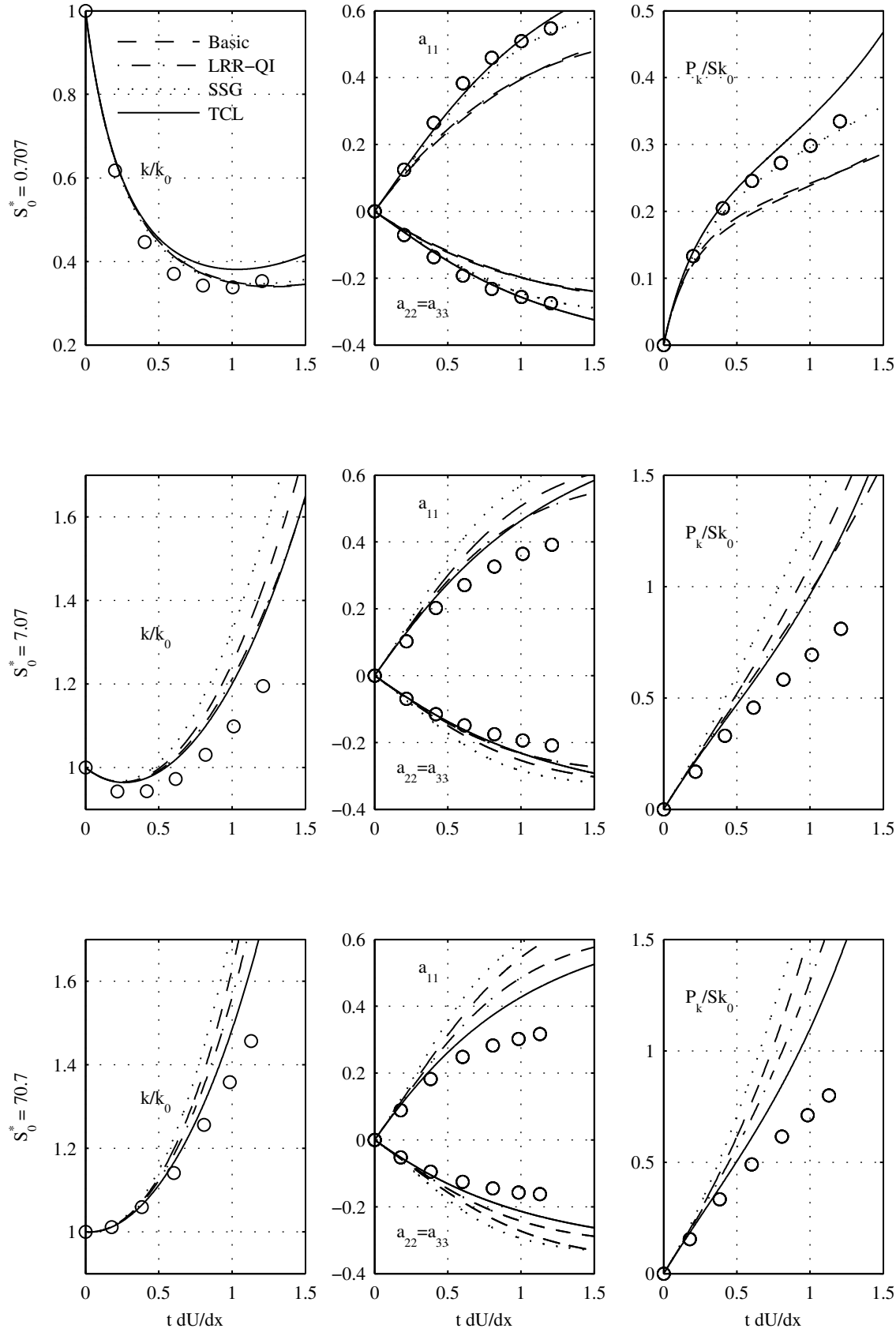

Figure 4.16: Evolution of k/k_0, anisotropy components and turbulence production rate in axisymmetric expansion flow at various rates. Symbols: DNS, Lee and Reynolds (1985). Lines: solid: TCL; dashed: Basic model; dash-dot: LRR-QI; dotted: SSG.

cases of Lee and Reynolds (1985). At the higher strain rates there is a clear over-prediction of all the turbulence statistics. The root cause of this is believed to be the over-prediction of anisotropy magnitudes. It can be seen in Figure 4.16 that the Low-Re TCL gives the least over-predicted anisotropies, and correspondingly the least over-predicted turbulence energy and production rate. To underline that the over-prediction of k is linked to over-predicted anisotropy (rather than an under-prediction of ε), a test was done in which $C_{\varepsilon 1}$ was increased by over 70%, in order to raise the dissipation rate. Despite this substantial increase in the rate of growth of ε, almost no effect was seen on the growth of k at the highest strain rate. At the lowest strain rate the SSG model gives the most accurate results for all three quantities considered.

As a further test in an axisymmetric contraction case, Figure 4.17 summarises data and results pertaining to the axisymmetric contraction experiment of Sjögren and Johansson (1998). The applied mean strain due to the contraction, and the mean velocity along it are shown in the top row. In this case the flow development occurs along the axial distance, x, as opposed to in time, as in the previous cases. The governing equations for the turbulent statistics, which involve convective terms, are thus now solved by an initial value problem marching in space after dividing the right hand side of the equations by the instantaneous mean velocity. Thus, for example, the $\overline{u^2}$ stress component is obtained by solving

$$\frac{\mathrm{d}\overline{u^2}}{\mathrm{d}x} = \frac{1}{U}\left(P_{11} + \phi_{11} - \varepsilon_{11}\right) .$$

The models correctly predict the evolution of turbulent kinetic energy up to the point of maximum strain about half way through the contraction. After that, the models over-predict the level of energy to various degrees, with the Basic model results being the closest to the experimental values, and those of the TCL model being the most over-predicted (by about 33-37%). The SSG and LRR-QI models give k evolutions that are similar to each other. A high degree of stress anisotropy is reached towards the end of the contraction, with a_{11} approaching the value corresponding to the two-component limit $a_{11} = -\frac{2}{3}$. The TCL model gives the best agreement with experimental results in this respect, while the other models under-predict the degree of anisotropy. The turbulence production rate is reasonably well predicted by all the models (within about 15% at the point of maximum straining), except the Basic model, which significantly under-predicts

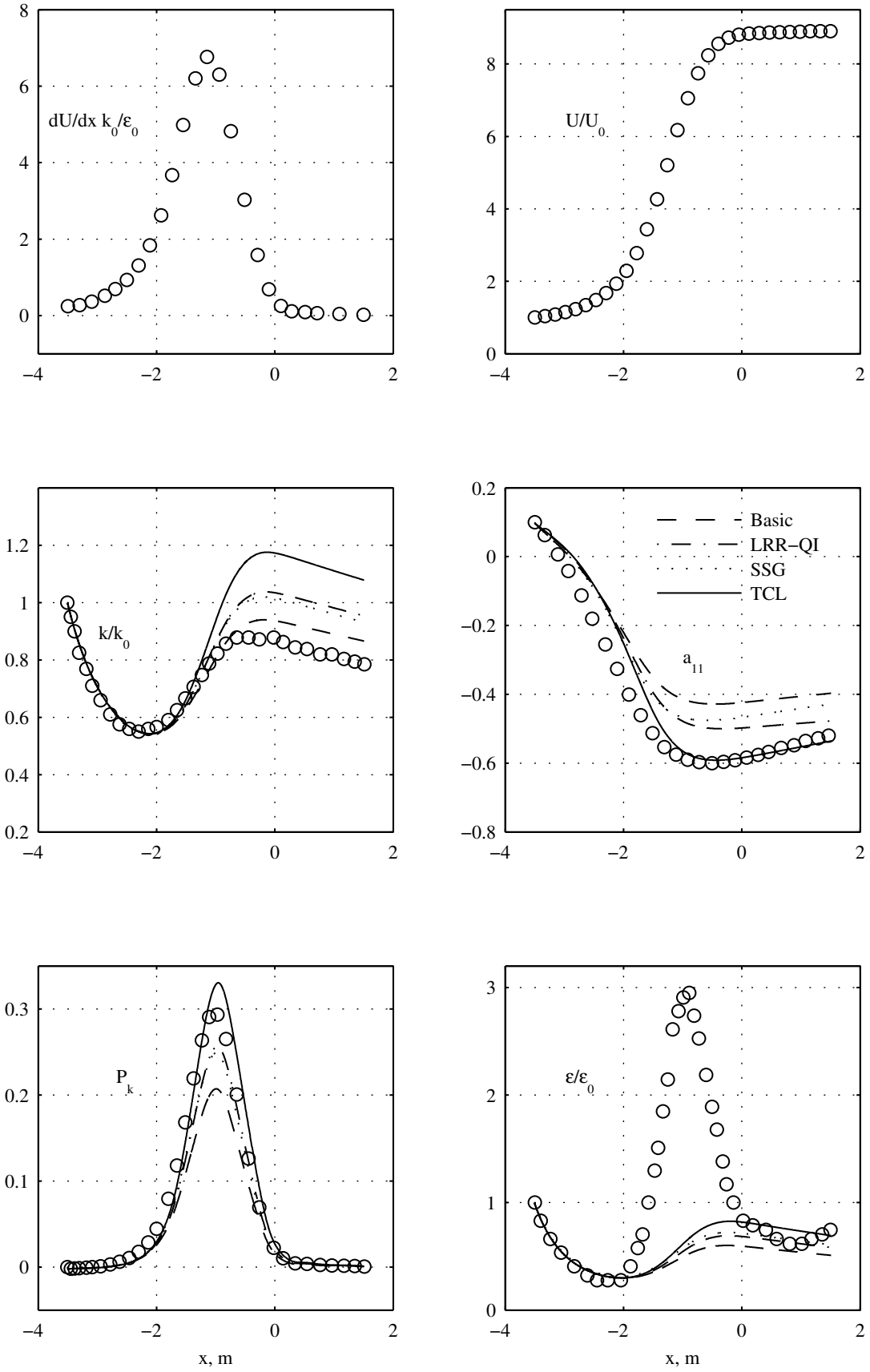

Figure 4.17: Applied mean velocity and strain, and the evolution of various turbulence statistics in the axisymmetric contraction experiment of Sjögren and Johansson (1998).

it, giving a peak that is about 30% lower than the experimental data. The experimental results show the dissipation rate to go through a strong peak which none of the models is able to pick up. During this peak the experimental value of the dissipation rate is more that 4.5 times greater than the largest value of dissipation from the models at the same instant (belonging to the TCL model), and about 3.6 times the peak value given by that model. The small model peaks for ε also slightly lag behind the experimentally observed one. The low values of ε returned by the models explains their tendency to predict k to continue to growing too much after the peak contraction.

The final irrotational strain case is the successive plane strain-relaxation-destraining experiment of Chen et al. (2006). The form of the mean velocity gradient is the same as in the Lee and Reynolds (1985) set of plane strain cases, but the strain rate, $S_{11} = \frac{\mathrm{d}U}{\mathrm{d}x}$, now varies in time. This time-varying applied strain rate is shown in the top plot of Figure 4.18, and the Reynolds stress components $\overline{u^2}, \overline{v^2}$ (labelled as R_{11} and R_{22}) are shown in the bottom plot normalised by their initial values. All the models return the correct $\overline{v^2}$ evolution up to the point at which $S_{11}(t)$ peaks, after which they all over-predict this stress component, with the TCL giving the least over-prediction. The magnitude of $\overline{u^2}$ is under-predicted throughout the cycle, but to a lesser extent. Unfortunately, since the third stress component was not measured in the experiment, it is not possible to tell to what extent these discrepancies are the result of an over-predicted level of turbulence energy, or degree of anisotropy. If one assumes that the redistribution is adequately accounted for, at least by the TCL as in the previous plane strain cases, the rapid decay of $\overline{v^2}$ after the peak of straining suggests an accelerated turbulence dissipation rate.

In the previous two cases it appears that there is scope for improved performance if the dissipation rate is increased. To explore this possibility, the previously introduced modified P_ε was tested in these two cases, in addition to a simple test of adjusting of the coefficient $C_{\varepsilon 1}$ to a higher value, $C_{\varepsilon 1} = 2.8$. The effect of these two modifications on the last two cases is shown in Figures 4.19 and 4.20 (the latter modification is denoted TCL mod $C_{\varepsilon 1}$). Also shown in the figures is the standard TCL as used in previous figures, for reference. It can be seen in Figure 4.19 that both modifications improve the modelled evolution of k/k_0 by increasing the dissipation rate level. In Figure 4.20, both modifications can also be seen to bring the $\overline{v^2}$ stress component closer to the experimentally

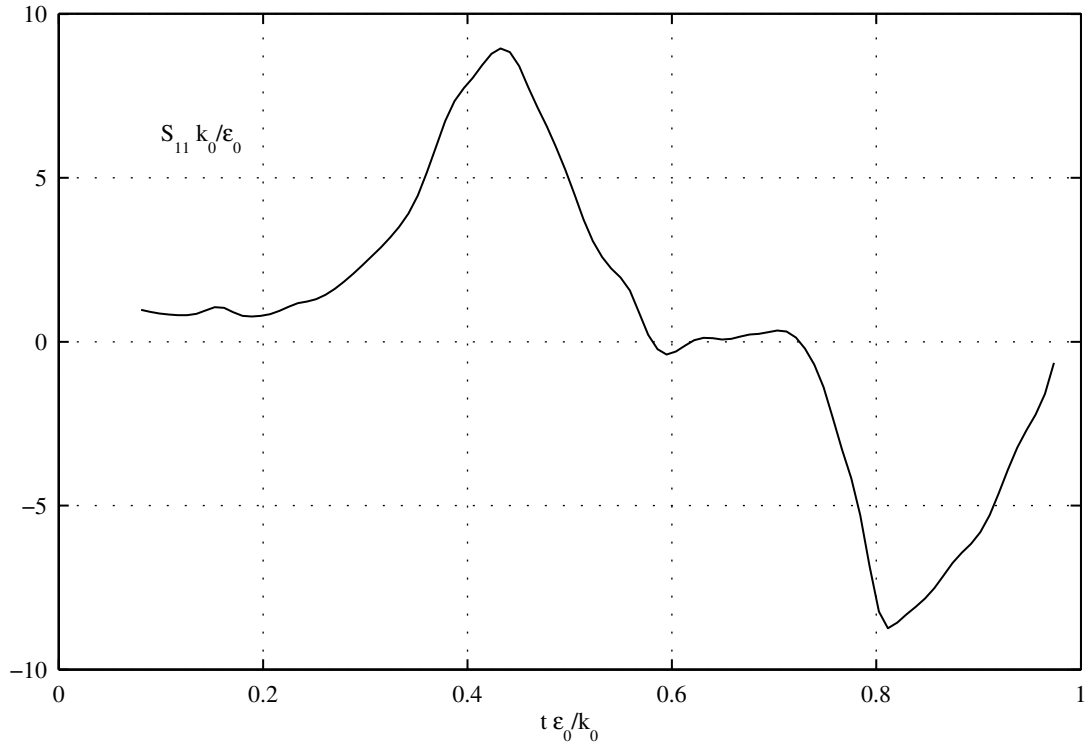

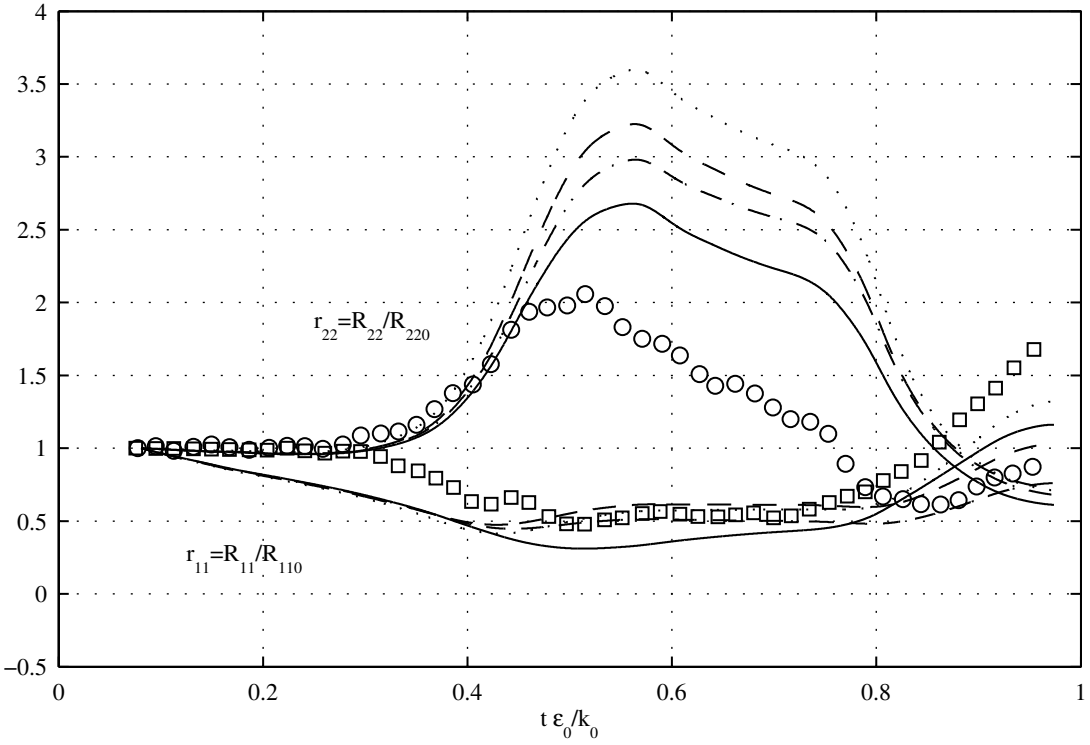

Figure 4.18: Applied strain history (top), and evolution of $\overline{u^2}$ and $\overline{v^2}$ normal stress components (bottom) in the plane strain experiment of Chen et al. (2006). The normal stresses are normalised by their initial values. Symbols in bottom figure: experimental data; solid lines: TCL; dashed: Basic model; dash-dot: LRR-QI; dotted: SSG.

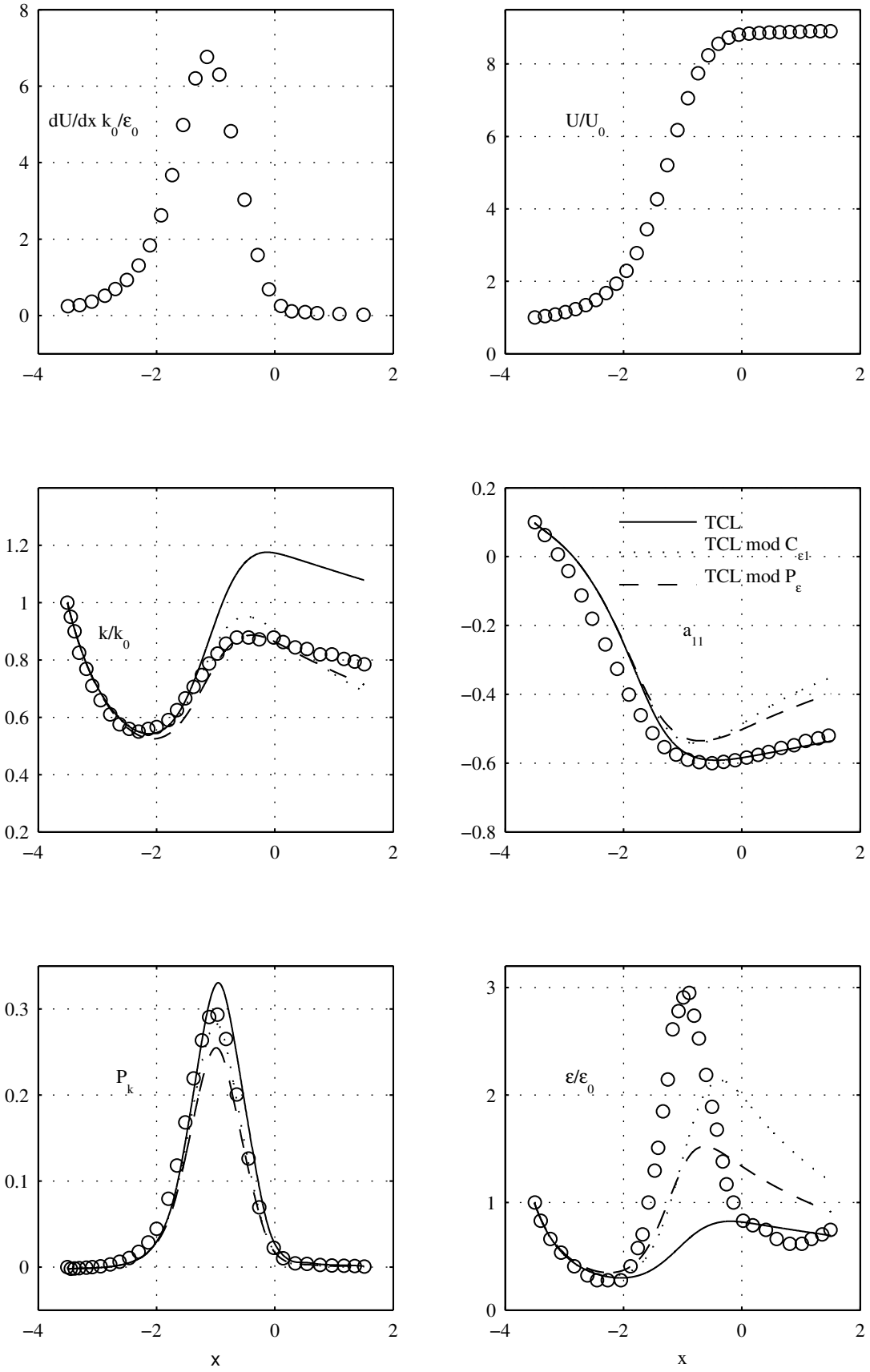

Figure 4.19: Applied mean velocity and strain, and the evolution of various turbulence statistics in the axisymmetric contraction experiment of Sjögren and Johansson (1998) using modified P_ε terms.

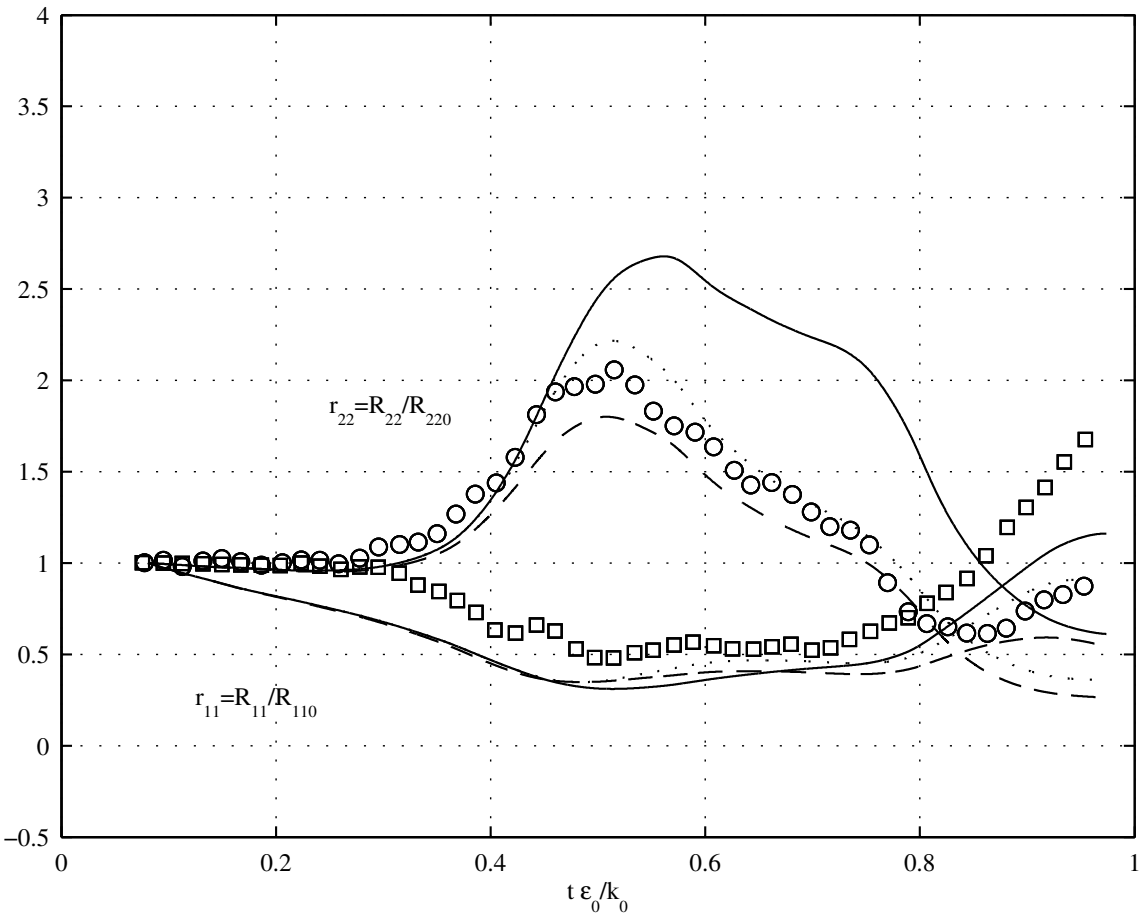

Figure 4.20: Evolution of $\overline{u^2}$ and $\overline{v^2}$ normal stress components in the plane strain experiment of Chen et al. (2006) using modified P_ε terms. The normal stresses are normalised by their initial values. Symbols: experimental data; solid lines: TCL; dashed: TCL mod P_ε; dotted: TCL mod $C_{\varepsilon 1}$.

measured levels.

4.5 Concluding remarks

This chapter has examined a number of homogeneous turbulence problems covering various modes of mean strain and a wide range of strain rates. The evolution of various turbulence statistics using several RST models was presented and discussed.

In simple shear it was generally found that models predict the correct evolution of turbulent kinetic energy k and dissipation rate ε at lower dimensionless shear rates $Sk/\varepsilon < 4$. Despite some variation among the models in the quality of the anisotropy prediction, the more important components a_{12}, a_{11} are reasonably well predicted by most models. A gradually decreasing trend was observed in the reference data for the long-time a_{12}, as the shear rate is increased. This trend is reflected in an increasingly over-predicted rate of production of turbulence energy by most models, which begins to be visible from the intermediate level of shear rate $Sk/\varepsilon \approx 4-5$, onwards. The variation in the 'equilibrium' (or long-time) level of anisotropy with the mean strain rate is something that the Basic and LRR-QI models, using constant coefficients, are unable to replicate, which is an argument *for* the use of variable coefficients, if one wishes to retain a linear tensorial expansion for ϕ^r_{ij}.

At the higher shear rates tested, $Sk/\varepsilon > 16$, existing models grossly over-predict the evolution of k and ε. This is attributed mainly to the inability of the models to replicate the decay of a_{12} at high shear rates as predicted by Rapid Distortion Theory (RDT), and observed in DNS results. In addition, the normal stress anisotropies are also under-predicted by the models. It is observed that with some modifications to the coefficients of the pressure-strain rate correlation, it is possible to correct or improve the a_{12} level at least, thus correcting the rate of evolution of k and ε. Specifically, the TCL model using constant C_2, C_2' coefficients was the only one found to have the desirable feature of a decreasing trend of long–time a_{12} with increasing shear rate. This feature perhaps needs to be restored in the Low-Re, variable coefficient, formulation of the model by re-associating the C_2 reduction, found by Craft (1998) to be desirable in some near-wall shear flows, with correction terms that only come into effect in regions of strong inhomogeneity.

It is worth noting that the RDT solution is an idealised limiting behaviour, and the reference data, as indicated above, suggest a *gradual* transition from the low–shear behaviour towards this high–shear RDT limit, the effect of which begins to be felt even at shear rates that are not typically considered 'high'. This gradual change in the long-time anisotropy behaviour is something that should be taken into account when re-tuning model coefficients, whether it be variable coefficients for the linear models, or the TCL model.

Some limited improvement in homogeneous shear flows was obtained with the alternative P_ε formulation, but the DNS data indicated that correction of a_{12} is a more critical factor in these cases.

In the case of homogeneous turbulence subjected to oscillating shear it was found that the models, owing to the intrinsic lag between stress and strain associated with solving an individual transport equation for each stress component, were able to return the correct qualitative trend of turbulence energy growth at low frequencies and decay at high frequencies. The critical frequency at which this change in behaviour occurs depends on the modulation of the shear stress and the applied shear, and is picked up most closely by the TCL model, although not all of the temporal variations shown by the DNS were reproduced.

Model performance was found to be consistent over a much wider range of strain rates in the homogeneous irrotational strain cases, where the Low-Re TCL model was found to return the best results. In the experimental irrotational strain cases examined (plane strain and axisymmetric contraction flows) there was evidence of an accelerated dissipation rate generation. Significant improvement was achieved through the use of the alternative P_ε mentioned earlier, and through a simple (though large) increase of the coefficient $C_{\varepsilon 1}$ in the conventional P_ε term. It would be interesting and worthwhile to further explore this trend of accelerated dissipation rate production through additional detailed experimentation or high quality simulations. If this trend is found to be generally applicable in irrotational strains, the modifications mentioned above, or others, might be selectively applied in irrotational strains and switched off in shear dominated flows. The additional data could contribute to the optimisation of the coefficient terms over a wider range of cases.

Chapter 5

Pulsatile Internal Flows

5.1 Introduction and literature review

This chapter considers the problem of fully-developed channel flow subjected to imposed pressure pulsations. The general problem of pulsatile shear flows is of relevance to many practical engineering problems such as pipe flows driven by reciprocating pumps, sediment transport in coastal and river flows, and physiological flows, to name some examples. The addition of imposed pulsation significantly complicates the physics of the problem relative to the corresponding steady flow situation. The flow pulsation, in conjunction with the no-slip condition at the wall, creates a periodic shearing action that starts at the wall and propagates into the flow. This introduces an additional time-scale and amplitude to the problem, and the flow characteristics have been observed to vary significantly in previous work according to the ranges of these parameters. The flow exhibits two limiting behaviours corresponding to the extremes of the imposed frequency. At the limit of very low frequencies, when the rate of variation of mean flow quantities is very slow, the turbulence has ample time to adjust to the changing flow conditions. The flow in this limit behaves as if progressing through a series of equilibrium states at different conditions, hence it is called the 'quasi-steady' limit. At the other extreme, when the frequency is sufficiently high, the inertia of the bulk flow confines fluctuations of flow quantities to a small region near the wall, and the turbulence is 'frozen' in the outer region. At the point when fluctuations are confined to the viscosity affected region, the mean flow modulation mimics the laminar Stokes solution of this problem, and this is hence called the 'quasi-laminar' limit.

There have been various suggestions in the literature regarding the scaling parameters appropriate for this class of flows (Tardu et al., 1994). For example, in their study of pulsatile turbulent pipe flow, Ramaprian and Tu (1983) recommended the parameter $\frac{\omega D}{\overline{u_\tau}}$, where ω is the angular frequency of the pulsations, D is the pipe diameter, and $\overline{u_\tau}$ is the mean friction velocity; other scalings based on outer variables have also been suggested. Ronneberger and Ahrens (1977) introduced the parameter l_s^+, which is the laminar Stokes layer thickness, $l_s = \sqrt{\frac{2\nu}{\omega}}$, normalised by the viscous length scale, $\delta_v = \frac{\nu}{u_\tau}$. The Stokes thickness is a measure of the penetration depth of oscillatory motion in the laminar problem, and the parameter is thus a ratio of the laminar penetration depth to the characteristic viscous scale. This scaling is especially useful in explaining the viscous behaviour observed in the high frequency regime. As the frequency is increased, the Stokes layer becomes progressively thinner until it is confined to the viscosity affected region near the wall, at which point the flow modulation is governed by viscous effects. The angular frequency normalised by wall variables, $\omega^+ = \omega\nu/u_\tau^2$, is related to l_s^+ by $\omega^+ = 2/l_s^{+2}$.

5.1.1 Experimental studies

There are numerous experimental studies of pulsatile turbulent pipe and channel flow reported in the literature. Among the earlier studies are those of Mizushina et al. (1973) and Mizushina et al. (1975), who studied pulsatile pipe flow at a mean Reynolds number of 10,000, subject to a range of frequencies. The quantities measured were the pressure gradient, velocity, and streamwise velocity fluctuations. The Reynolds stresses were deduced from the momentum equation. The authors observed different flow regimes over the range of frequencies studied, identifying a critical frequency, which they suggested is related to the so-called turbulence 'bursting' frequency.

A range of experiments was also carried out by Tu and Ramaprian (1983) who examined fully-developed turbulent pipe flow subjected to controlled sinusoidal oscillations of the bulk velocity. The authors used single channel Laser-Doppler anemometry to measure the instantaneous streamwise velocity, as well as flush-mounted heat transfer probes to measure the wall shear stress. The mean Reynolds number of the bulk flow was approximately 50,000. Detailed measurements were made at two conditions of frequency and amplitude of bulk velocity, 0.5 Hz at 65% amplitude, and 3.6 Hz at 15% amplitude, respectively. The aim of

the study was to investigate the effects of flow pulsations on the time-mean, phase-averaged and fluctuating flow properties. The time-mean bulk velocity was found to differ slightly from that of a steady flow at the mean Reynolds number. Profiles of phase-averaged velocity, longitudinal turbulence intensity, and Reynolds shear stress (obtained from the integrated momentum equation) were all found to exhibit marked departures from corresponding quasi-steady profiles. It should be noted that later studies (Burnel et al., 1990) at similar conditions have disagreed with important aspects of the high frequency data of Tu and Ramaprian (1983). Specifically, the data of Tu and Ramaprian show the phase-averaged streamwise velocity fluctuation intensity to be 'frozen', while the profiles of phase-averaged Reynolds shear stress continue to exhibit large amplitudes across the flow at high frequency, an unexpected result that is probably due to the indirect determination of the Reynolds shear stress. In addition, Mao and Hanratty (1986) criticised the wall shear stress data of Tu and Ramaprian (1983) for not accounting for the frequency response of the probes.

The problem was also studied by Mao and Hanratty (1986) and Finnicum and Hanratty (1988), who investigated fully-developed turbulent pipe flow subject to controlled oscillations of the pressure gradient. The frequencies varied over the range $0.00012 < \omega^+ < 0.0912$ in the earlier study and over the range $0.0075 < \omega^+ < 0.21$ in the later study. The amplitude of the phase-averaged centreline velocity was fixed at 10% of the mean velocity at that location, and the mean Reynolds number was varied between 15,000-70,000, and 8,650-44,900, in the first and second studies, respectively. The researchers used electrochemical techniques to measure the instantaneous velocity gradient at the wall. The instantaneous velocity across the pipe was not measured, and their study was focused on the characteristics of the modulation of wall shear stress (or velocity gradient at the wall) at different frequencies.

A series of studies of pulsating channel flow was carried out by Binder and co-workers for a wide range of amplitudes and frequencies (Binder and Kueny, 1981; Binder et al., 1985; Tardu et al., 1994). In the later study, Tardu et al. (1994) used LDA and hot film techniques to measure instantaneous velocity and wall shear stress in turbulent channel flow subjected to controlled pulsations of the flow rate. The pulsation frequencies varied in the range $0.0005 < \omega^+ < 0.03$ and the amplitudes varied in the range of 10 to 70% of the centreline velocity. Measurements of phase-averaged streamwise velocity and turbulence intensity

across the flow cross section, as well as phase-averaged wall shear stress and wall shear stress fluctuations are reported.

5.1.2 Computational studies

A number of early computational studies of pulsatile turbulent flows used Prandtl's mixing length hypothesis (MLH) to provide the necessary closure of the phase-averaged momentum equation. These include Ronneberger and Ahrens (1977), who studied turbulent boundary layer flow subjected to small amplitude periodic perturbations, and Mao and Hanratty (1986) whose previously mentioned experimental study of pulsatile pipe flows also included calculations based on the MLH. It was found that, without modification, the MLH is unable to reproduce the experimentally observed modulation of the wall shear stress. Some improvement was achieved by Mao and Hanratty by modifying the basic MLH to account for 'lag' effects in response to the varying pressure gradient.

Several computational studies targeted the experimental results of Tu and Ramaprian (1983), employing a number of different turbulence models to simulate the flows. Blondeux and Colombini (1985) and Cotton and Ismael (1991) used two-equation eddy-viscosity models (EVM), of the k–ω and k–ε type, respectively, while Kebede et al. (1985) compared the results of an EVM with those of an RSTM. Generally, these computational studies obtained reasonable qualitative and quantitative agreement with the low frequency data, but differed qualitatively with the high frequency data. As previously mentioned, there is reason to question the accuracy of this subset of the data.

Ismael and Cotton (1996) used the Launder and Sharma (1974) k–ε model to carry out a detailed study of the characteristics of wall shear stress modulation in pulsating pipe flow over a wide range of frequencies, making comparisons with the Finnicum and Hanratty (1988) data.

Cotton et al. (1997) and Cotton et al. (2001) carried out studies using the Launder and Sharma (1974) k–ε as well as the Shima (1989) RSTM, examining these models against the data of Finnicum and Hanratty (1988) and Tu and Ramaprian (1983). The RSTM was found to yield better accuracy in the near wall region up to one quarter of the diameter, while both models performed relatively poorly in the core region.

Scotti and Piomelli (2001) carried out a DNS and LES study of pulsatile turbulent channel flow at various frequencies. The flow was subjected to a specified

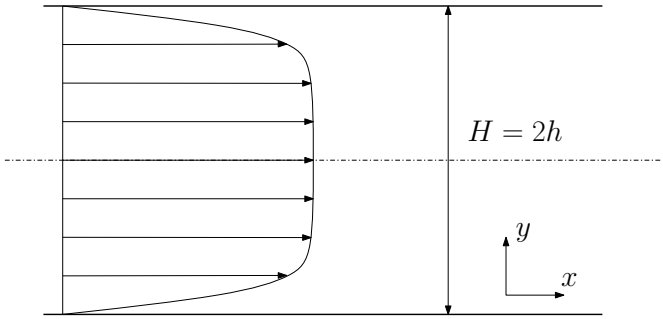

Figure 5.1: Channel geometry.

Table 5.1: Parameters of applied pressure gradient tests

	Low	Intermediate	High
ω (rad/s)	0.0056	0.035	0.14
ω^+	0.0016	0.01	0.04
γ_p	8	50	200

pressure gradient oscillating sinusoidally about a fixed mean value. Since the mean pressure gradient is fixed in all cases, the mean wall shear stress, $\overline{\tau_w}$, when a periodic state is reached, is also fixed. The friction Reynolds number based on the channel half-height, h, and the mean friction velocity, $\mathrm{Re}_\tau = \frac{\overline{u_\tau} h}{\nu}$, is thus constant at 350. This set of cases forms the basis for comparison in the present study. A schematic of the flow configuration is presented in Figure 5.1.

Scotti and Piomelli used a pseudo-spectral code with Fourier expansions in the homogeneous directions and Chebyshev collocation across the channel height. A number of different grids were used, but only results using a mesh of $32 \times 32 \times 49$ nodes, for the three frequencies listed in Table 5.1, were made available. A dynamic eddy-viscosity model was used for the sub-grid scale stresses. The LES results were validated against a DNS study the researchers carried out for the high frequency case. It was found that LES results obtained using the aforementioned grid ('LES1' in the paper of Scotti and Piomelli (2001)) were in good agreement with both the time-mean velocity, and the amplitude of the fundamental mode of velocity oscillation in the corresponding DNS results. Similarly, the amplitudes of the fundamental modes of the Reynolds stress components were also in good agreement with the DNS. However, the time-mean profile of $\overline{v^2}$, which is the component most affected by the small scales, was significantly under-predicted, while that of $\overline{u^2}$ was somewhat over-predicted in comparison with the DNS.

5.2 Governing equations

The flow is subjected to a specified applied pressure gradient given by

$$\frac{\partial P}{\partial x} = \overline{\frac{\partial P}{\partial x}}\left[1 + \gamma_P \cos\left(\omega t + \tfrac{\pi}{2}\right)\right] \tag{5.1}$$

where, following Scotti and Piomelli (2002), the mean pressure gradient $\overline{\frac{\partial P}{\partial x}}$ is held fixed at -10^{-4} in all the calculations. The amplitude factor γ_p, and the angular frequency are varied as in Table 5.1. The $\frac{\pi}{2}$ phase shift is added purely for numerical convenience, since it was found in some cases that starting with the deceleration part of the cycle aided convergence to a turbulent periodic solution.

The flow is governed by the x-momentum equation for fully-developed flow

$$\frac{\partial U}{\partial t} = -\frac{1}{\rho}\frac{\partial P}{\partial x} + \frac{\partial}{\partial y}\left(\nu\frac{\partial U}{\partial y} - \overline{uv}\right) \tag{5.2}$$

To provide the necessary closure of Equation (5.2), four turbulence models have been used in this chapter: the Launder and Sharma (1974) k–ε model ('LS'), the Shima (1998) model, the Jakirlić and Hanjalić (1995) model ('HJ'), and the Craft (1998) model ('TCL').

5.3 Numerical implementation

The problem was computed using the STREAM code, in which a single column of finite volume cells discretised the bottom half of the channel. Therefore a wall boundary condition was specified at the lower edge of the domain, and a symmetry (zero-gradient) condition at the top edge corresponding to the channel axis. The domain was discretised using 101 nodes, with 51 nodes in the region from the wall up to $y^+ = 60$, and 50 nodes for the remainder of the channel half-height (up to $y^+ = 350$). Since the flow is fully-developed in the axial direction, zero-gradient boundary conditions are applied to the east and west walls of all cells for all transport equations, so that for all variables other than the pressure, only variation in the vertical, y-direction, is allowed. The pressure is set at each node at each time-step according to (5.1) and

$$P_n(t) = \frac{\partial P}{\partial x}\, x_n\,, \tag{5.3}$$

where n is the index of the node in question. Since a single column of cells was used, the east and west faces of the cells correspond to boundary nodes, and setting the pressure according to (5.3) insures that the instantaneous pressure gradient is given by (5.1), as required. The pressure-correction equation is prevented from changing the specified pressure by setting its source term coefficients to $S_u = 0.0$, $S_p = -10^{20}$.

Since interest is currently directed to the purely periodic state, which is independent of the initial state, the initial conditions are inconsequential from a physical point of view. From a numerical point of view, however, (and considering that the problem admits a laminar solution), it is found that the choice of initialisation can affect the ability of the code to obtain a turbulent periodic solution. For all cases examined the flow was initialised using the results of a steady channel flow. This was done by setting γ_P to zero in (5.1). It was also found helpful, as previously mentioned in Section 5.2, to shift the phase of the pressure gradient so as to start the solution in the deceleration part of the cycle. Despite that, it was not possible to obtain a turbulent periodic solution at the lowest frequency with the Shima or HJ models, both of which returned laminar solutions. This is discussed further in Section 5.5.

As a measure of code verification, the present code was used to reproduce the calculations of Cotton et al. (2001) (who used a different code) for the pulsatile pipe flow case of Tu and Ramaprian (1983). The Launder-Sharma k–ε model was used. As can be seen in Figure 5.2, very good agreement with the previous calculations is achieved.

5.4 Steady turbulent channel flow results

To provide a reference for the pulsatile flow cases to follow, the performance of the selected turbulence models in steady turbulent channel flow is briefly presented in this section. The velocity profiles returned by the models are shown in Figure 5.3 along with the DNS results of Moser et al. (1999) for $\mathrm{Re}_\tau = 395$. As previously mentioned, the simulations were carried out by specifying the applied pressure gradient (in this case, in order to match Re_τ of the DNS), rather than the bulk velocity, and it is thus to be expected that there will be variations in the bulk velocities returned by the models compared to the DNS results; these

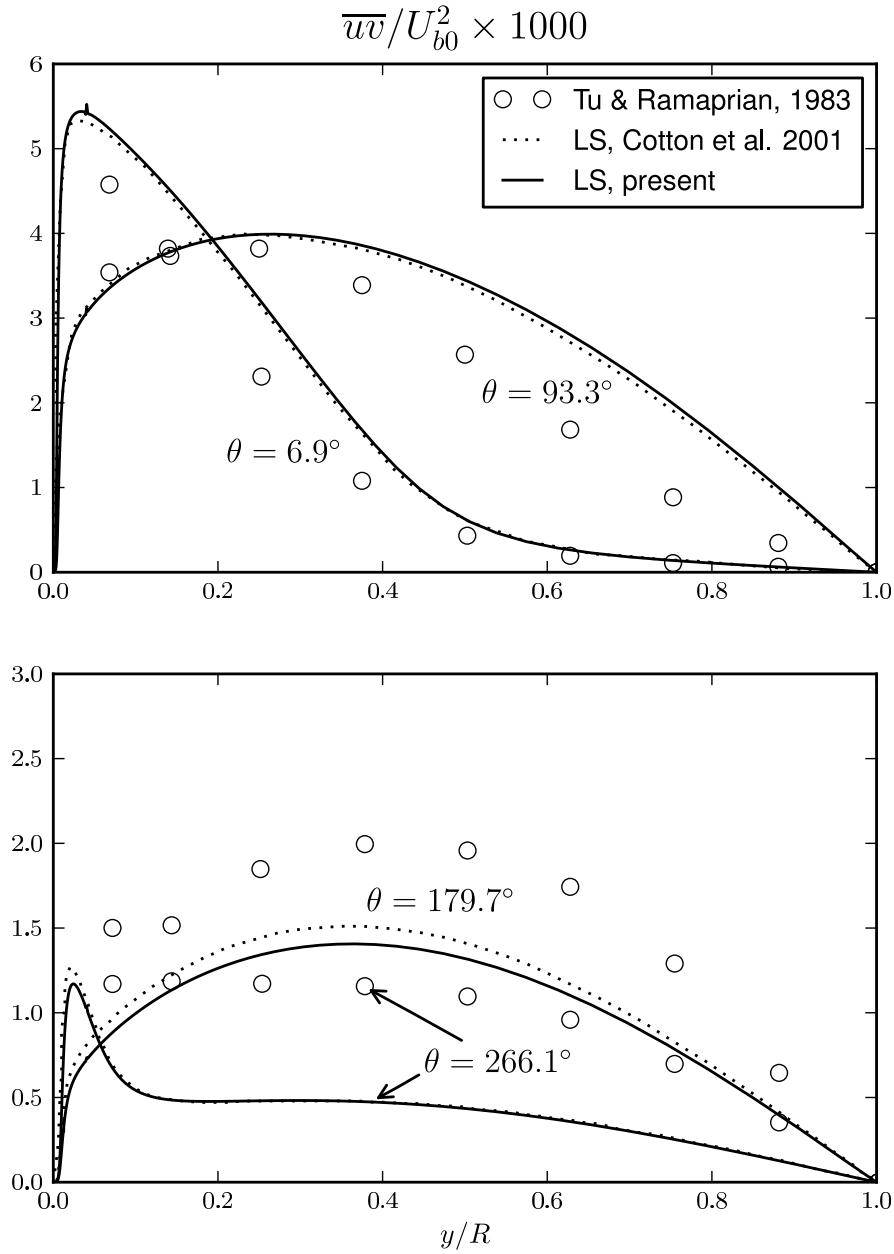

Figure 5.2: Reynolds shear stress profiles in the 0.5 Hz pulsatile pipe flow case of Tu and Ramaprian (1983).

Table 5.2: Bulk velocity returned by turbulence models in steady turbulent channel flow at $\mathrm{Re}_\tau = 395$ compared to the DNS of Moser et al. (1999)

	DNS	TCL	Shima	HJ	LS
U_b^+	17.5	18.3	16.0	15.5	18.4
% difference	-	+4.2%	-9.3%	-11.8%	+5%

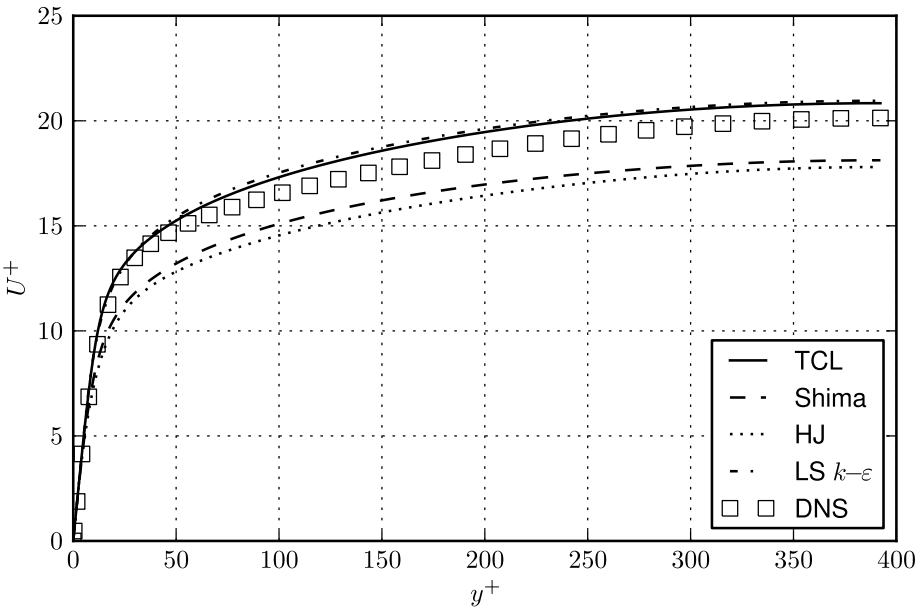

Figure 5.3: Velocity profiles returned by various turbulence models for steady turbulent channel flow at $\mathrm{Re}_\tau = 395$. (Every fourth symbol shown for DNS).

are summarised in Table 5.2. The TCL and LS models return very similar velocity profiles and slightly over-predict the bulk velocity compared to the DNS by about 4-5%. The Shima and HJ models both under-predict U_b^+ by 9 and 12% respecively.

The TCL and LS models more accurately reproduce the shape of the mean velocity gradient profile in the near wall region, as shown in Figure 5.4, while the Shima and HJ models under-predict the mean velocity gradient in the near-wall region.

Profiles of turbulent kinetic energy are shown in Figure 5.5, where it is seen that, characteristically, none of the models is able to reproduce accurately the peak in k near the wall. The HJ model gives the closest prediction of the peak k value, with an under-estimate of 11%, followed by the TCL model which gives a 17% under-estimate. The Shima and LS models under-estimate the peak by

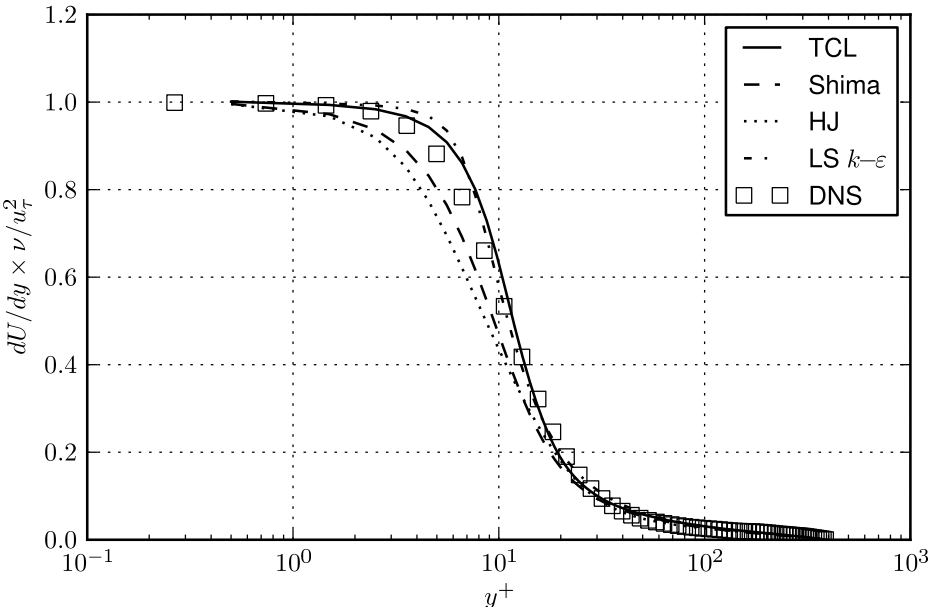

Figure 5.4: Velocity gradient profiles returned by various turbulence models for steady turbulent channel flow at $\mathrm{Re}_\tau = 395$.

about 30%. In the region between $y^+ \approx 70$ and $y^+ \approx 200$ the level of k is fairly well predicted by the HJ, Shima and LS models, but somewhat over-predicted by the TCL model. Beyond that, in the central region of the channel, the level is over-predicted by all four models.

Figure 5.6 shows the normal Reynolds stresses (RSTM only). Here it is seen that, in general, the HJ and TCL models more accurately predict the near-wall profiles of the normal stresses, compared to the Shima model. All three models under-predict the peak in $\overline{u^2}$ component, but less dramatically so in the case of the HJ and TCL models than the Shima model. By over-predicting the $\overline{v^2}$ component in the region $y^+ < 50$, in addition to dramatically under-predicting the $\overline{u^2}$ component, the Shima model is closer to isotropy than it should be in this region. All three models over-predict $\overline{u^2}$ at the centre of the channel. The HJ and TCL model over-predict the $\overline{w^2}$ for most of the channel cross-section away from the wall, $y^+ > 10$. The Shima model is superior in the near-wall region, but over-predicts $\overline{w^2}$ in the region $y^+ > 150$.

Reynolds shear stress profiles, and profiles of the production rate of turbulent kinetic energy, are shown in Figures 5.7 and 5.8, respectively. The magnitude of Reynolds shear stress can be seen to be over-predicted by the HJ and Shima

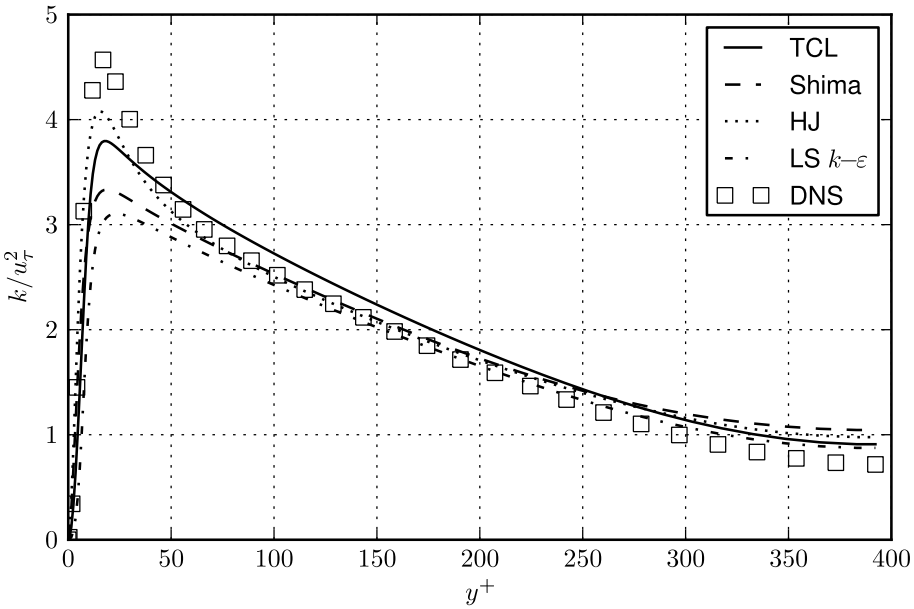

Figure 5.5: Turbulent kinetic energy profiles returned by various turbulence models for steady turbulent channel flow at $\mathrm{Re}_\tau = 395$.

models in the near-wall region, while the LS and TCL return more accurate levels over the whole profile. The production rate profiles reflect the previous observations on the mean velocity gradient in Figure 5.4, and the Reynolds shear stress 5.7. In the case of the Shima and HJ models, it appears that the overprediction of the magnitude of $\overline{uv}$ has a larger effect than the underprediction of $\frac{\mathrm{d}U}{\mathrm{d}y}$ in the near wall region, as evidenced by the over-estimated production rate in Figure 5.8.

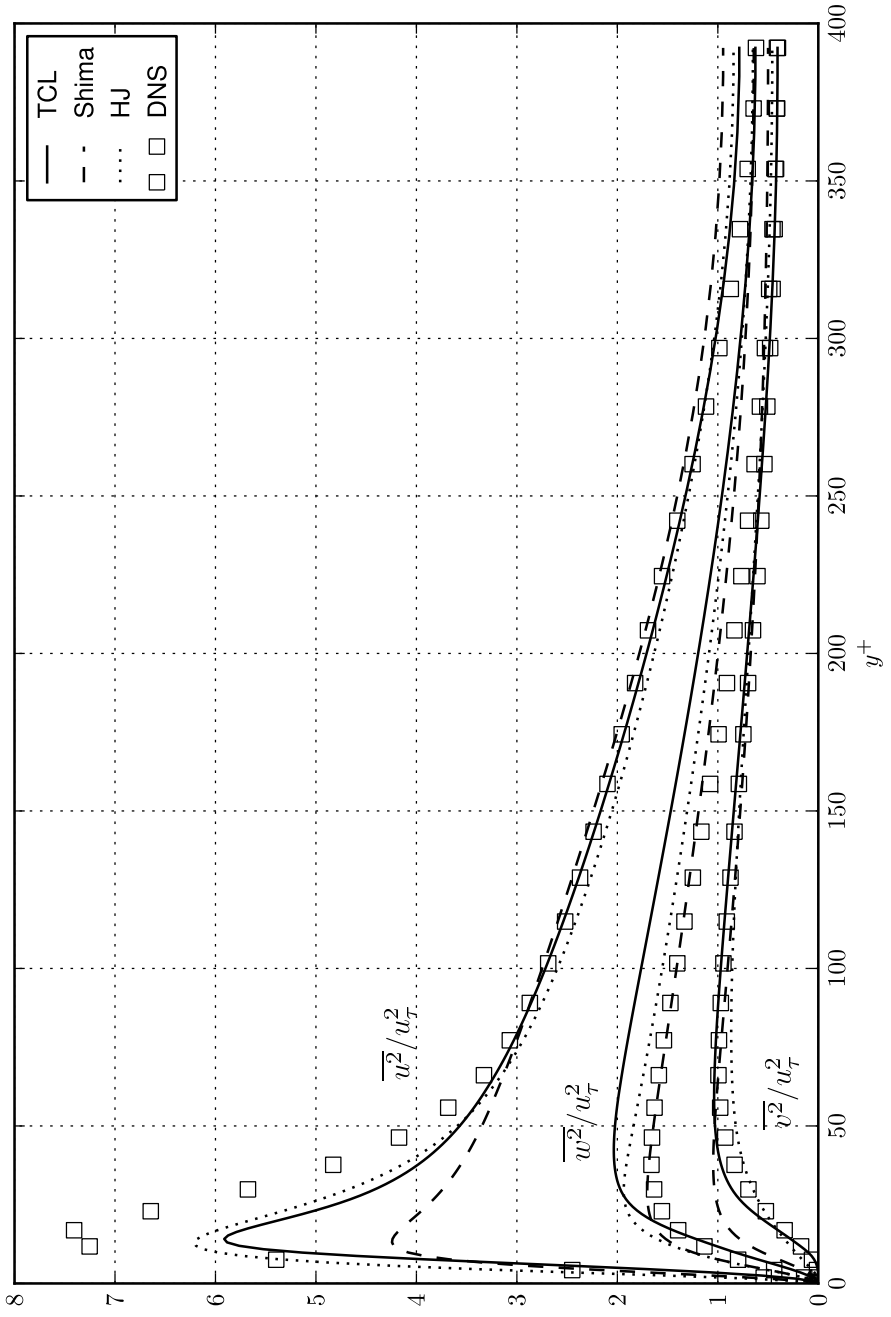

Figure 5.6: Profiles of the normal Reynolds stresses in wall units returned by various turbulence models for steady turbulent channel flow at $\mathrm{Re}_\tau = 395$.

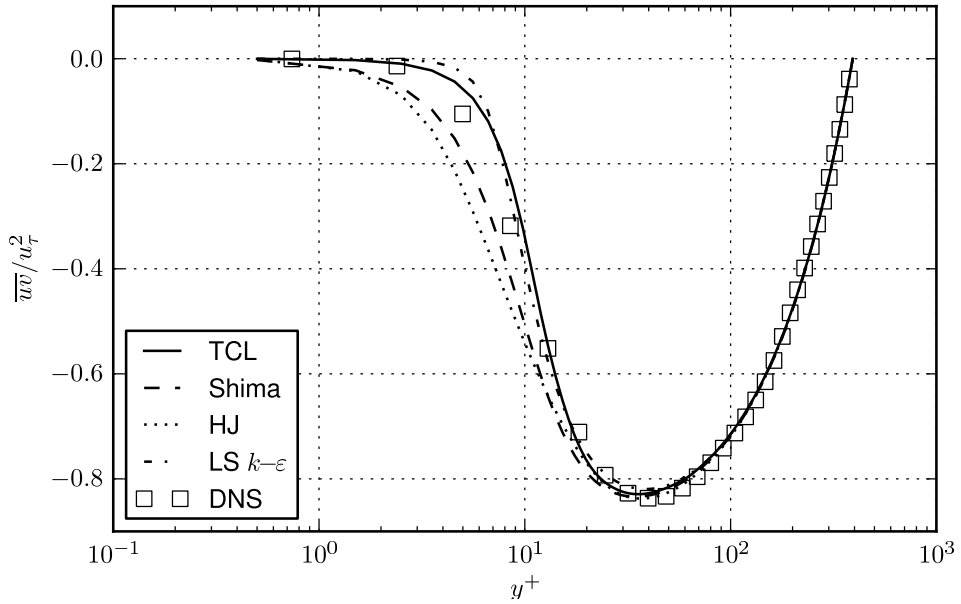

Figure 5.7: Profiles of Reynolds shear stress returned by various turbulence models for steady turbulent channel flow at $\mathrm{Re}_\tau = 395$.

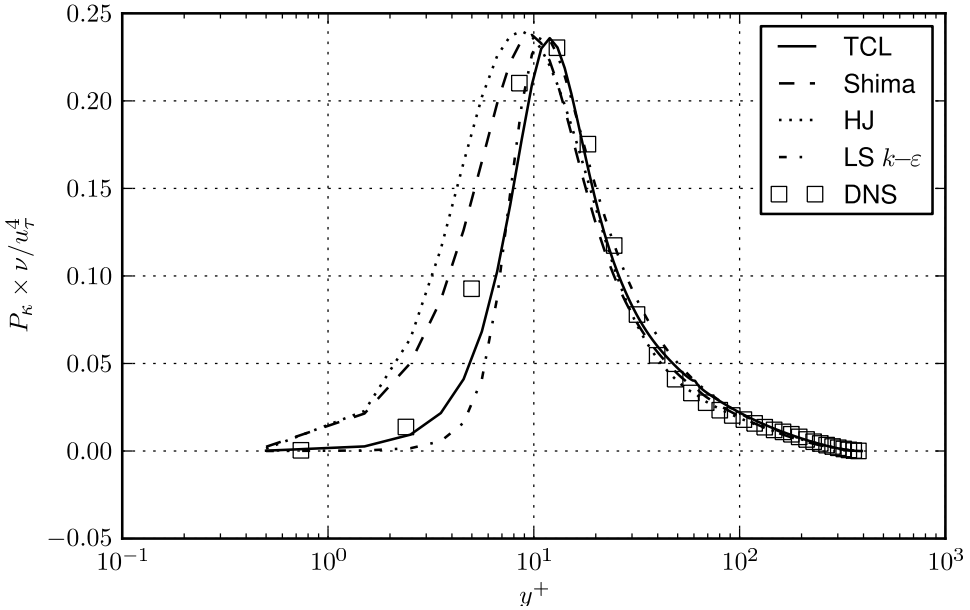

Figure 5.8: Profiles of turbulent energy production returned by various turbulence models for steady turbulent channel flow at $\mathrm{Re}_\tau = 395$.

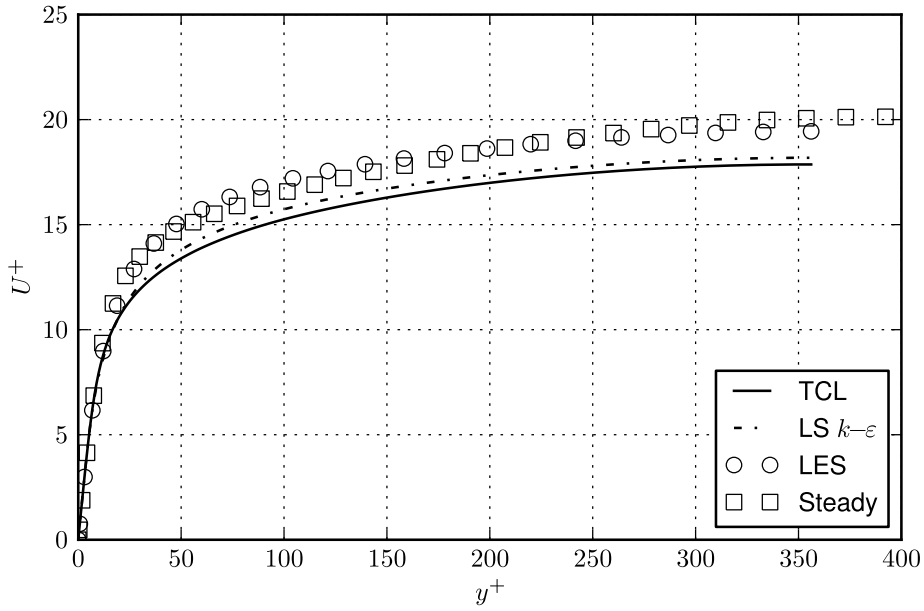

Figure 5.9: Time mean profile of velocity in wall units for the low frequency case $\omega^+ = 0.0016$.

5.5 Low frequency results

5.5.1 Time-mean behaviour

The time-mean velocity profiles returned by the TCL and LS models for the low frequency case, $\omega^+ = 0.0016$, are compared against time-mean LES results and steady DNS results at $\mathrm{Re}_\tau = 395$, in Figure 5.9. At this low frequency the time-mean velocity profile of the pulsatile flow LES is in close agreement with the steady channel flow DNS profile at a comparable Re_τ. Both turbulence models underestimate the velocity, and thus under-estimate the time-mean bulk velocity. This is somewhat surprising, since these same models were seen to over-predict the bulk-velocity in steady channel flow (Figure 5.3). It will be seen later, when the phase-averaged behaviour is examined, that this is most likely due to periodic laminarisation and re-transition within each cycle. The profile of the time-mean velocity gradient, shown in Figure 5.10 is reasonably well predicted by both models.

In the time-mean turbulent kinetic energy profiles, shown in Figure 5.11, there appears to be some difference between the time-mean pulsatile flow profile (LES) and the steady flow profile (DNS). The pulsatile mean profile exhibits a sharper

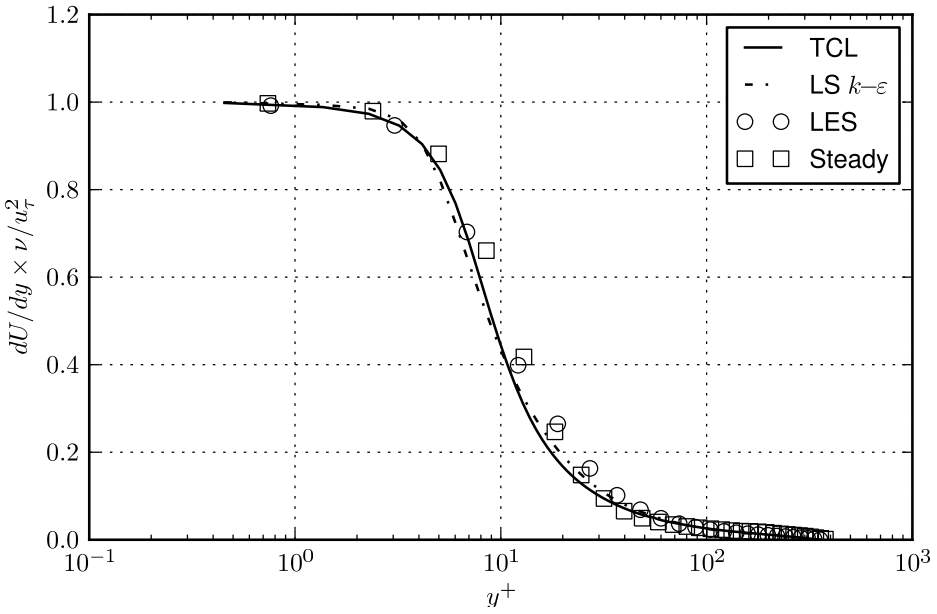

Figure 5.10: Time mean profile of velocity gradient in wall units for the low frequency case $\omega^+ = 0.0016$.

peak near the wall ($y^+ \approx 10$), and a consistently lower level of k in the inner region ($y^+ > 50$). Setting aside the models' inability to fully reproduce the peak in the k profile, their time-mean profiles appear to follow the steady channel flow rather than the time-mean profile of the pulsatile LES results. Examination of the normal stresses, shown in Figure 5.12, shows that in the pulsatile case there is increased energy in the time-mean $\overline{u^2}$ component near the wall, and decreased energy in the two other components compared to the steady channel case. The previous observations suggest that the pulsations tend to polarise the energy distribution across the cross-section, and enhance the streamwise velocity fluctuations at the expense of the normal and spanwise fluctuations. However, by reference to the LES validation that Scotti and Piomelli (2001) carried out (Figure 4 in their paper), these effects appear to be a result of under-resolution of the small scales in the near-wall region of the LES, rather than an actual physical effect of the pulsations. Their validation (at a higher frequency than the present case) shows the mean normal Reynolds stresses of the LES to deviate from the DNS at the same conditions. The mean normal stresses of their pulsatile DNS agreed more with the profiles of the steady flow DNS, shown Figure 5.12. Notably, profiles of normal stress amplitudes (to be examined later) of the LES were in

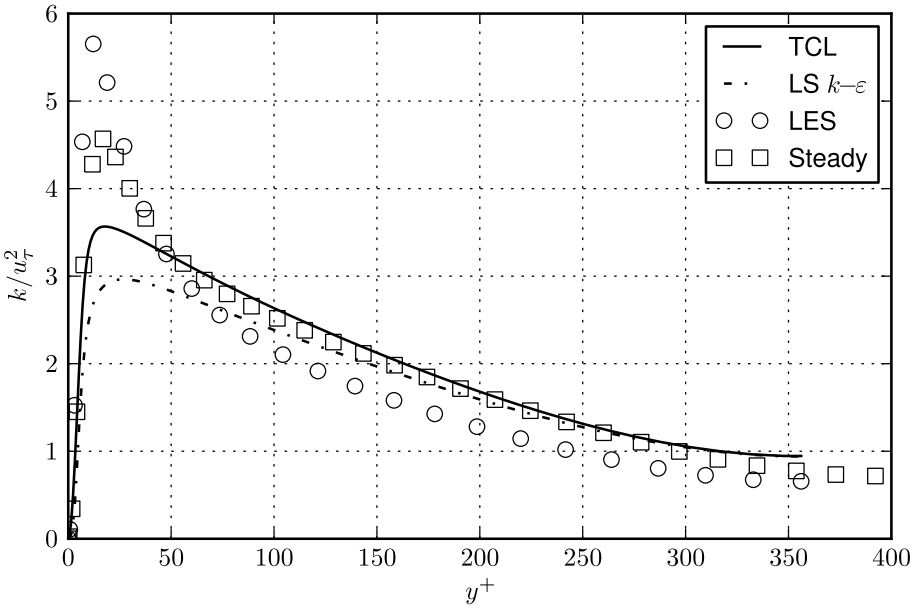

Figure 5.11: Time mean profile of turbulent kinetic energy in wall units for the low frequency case $\omega^+ = 0.0016$.

good agreement with the amplitudes of their pulsatile DNS. Comparing Figure 5.6 and Figure 5.12, it is seen that this trend is not mimicked by the TCL model, which returns fairly similar time-mean profiles of normal stress components in the steady and pulsatile cases.

Figures 5.13 and 5.14 show the time-mean Reynolds shear stress and the time-mean production of k, respectively. Both quantities show a decrease in the pulsatile compared to the steady case. This decrease is over a large portion of the cross section, $y^+ > 10$, in the case of $\overline{uv}$, and over a limited near-wall region, $y^+ \approx 5-20$, in the case of P_κ. Again, the models return profiles that more closely follow the steady case profiles.

5.5.2 Phase-averaged behaviour

Figures 5.15, 5.16 and 5.17 show profiles of phase-averaged velocity, k, and $\overline{uv}$, respectively, over a period of oscillation T, at $\frac{T}{8}$ intervals. The velocity profiles returned by both models are in phase with the phase-averaged LES profiles and, aside from a general tendency to slightly under-predict the velocity in the core region (more visible around mid-cycle because of the varying plot scale in Figure 5.15), they can be said to be in good agreement with the reference data. The

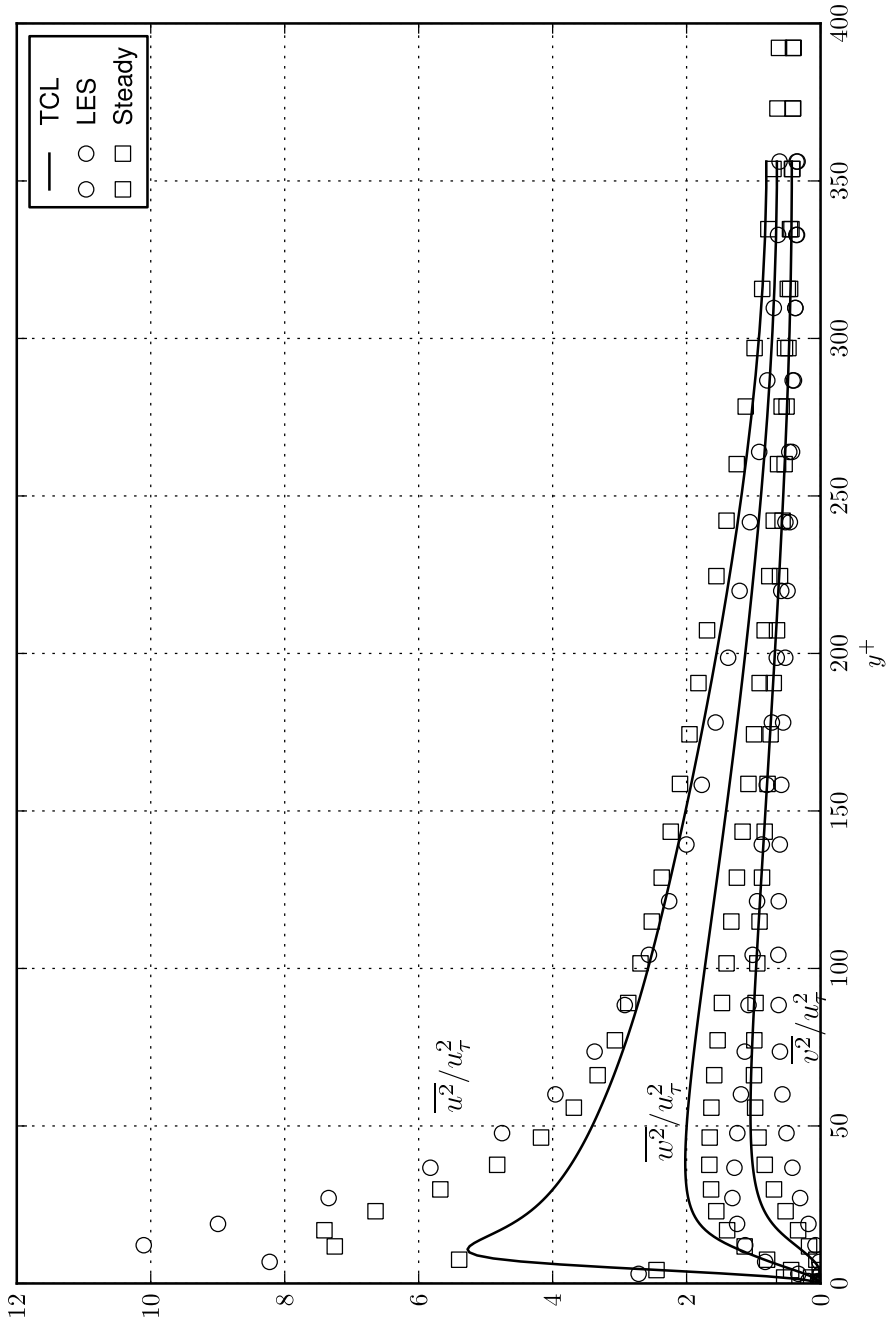

Figure 5.12: Time mean profile of normal Reynolds stresses in wall units for the low frequency case $\omega^+ = 0.0016$.

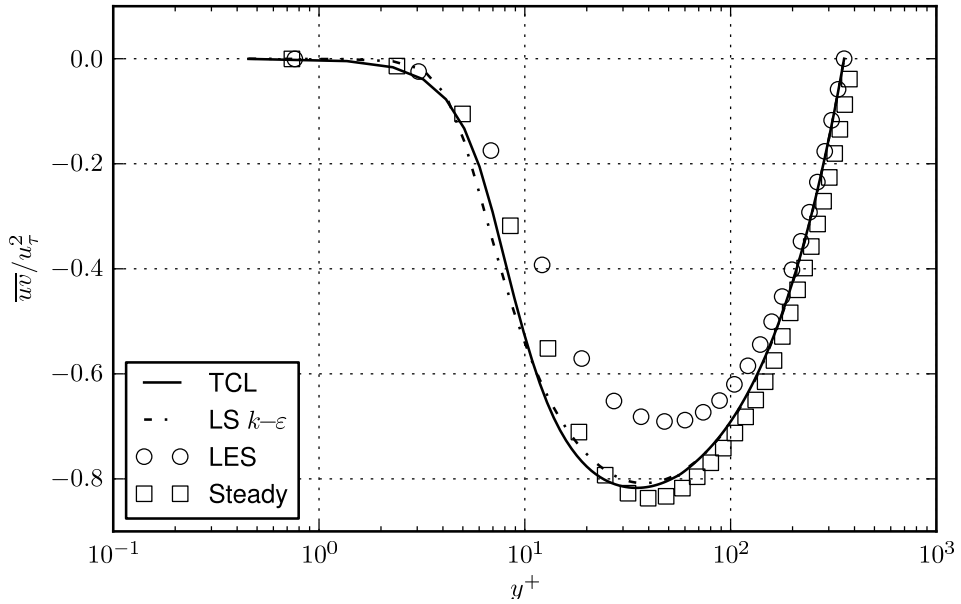

Figure 5.13: Time mean profile of Reynolds shear stress in wall units for the low frequency case $\omega^+ = 0.0016$.

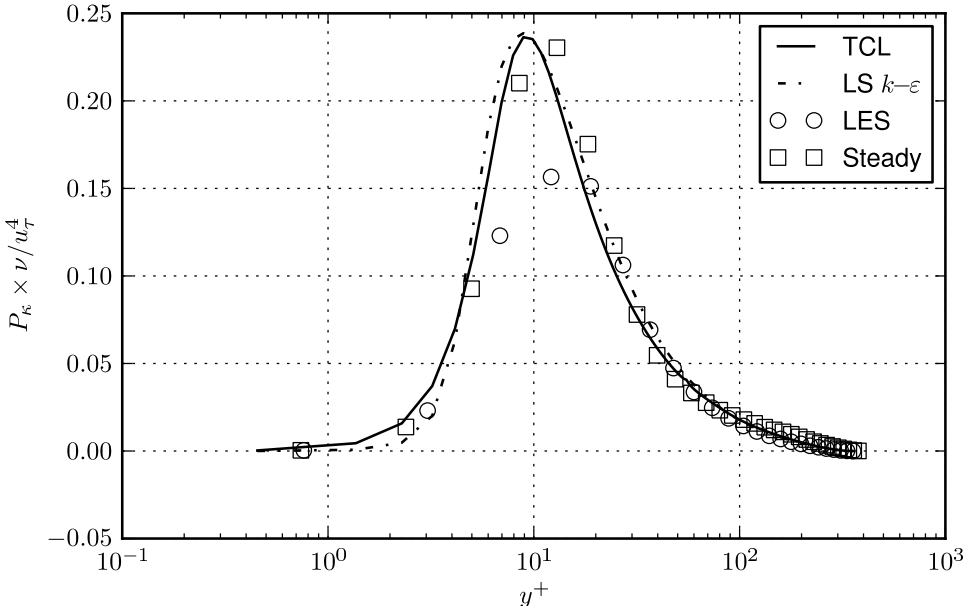

Figure 5.14: Time mean profile of production of turbulent kinetic energy in wall units for the low frequency case $\omega^+ = 0.0016$.

turbulent kinetic energy profiles in Figure 5.16 generally exhibit a significant departure from the characteristic shape associated with steady channel flow. This indicates that, even at this low frequency, the modulation of k is not a simple harmonic oscillation about the steady flow profile, and this frequency therefore does not fall in the quasi-steady regime. Throughout most of the cycle, the LES profiles exhibit a larger near-wall peak, followed by a more rapid decrease, than the profiles returned by both models, which seem to distribute the energy more evenly over the cross-section. Towards the centre of the channel the level of turbulence is fairly well predicted by both models throughout the cycle. Slightly after mid-cycle the level of turbulence decreases to the point that the flow is partially laminarised. In the period between $6T/8$ to $7T/8$ there is an abrupt and dramatic increase in both model profiles causing them to overshoot the reference LES data. The phase-averaged Reynolds shear stress, shown in Figure 5.17, is well predicted by the models during the first half of the cycle, after which it is under-predicted in the near-wall region during the laminarised part of the cycle. At around $6T/8$ a small peak appears in the profile returned by the TCL model, and a similar peak appears slightly later in the LS profile (not shown). This is then followed by a dramatic overshoot in both model profiles, similar to that seen in the k profiles in the previous figure.

An alternative view of the data is provided in Figures 5.18, 5.19 and 5.20, which show the cyclic variation of the four phase-averaged quantities: U, dU/dy, k and $\overline{uv}$, normalised by wall variables, at three locations, $y^+ = 19$, 74 and 265, respectively. What immediately stands out in these three figures are local discontinuities in the TCL results in what are otherwise smooth curves. This effect occurs at about 0.8 of the full cycle (slightly later as one moves away from the wall, in Figure 5.20, due to the time it takes for the disturbance to propagate outwards), and it appears to be related to the process of re-transition to turbulence. The wall shear stress modulation is shown in Figure 5.21. In this figure it is seen that both models are generally in reasonable agreement with the reference data (LS giving better agreement), only slightly under-estimating the wall shear stress, up to their respective re-transition points (i.e. time instances), at which point they over-shoot the reference data for a portion of the cycle. Since the mean wall shear stress is set by the imposed mean pressure gradient, the slight under-estimation of τ_w over most of the cycle is to compensate for the over-shoot that follows re-transition, and since the re-transiton is more abrupt in the TCL

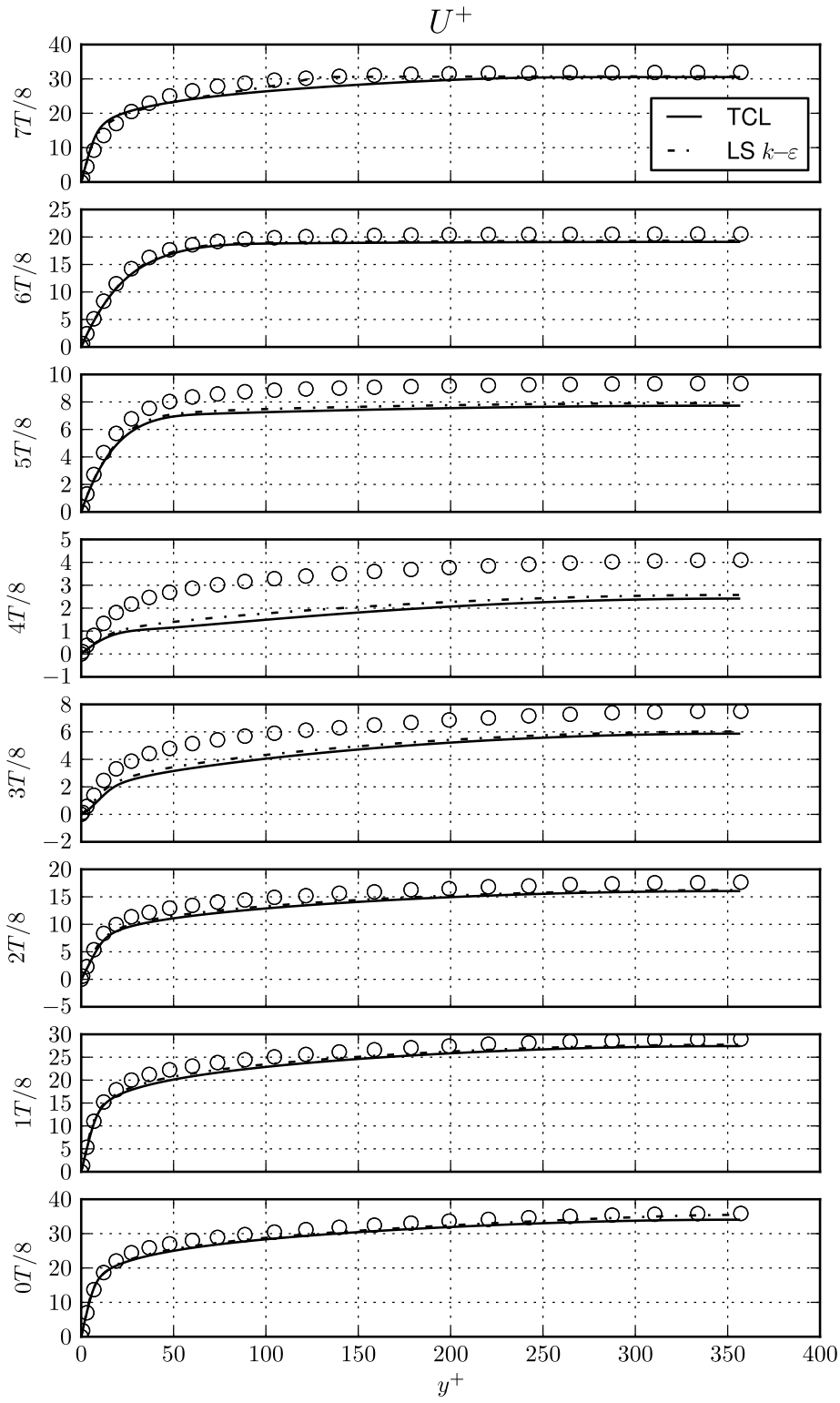

Figure 5.15: Profiles of phase-averaged velocity in wall units for the low frequency case $\omega^+ = 0.0016$.

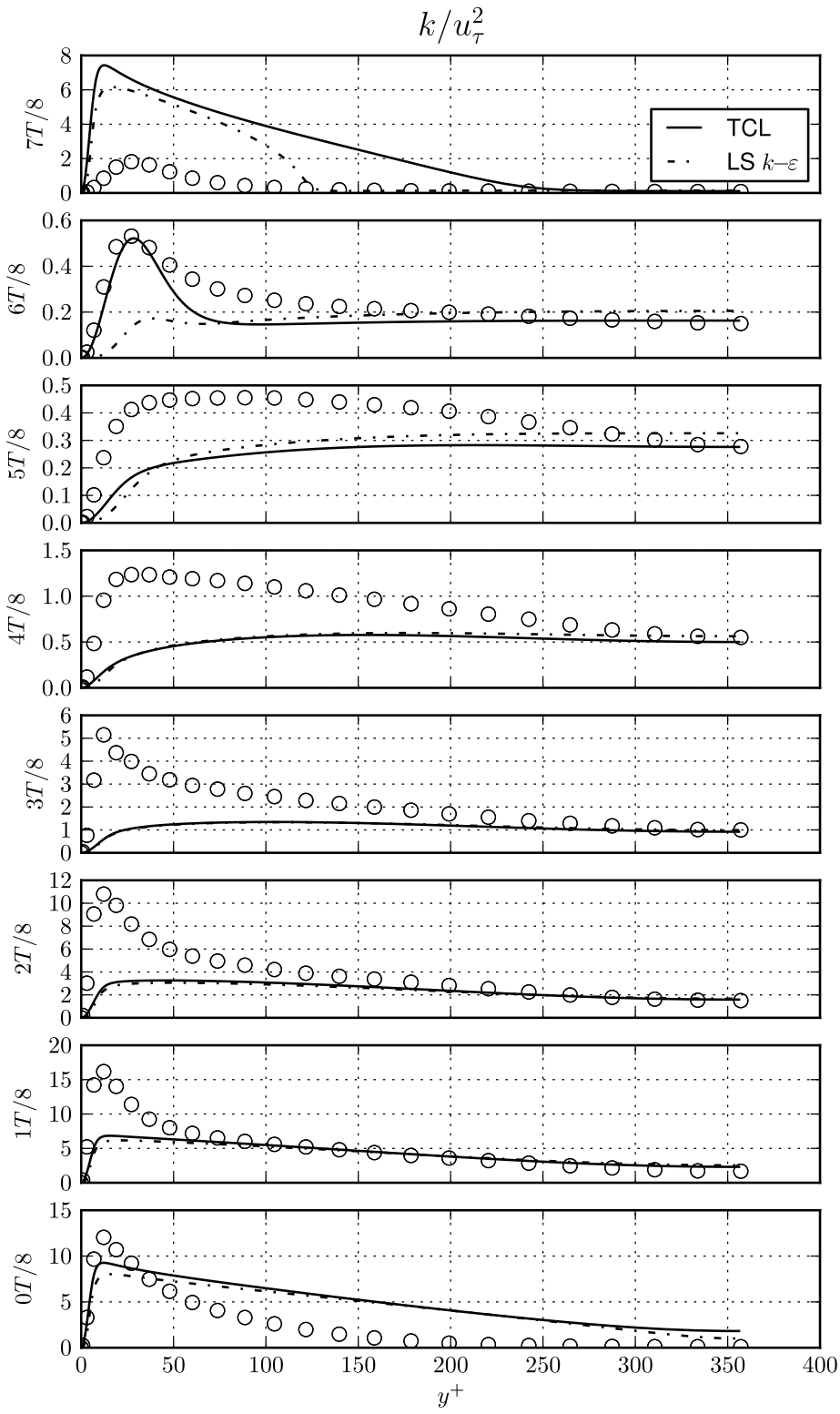

Figure 5.16: Profiles of phase-averaged turbulent kinetic energy in wall units for the low frequency case $\omega^+ = 0.0016$.

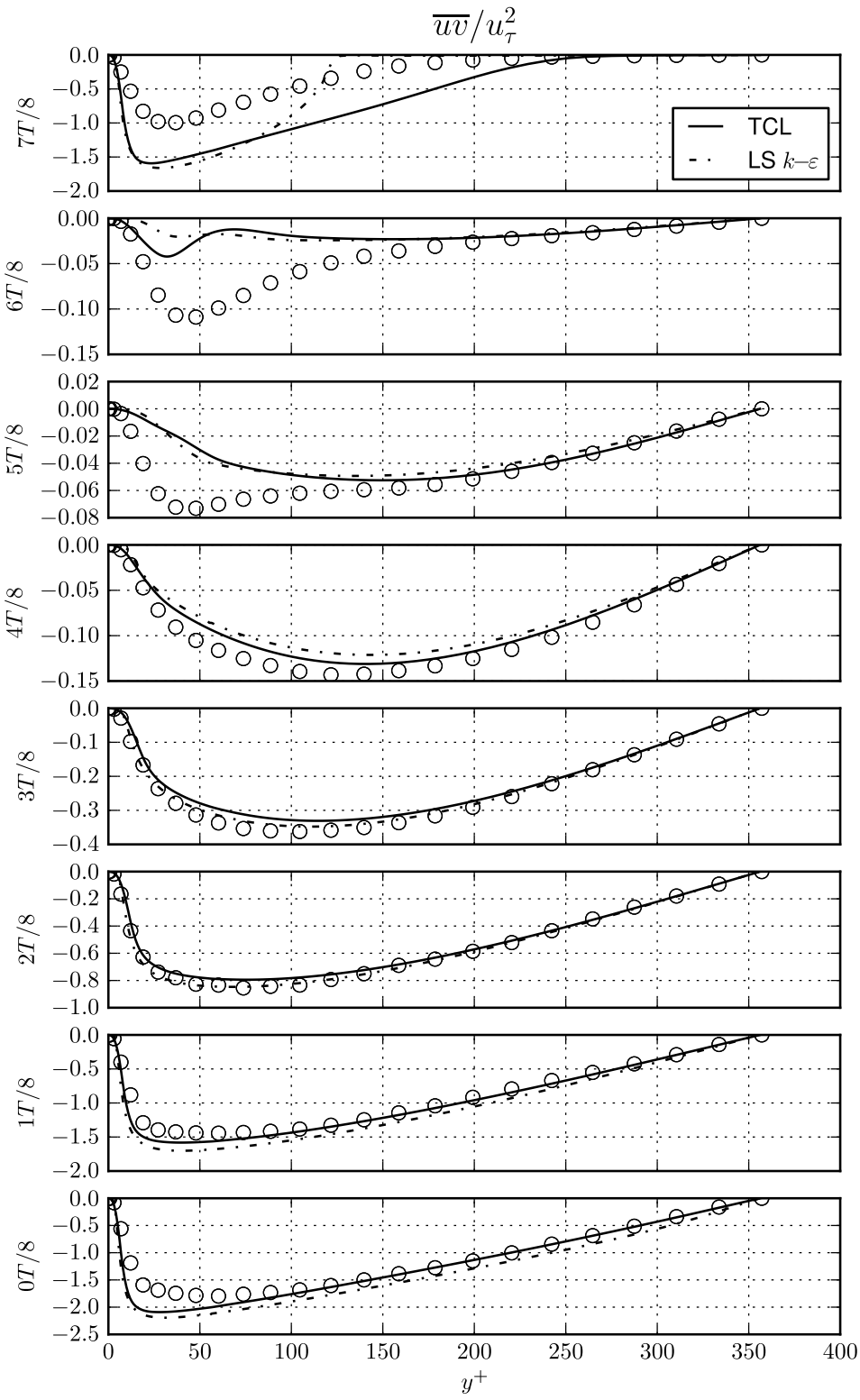

Figure 5.17: Profiles of phase-averaged Reynolds shear stress $\overline{uv}$ energy in wall units for the low frequency case $\omega^+ = 0.0016$.

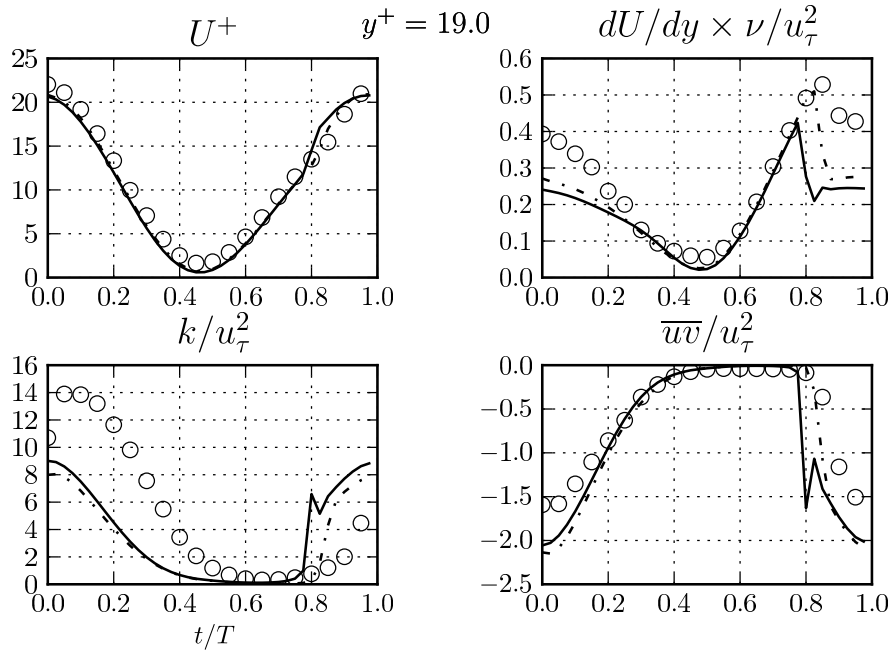

Figure 5.18: Cyclic variation of various phase-averaged flow quantities in wall units for the low frequency case $\omega^+ = 0.0016$ at the location $y^+ = 19$.

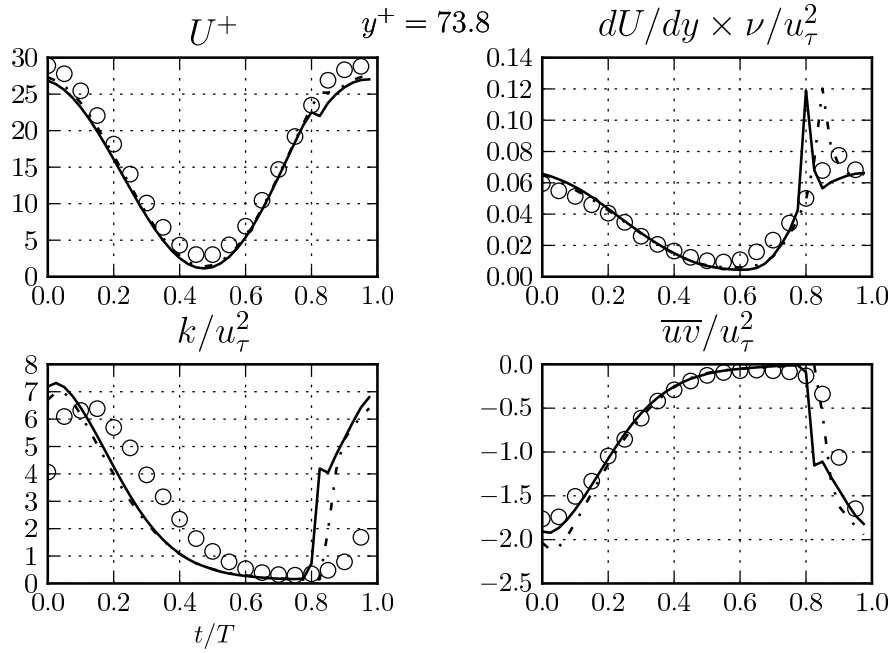

Figure 5.19: Cyclic variation of various phase-averaged flow quantities in wall units for the low frequency case $\omega^+ = 0.0016$ at the location $y^+ = 74$.

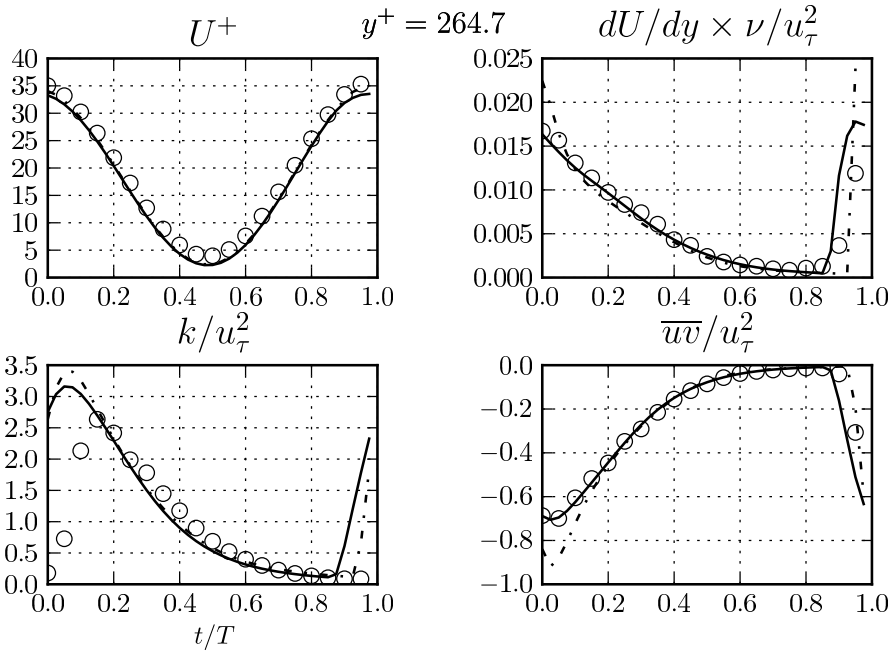

Figure 5.20: Cyclic variation of various phase-averaged flow quantities in wall units for the low frequency case $\omega^+ = 0.0016$ at the location $y^+ = 265$.

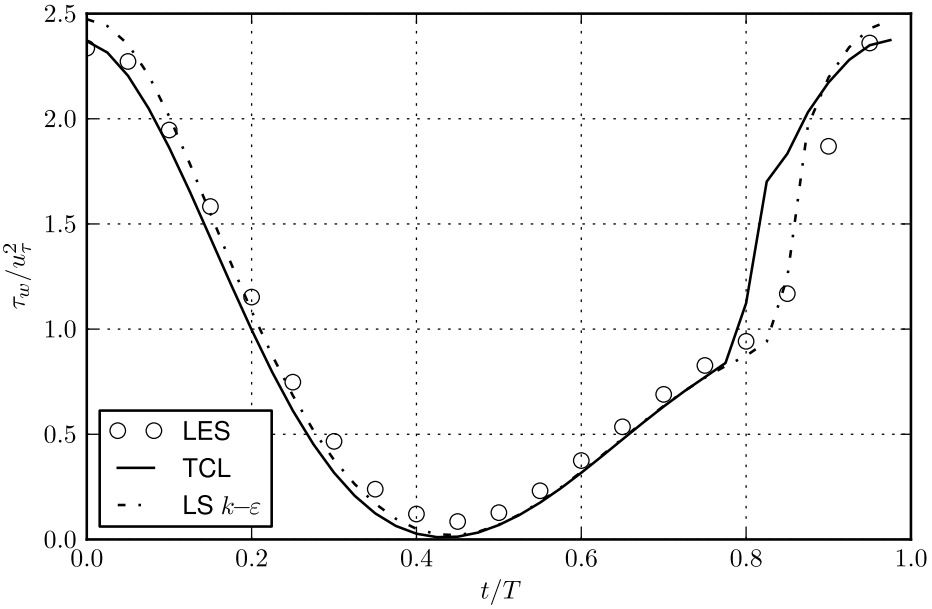

Figure 5.21: Modulation of phase-averaged wall shear stress in wall units for the low frequency case $\omega^+ = 0.0016$.

case, its under-estimation is necessarily larger.

While it is known that transition to turbulence generally presents a serious challenge to turbulence models, it is believed that what is observed here is partly due to the low-Re corrections of the TCL model. Low-Re model coefficients are generally tuned to the typical spatial variation of $\mathrm{Re_t}$ in steady thin-shear flows. In this case however, there is an additional challenge in that the $\mathrm{Re_t}$ profile varies in time, and because of the periodic laminarisation and re-transition, the phase-averaged profiles of $\mathrm{Re_t}$ will understandably be largely different from the profile in steady turbulent channel flow. Over a cycle, $\mathrm{Re_t}$ periodically oscillates, in a large portion of the flow, about the values used to tune the *near-wall* corrections.

The previous comments are demonstrated in the time-series plots of $\mathrm{Re_t}$ and the main TCL pressure-strain rate coefficients, C_1, C_2, C_2', presented in Figure 5.22 and 5.23, at $y^+ = 19$ and 74, respectively. The coefficients were presented in equations (2.84), and are repeated here, omitting terms that evaluate to zero in the present case,

$$C_1 = 3.1 f_A A_2^{1/2} \min\left[\left(\frac{\mathrm{Re_t}}{160}\right)^2, 1\right] \tag{5.4a}$$

$$C_2 = \min\left\{0.55\left[1 - \exp\left(\frac{-A^{1.5}\mathrm{Re_t}}{100}\right)\right],\ \frac{3.2A}{1+S^*}\right\} \tag{5.4b}$$

$$C_2' = \min(0.6, A). \tag{5.4c}$$

Examination of Figures 5.22 and 5.23, reveals that the coefficients do indeed go through an abrupt change at about $0.8\,T$. To explore this issue further, Figure 5.24 presents profiles of $\mathrm{Re_t}$ based on TCL results, and Figures 5.25-5.27 present profiles of the TCL coefficients listed above, all around the time of the abrupt re-transition. Also shown in these figures is the corresponding level of the variables in steady channel flow at $\mathrm{Re}_\tau = 395$ as a reference for comparison (dashed-lines). It can be seen in Figure 5.24 that by $0.75\,T$ $\mathrm{Re_t}$ has dropped over most of the profile to less than 160-180, with the region $y^+ < 100$ having $\mathrm{Re_t} < 100$. As the cycle progresses, the level of $\mathrm{Re_t}$ increases far more rapidly in this near-wall region than over the rest of the flow. The peak is then diffused away from the wall, causing it to drop slightly at first, then recovering slightly as the level of turbulence continues both to grow and spread outwards. Considering that the whole of Figure 5.24 represents only 10% of the cycle, and that between $0.775\,T$ and $0.8\,T$ (corresponding to 2.5% of the cycle) there is almost a threefold increase

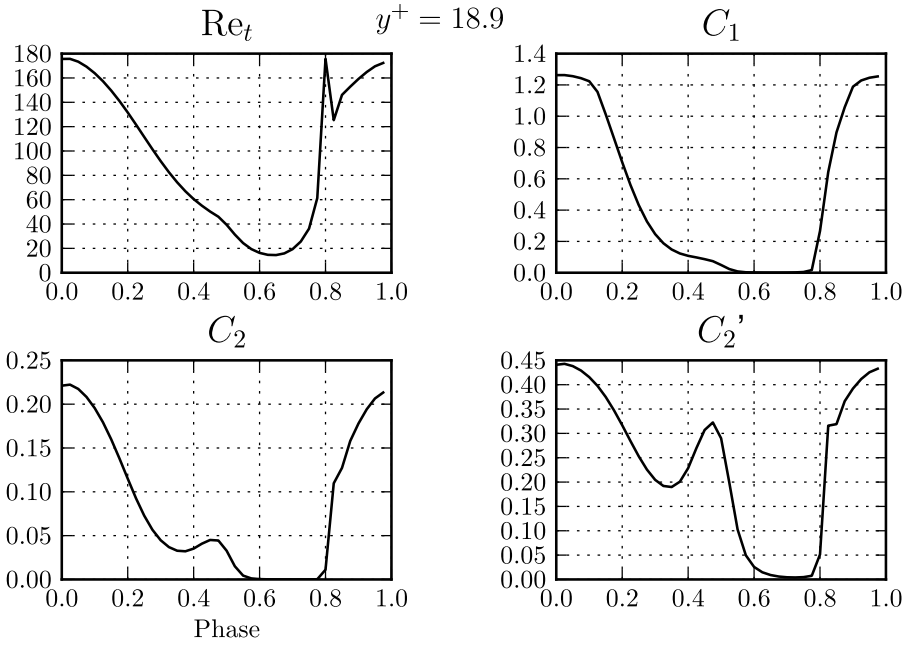

Figure 5.22: Cyclic variation of TCL model coefficients for the low frequency case $\omega^+ = 0.0016$ at the location $y^+ = 18.9$.

in the near-wall peak of $\mathrm{Re_t}$, it can be seen that these observed changes are quite abrupt. Profiles of the coefficients C_1, C_2 in Figures 5.25, 5.26 follow a similar trend to $\mathrm{Re_t}$, while C_2' is affected indirectly through its dependence on A (when $A < 0.6$). To examine the possible impact of these coefficients on the observed behaviour, Figure 5.28 shows profiles of Reynolds stress production, as well as the modelled slow and rapid pressure-strain rate correlations, for the $\overline{uv}$, $\overline{u^2}$, and $\overline{v^2}$ stress components. The bottom row shows the profiles at $0.775\,T$ just before the observed transition, and the top row shows the profiles at $0.8\,T$. There is a huge jump in all the variables plotted in this figure within the short time of $0.025\,T$. Considering the relative magnitude of the various quantites, it is seen that in the $\overline{uv}$ and $\overline{u^2}$ components both pressure-strain terms are relatively small compared to the production terms. It is therefore concluded that the abrupt change in the pressure strain model coefficients, C_1 in particular, first causes a jump in the production-less $\overline{v^2}$ stress component, which in turn feeds into $\overline{uv}$ through its production term, which in turn feeds into $\overline{u^2}$, thus raising the levels of all turbulence quantities.

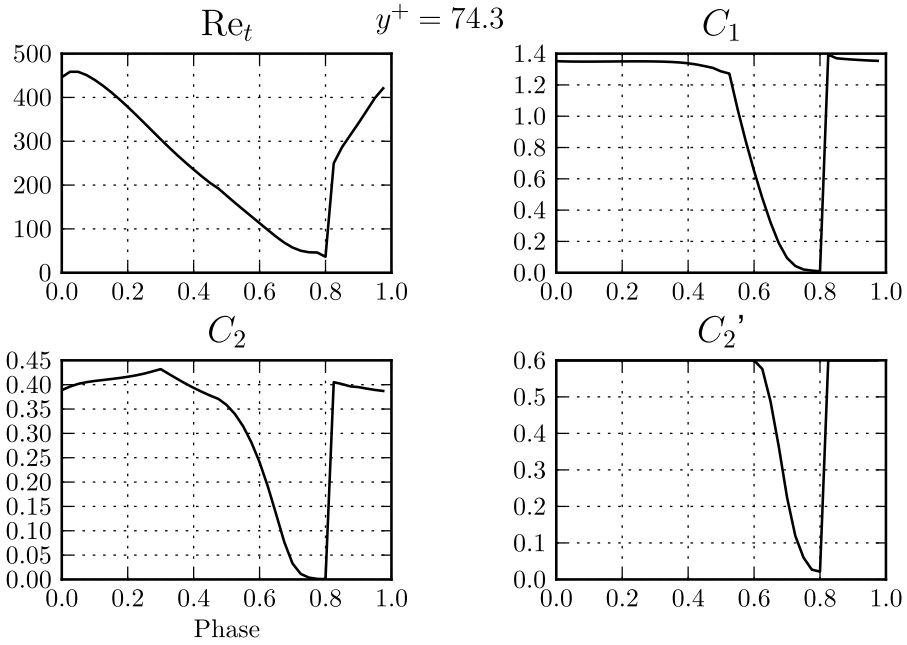

Figure 5.23: Cyclic variation of TCL model coefficients for the low frequency case $\omega^+ = 0.0016$ at the location $y^+ = 74$.

5.5.3 Harmonics

Some further insight is gained by examining the fundamental mode of modulation of the various quantities by fitting pure sinusoids to represent the data. For a scalar quantity ϕ the data can be represented in the form:

$$\phi \approx \overline{\phi} + A_\phi \cos(\omega t - \varphi_\phi). \tag{5.5}$$

From a practical point of view however, it was found that using the equivelent form

$$\phi \approx \overline{\phi} + A_c \cos(\omega t) + A_s \sin(\omega t), \tag{5.6}$$

is more numerically robust, because of the difficulty associated with finding A_ϕ, and φ_ϕ directly (such as converging on negative amplitudes with largely shifted phases). Thus, a least-squares fit was performed to find the mean $\overline{\phi}$, and the amplitudes of the cosine and sine, A_c, A_s, that minimise the residual r in:

$$r = \phi - \big(\overline{\phi} + A_c \cos(\omega t) + A_s \sin(\omega t)\big). \tag{5.7}$$

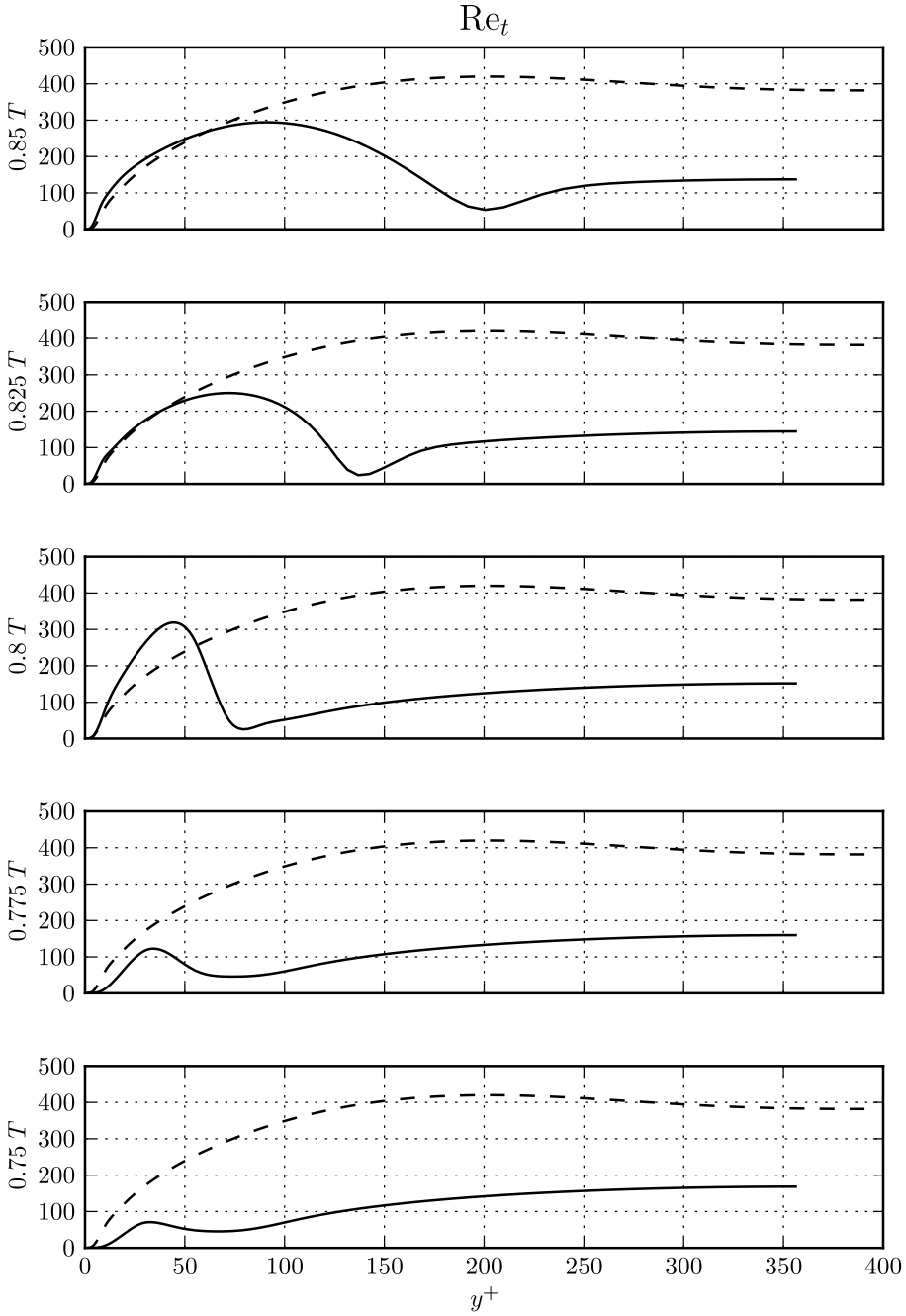

Figure 5.24: Profiles of phase-averaged turbulence Reynolds number returned by the TCL model around the phase of re-transition to turbulence, for the low frequency case $\omega^+ = 0.0016$.

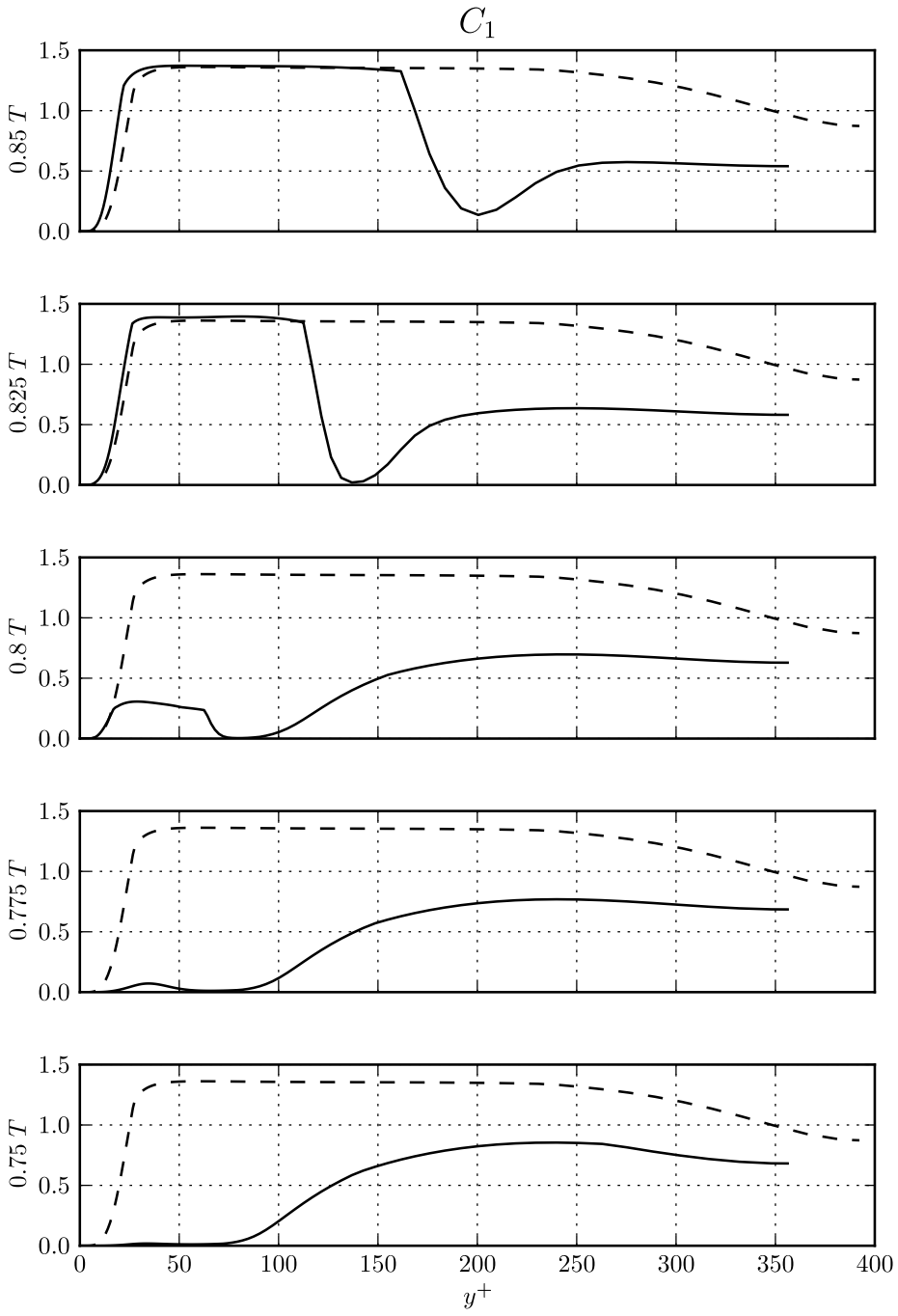

Figure 5.25: Profiles of the TCL coefficient C_1 around the phase of re-transition to turbulence, for the low frequency case $\omega^+ = 0.0016$.

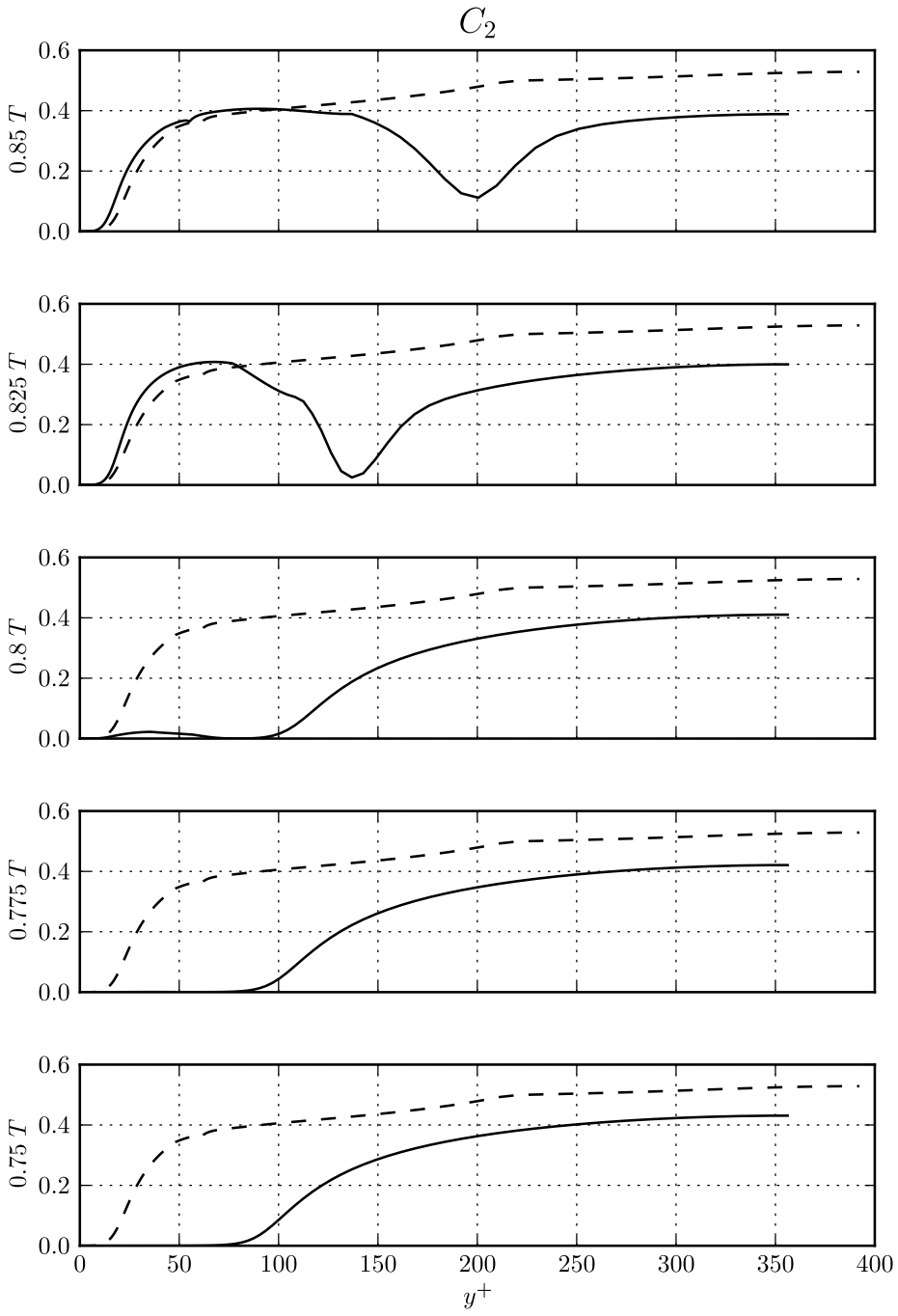

Figure 5.26: Profiles of the TCL coefficient C_2 around the phase of re-transition to turbulence, for the low frequency case $\omega^+ = 0.0016$.

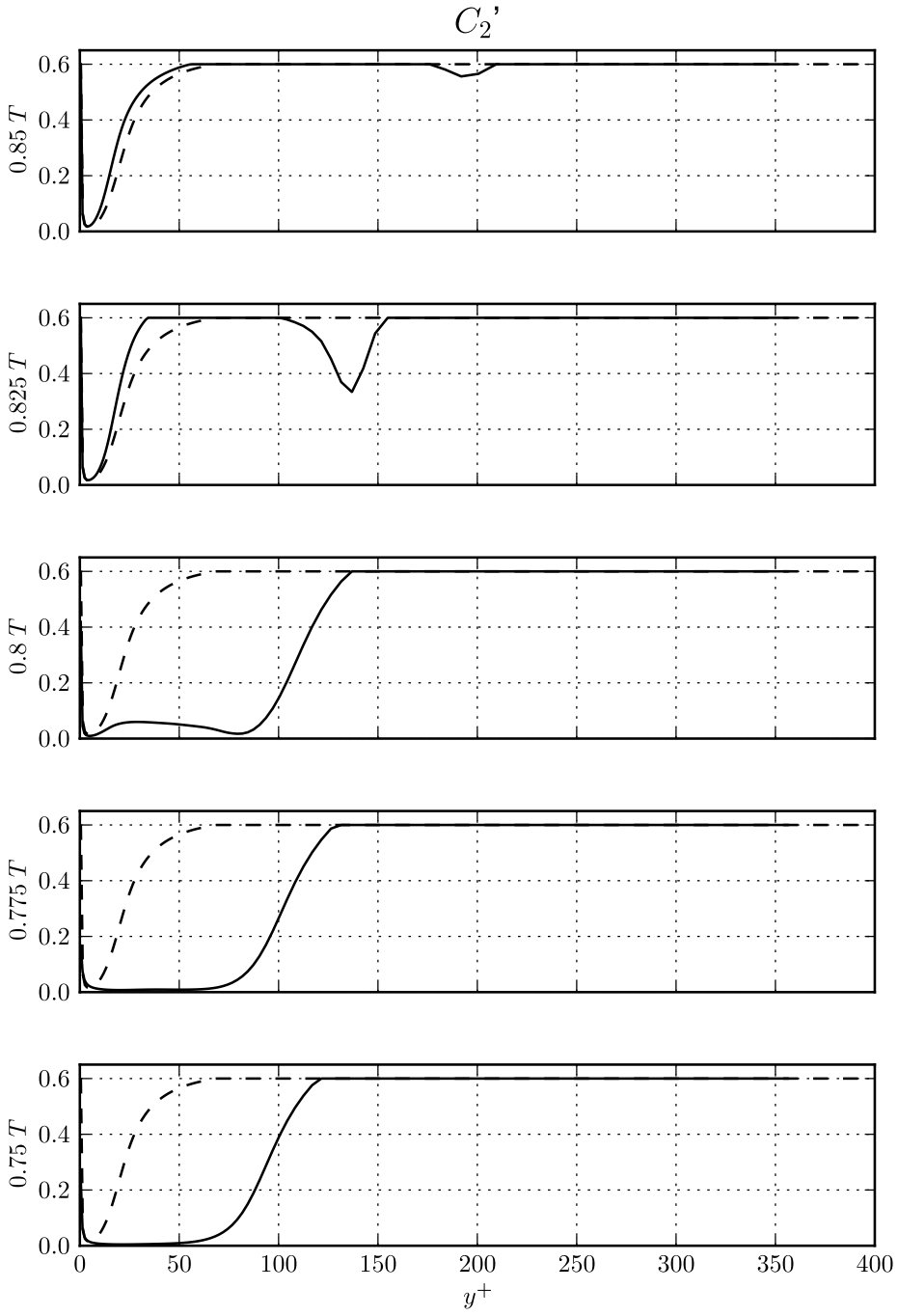

Figure 5.27: Profiles of the TCL coefficient C_2' around the phase of re-transition to turbulence, for the low frequency case $\omega^+ = 0.0016$.

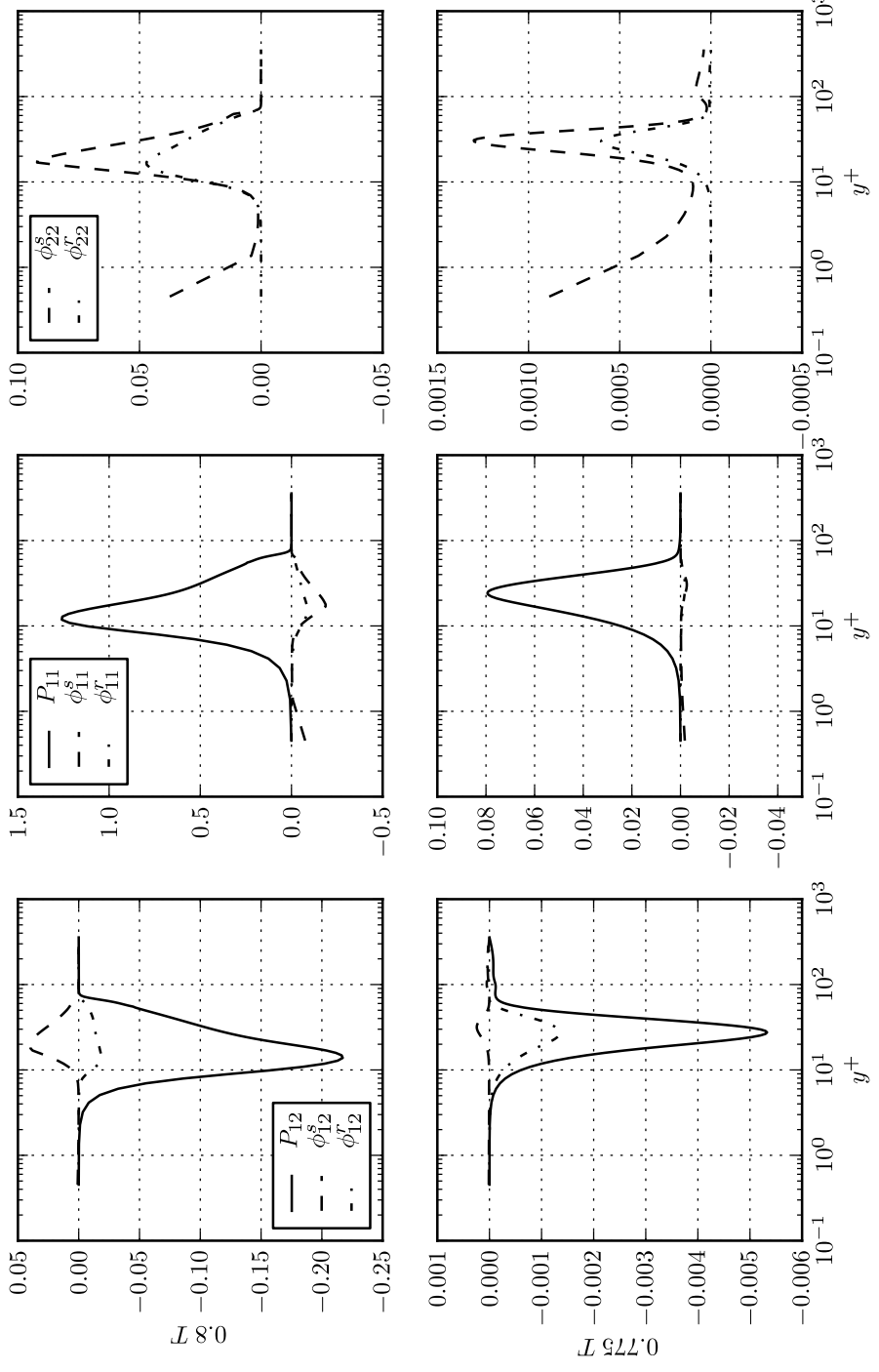

Figure 5.28: Partial balances of $\overline{uv}$ (left column), $\overline{u^2}$ (centre column) and $\overline{v^2}$ (right column), before (bottom row) and after (top row) the abrupt jump observed in the cycle.

The desired amplitude and phase angle in (5.5) were then obtained by

$$A_\phi = \sqrt{A_c^2 + A_s^2}, \quad \varphi_\phi = \tan^{-1}(\frac{-A_s}{A_c}). \tag{5.8}$$

A measure of the significance of the higher harmonics contribution is provided by the amplitude-normalised discrete rms error,

$$\epsilon_\phi = \frac{1}{A_\phi}\sqrt{\frac{\sum r^2 \delta(\omega t)}{\Delta(\omega t)}} \tag{5.9}$$

Figures 5.29, 5.30, 5.31 present the amplitude and phase angle of the fundamental modes of U^+, $k/\overline{u_\tau}^2$ and $\overline{uv}/\overline{u_\tau}^2$, respectively, using the least-squares fit described above. The contribution of higher harmonics in the case of U^+ is less than 5% for the whole region $y^+ > 50$, but it increases near the wall to reach a maximum of around 20%. This information is shown in Figure 5.32. It can thus be said that the modulation in this case is well represented by the fundamental mode alone. As seen in Figure 5.29, the amplitudes and phase angles of phase averaged velocity modulation predicted by the models are in very good agreement with the reference LES data.

In the case of the k and $\overline{uv}$ modulation, the estimated contribution of the higher harmonics is higher, as seen in Figure 5.32. This might be expected, considering that the modulation of these quantities, as seen in the time series plots on Figures 5.18-5.20, does not follow a symmetrical sinusoid-like pattern, but rather has a gradual decrease from a peak value during the laminarisation part of the cycle, followed by a steep increase in the re-transition part. This is further illustrated in Figure 5.33, which shows discrete Fourier transforms (DFT) of the phase-averaged quantities U^+ and k^+ at location $y^+ = 265$ (LES and TCL). Compared to U^+, which has a single modulation frequency, the DFTs of k^+, for the reference LES and of the TCL results, contain signifant amplitudes at higher frequencies.

Figure 5.30 shows that the models adequately predict the amplitude of the fundamental mode of k^+, with slight over-estimation, for the region $y^+ > 50$. For the remaining near-wall part of the cross-section the models under-predict the amplitude. In addition, they are out of phase with the reference data by about 35°-40°. As for $\overline{uv}^+$, Figure 5.31 shows that the models significantly over-estimate the amplitude of the fundamental within the approximate region $10 < y^+ < 100$.

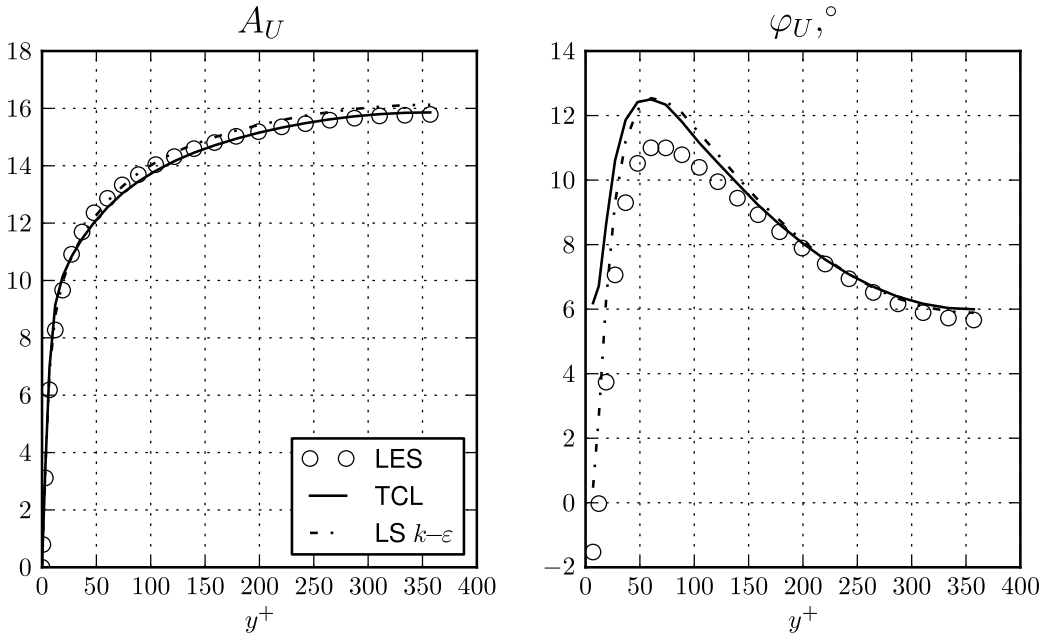

Figure 5.29: Amplitude and phase angle of the fundamental mode of phase-averaged velocity oscillation for the low frequency case $\omega^+ = 0.0016$.

The TCL adequately reproduces the amplitude outside this region, while the LS model slightly over-estimates it. The model results for $\overline{uv}^+$ are out of phase with the reference data by about 3° for the LS model and about 10° for the TCL model.

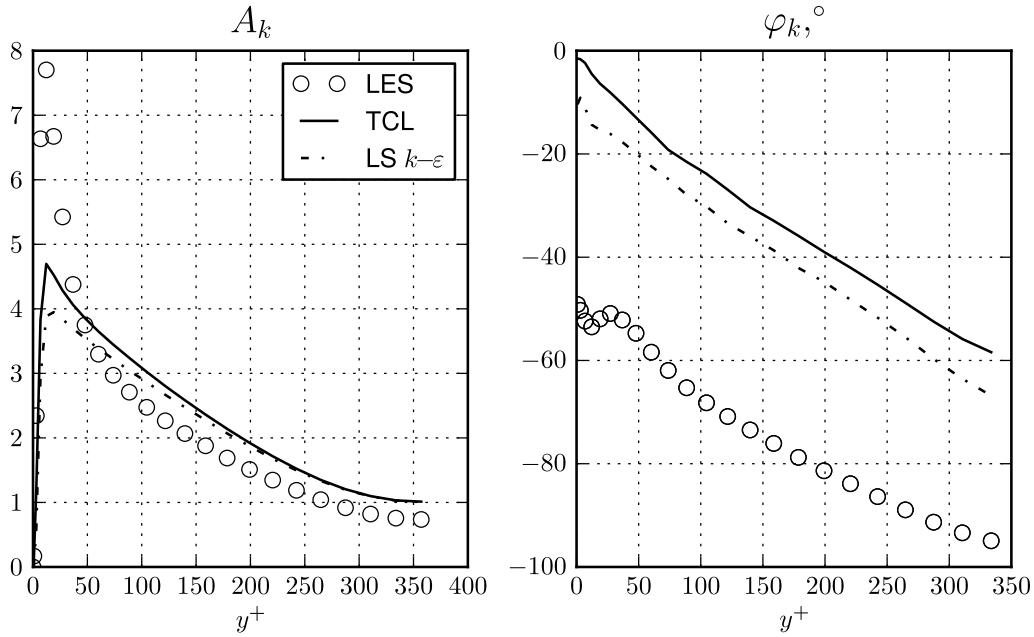

Figure 5.30: Amplitude and phase angle of the fundamental mode of phase-averaged turbulent kinetic energy oscillation for the low frequency case $\omega^+ = 0.0016$.

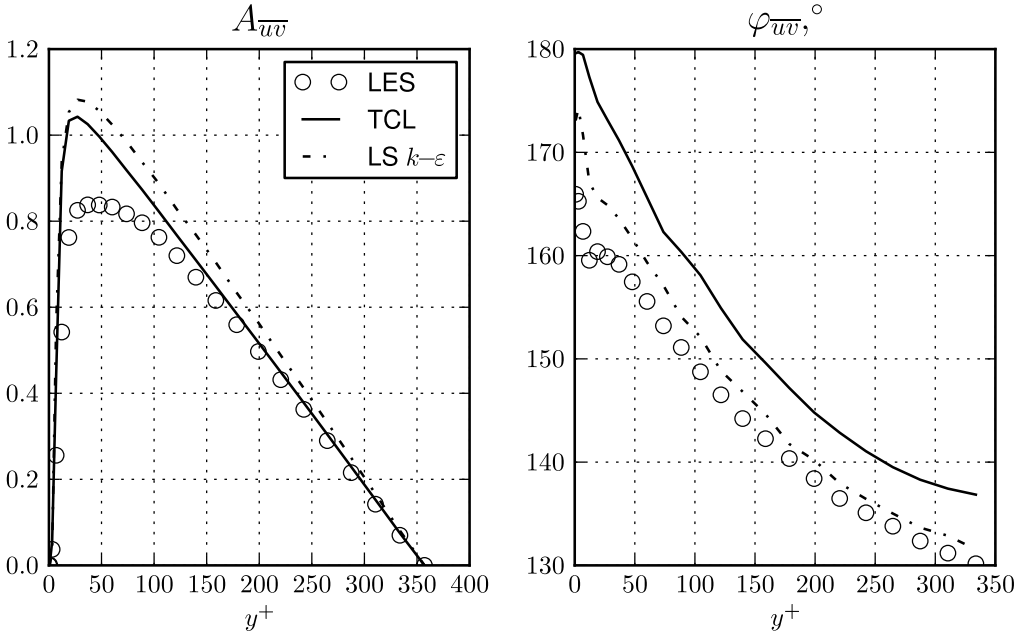

Figure 5.31: Amplitude and phase angle of the fundamental mode of phase-averaged Reynolds shear stress oscillation for the low frequency case $\omega^+ = 0.0016$.

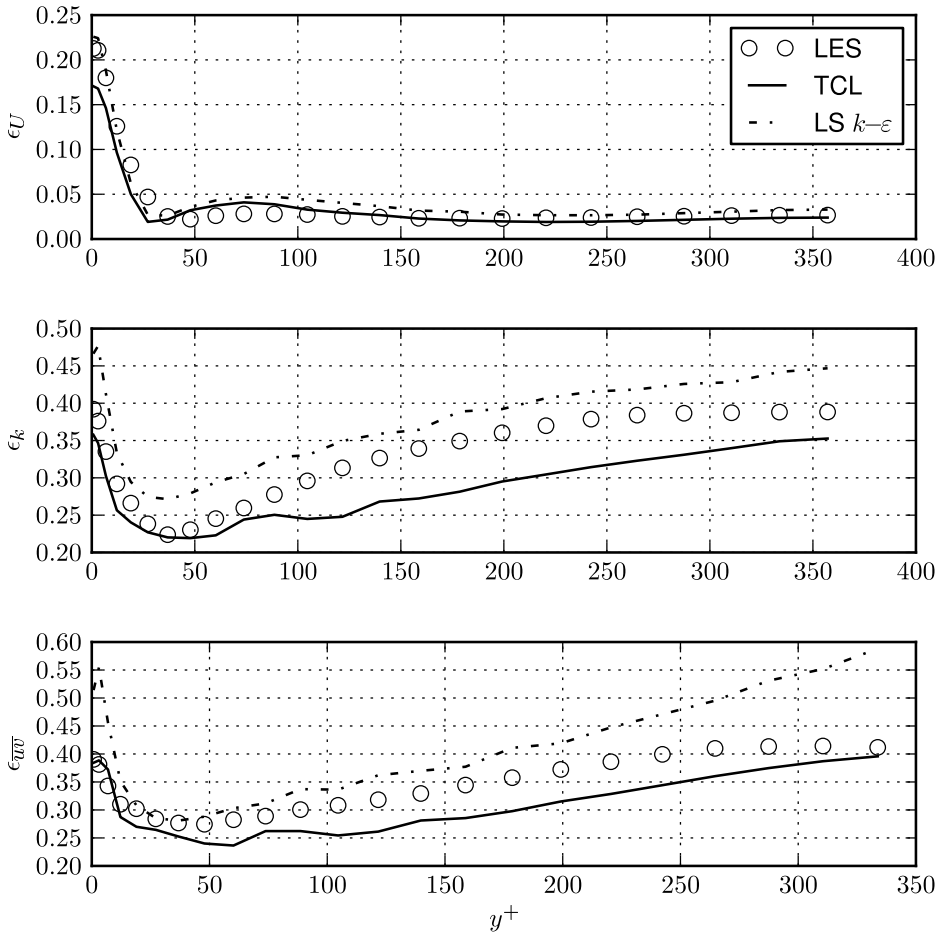

Figure 5.32: Estimated contribution of higher harmonics in the modulation of phase-averaged U^+ (top), $k/\overline{u_\tau}^2$ (middle), and $\overline{uv}/\overline{u_\tau}^2$ for the low frequency case $\omega^+ = 0.0016$.

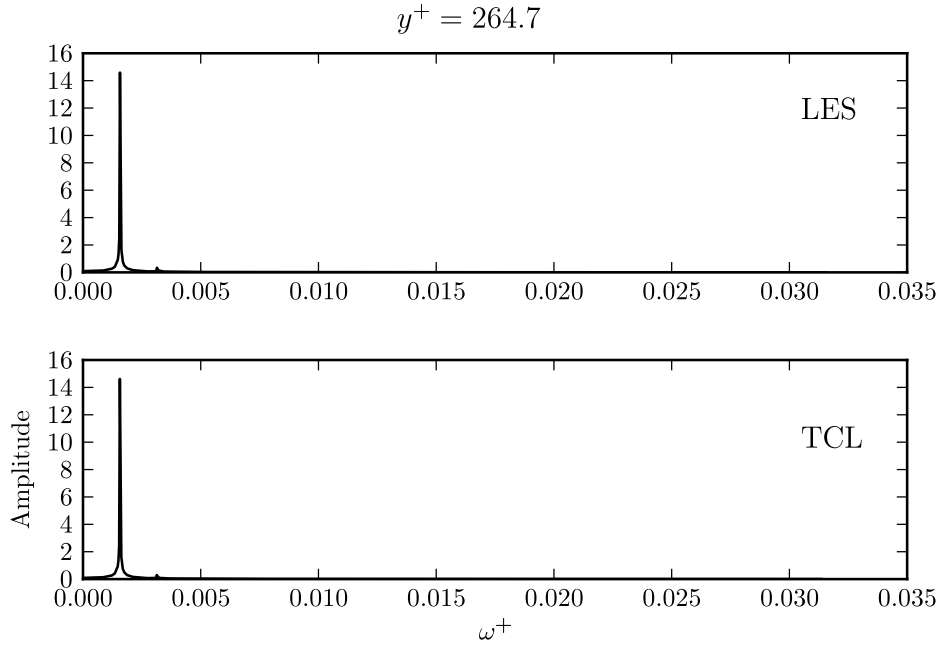

(a) DFT of phase-averaged U^+

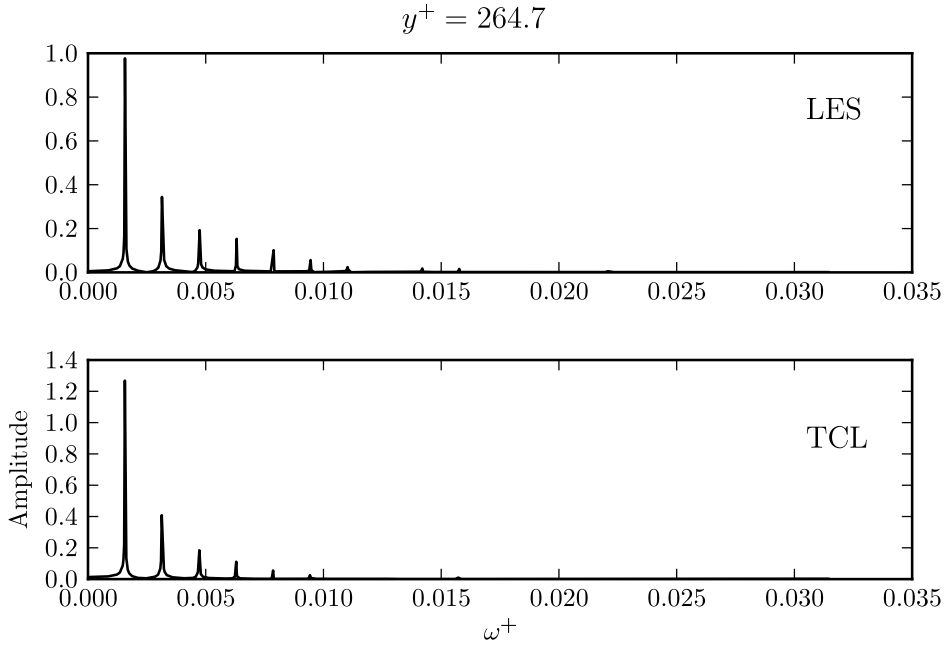

(b) DFT of phase-averaged k^+

Figure 5.33: Discrete Fourier transform of phase-averaged U^+ and k^+ at the location $y^+ = 264.7$ for the low frequency case $\omega^+ = 0.0016$.

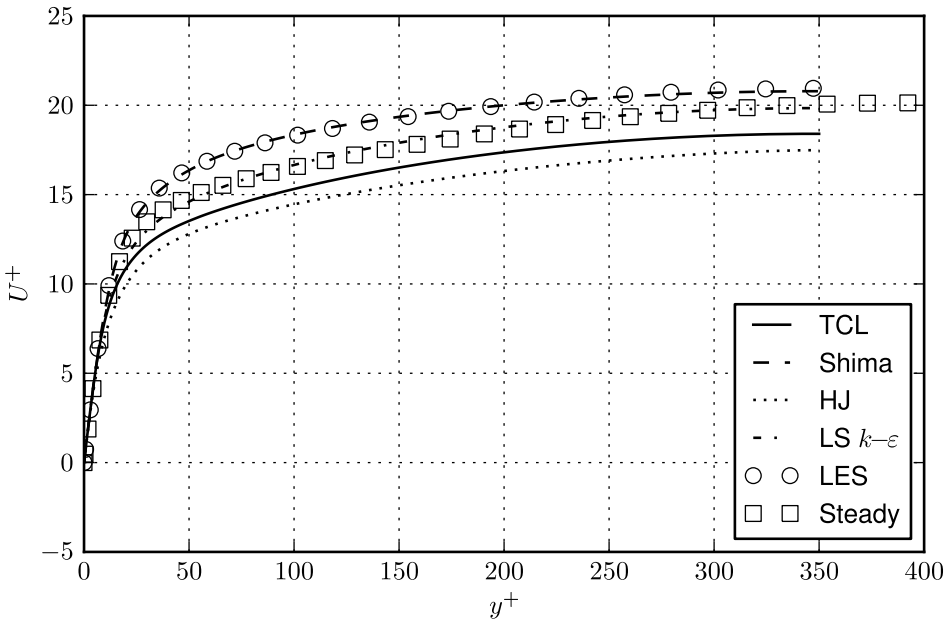

Figure 5.34: Time mean profile of velocity in wall units for the intermediate frequency case $\omega^+ = 0.01$.

5.6 Intermediate frequency

5.6.1 Time-mean behaviour

Time-averaged profiles of the flow variables: U, dU/dy, k, $\overline{u_\alpha u_\alpha}$, $\overline{uv}$ and P_κ, normalised by wall variables, for the intermediate forcing frequency $\omega^+ = 0.01$ are shown in Figures 5.34-5.39. Considering first the time-averaged velocity profile, shown in Figure 5.34, it is noted that at this frequency, in contrast to the previous lower frequency, the time-mean bulk velocity of the pulsatile flow (LES) is slightly higher (6%) than steady channel flow at a similar Re_τ (DNS). The time-mean profile of the pulsatile flow is most closly matched by the Shima model in this case. The three remaining models all under-estimate the time-averaged bulk velocity, by up to 18.8% in the case of HJ model (See Table 5.3). Similarly, the time-averaged velocity gradient, shown in Figure 5.35, is most closely matched by the Shima model.

In this case, as in the previous lower frequency case, the time-mean turbulent kinetic energy (Figure 5.36) of the pulsatile flow (LES) has a higher near-wall peak than in the steady case. The Shima model similarly has a much higher peak in this case, in agreement with the LES, but it over-predicts the level of turbulence

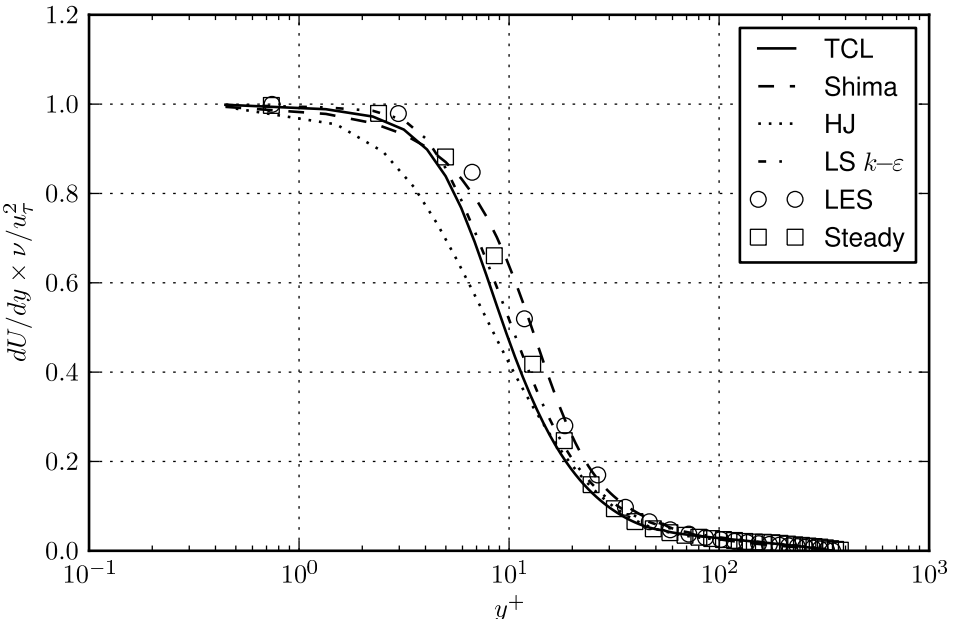

Figure 5.35: Time mean profile of velocity gradient in wall units for the intermediate frequency case $\omega^+ = 0.01$.

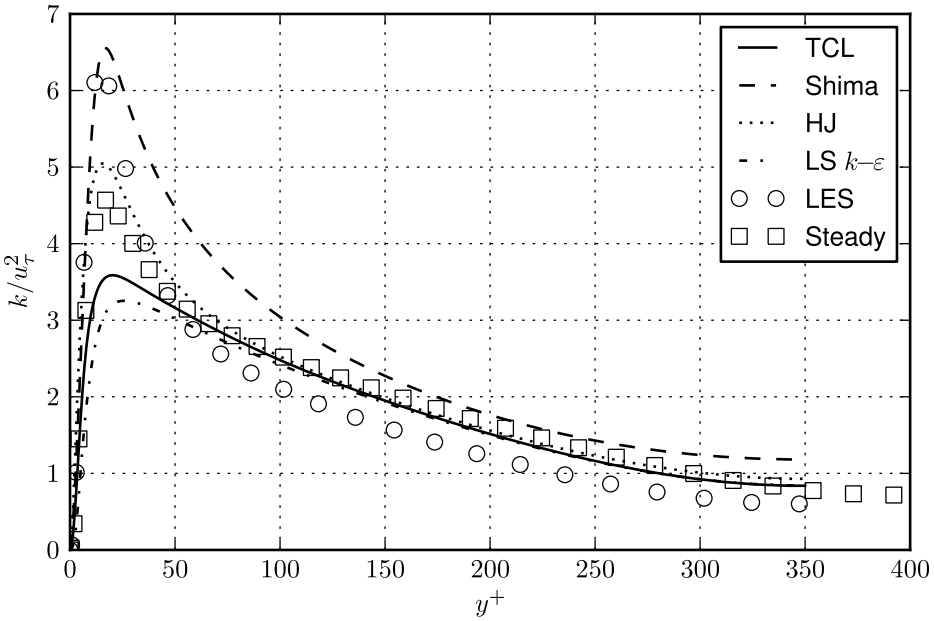

Figure 5.36: Time mean profile of turbulent kinetic energy in wall units for the intermediate frequency case $\omega^+ = 0.01$.

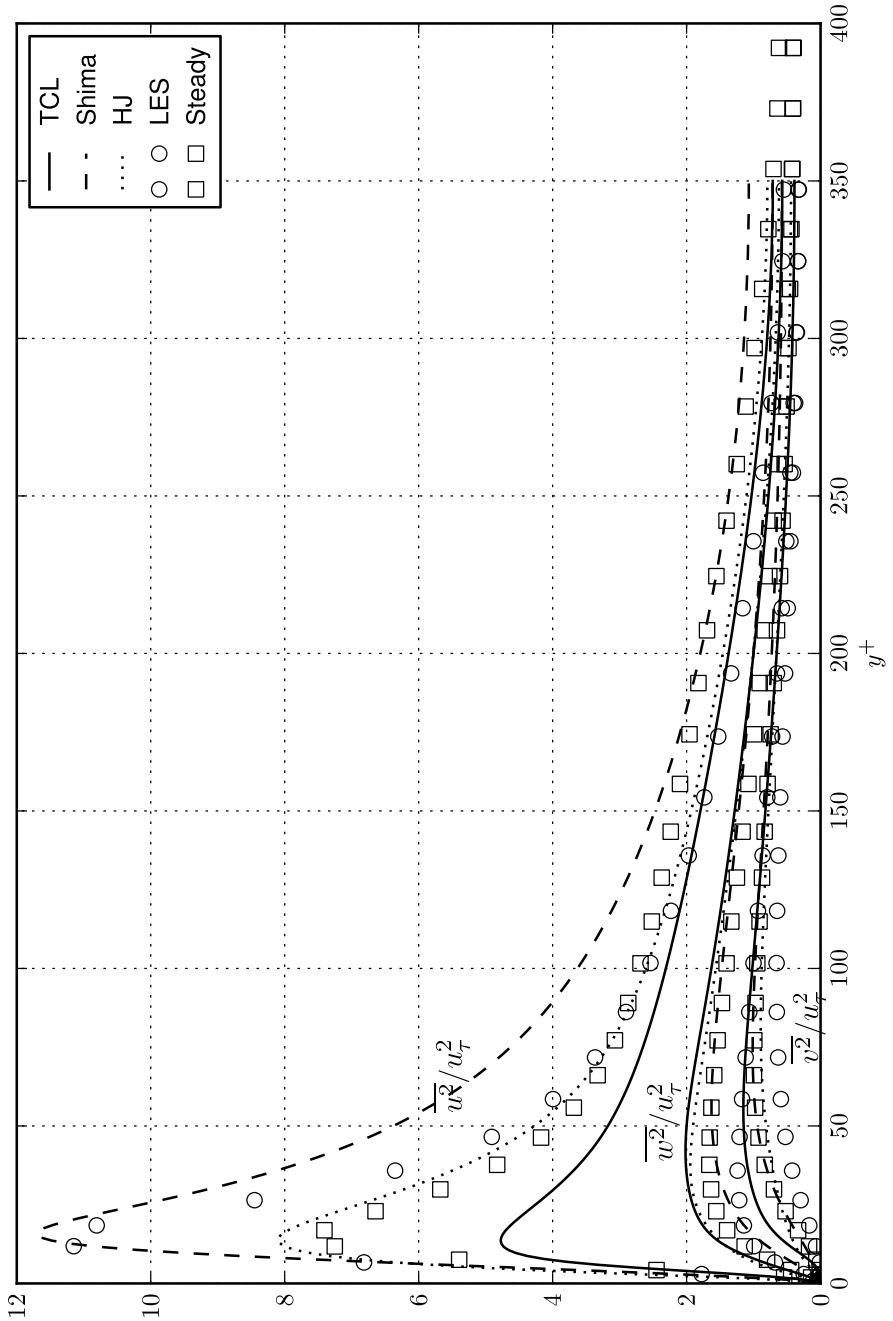

Figure 5.37: Time mean profile of normal Reynolds stresses in wall units for the intermediate frequency case $\omega^+ = 0.01$.

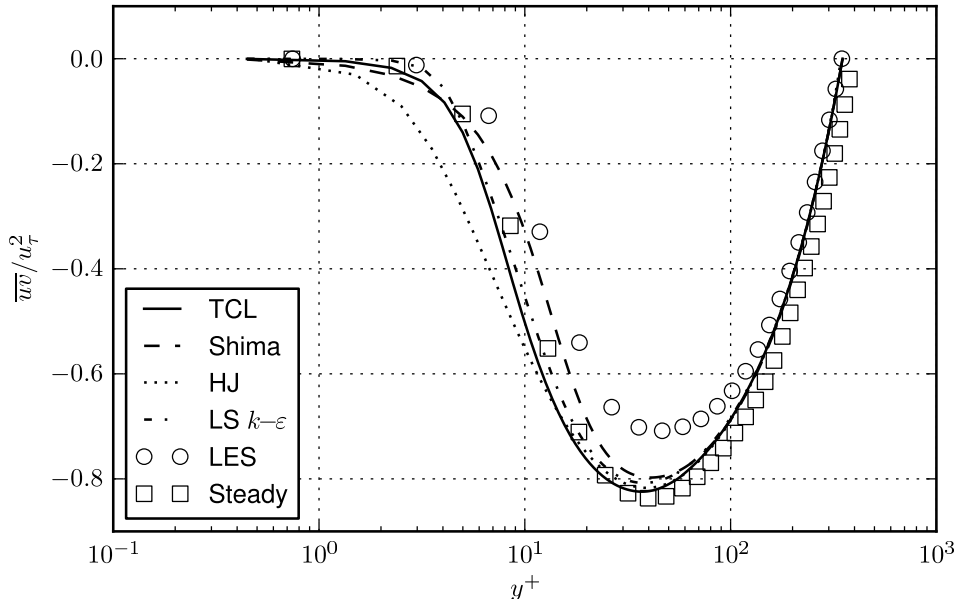

Figure 5.38: Time mean profile of Reynolds shear stress in wall units for the intermediate frequency case $\omega^+ = 0.01$.

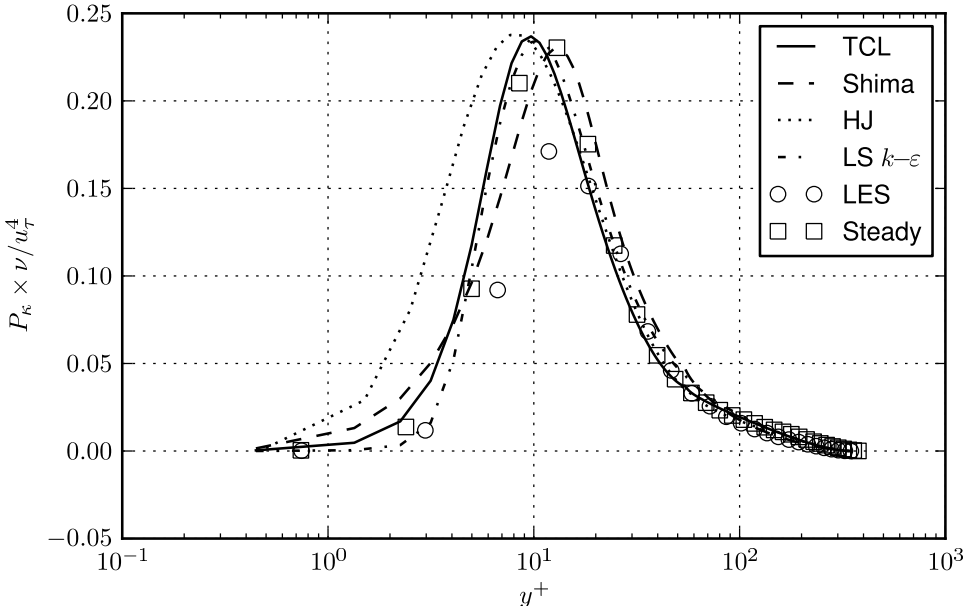

Figure 5.39: Time mean profile of production of turbulent kinetic energy in wall units for the intermediate frequency case $\omega^+ = 0.01$.

for the remainder of the channel cross-section. The HJ model returns a profile that closely follows the steady profile, while the TCL and LS models, once again, under-estimate the peak, then follow the steady profile in the inner region. This pattern is also to some extent reflected in the profiles of the streamwise normal stress, shown in Figure 5.37, where the same observations on the time-averaged k are reflected in the profiles of the time averaged $\overline{u^2}$ of the models. All four models over-predict the magnitude of the time-averaged Reynolds shear stress, shown in Figure 5.38, over a large portion of the channel cross-section, resulting in a higher peak in energy production, as seen in Figure 5.39.

5.6.2 Phase-averaged behaviour

Profiles of phase-averaged velocity, turbulent kinetic energy, and Reynolds shear stress for the case $\omega^+ = 0.01$ over a period are shown in Figures 5.40, 5.41 and 5.42 respectively. Time series of the cyclic variation of these variables, in addition to the phase-averaged velocity gradient, at four locations $y^+ = 0.7$, 18.4, 71.8 and 257.4 are shown in Figures 5.43-5.46. Bearing in mind the varying scale of the axes in Figure 5.40, it can be said that the models are generally able to reasonably mimic the phase-averaged profiles of U^+. Flow separation in the near-wall region is observed at this frequency around mid-cycle (more visible in Figure 5.43). The extent of the region experiencing flow separation is over-estimated by the models–slightly so by the Shima and LS models, but more significantly by the TCL and HJ models. Figure 5.43 makes it clear that the TCL model, as in the lower frequency case, suffers from an abrupt jump at the end of the laminarisation portion of the cycle as the flow re-transitions to turbulence. As discussed previously, this is most likely attributed to the $\mathrm{Re_t}$-dependencies in the model coefficients.

Examining the phase-averaged kinetic energy profiles in Figure 5.41, it is seen that in the near-wall region k is at its lowest at the end of the cycle and gradually increases until it reaches its peak at around $\frac{3T}{8}$ and gradually decreases afterwards. Most of the modulation in k is confined to the region $y^+ < 150$. The models are all in advance of the reference data, all having their highest near-wall peak within the first quarter cycle.

Regarding the phase-averaged $\overline{uv}$, shown in 5.42, there is considerable variation among the models in the region $y^+ < 150$, particularly in the portion of the cycle wher $\overline{uv}$ is increasing in magnitude (roughly $\frac{7T}{8}$ to $\frac{2T}{8}$). The TCL, HJ and

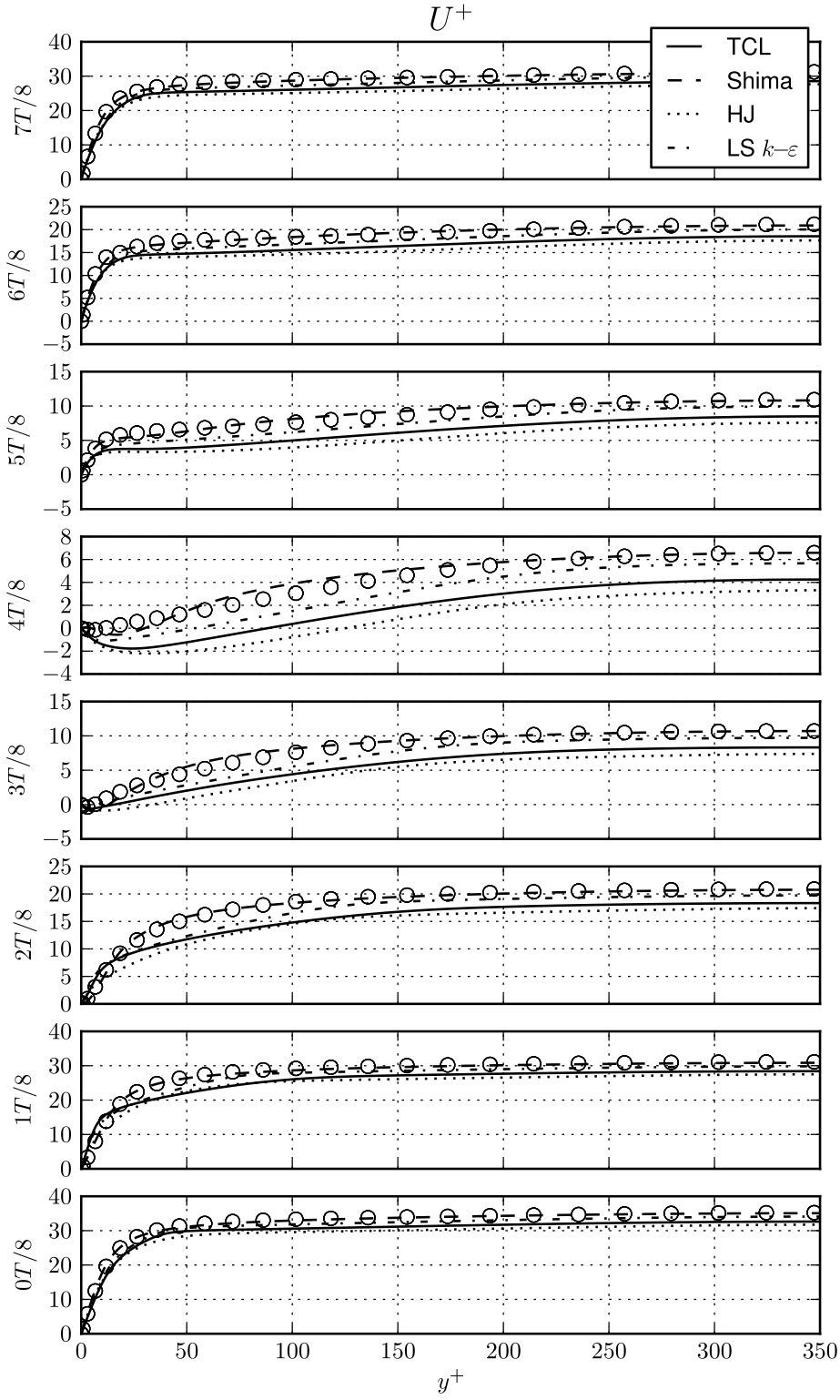

Figure 5.40: Phase-averaged profiles of phase-averaged velocity in wall units for the intermediate frequency case $\omega^+ = 0.01$.

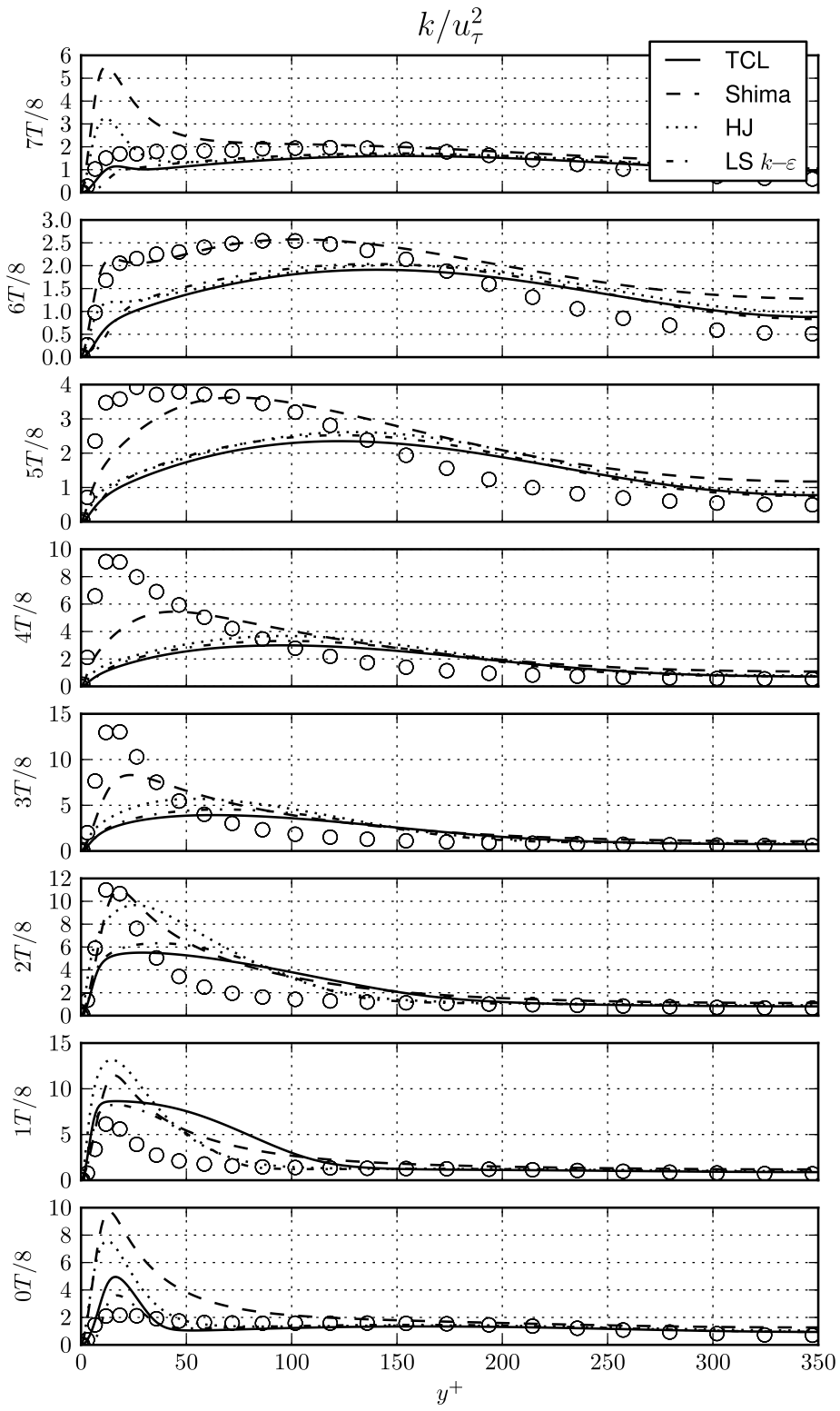

Figure 5.41: Phase-averaged profiles of phase-averaged turbulent kinetic energy in wall units for the intermediate frequency case $\omega^+ = 0.01$.

LS models tend to over-estimate phase-averaged $\overline{uv}$ within the first quarter of the cycle, but are in better agreement with the reference data afterwards. The Shima model tends to over-estimate $\overline{uv}$ during the second half of the cycle. Agreement between the models and the reference data, and among the models themselves, is improved in the outer region of the flow $y^+ > 150$, as can be seen in Figure 5.46.

Modulation of the phase-averaged wall shear stress is shown in Figure 5.47. The Shima model is in good agreement with the reference data in this case. The HJ and LS models slightly under-estimate the amplitude of the modulation, and are somewhat out of phase with the reference data. The TCL model's wall shear stress modulation is adversely affected by the kink at the start of the re-transition portion of the cycle.

5.6.3 Harmonics

The fundamental mode of modulation of the phase-averaged U^+, k^+ and $\overline{uv}^+$ was calculated using the least-squares technique described in Section 5.5.3. The estimated contribution of higher harmonics in this case is plotted in Figure 5.48. As might be expected from the previous time series plots in Figures 5.43-5.46, it is found that the fundamental modes of k^+ and $\overline{uv}^+$ are inadequate for describing the TCL model results in the approximate region $y^+ < 100$. This is due to the sharp rise followed by a slow and gradual decrease in this model's results. The Shima and, to a slightly lesser extent, the HJ results, are closer to pure sinusoids.

The amplitude and phase angle of the fundamental mode of U^+ are shown in Figure 5.49, where it is seen that the models successfully reproduce the amplitude of U^+ modulation, as well as the phase angle over most of the profile. The shape of the A_U profile at this frequency has changed from that at the lower frequency case, with the amplitude becoming essentially constant over $y^+ > 200$. The amplitude of the k^+ fundamental predicted by the models, shown in Figure 5.50, is in fair agreement with that of the reference data, particularly in the outer region of the flow profile. There is however roughly a 70° phase advance between the models (higher for TCL) and the reference data modulation. Finally, the amplitude of $\overline{uv}$, shown in Figure 5.51, is over-estimated by the TCL, HJ and LS models over the approximate region $10 < y^+ < 150$, and is under-predicted by the Shima model over the whole flow cross-section.

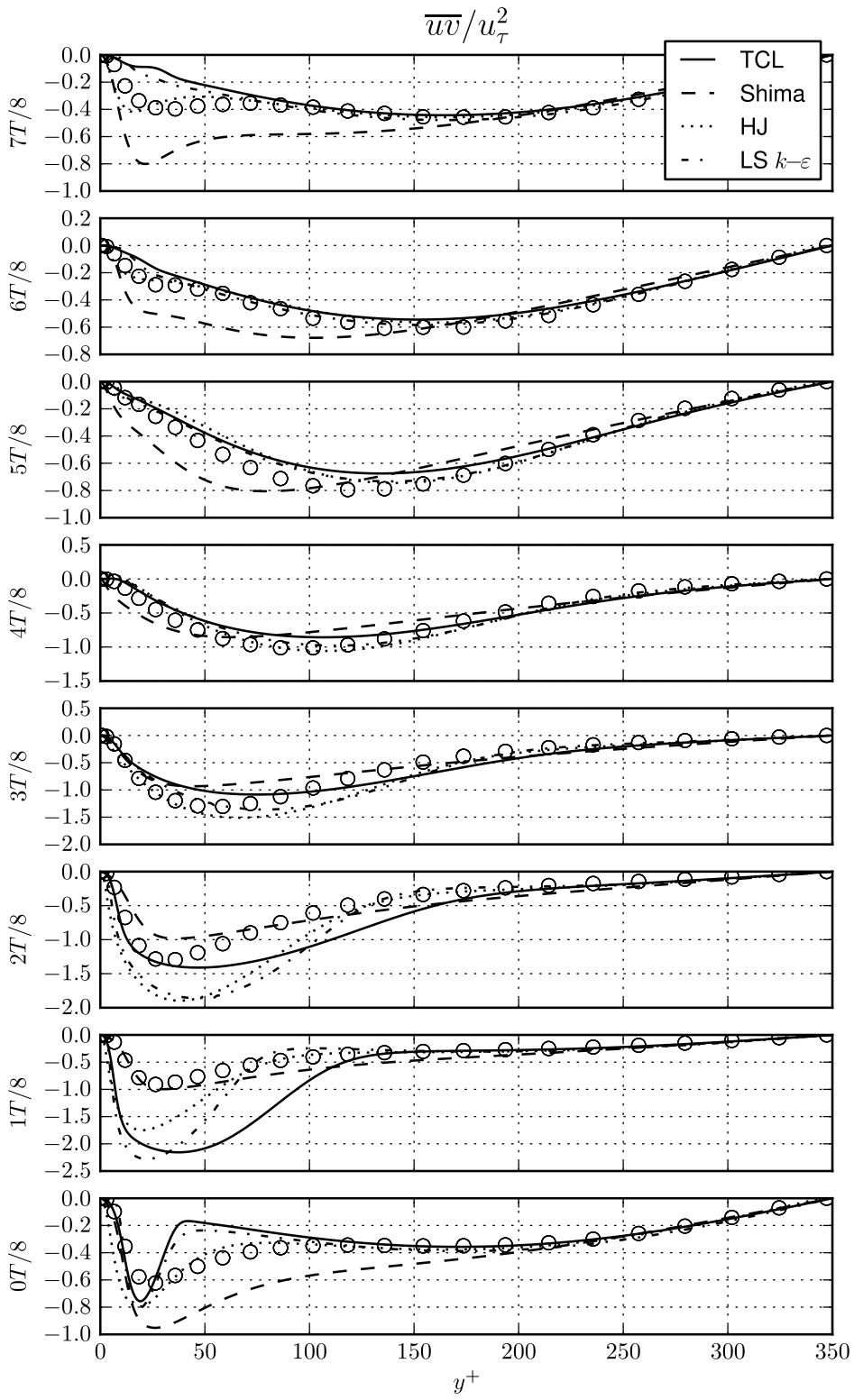

Figure 5.42: Phase-averaged profiles of phase-averaged Reynolds shear stress $\overline{uv}$ energy in wall units for the intermediate frequency case $\omega^+ = 0.01$.

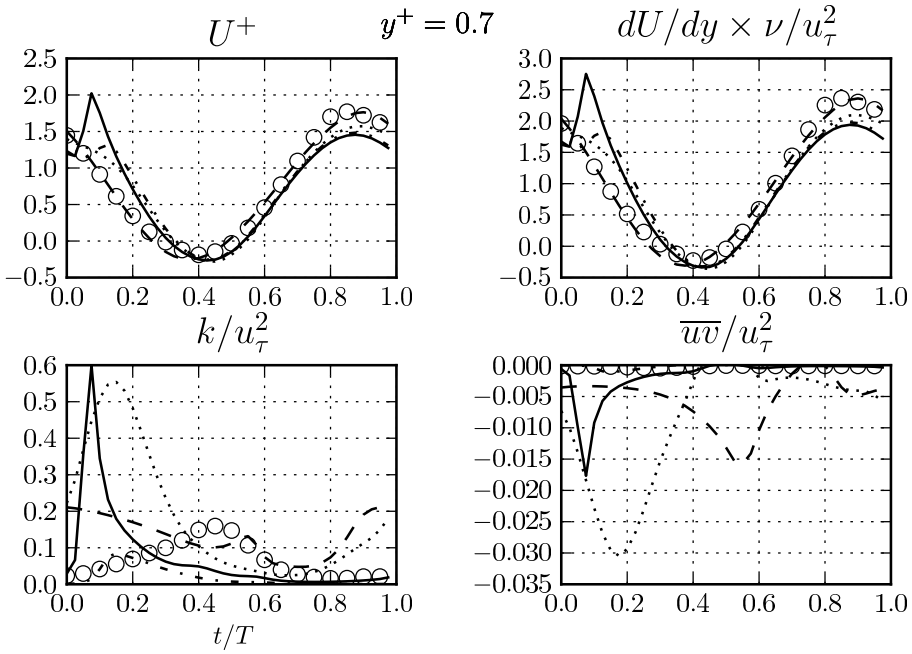

Figure 5.43: Cyclic variation of various phase-averaged flow quantities in wall units for the intermediate frequency case $\omega^+ = 0.01$ at the location $y^+ = 0.7$.

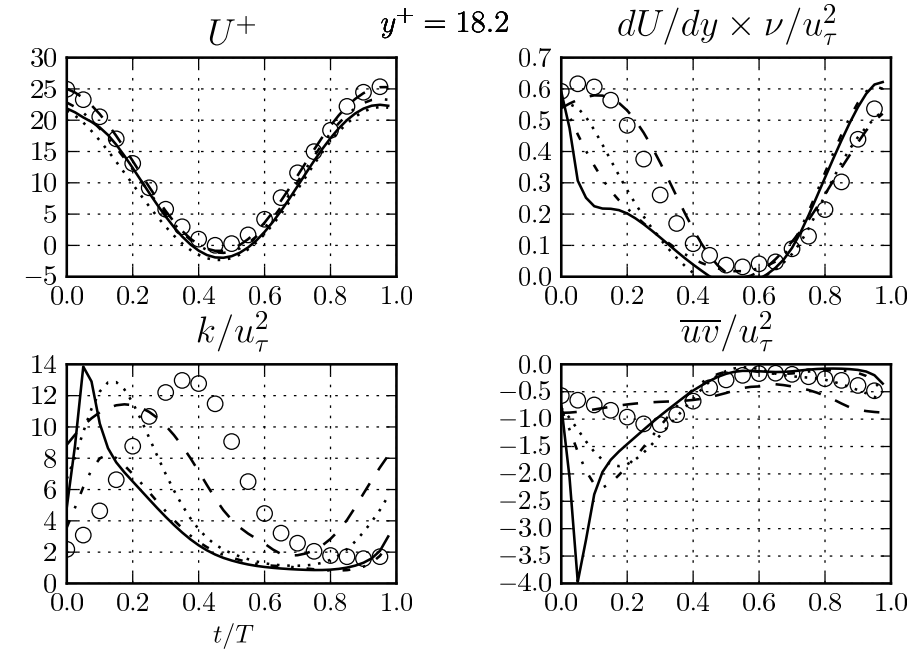

Figure 5.44: Cyclic variation of various phase-averaged flow quantities in wall units for the intermediate frequency case $\omega^+ = 0.01$ at the location $y^+ = 18.4$.

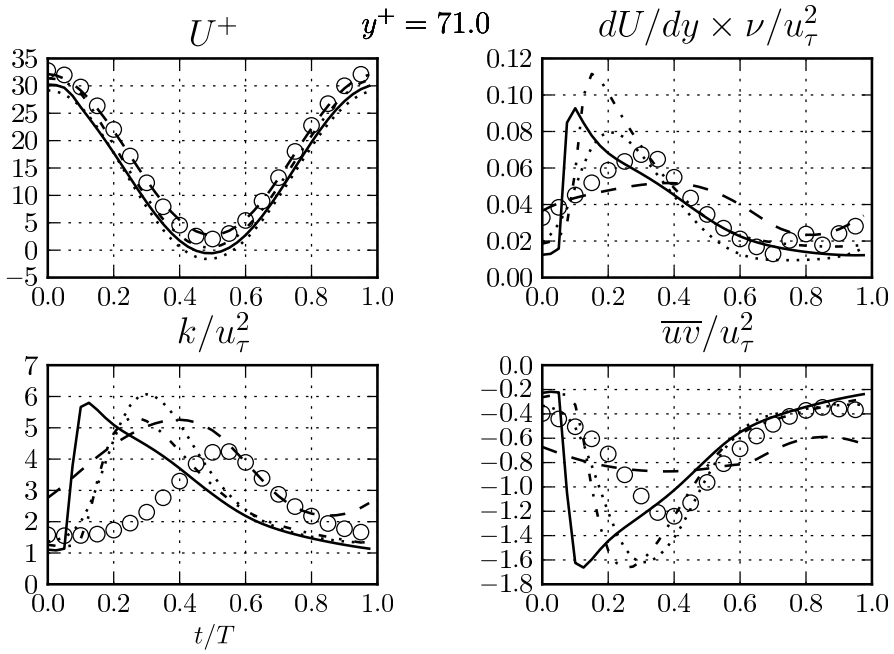

Figure 5.45: Cyclic variation of various phase-averaged flow quantities in wall units for the intermediate frequency case $\omega^+ = 0.01$ at the location $y^+ = 71.8$.

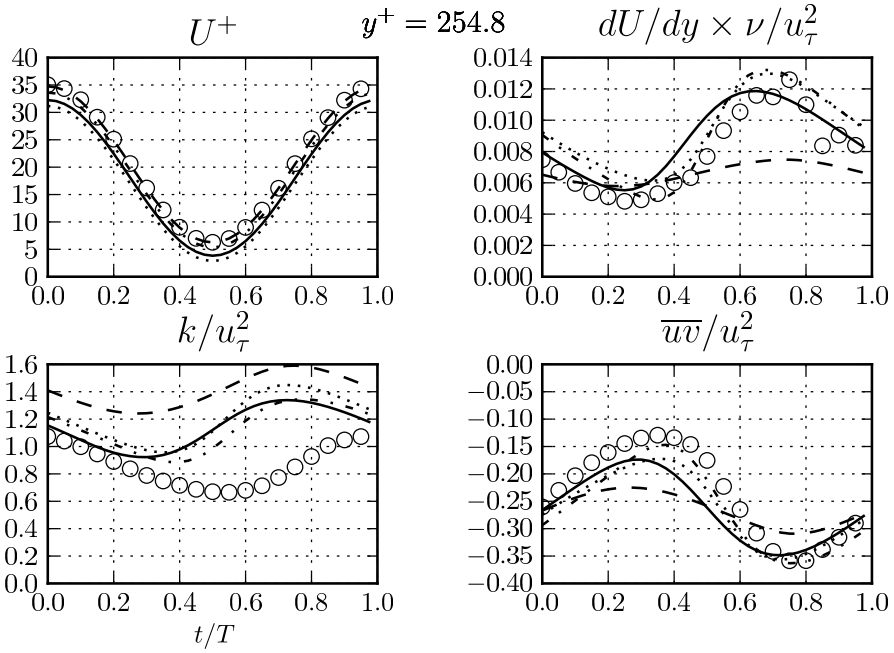

Figure 5.46: Cyclic variation of various phase-averaged flow quantities in wall units for the intermediate frequency case $\omega^+ = 0.01$ at the location $y^+ = 257.4$.

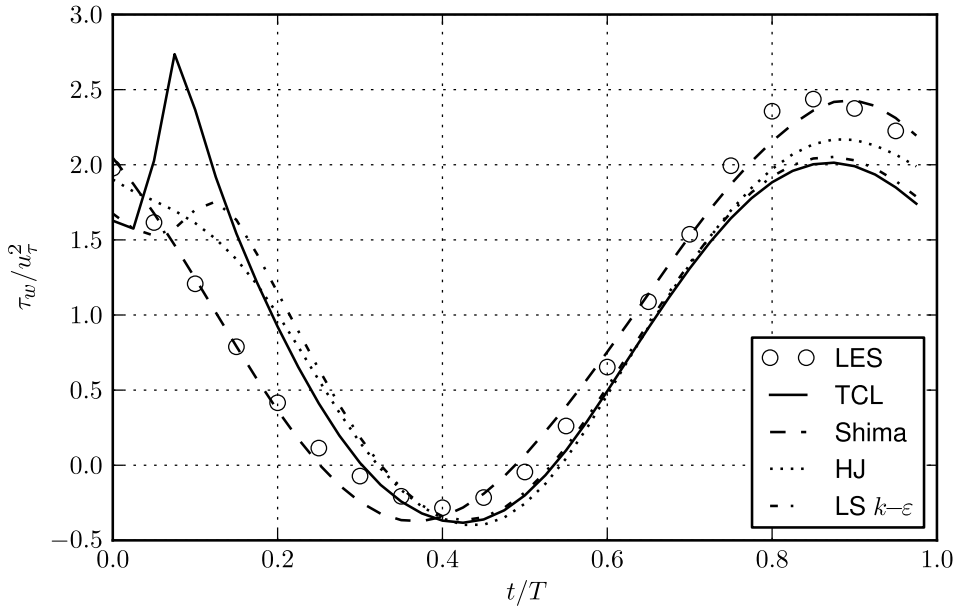

Figure 5.47: Modulation of phase-averaged wall shear stress in wall units for the intermediate frequency case $\omega^+ = 0.01$.

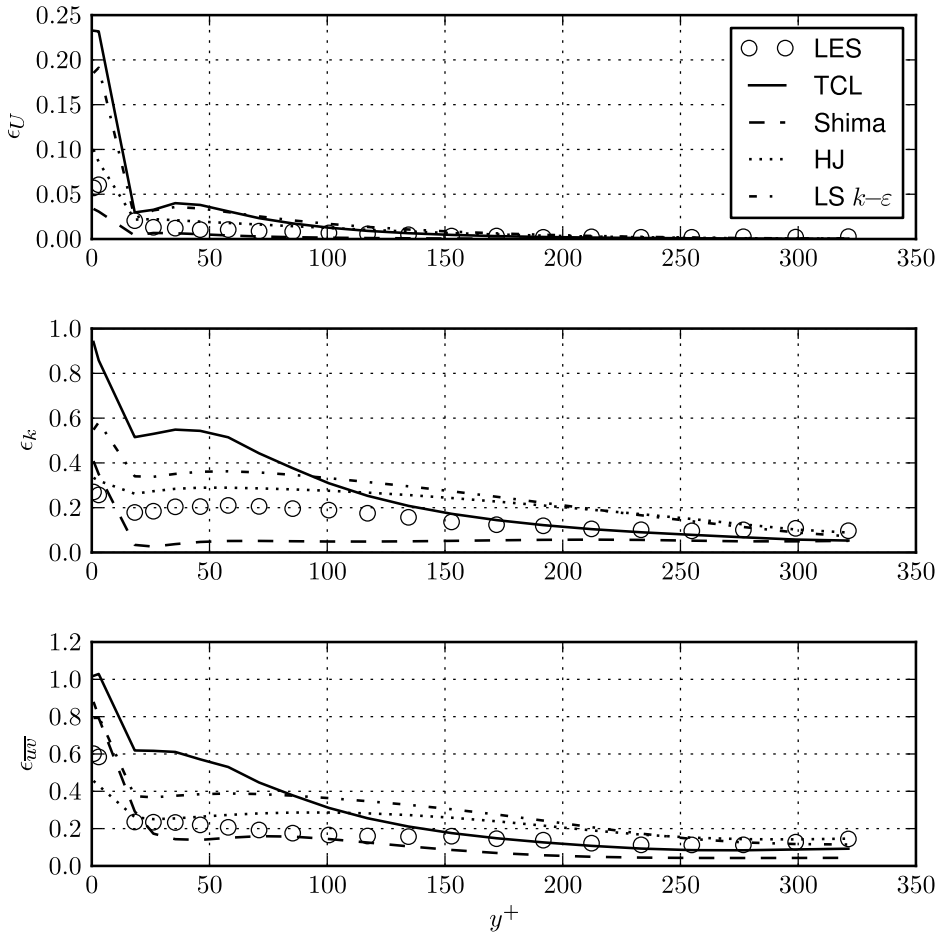

Figure 5.48: Estimated contribution of higher harmonics in the modulation of phase-averaged U^+ (top), $k/\overline{u_\tau}^2$ (middle), and $\overline{uv}/\overline{u_\tau}^2$ for the intermediate frequency case $\omega^+ = 0.01$.

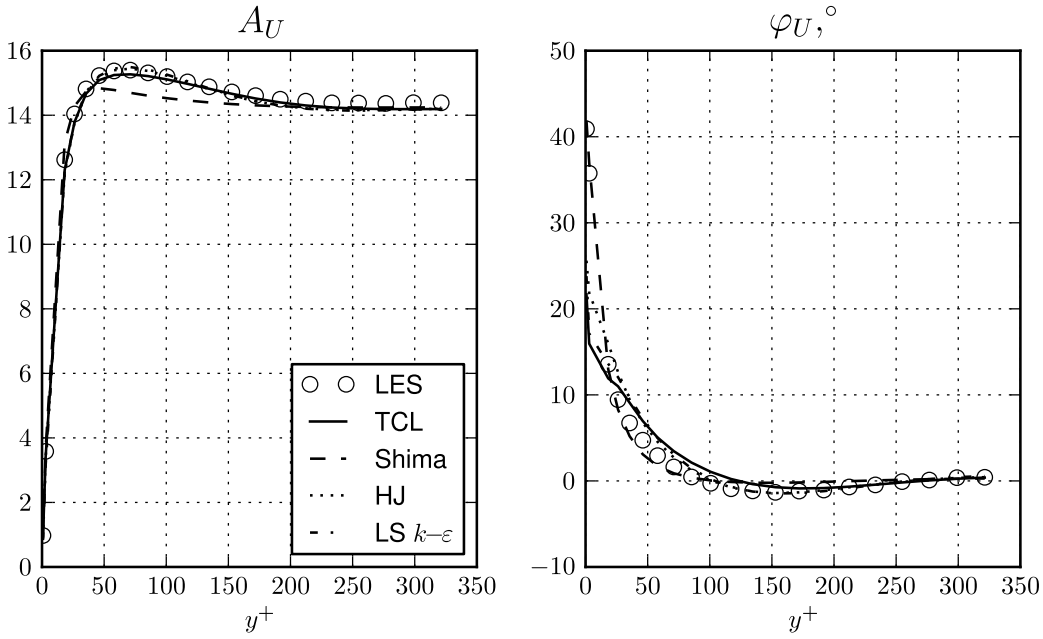

Figure 5.49: Amplitude and phase angle of the fundamental mode of phase-averaged velocity oscillation for the intermediate frequency case $\omega^+ = 0.01$.

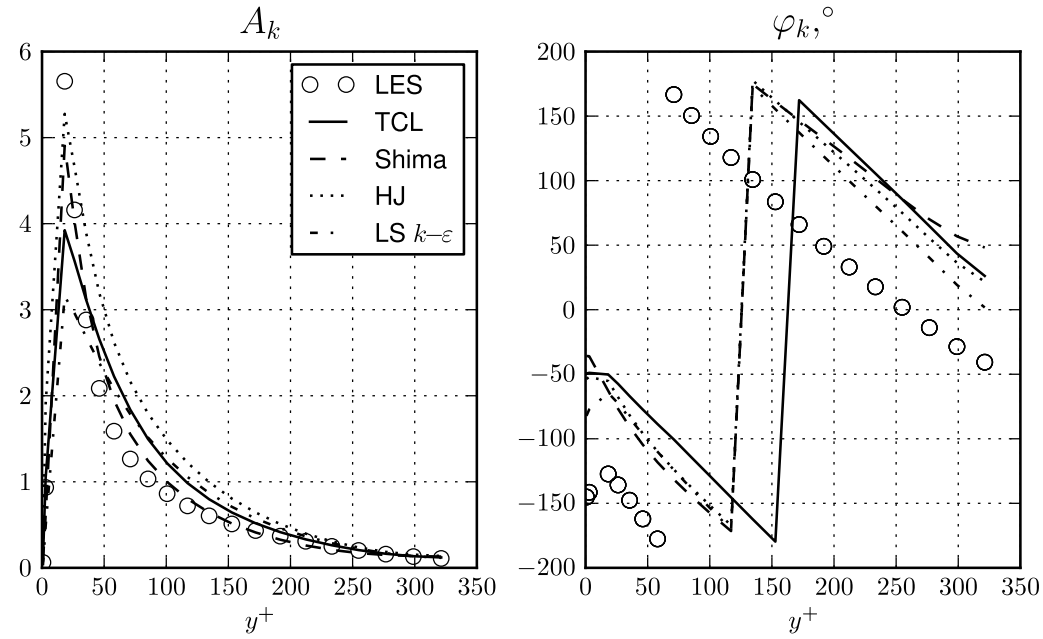

Figure 5.50: Amplitude and phase angle of the fundamental mode of phase-averaged turbulent kinetic energy oscillation for the intermediate frequency case $\omega^+ = 0.01$.

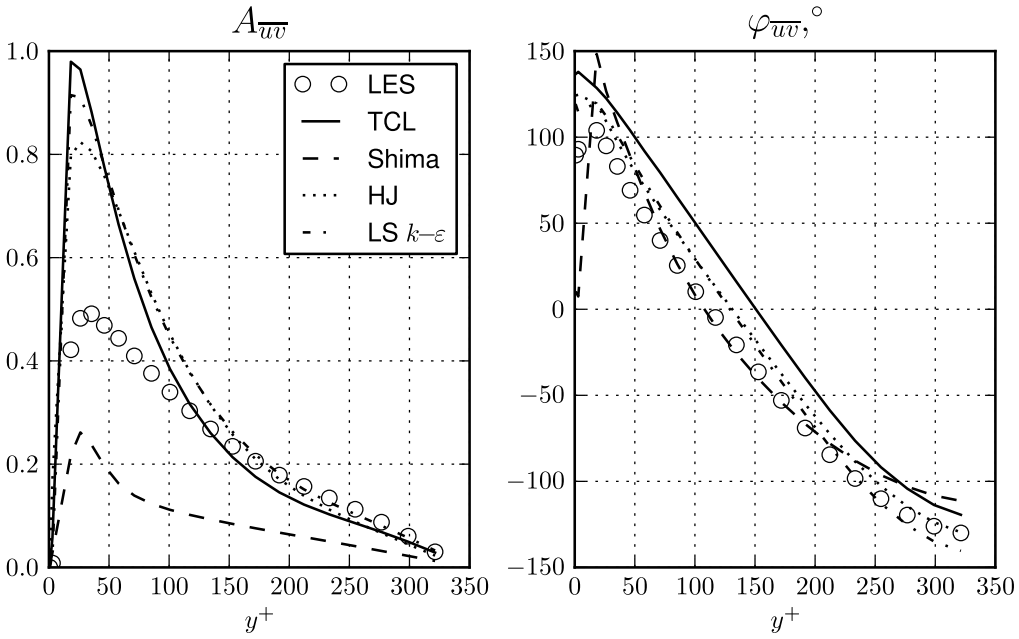

Figure 5.51: Amplitude and phase angle of the fundamental mode of phase-averaged Reynolds shear stress oscillation for the intermediate frequency case $\omega^+ = 0.01$.

5.7 High frequency

5.7.1 Time-mean behaviour

Time-averaged results for the highest frequency case $\omega^+ = 0.04$ are presented in Figures 5.52-5.57. At this frequency, the TCL model gives the closest agreement with thereference data for the time-averaged velocity and velocity gradient profiles, shown in Figures 5.52 and 5.53, respectively. The LS model overpredicts the time-averaged bulk velocity by about 7% and the remaining two models under-estimate it by about 13% (Table 5.3). At this frequency, as in the previous intemediate frequency, the time-averaged bulk velocity of the pulsatile flow is higher than the bulk velocity of the steady flow DNS.

The turbulent kinetic energy profiles returned by the models, shown in Figure 5.54, are similar to their steady channel flow profiles (Figure 5.5). The exception being the Shima model which returns a slightly higher level of turbulence than its steady solution, and in this respect it seems to be the most sensitive to the imposed frequency.

The time-mean profiles of the normal Reynolds stresses is shown in Figure 5.55. As mentioned previously, the tendency for the energy in the time-mean LES to be intensified in the streamwise fluctuations, $\overline{u^2}$, and drawn away from the fluctuations in the other directions, $\overline{w^2}, \overline{v^2}$, compared to the steady channel reference case is a questionable feature of data, and is most likely a result of under-resolved small scales.

When comparing time-mean profiles returned at various frequencies (Figures 5.12, 5.37 and 5.55), it is evident that the normal stresses returned by the Shima model, and to a lesser extent the HJ model, are more sensitive to the imposed frequency than the TCL model. The insensitivity in this case is perhaps a desirable feature, since the corresponding LES data do not show significant variation with frequency.

The time-averaged Reynolds shear stress is shown in Figure 5.56. While it still over-predicted in magnitude, as was observed at lower frequencies, this is true over a significantly smaller portion of the channel profile in the case of the TCL and LS models. This is also reflected in the profiles of P_κ shown in Figure 5.57.

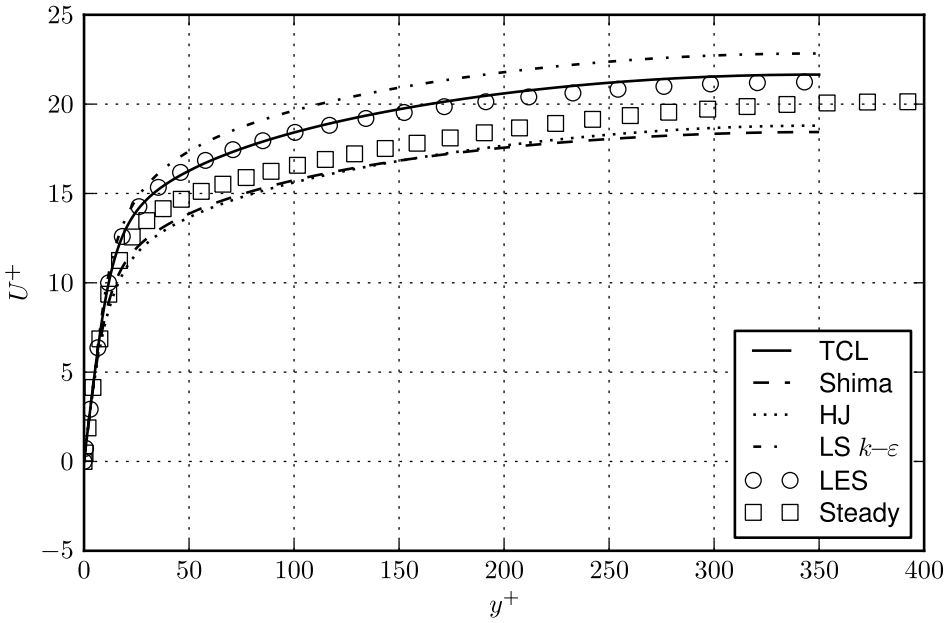

Figure 5.52: Time mean profile of velocity in wall units for the high frequency case $\omega^+ = 0.04$.

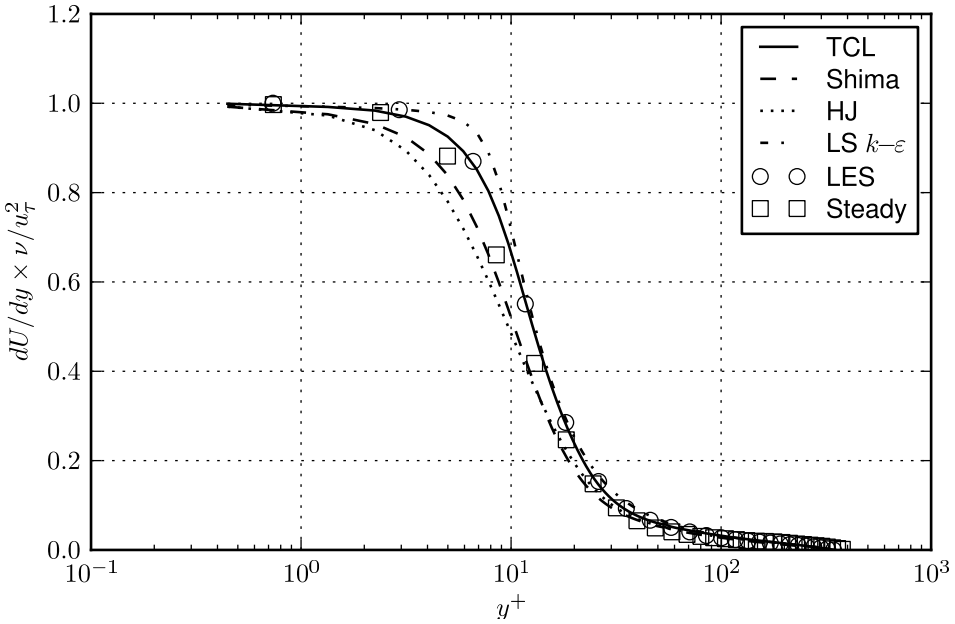

Figure 5.53: Time mean profile of velocity gradient in wall units for the high frequency case $\omega^+ = 0.04$.

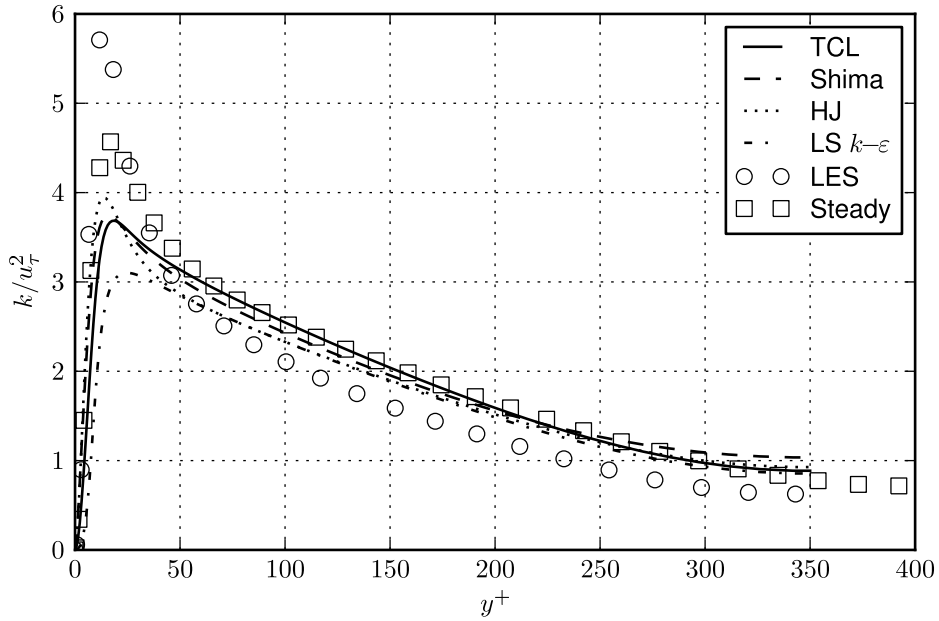

Figure 5.54: Time mean profile of turbulent kinetic energy in wall units for the high frequency case $\omega^+ = 0.04$.

5.7.2 Phase-averaged behaviour

Profiles of phase-averaged velocity, turublent kinetic energy and Reynolds shear stress over a full cycle are shown at $\frac{T}{8}$ intervals in Figures 5.58, 5.59 and 5.60, respectivly, while Figures 5.61, 5.62 and 5.63 show the time-series of these variables, in addition to the phase-averaged velocity gradient, at the fixed locations, y^+ =18.2, 70.9 and 254.3, respectively. It is evident in Figure 5.58 that the models, particularly the LS and TCL models, more closely reproduce the phase-averaged velocity profiles in this case than in the lower frquency cases. There is a significant degree of flow reversal towards the end of the deceleration portion of the cycle. The phase position at which this occurs and the extent of the region affected is very well reproduced by the LS and TCL models. The Shima and HJ models produce almost indistinguishable velocity profiles that are slightly under-estimated throughout the cycle.

Comparing the cyclic profiles of phase-averaged k in Figure 5.59, with corresponding ones at the two lower frequencies (Figures 5.16, 5.41), it can be seen that the level of turbulence and the shape of the profiles varies less throughout the cycle in the present high-frequency case. Correspondingly, there is generally

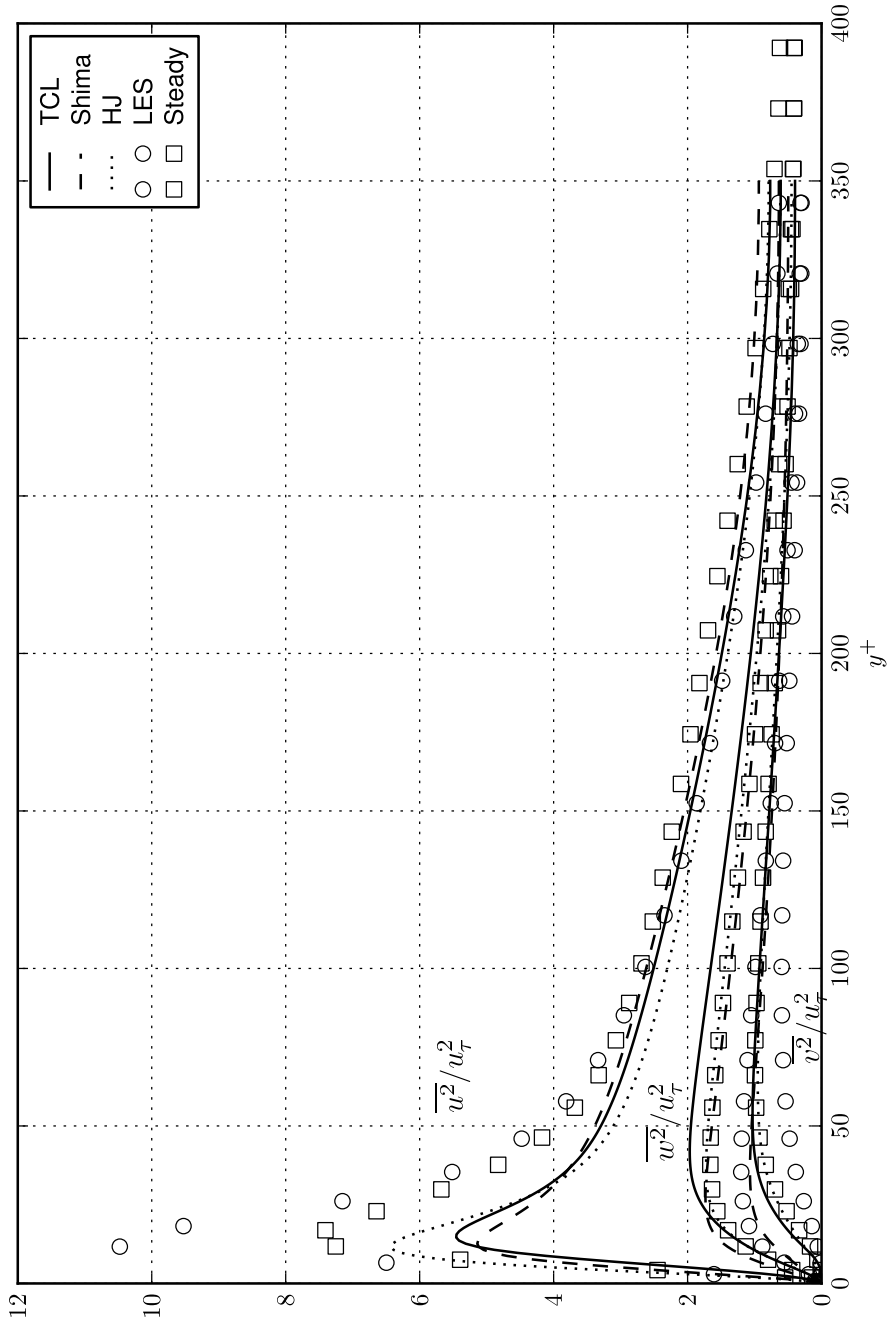

Figure 5.55: Time mean profile of normal Reynolds stresses in wall units for the high frequency case $\omega^+ = 0.04$.

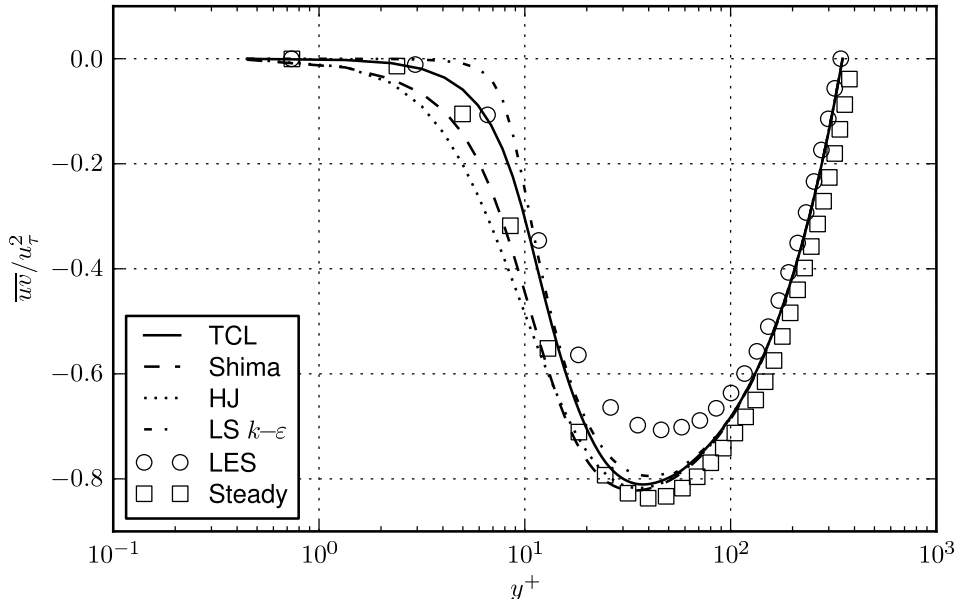

Figure 5.56: Time mean profile of Reynolds shear stress in wall units for the high frequency case $\omega^+ = 0.04$.

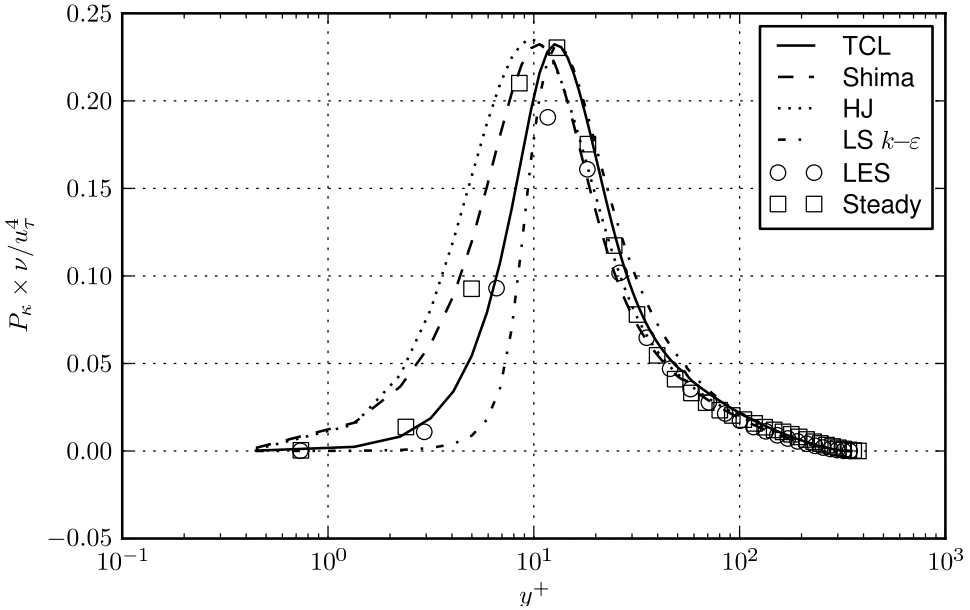

Figure 5.57: Time mean profile of production of turbulent kinetic energy in wall units for the high frequency case $\omega^+ = 0.04$.

better agreement between the models and the reference data in this case. However, the near-wall peak in the k profile remains to be the most difficult feature for the models to reproduce. Similar comments can be made regarding the phase-averaged Reynolds shear stress, shown in Figure 5.60, where it is seen that there is good agreement between the models and the reference data over a large portion of the cross-section.

There is also excellent agreement between the models and the reference data for the modulation of wall shear stress at this frequency, as shown in Figure 5.64.

5.7.3 Harmonics

The estimated contributions of higher harmonics in the modulation of the phase-averaged variables U^+, k^+ and $\overline{uv}$ are presented in Figure 5.65. Velocity modulation in this case is closer to a pure sinusoid, over a larger portion of the channel, than in the lower frequency cases. The scatter and relatively high values of ϵ_k and $\epsilon_{\overline{uv}}$ of the reference data in the outer part of the profile are a result of the small amplitudes in this region, which means that the randomness in the data becomes more significant. Consider, for example, the time-series in Figure 5.63.

The velocity modulation predicted by the models is in excellent agreement with the reference data, as seen in Figure 5.66. At this frequency, the velocity over most of the flow cross-section ($y^+ > 50$) oscillates in phase with the applied pressure gradient with a uniform amplitude. There is a small increase in amplitude as one approaches the wall, followed by a sharp decease dictated by the no-slip condition, and there is about 43° phase-shift between the velocity modulation adjacent to the wall and that in the core region.

The amplitude and phase angle of the fundamental mode of k^+ is shown in Figure 5.67. Because of the small amplitudes involved, phase angle data beyond $y^+ = 150$ is unreliable and is therefore not shown in the figure (and in Figure 5.68). Both the amplitude and phase angle are most closely reproduced by the HJ model, which is in very good agreement with the reference data. The Shima and LS models give good predictions for the amplitude in the outer region of the channel, but are out of phase with the reference data. The TCL model tends to over-estimate the amplitude over a significant portion of the cross-section, but is mostly in phase with the data.

As for the amplitude and phase of $\overline{uv}^+$, plotted in Figure 5.68, the TCL

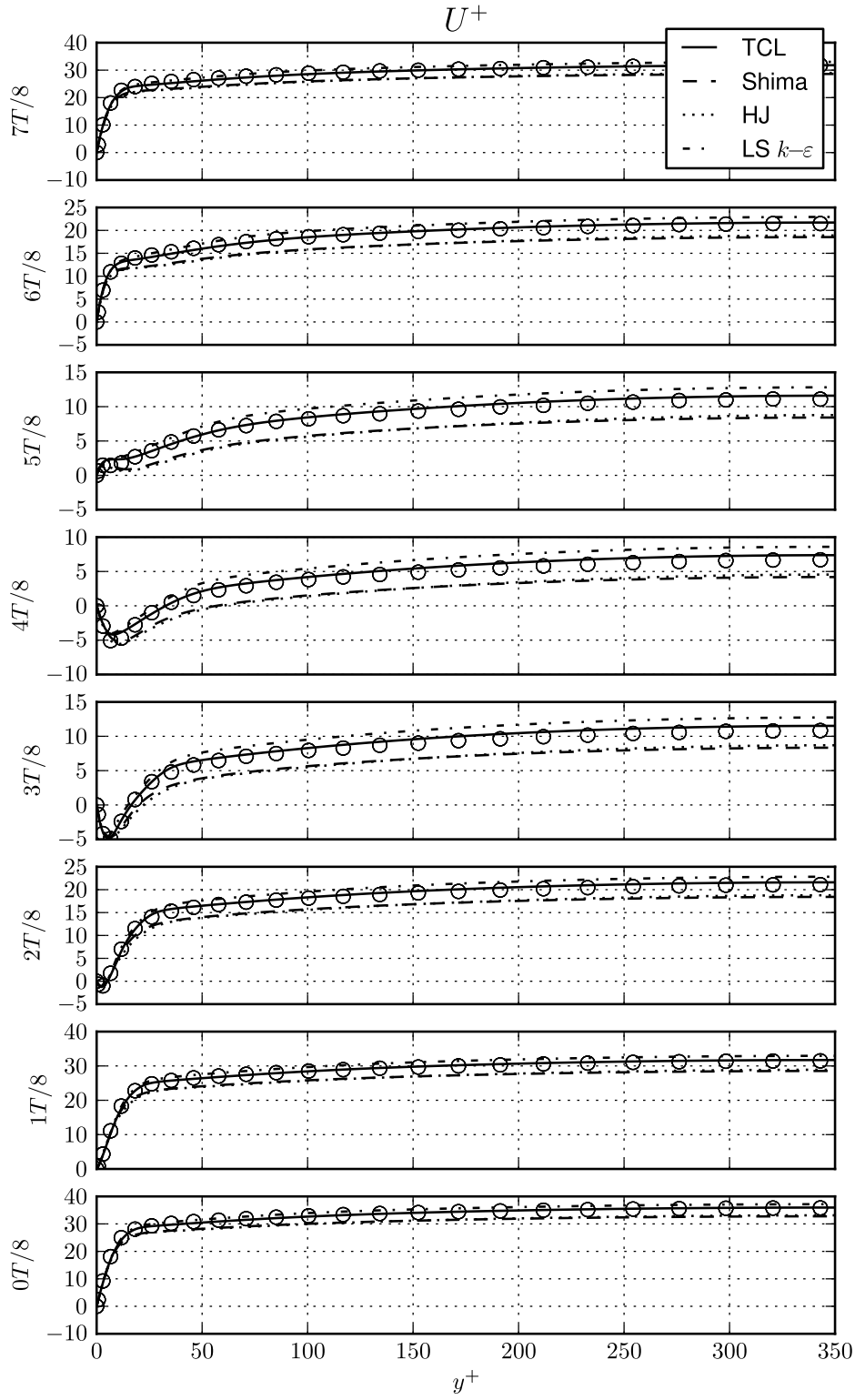

Figure 5.58: Phase-averaged profiles of phase-averaged velocity in wall units for the high frequency case $\omega^+ = 0.04$.

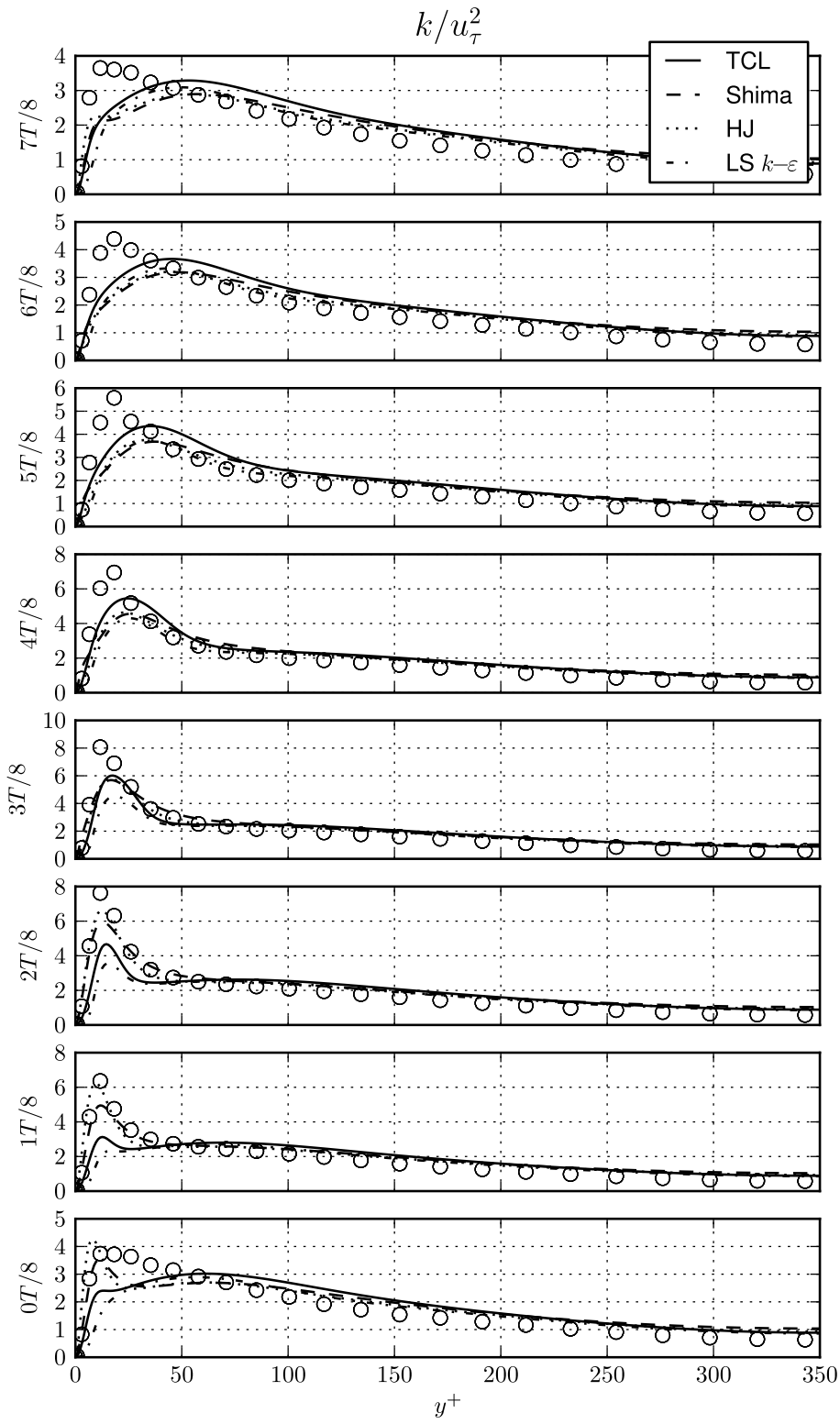

Figure 5.59: Phase-averaged profiles of phase-averaged turbulent kinetic energy in wall units for the high frequency case $\omega^+ = 0.04$.

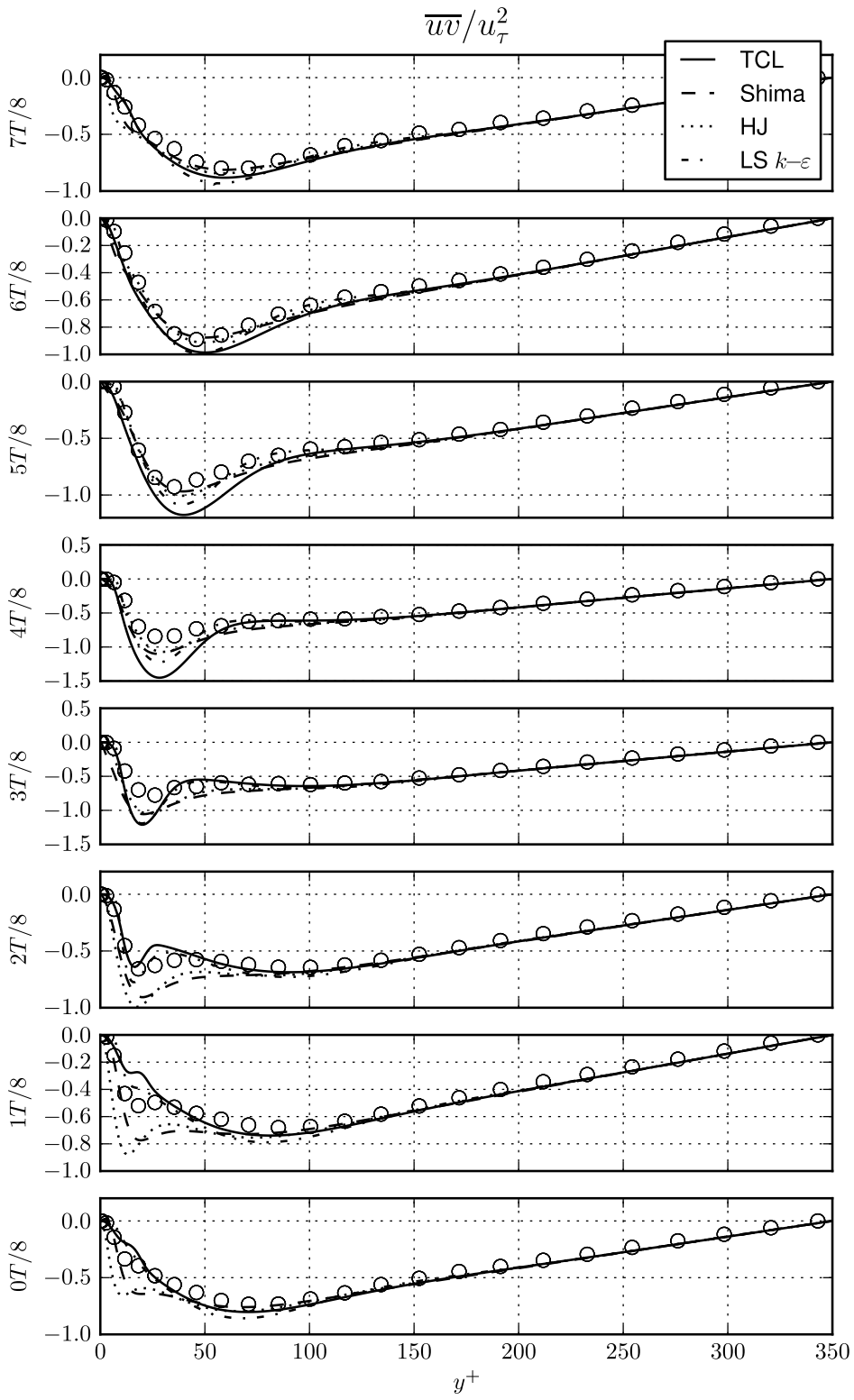

Figure 5.60: Phase-averaged profiles of phase-averaged Reynolds shear stress $\overline{uv}$ energy in wall units for the high frequency case $\omega^+ = 0.04$.

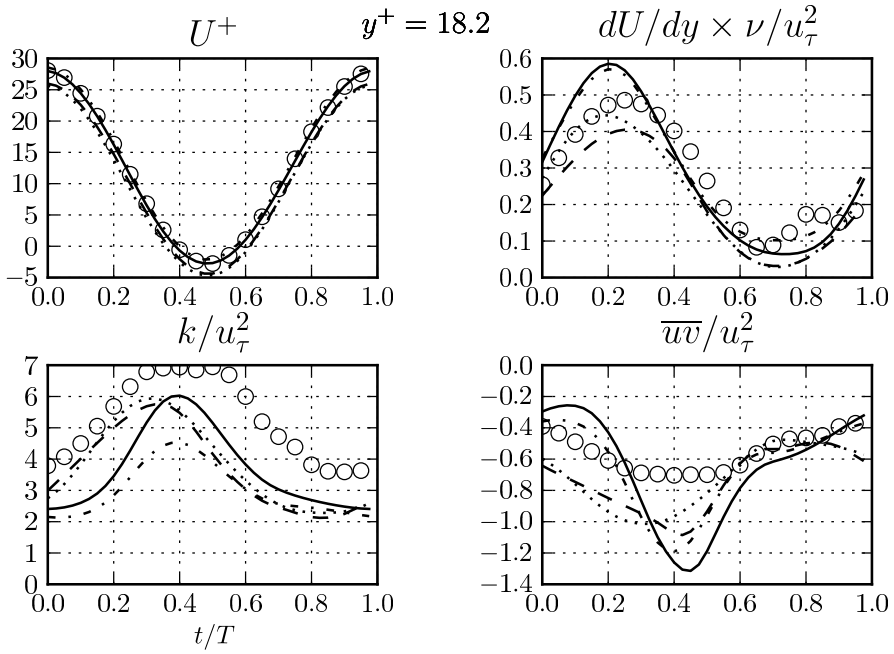

Figure 5.61: Cyclic variation of various phase-averaged flow quantities in wall units for the high frequency case $\omega^+ = 0.04$ at the location $y^+ = 18.2$.

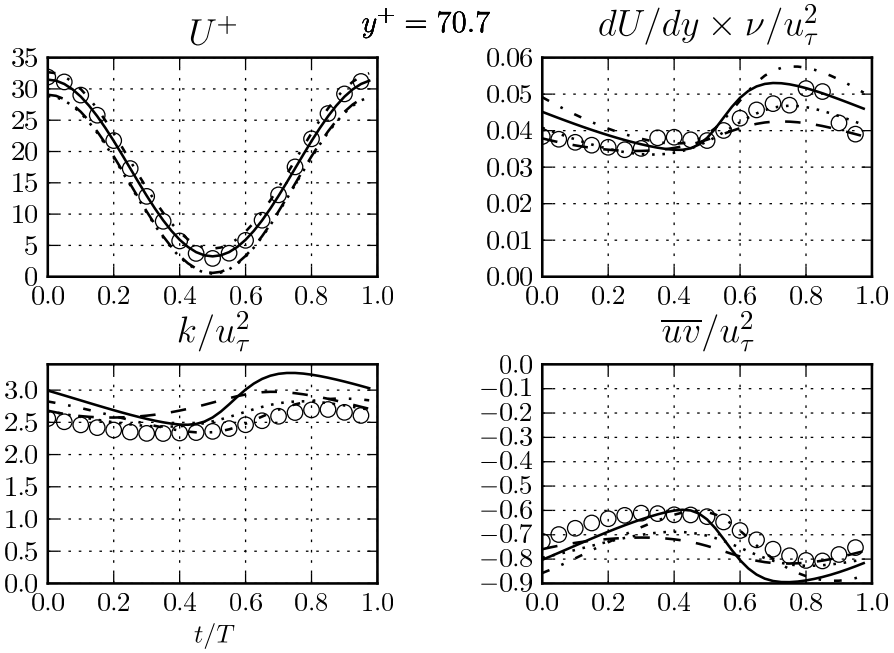

Figure 5.62: Cyclic variation of various phase-averaged flow quantities in wall units for the high frequency case $\omega^+ = 0.04$ at the location $y^+ = 70.9$.

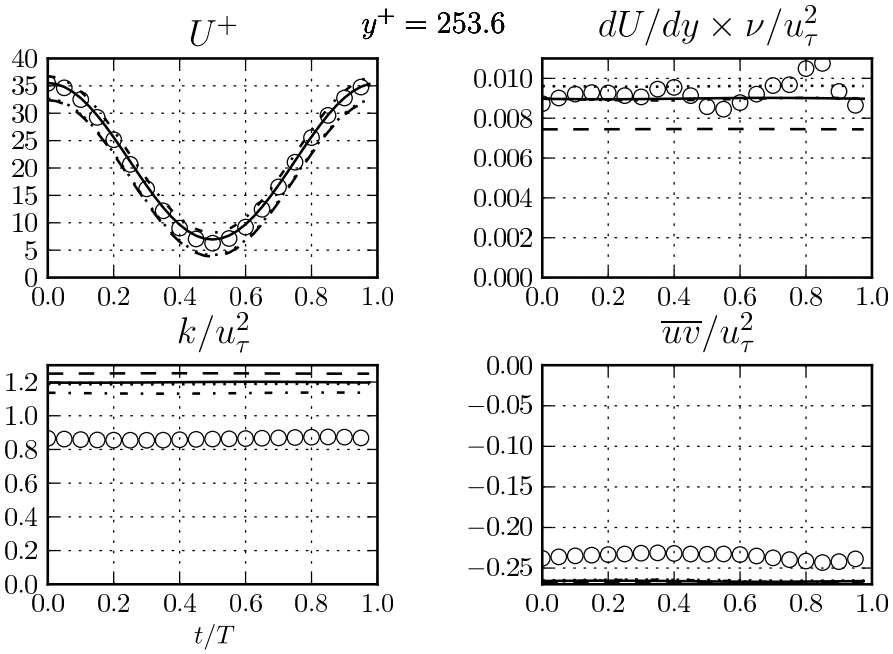

Figure 5.63: Cyclic variation of various phase-averaged flow quantities in wall units for the high frequency case $\omega^+ = 0.04$ at the location $y^+ = 254.3$.

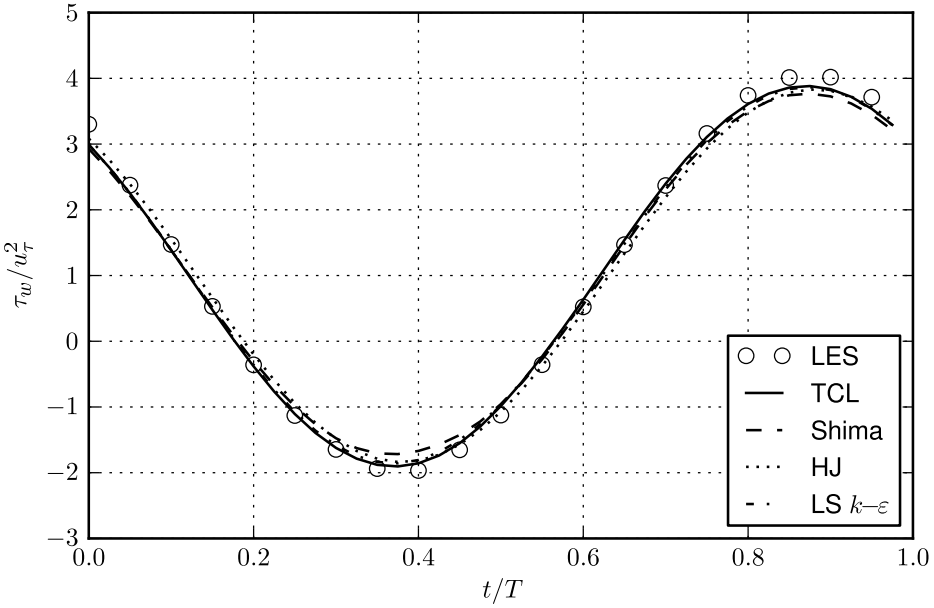

Figure 5.64: Modulation of phase-averaged wall shear stress in wall units for the high frequency case $\omega^+ = 0.04$.

Table 5.3: Time-mean bulk velocity returned by models at various frequencies.

ω^+	Steady	LES	TCL	Shima	HJ	LS
0.0016	17.5	17.3	15.7 (-9.1%)	–	–	16.1 (-7.1%)
0.01	17.5	18.6	16.0 (-13.8%)	18.5 (-0.1%)	15.1 (-18.8%)	17.3 (-7.0%)
0.04	17.5	18.7	19.0 (+1.4%)	16.2 (-13.4%)	16.3 (-13.1%)	20.1 (+7.4%)

model also tends to over-predict the amplitude over a large portion of the cross section, but is in reasonable agreement with the data for the phase angle. Similar comments can be made about the LS model results. The Shima model under-predicts the amplitude in the outer region and is largely out of phase with the data. The HJ model does the best job in predicting both the amplitude and the phase over the largest portion of flow, compared to the other models.

5.8 Concluding remarks

The problem of fully-developed channel flow subject to imposed sinusoidal pressure pulsations has been examined in this chapter. Three frequencies were selected for examination, corresponding to the low, intermediate, and high frequency regimes as described in the literature. None of the models tested reproduce all the flows correctly.

As summarised in Table 5.3, there was a considerable degree of variation in the model predictions of mean bulk velocity, which tend to be under-predictions, compared to the LES. At intemediate and high frequencies, the time-mean bulk velocity of the LES was higher than the mean bulk velocity of the steady channel DNS by about 6–7%, a feature that the models did not in general seem to mimic, and which contributes to their general tendency to underpredict the time mean U_b^+.

Notably, the flow feature that was most consistently well reproduced by the models over the range of frequencies examined is the fundamental mode of phase-averaged velocity modulation. Both the amplitudes and phase angles were well reproduced by the models over most of the channel height. Figure 5.69 shows the amplitude profiles, over the frequency range examined, using the TCL model. Very similar profiles are returned by the LS model at the same frequencies, and

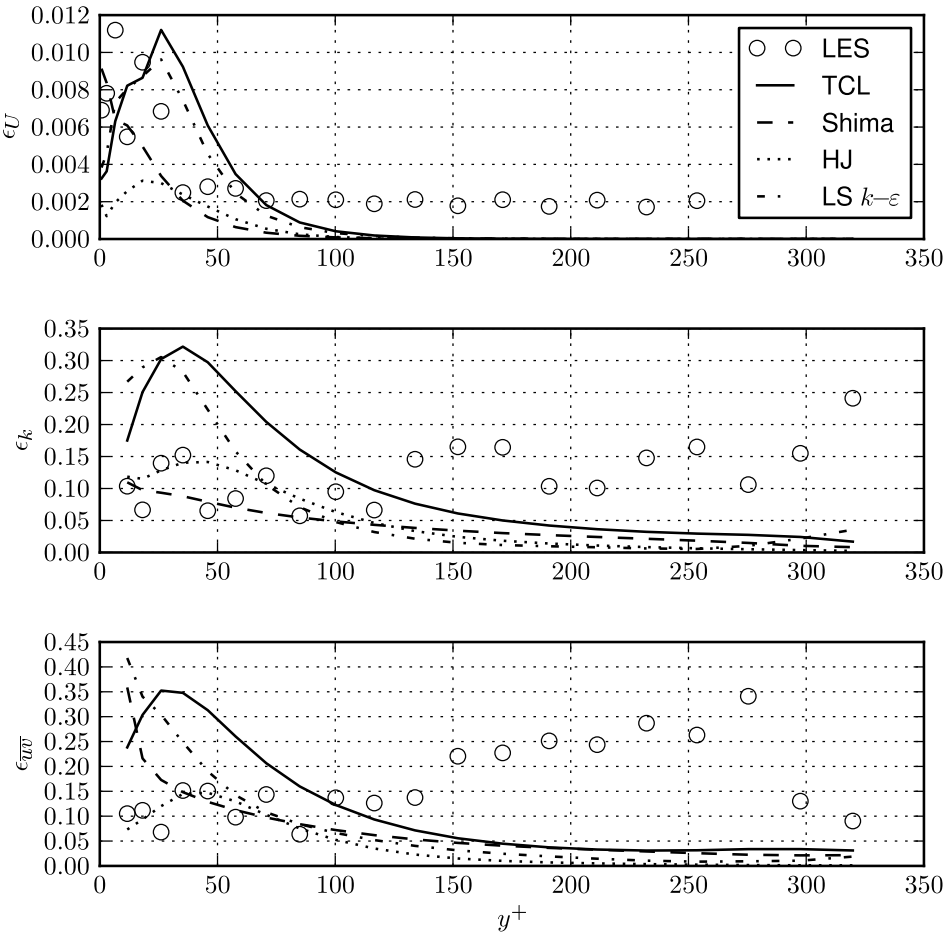

Figure 5.65: Estimated contribution of higher harmonics in the modulation of phase-averaged U^+ (top), $k/\overline{u_\tau}^2$ (middle), and $\overline{uv}/\overline{u_\tau}^2$ for the high frequency case $\omega^+ = 0.04$.

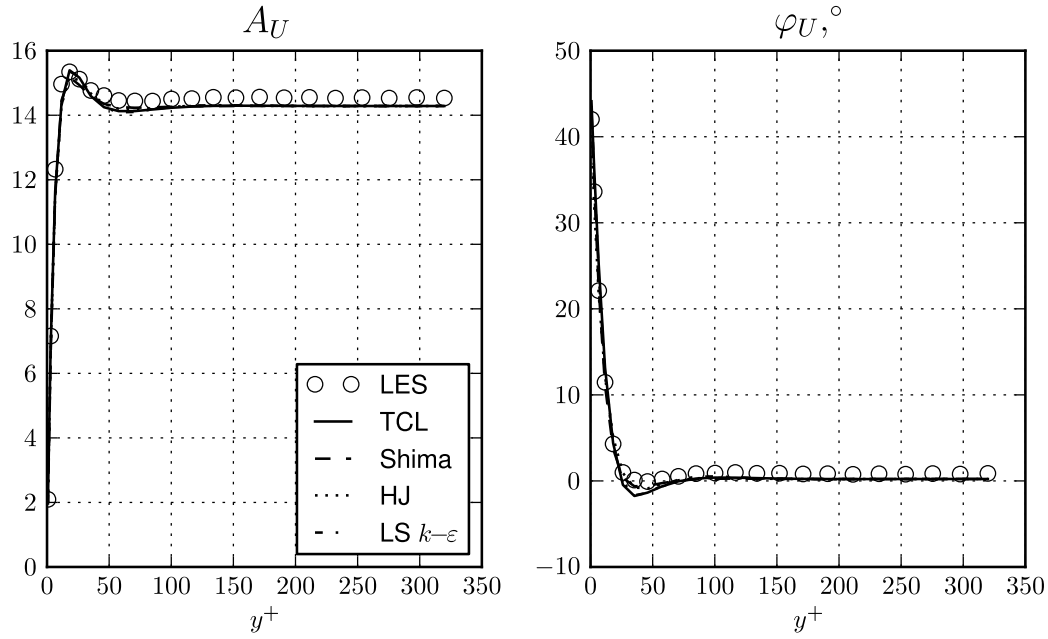

Figure 5.66: Amplitude and phase angle of the fundamental mode of phase-averaged velocity oscillation for the high frequency case $\omega^+ = 0.04$.

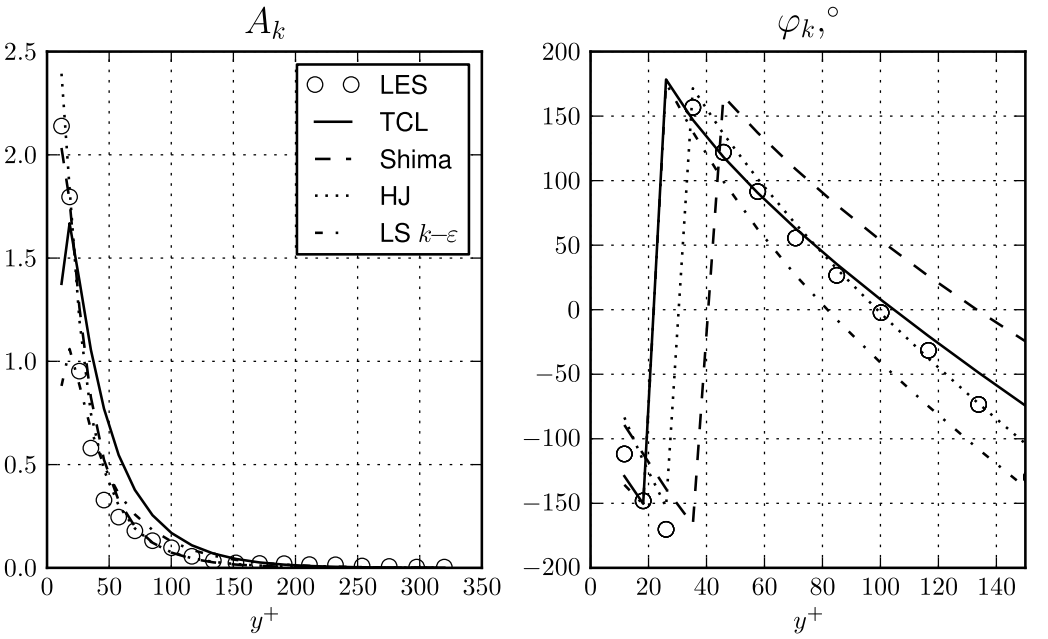

Figure 5.67: Amplitude and phase angle of the fundamental mode of phase-averaged turbulent kinetic energy oscillation for the high frequency case $\omega^+ = 0.04$. Phase angle data only shown up to $y^+ = 150$.

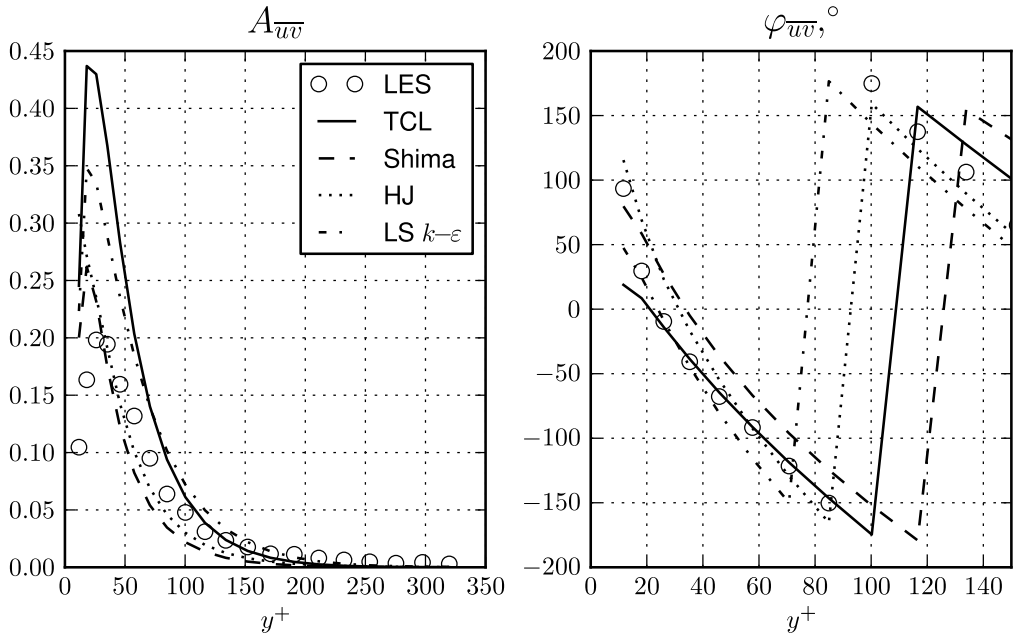

Figure 5.68: Amplitude and phase angle of the fundamental mode of phase-averaged Reynolds shear stress oscillation for the high frequency case $\omega^+ = 0.04$. Phase angle data only shown up to $y^+ = 150$.

by the HJ and Shima models at the intermediate and high frequencies (not shown in Figure 5.69, but appeared in previous figures).

The phase-averaged velocity profiles were not as well reproduced as the (fundamental mode) velocity amplitude profiles, and were often somewhat under-predicted. The preceding observations imply that this is a result of errors in the time-mean velocity.

The wall shear stress modulation returned by the LS and TCL models at the lowest frequency, $\omega^+ = 0.0016$, was in reasonable agreement with the reference data up to the re-transition phase of the cycle, where both models tended to overshoot the reference data modulation. The LS model performed better than the TCL at this frequency. At the highest frequency, $\omega^+ = 0.04$, the wall shear stress modulation predicted by all four models was in very good agreement with the reference data. The largest variation between the models in wall shear stress modulation was observed at the intermediate frequency, $\omega^+ = 0.01$. The LS and HJ models under-predicted the amplitude of the modulation, and were out of phase with the reference data, while the TCL model once again performed poorly due to the abrupt re-transition. The Shima model in this case was in very good agreement with the LES wall shear stress modulation.

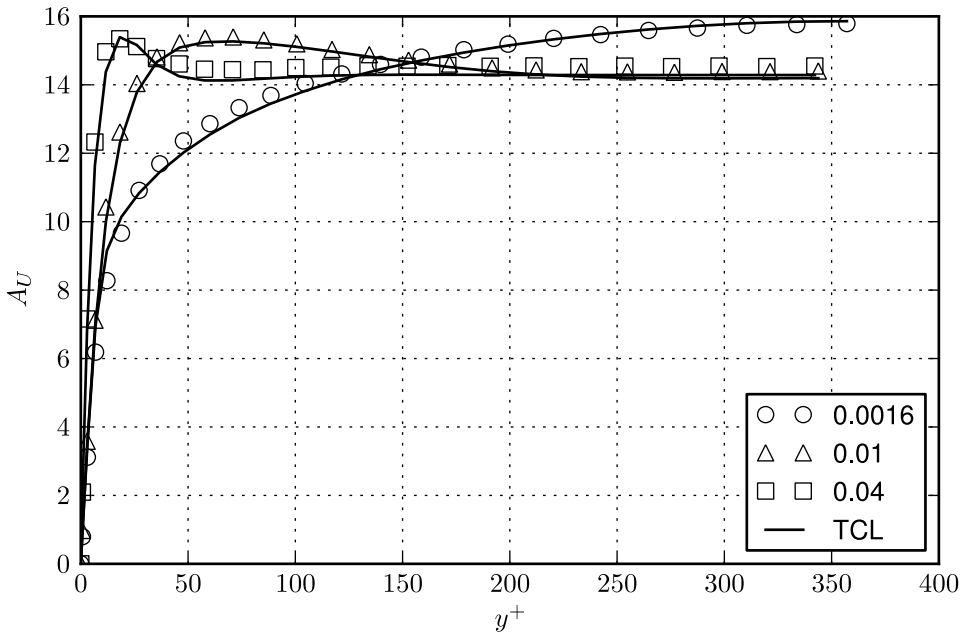

Figure 5.69: Amplitude of the fundamental mode of phase-averaged velocity oscillation at various frequencies.

The time-mean turbulence statistics of the pulsatile flow LES generally exhibited some differences compared to a steady turbulent channel DNS at a comparable Re_τ. However, this aspect of the LES data is somewhat questionable as has been pointed out earlier. The time-mean turbulence statistics returned by the Shima model was found to be particularly sensitive to the forcing frequency. This was also true, to a lesser extent, for the HJ model. The LS and TCL models generally returned time-mean turbulence statistics that were fairly similar to their steady flow results, showing little sensitivity to the forcing frequency.

The phase-averaged turbulent kinetic energy at the low and intermediate frequencies was generally poorly predicted by the models. This appeared to be due mainly to the partial laminarisation and retransition that occured cyclically at these frequencies. At the lowest frequency, the Shima and HJ models could not recover from the laminarisation portion of the cycle, and a periodic turbulent solution could not be obtained using these models. The TCL model, on the other hand, suffered from excessively abrupt re-transition at the low and intermediate frequencies, which adversely affected the accuracy of its predictions. The cause of this behaviour was attributed to low-Re_t dependecies in some of the TCL model coefficients. This suggests the need to reformulate the near-wall damping in some

of the model coefficients to allow the model to handle the cyclic transition more gracefully. At the highest frequency examined, all four models were in much better agreement with the LES data for the phase averaged turbulent kinetic energy over most of the channel height ($y^+ > 50$). The near wall modulation of k however, remained a difficult feature for the models to reproduce. Similar comments can be made regarding the phase-averaged Reynolds shear stress.

Chapter 6

Jet-Cavity Interaction

6.1 Introduction

This chapter reports on a brief comparative study of turbulence model performance in the problem of a turbulent planar jet issuing into a dead-end enclosure. The case is based on the experimental and computational studies of Mataoui et al. (2001) and Mataoui et al. (2003).

The experimental setup used by Mataoui et al. consists of a wind tunnel supplying air to a rectangular enclosure through a plane duct. Air flows into the enclosure through a nozzle designed to reduce the level of turbulence. The rectangular cavity is closed downstream of the issuing jet and open to the atmosphere at the opposite end, and the location of the jet inlet can be moved within the cavity. The geometric configuration and dimensions of the cavity are shown schematically in Figure 6.1. Velocity measurements were made using a single hot wire probe, and the signal was filtered to remove the high-frequency turbulent fluctuations using a signal conditioning system. Flow visualisation was also carried out using smoke injected at the inlet channel (Mataoui et al., 2003).

Mataoui et al. observed that different flow regimes develop in the cavity depending on the location of the jet inlet. When the jet inlet is brought close to a wall, a steady flow pattern results. When it is placed in a more central location, away from any wall, the resulting flow is unsteady. The unsteadiness can be either stable (periodic), or unstable (transitory), depending on the distance of the jet inlet to the end wall. The regions associated with each of these regimes are shown in Figure 6.2, taken from Mataoui et al. (2003).

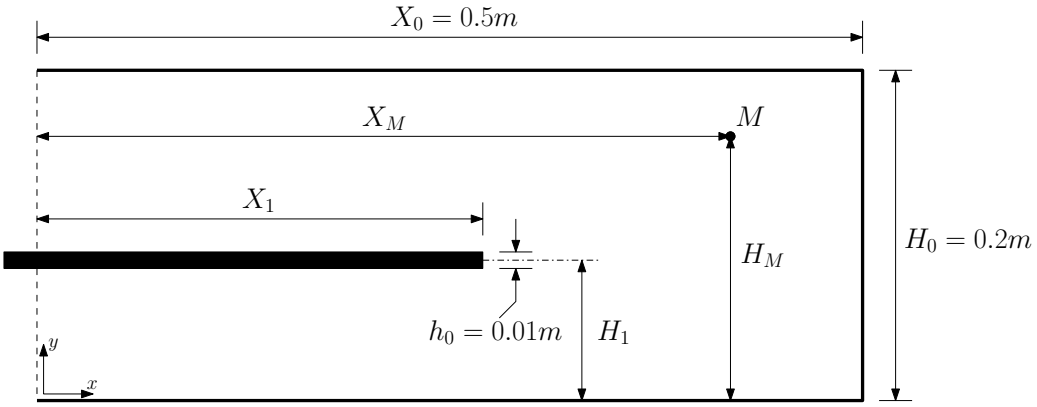

Figure 6.1: Schematic diagram of the plane jet in an enclosed cavity.

6.2 Problem description

The simplified flow domain used for computational modelling is shown in Figure 6.1, along with the employed geometrical notation. The following definitions are used for non-dimensionalising the geometrical and flow parameters:

- Dimensionless 'impingement distance':

$$X = \frac{X_0 - X_1}{X_0}. \tag{6.1}$$

- Dimensionless jet exit height:

$$H = \frac{H_1}{H_0}. \tag{6.2}$$

- Dimensionless (horizontal) distance between monitor point M and jet exit:

$$d_M = \frac{X_M - X_1}{X_0 - X_1}. \tag{6.3}$$

- Dimensionless height of monitor point:

$$h_M = \frac{H_M}{H_0}. \tag{6.4}$$

- Jet Reynolds number:

$$\mathrm{Re}_{\mathrm{jet}} = \frac{U_0 h_0}{\nu}. \tag{6.5}$$

- Strouhal number:

$$St = \frac{f h_0}{U_0} \tag{6.6}$$

In the above definitions U_0 is the jet exit velocity and f is the fundamental or dominant frequency in an unsteady case.

Following Mataoui et al. (2003), the following fixed boundary conditions were applied to the jet inlet:

$$U = U_0, \quad V = 0, \quad k = 0.03U_0^2, \quad \varepsilon = 10\frac{k^{3/2}}{h_0} \tag{6.7}$$

On the plane at the open end of the cavity (dashed line in Figure 6.1), a zero (plane-normal) gradient condition is applied to all flow variables except pressure, which is set to zero on that plane.

Two configurations have been examined in the present work. The first is $X = 0.2$, $H = 0.425$, which lies in the region reported to yield a steady flow regime, and the second is $X = 0.8$, $H = 0.425$, which is reported to yield a stable periodic flow regime. In both cases the jet Reynolds number is $\mathrm{Re}_{\mathrm{jet}} = 4000$. The working fluid is assumed to be air at 20°C, for which the density is $\rho = 1.2$ kg/m^3, and the dynamic viscosity is $\mu = 1.837 \times 10^{-5}$ Pa s.

6.3 Numerical implementation

The flow domain was discretised by a uniform grid of 100×120 finite volume cells. The jet inlet boundary conditions are applied at the exit of the nozzle, and the cells lying in the inlet duct of the jet are thus effectively blocked out of the computations by specifying values of their variables to be the same as the jet inlet boundary conditions. This is implemented by setting the following modifications to the discretised equations for each variable ϕ at each node within the blocked-off

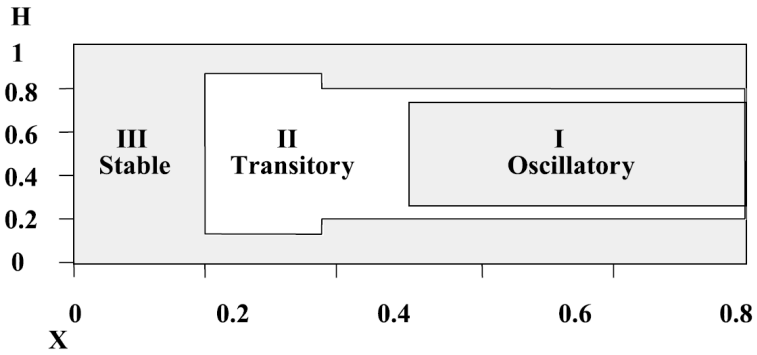

Figure 6.2: Observed flow regimes for various jet inlet placements, from Mataoui et al. (2003). The orientation of the figure is opposite to the one adopted here.

region:

$$\begin{aligned} a_E &= a_W = a_N = a_S = 0 \\ S_P &= -10^{20} \\ S_U &= 10^{20} \times \phi_{inlet} \end{aligned} \tag{6.8}$$

where a_E, a_W, etc. are the terms appearing in the discretised scalar-transport equation (3.16); S_U and S_P are the terms of the linearised source term in (3.19). This essentially ensures that the variable ϕ at the node retains its preset value and remains unaltered.

The near-wall viscous regions are not believed to be the most influential in this application, and so, to reduce the overall grid size required, the wall function approach described in Section 3.7 has been applied. Low-Re terms were, nevertheless, still retained in the turbulence models employed in the calculations, since in this type of complex flow it is difficult to ensure that the grid spacing is such that all the near-wall nodes lie fully outside the viscous sublayer.

The selection of the grid was a balancing process between accuracy and computational cost. The RSTM calculations were especially difficult because of their slower rate of convergence and higher computational cost compared to the LS model, in addition to difficulties of computational stability. The steady case was considered first, primarily to simplify the grid selection. The near wall grid requirements differ somewhat between these cases, because in the unsteady case the end wall is relatively far from the jet exit and the velocity at that wall is thus relatively low. The top and bottom walls on the other hand become sites of alternating jet impingement in the unsteady case, so these walls become the

more important ones in setting the spacing. The selected grid results in non-dimensional distances y^* (or x^*) between the wall and the wall-adjacent nodes of around 20-25 in the unsteady case at active regions of interaction with the wall, but can fall to around 5 in other places.

All calculations were run as unsteady cases. For the first configuration examined, $X = 0.2$, $H = 0.425$, identified in Figure 6.2 to correspond to a steady regime, a large step-size was used to accelerate convergence to a steady-state solution. For the second configuration, $X = 0.8$, $H = 0.425$, corresponding to a periodic regime in Figure 6.2, the code was left to run the intial flow development was surpassed, and around four to five periodic cycles could be identified. Results were only taken after this period of development.

Figure 6.3 shows a comparison of solutions obtained using the LS model for the steady case $X = 0.2$, $H = 0.425$ using grids of 80×100 and 100×120 cells. It can be seen that the difference between the two solutions is small, and this is consistent with the findings of Mataoui et al. (2003), who used a grid of 80×100 in their computations.

As a further demonstration of numerical accuracy, for the unsteady case $X = 0.8$, $H = 0.425$, Figure 6.4 shows the frequency spectra of four variables at two monitor locations, using the 80×100 grid and a time step of 0.002 seconds, and the 100×120 grid and time step of 0.001 seconds. The difference in the frequencies of the observed harmonics is only around 2-3%, and a time step of 0.001 seconds was thus used for all the unsteady results presented here.

6.4 Results

6.4.1 Steady case

Figure 6.5 shows the flow patterns obtained for the case $X = 0.2$, $H = 0.425$, using the LS, TCL and HJ models, and Figures 6.6, 6.7 show corresponding contours of pressure and turbulent kinetic energy for theses same models. This geometric configuration lies in the region which Mataoui et al. report to give a steady flow, and all three models did indeed reach a steady solution. In this configuration the nozzle is relatively close to the end-wall and there is direct impingement of the issuing jet onto this wall. The jet then splits into two streams which flow in both directions along the end-wall until they are forced to turn at

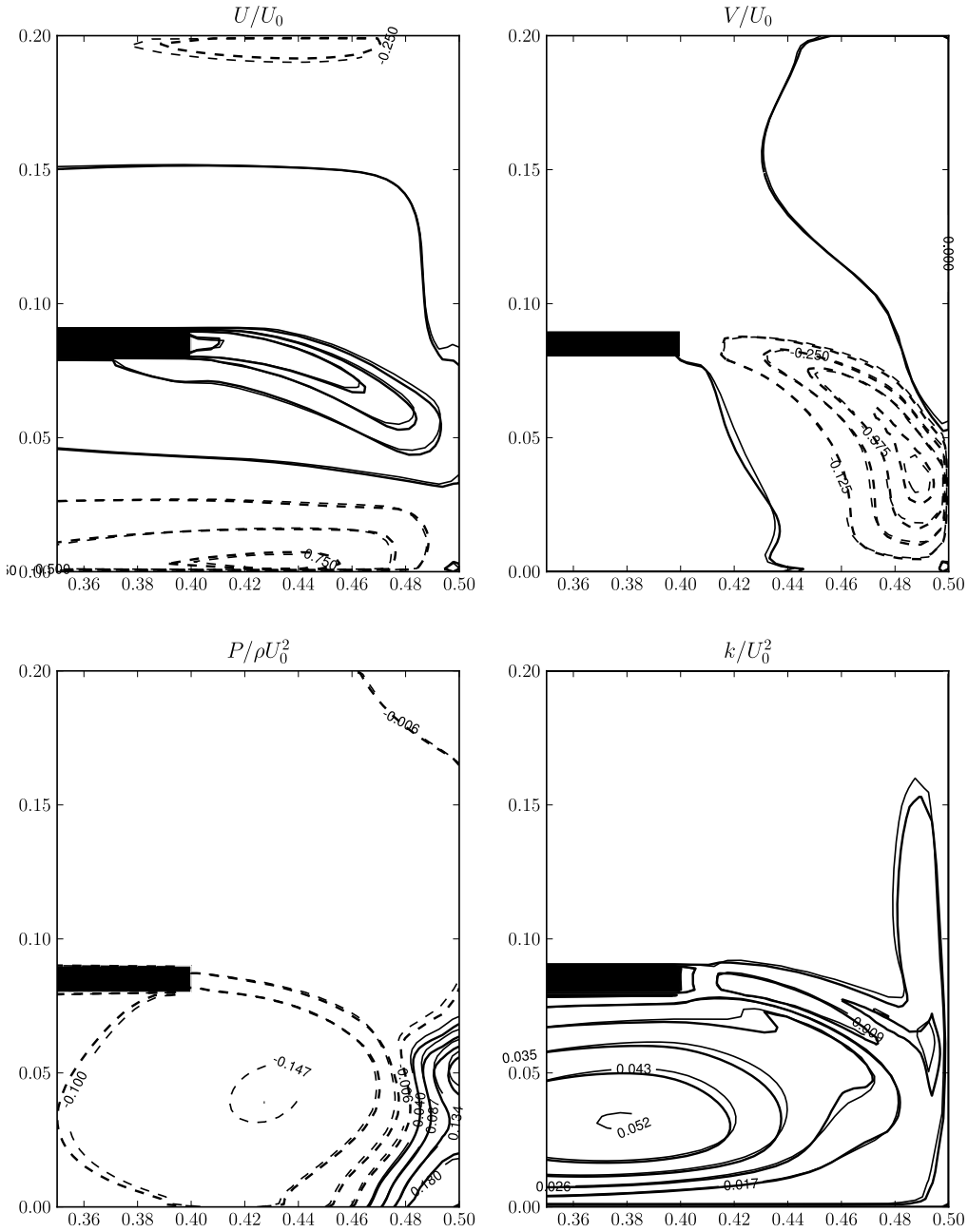

Figure 6.3: Contours of U and V velocity components, pressure, and turbulent kinetic energy obtained for the case $X = 0.2$, $H = 0.425$ at $\mathrm{Re}_0 = 4000$ using two different grids. Thick lines correspond to a grid of 100×120 cells, and thin lines correspond to a grid of 80×100.

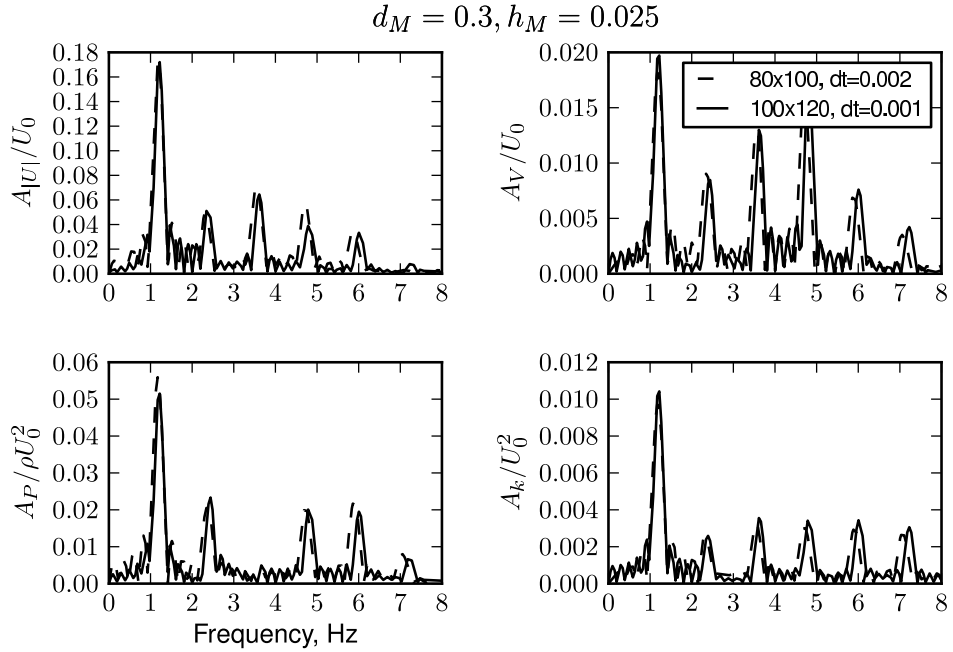

(a) Monitor location near bottom wall.

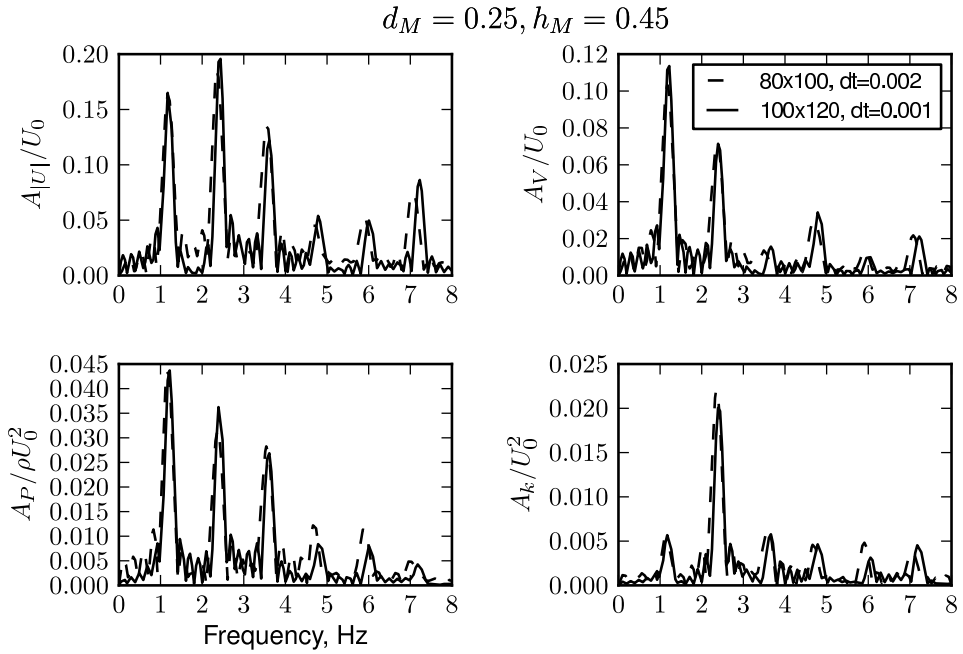

(b) Monitor location near mid-plane.

Figure 6.4: Comparison of frequency spectrum of velocity magnitude, V-velocity component, pressure, and turbulent kinetic energy returned by two solutions, the first obtained using a grid of 80×100 cells and a time step of .002 seconds (dashed lines), and the second using 100×120 cells and a time-step of 0.001 seconds, for the case $X = 0.8$, $H = 0.425$ at $\mathrm{Re}_{\mathrm{jet}} = 4000$ using the TCL model.

the corners. Fluid near the jet inlet on both sides of the nozzle is entrained along the jet. A larger negative pressure develops below the jet than above it, which causes the jet to deflect downwards and the impingement point on the wall is moved correspondingly. The general flow pattern returned by the models is qualitatively similar, with differences arising in the degree of downward deflection of the impinging jet. The lowest pressure develops in the LS case, as can be seen in Figure 6.6, followed by the TCL, then the HJ cases, respectively. Correspondingly, the jet is deflected downwards the most in the LS case, and a noticeably larger stream of air flows along the lower wall than that along the top wall. The jet impingement point is deflected least in the case of the HJ flow pattern, which causes the flow along the top wall to be the largest in this case. The top wall stream is then deflected because of the low pressure region, causing the stream to impinge on the top wall of the inlet duct and split in two directions.

Figure 6.7 shows that the highest levels of turbulence energy are at the location of jet impingement on the end-wall, and at the edge of the stream along the lower wall. The level of energy is highest in the TCL and LS flow fields, and is substantially lower in the HJ case. This might be due to the proximity of the shear layers from the edge of the lower wall stream and the entrainment stream under the jet in the former two model results, causing a concentration of the turbulence generated at these two locations. In the TCL case there is substantial spreading of the lower wall stream and this tends to shrink the region between the two mentioned shear layers where the fluid is relatively stagnant (in the mean). This spreading also explains the tilt in the contours of k/U_0^2 observed in the TCL case, and to a lesser extent in the HJ case.

6.4.2 Unsteady case

When the jet inlet was moved to $X = 0.8$, $H = 0.425$, all the models returned unsteady solutions. The simulations were run for at least 4 to 5 cycles, beyond the initial flow development, to ensure periodicity. In the case of the LS and TCL models, purely periodic solutions were obtained. For the HJ and Shima models, on the other hand, purely periodic solution were not obtained. Even after running the simulations for 10 additional cycles, the results obtained exhibited significant cycle-to-cycle variation in amplitude and period, as will be seen later.

The flow patterns over an approximate cycle and the corresponding pressure contours using the LS model are shown in Figure 6.8. The jet flapping motion

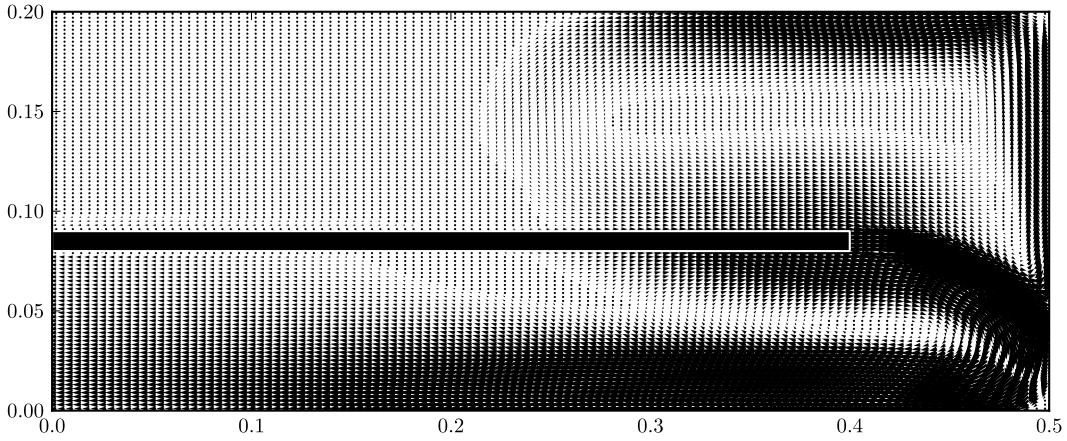

(a) LS model

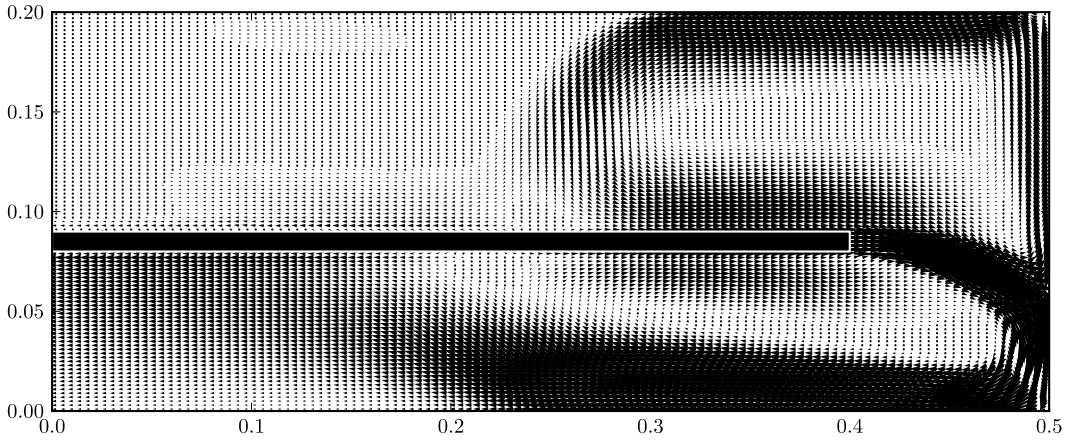

(b) TCL model

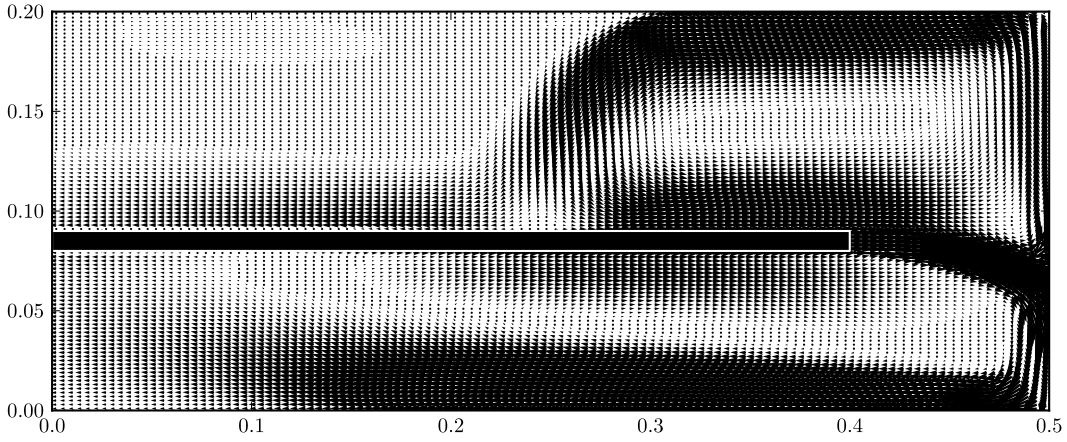

(c) HJ model

Figure 6.5: Flow patterns for the steady case $X = 0.2$, $H = 0.425$ using three different turbulence models.

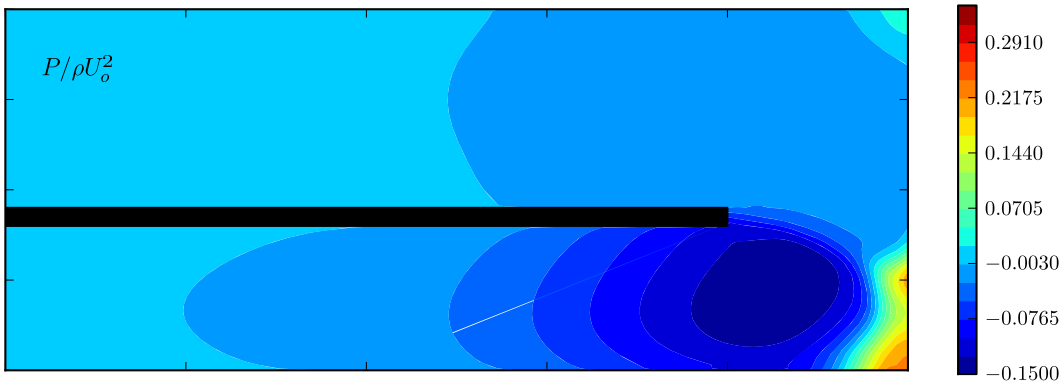

(a) LS model

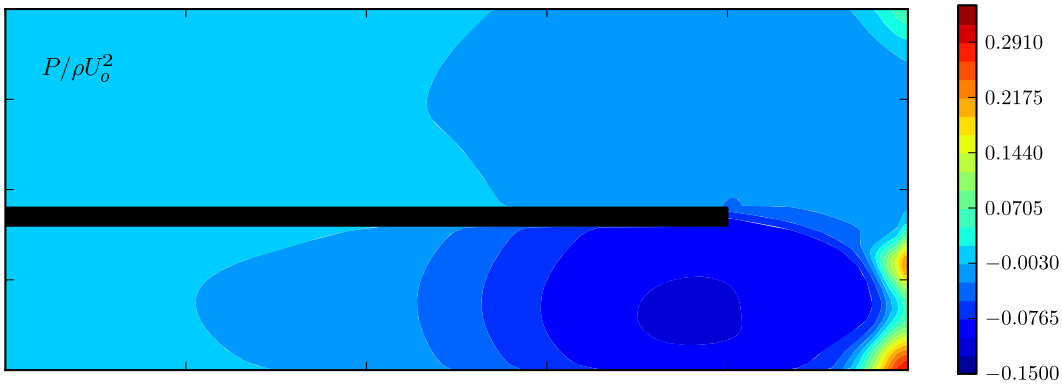

(b) TCL model

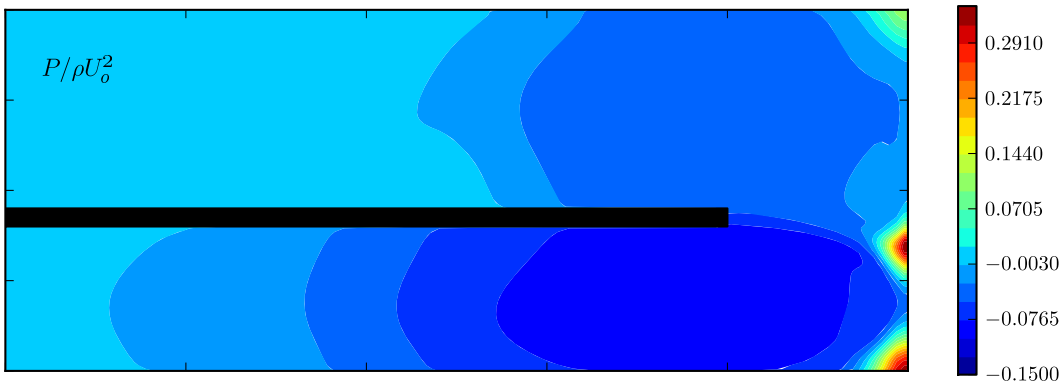

(c) HJ model

Figure 6.6: Pressure contours for the steady case $X = 0.2$, $H = 0.425$ using three different turbulence models.

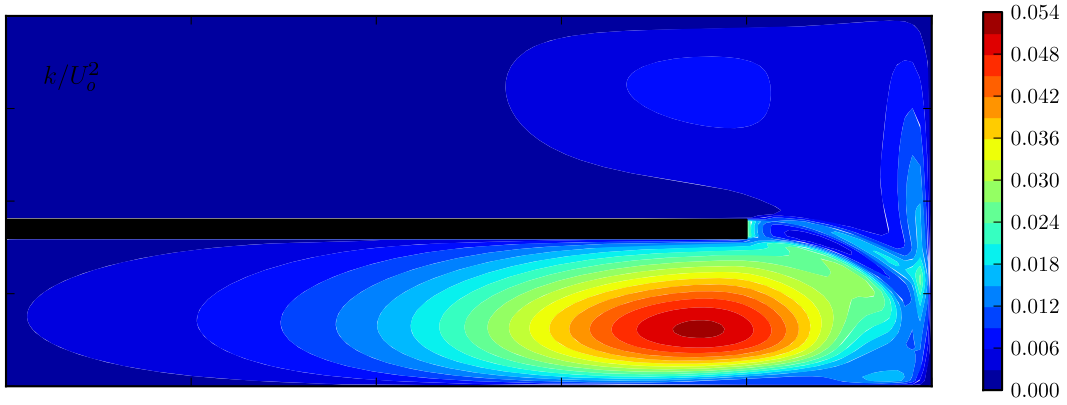

(a) LS model

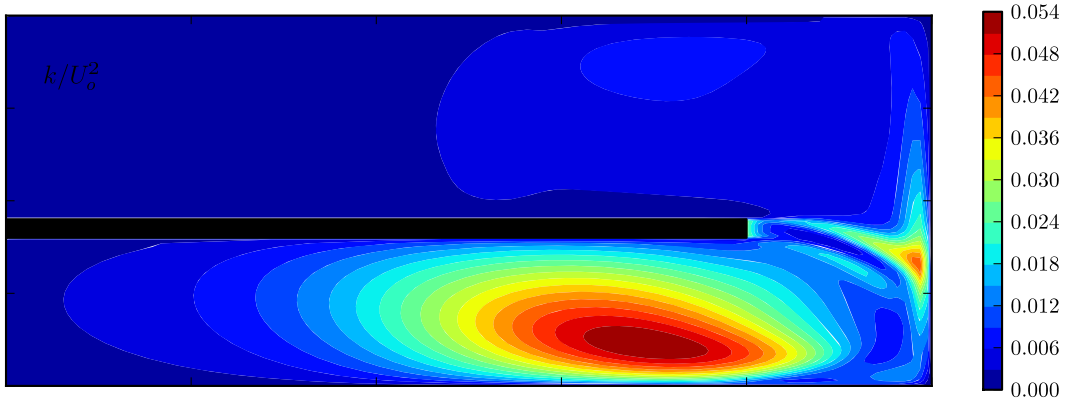

(b) TCL model

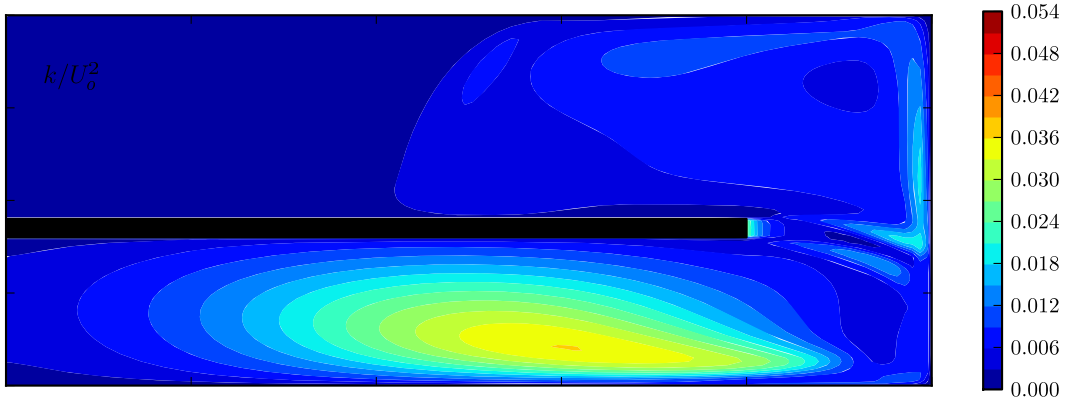

(c) HJ model

Figure 6.7: Turbulent kinetic energy contours for the steady case $X = 0.2$, $H = 0.425$ using three different turbulence models.

is driven by the low pressure regions that appear above and below the jet in an alternating fashion, and the impingement on the top and bottom walls causes splitting of the main jet stream to cause weaker secondary streams. Figure 6.9 shows contours of velocity magnitude and turbulent kinetic energy. Also shown in Figures 6.8 and 6.9 are the locations of two monitor points at which the time series of selected flow variables will be examined and analysed. Figure 6.10 shows the time series and frequency spectra of normalised velocity magnitude, transverse velocity component, pressure, and turbulent kinetic energy at the near wall monitor location. The time series of all four variables are clearly periodic with a main period of oscillation and higher frequency spikes. Observation of the monitor points over a period on the contour plots of Figures 6.8 and 6.9 sheds some light over the nature of the time series behaviour. The contours in these figures are annotated with the normalised time of the snapshot that corresponds to the times appearing in the time-series in Figure 6.10. Following the velocity magnitude at the near-wall monitor in Figures 6.9 and 6.10, it can be seen that at $tU_0/h_0 = 30$ the monitor lies in a stagnant region of the flow, and remains so over the next 1/6 of the cycle while the jet is heading towards the upper wall. However, the monitor point during this time is being approached by a secondary stream along the lower wall, and the velocity magnitude thus is increasing. Slightly after $tU_0/h_0 = 200$, the velocity tends to plateau slightly as a stream of fluid of slowly varying velocity crosses the monitor point, but the main jet is now in its downwards motion and the velocity is set to increase rapidly as the main jet approaches. Between $tU_0/h_0 = 367$ and 453, the main jet traverses the monitor point, and the velocity reaches a local peak, followed by a sharp trough and then another peak (absolute maximum). The trough is due to the stagnation region between the splitting streams of the impinging jet. The second peak is then followed by a sharp decrease in velocity magnitude as the jet proceeds in its upwards motion and the monitor point lies in the stagnant region beneath the lower entrainment stream, and the process is then repeated cyclically. The spikes in the time series of the other variables are also due to traversal of the jet impingement across the monitor point.

Similar time series of the same four variables and their frequency spectra at the second monitor near the centre of the cavity are shown in Figure 6.11. The velocity magnitude signal now shows two clear peaks of unequal magnitude in each cycle. Following the velocity magnitude contours in Figure 6.9, it can be

seen that the jet tends to be relatively straight when it crosses this monitor point on its way up at around $tU_0/h_0 = 120$, and more bent as it heads towards the monitor point on its way down (peak at around $tU_0/h_0 = 320$, as determined from Figure 6.11, not shown in Figure 6.9). This is due to the asymmetry of the jet inlet location with respect to the upper and lower walls; because of the larger distance, the jet sweeps through a larger angle before it impinges on the upper wall than when it impinges on the lower wall. The turbulent kinetic energy signal also has two clear peaks that correspond to the passing of the jet on its upward and downwards motion, with the width of the peak reflecting the asymmetry in the width of the contours and their degree of penetration in the cavity during these two strokes.

The frequency spectra shown in Figures 6.10 and 6.11 show an essentially purely periodic oscillation with a fundamental frequency of 1.23 Hz ($St = 0.002$), or a period $T = 0.81s$. According to Figure 11 in Mataoui et al. (2003) the frequency they observe experimentally for this configuration and Reynolds number is 0.51 Hz. However, it is not entirely clear how their frequency data was processed, and there seems to be a consistent factor of two difference between what can be read from their graphs and what they report. For example, Figure 6.12, taken from Mataoui et al. (2003), shows the time series of normalised velocity magnitude for the configuration $X = 0.8$, $H = 0.5$ at $\mathrm{Re}_{\mathrm{jet}} = 4500$ obtained experimentally, and that obtained using the standard high-Re k–ε and a two-scale eddy-viscosity model. Mataoui et al. report that the period obtained experimentally for this case is 1.83 s, and computationally, 1.785 s and 1.875 s for the single-scale and multiple-scale models, respectively. However, reading directly off the graphs in Figure 6.12, the periods in normalised time units are roughly 580, 580, and 595, in the order of the graphs. Given that they state $U_0 = 6$ m/s at $\mathrm{Re}_{\mathrm{jet}} = 4000$, the jet velocity at $\mathrm{Re}_{\mathrm{jet}} = 4500$ is $U_0 = 6.75$ m/s, and the nozzle height is given to be $h_0 = 0.01$m; the respective periods according to Figure 6.12 are thus $\Delta t = 0.86$ s, 0.86 s, and 0.88 s. These are roughly half the values they report, allowing for small differences between reading the period graphically and obtaining it by processing the time series using a discrete Fourier transform. Similarly, Figure 11 in Mataoui et al. (2003) states that the frequency of oscillation obtained for the case $X = 0.8$, $H = 0.425$ at $\mathrm{Re}_{\mathrm{jet}} = 4000$ (equivalent to the presently considered case) using the standard k–ε model is 0.56 Hz, whereas reading the peak-to-peak time interval directly off Figure 6 (for the same

configuration and Reynolds number) in the same reference implies a frequency of 1 Hz. Therefore there appears to be a systematic factor of two difference between the frequencies they report and what can be inferred from their time-series plots, and this would result in the present LS prediction of the frequency being only slightly higher than that measured.

The time series and frequency spectra obtained using the TCL model for the same variables and monitor points described previously for the LS model are shown in Figures 6.13 and 6.14. In this case, as in the case of the LS model, the flow reaches a purely periodic state, as seen in the time series and frequency spectra shown in these figures. The fundamental frequency of oscillation, as determined by the lowest dominant frequency in the shown spectra, is 1.20 Hz. Figure 6.15 shows the flow patterns and pressure contours over a cycle, and Figure 6.16 shows the velocity magnitude and turbulent kinetic energy contours for the same model. The contour snapshots are annotated with the normalised time that corresponds to that shown on Figures 6.13 and 6.14.

The flow patterns obtained using the TCL model are qualitatively similar to those obtained using the LS model presented previously. Although it is difficult to make direct comparisons between the flow fields at various instances, due to the difficulty of identifying a common starting point for the cycles, it was generally observed that the TCL model tends to predict stronger recirculation of the jet stream to the left of the impingement point. This can be seen in the top velocity magnitude contours in Figures 6.9 and 6.16, and at other instances not shown in these figures. Notably, the pressure gradient in these regions of recirculation tend to be larger (closer contours) in the case of the TCL model than in the LS, which leads to the stream being pulled laterally towards the lower pressure.

Corresponding time series and frequency spectra plots using the HJ model are shown in Figures 6.17 and 6.18, and using the Shima model in Figures 6.21 and 6.22. Contour plots of flow variables similar to those presented previously are shown in Figures 6.19 and 6.20 for the HJ model, and in Figures 6.23 and 6.24 for the Shima model. The first observation that stands out from the time series of the HJ and Shima models is that these models do not reach a purely periodic state. From the frequency spectra it is possible to identify a dominant frequency that is associated with the flapping motion, but the degree of cycle-to-cycle variation is enough to make it difficult to identify this frequency (its associated period) in the time domain plots. The lowest dominant frequency identified is 1.16 Hz

for the HJ model, and 0.95 Hz for the Shima model. The number of variables solved for in RST models is larger than in eddy-viscosity models and these variables are thus free to have independent time scales. It might thus be expected that this feature of RST models would lead to increased complexity of interaction between the time-scales. The TCL model does not exhibit this behaviour however, and, in agreement with the experimental observations, it returns a periodic solution. This suggests that, since the Shima and HJ models are closer to linear RSTM's, it would appear that these do not return the correct interaction between processes. Notably, Guo et al. (2001) who studied computationally a two-dimensional confined jet using three different eddy viscosity models and the Basic Reynolds stress transport model (LRR-IP), in a slightly different geometry than the present one, similarly found that all the eddy-viscosity models returned purely periodic oscillatory solutions. The RST model, on the other hand, returned a complex oscillation pattern with significant cycle-to-cycle variations in amplitude and period. The dominant frequency of these oscillations was comparable however to the eddy-viscosity results. These observations are similar to the present findings.

Unfortunately, Mataoui et al. (2003) present very limited quantitative experimental data to compare with. The experimental time series introduced previously in Figure 6.12, for a slightly different configuration, shows a signal that is not purely periodic, and some cycle-to-cycle variation is clearly evident (although the configuration does lie in the region identified in Figure 6.2 as producing a periodic flow). However, the small cycle-to-cycle variation shown in the measurements is significantly less than that returned by the HJ and Shima models, and to within measurement error, the series shown in Figure 6.12 can be said to be essentially periodic.

Comparing the time series at the two monitor points, across the various models, it is observed that the velocity magnitude fluctuations generally tend to contain more frequency components at the central monitor location than at the near wall one. The opposite is true for the pressure fluctuations, where the spectrum can be seen to decay faster at the central monitor. The latter observation is attributed to the pressure spikes that correspond to impingement at the wall and the pressure rise associated with stagnation. At the central monitor the LS pressure signal is dominated by the fundamental mode and the first harmonic,

having almost equal amplitudes, with small contributions from higher frequencies. The TCL pressure signal at this location is dominated by the first three frequencies. The HJ and Shima pressure signal frequencies cluster around the dominant frequency identified previously, up to around 5 Hz, and tend to be negligible beyond that. A notable feature in the pressure signal of these two models at both monitor points is the relatively large negative pressures compared to the LS and TCL models. These larger negative pressures are associated with stronger vortex rings, as observed when the respective flow patterns are examined. The largest amplitudes of pressure fluctuations are observed in the HJ results.

6.5 Concluding remarks

The problem of a turbulent planar jet issuing into a dead-end enclosure has been examined in this chapter. Two configurations have been selected for simulation: the first corresponding to the steady regime, as reported in the literature, and the second belonging to the periodic regime.

In the steady case, the general flow pattern returned by the models was qualitatively similar, with differences arising in the degree of downward deflection of the impinging jet. Due to the asymmetric position of the jet inlet, a larger negative pressure develops below the jet than above it, causing the jet to deflect downwards. A lower negative pressure results in a larger deflection, which in turn lowers the location of the impingement point on the lower wall, and increases the flow rate of the lower exiting stream relative to the upper stream. The lowest negative pressure developed in the LS case, followed by the TCL case. This explains the difference in the flow patterns returned by the models. In all cases, a higher level of turbulent kinetic energy develops in the lower part of the cavity, below the jet inlet duct, than in the upper part. The level of turbulent kinetic energy returned by the TCL and LS models was significantly higher than that returned by the HJ model. This was attributed to the larger lower stream in the LS and TCL cases, which brings the two shear layers from the lower wall stream and entrainment stream closer to each other, causing a concentration of the turbulence generated at these two shear layers.

In the unsteady case, a jet flapping motion arises, which is driven by low pressure regions that develop above and below the jet in an alternating fashion. The flapping motion is experimentally observed to be periodic for the configuration

examined (Mataoui et al., 2001, 2003). However only the LS and TCL models, in this case, returned purely periodic solutions. The Shima and HJ models returned unsteady flow patterns that exhibited complex oscillations with significant cycle-to-cycle variations. Since each of the four indepndent Reynolds stress components is obtained from its own transport equation in RSTM's, each is free to have its own time-scale, and the potential interactions between the various time-scales is much more complex than in eddy-viscosity models. Since the TCL model in this case is the only RSTM that correctly returns a periodic solution, it appears that, being closer to linear RSTM's, the Shima and HJ models do not return the correct interaction between processes.

The lowest dominant frequencies returned by the LS, TCL, and HJ models were relatively close to each other, having a mean value of 1.2 Hz and a standard deviation that is 2.4% of the mean. The Shima model returned a frequency that was 20% lower than the mean frequency returned by three other models. Unforunately, differences between the reported freuquencies in the reference case of Mataoui et al. (2003), and values implied by their graphs make it difficult to make a reliable comparison with the experimental data.

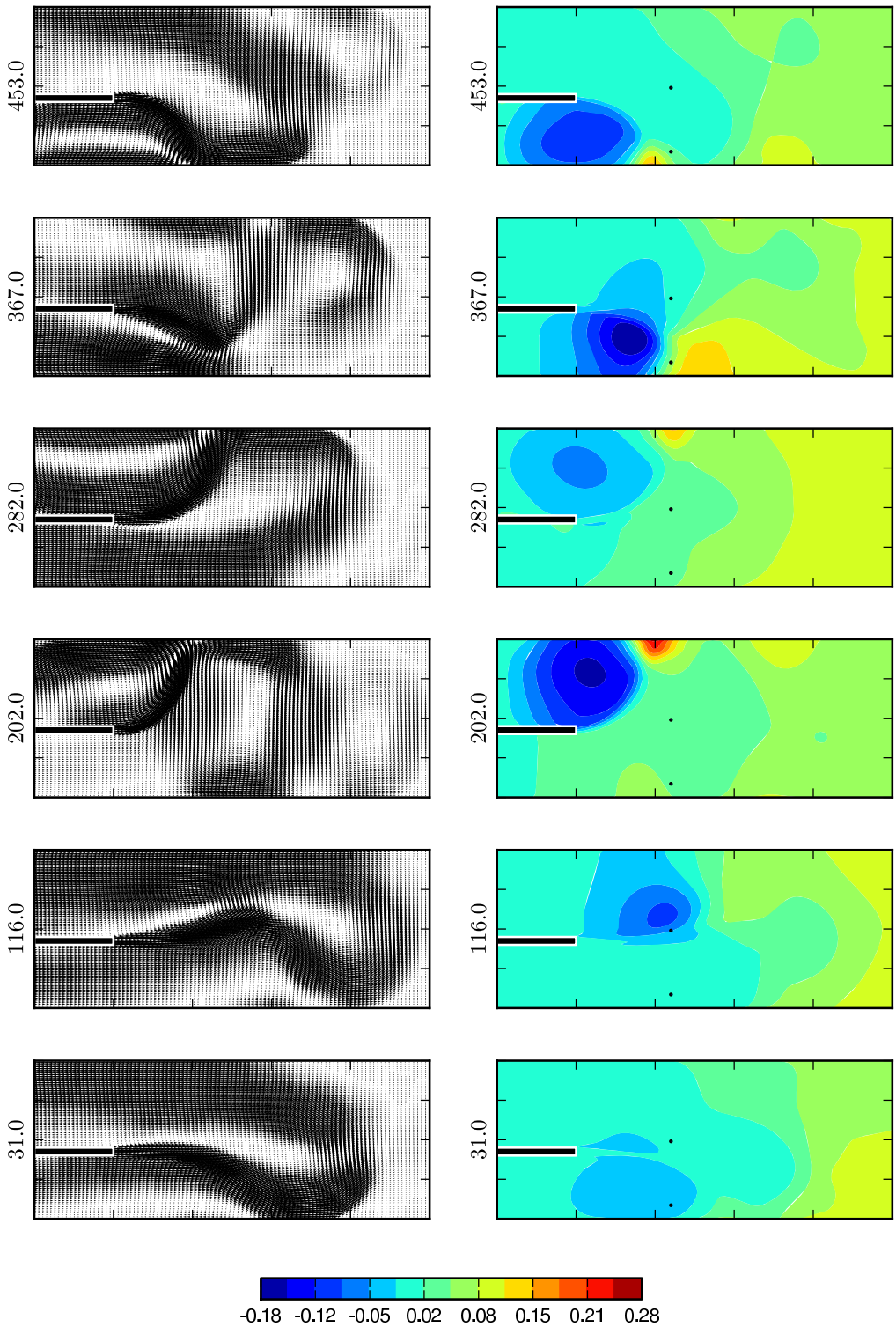

Figure 6.8: Velocity vectors and pressure contours over the dominant period of oscillation for the case $X = 0.8$, $H = 0.425$ obtained using the LS model.

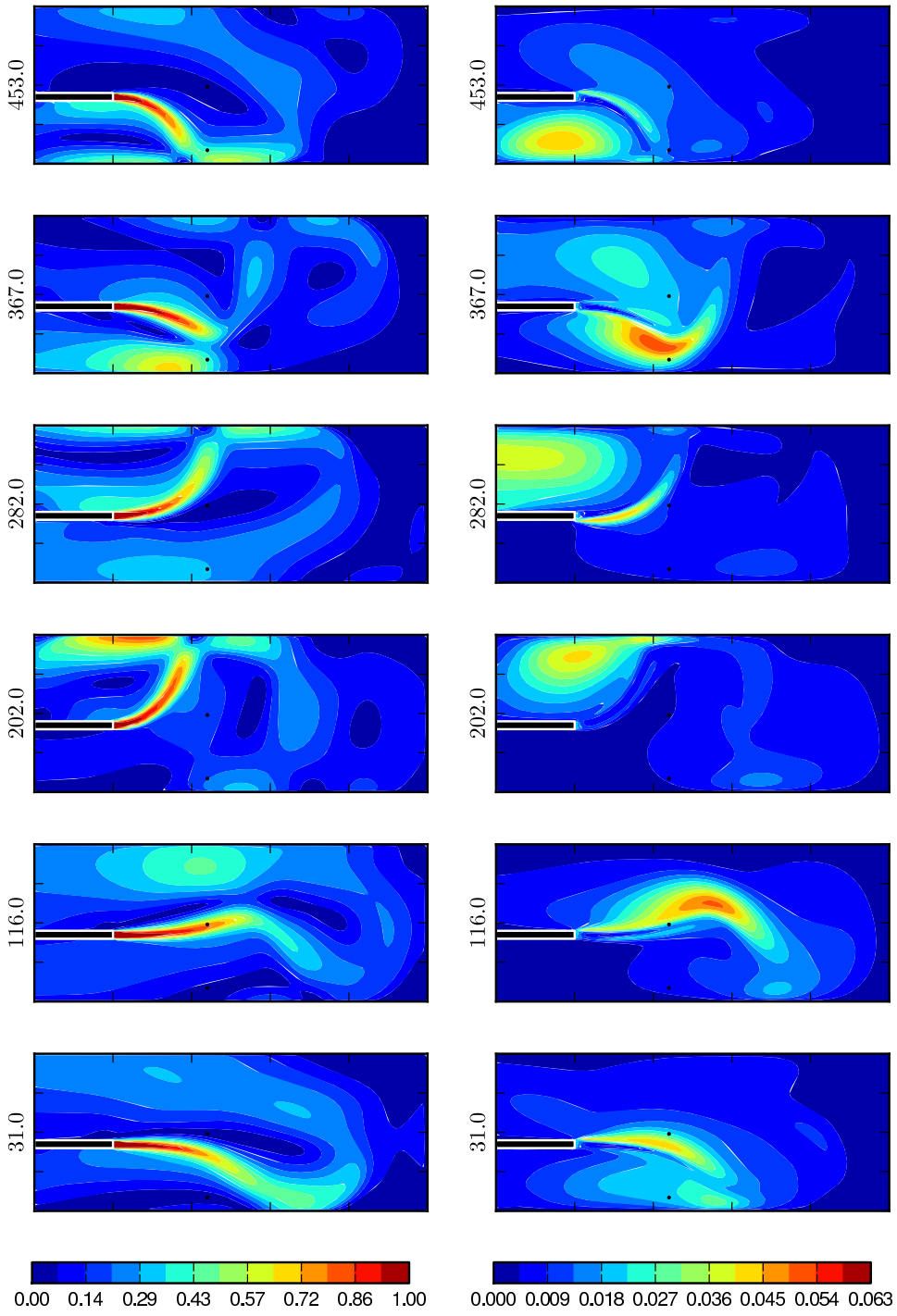

(a) Velocity magnitude (b) Turbulent kinetic energy

Figure 6.9: Contours of normalised velocity magnitude and turbulent kinetic energy over the dominant period of oscillation for the case $X = 0.8$, $H = 0.425$ obtained using the LS model.

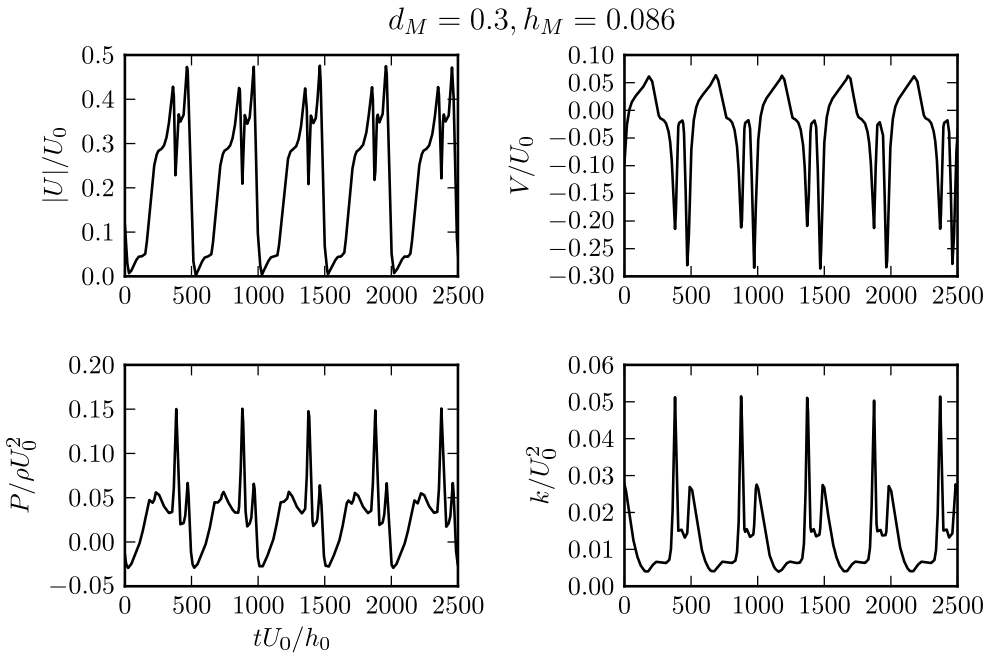

(a) Time series.

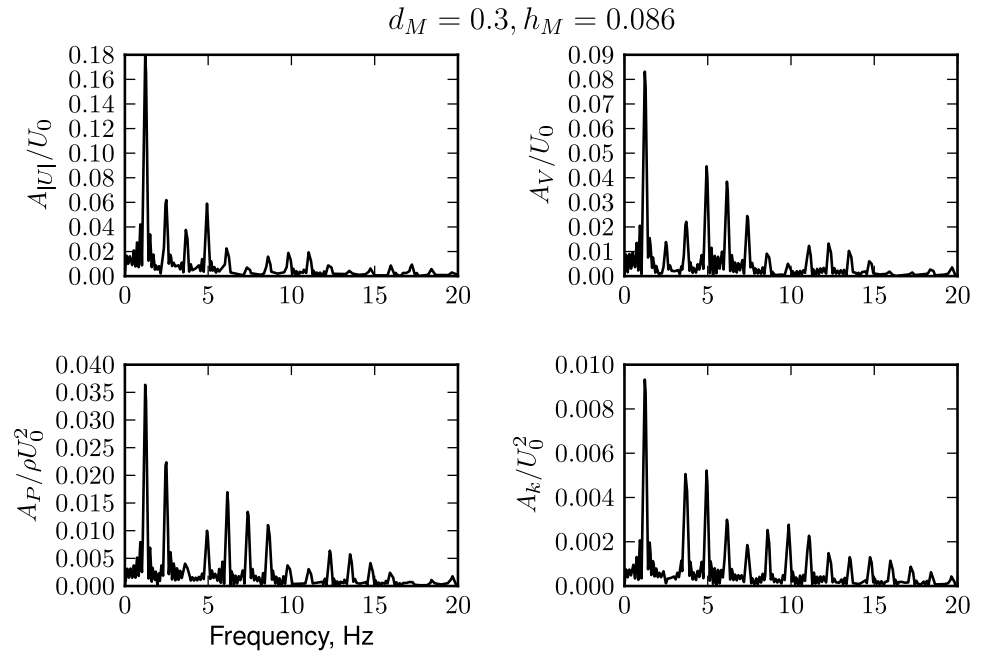

(b) Fourier transform.

Figure 6.10: Time series and frequency spectra of the variables $|\vec{U}|/U_0$, V/U_0, $P/\rho U_0^2$ and k/U_0^2 for a monitor located at $d_M = 0.3$, $h_M = 0.086$ obtained using the LS model.

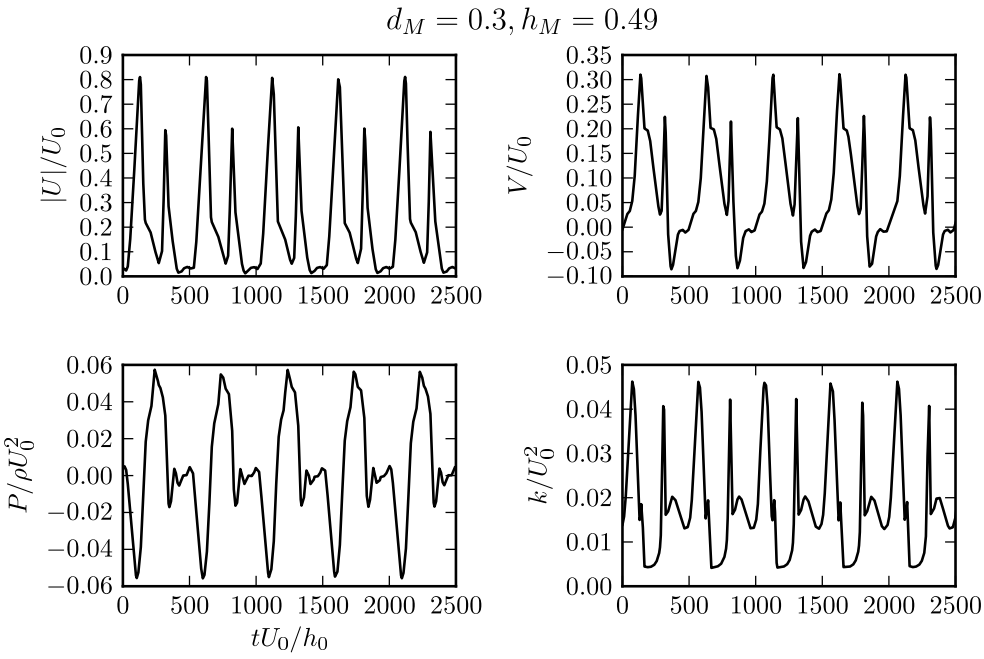

(a) Time series.

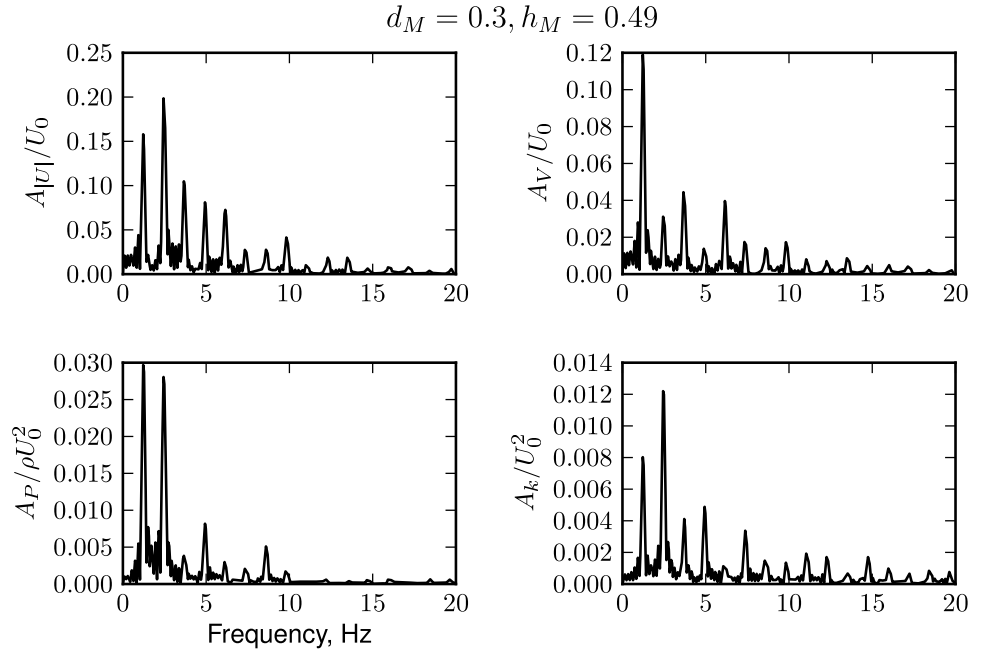

(b) Fourier transform.

Figure 6.11: Time series and frequency spectra of the variables $|\vec{U}|/U_0$, V/U_0, $P/\rho U_0^2$ and k/U_0^2 for a monitor located at $d_M = 0.3$, $h_M = 0.49$ obtained using the LS model.

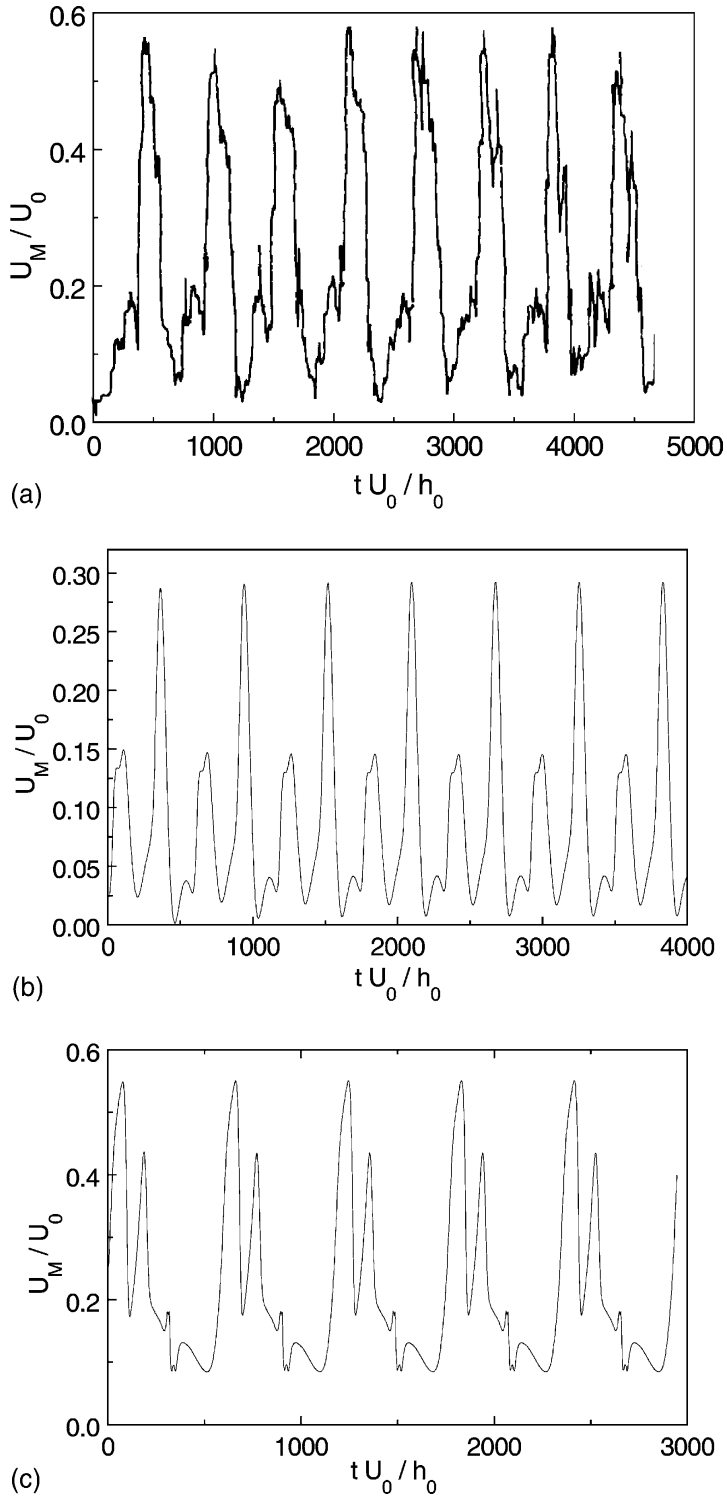

Figure 6.12: Time series of normalised velocity magnitude for the case $X = 0.8$, $H = 0.5$ at $\mathrm{Re}_{\mathrm{jet}} = 4500$ obtained by Mataoui et al. (2003).

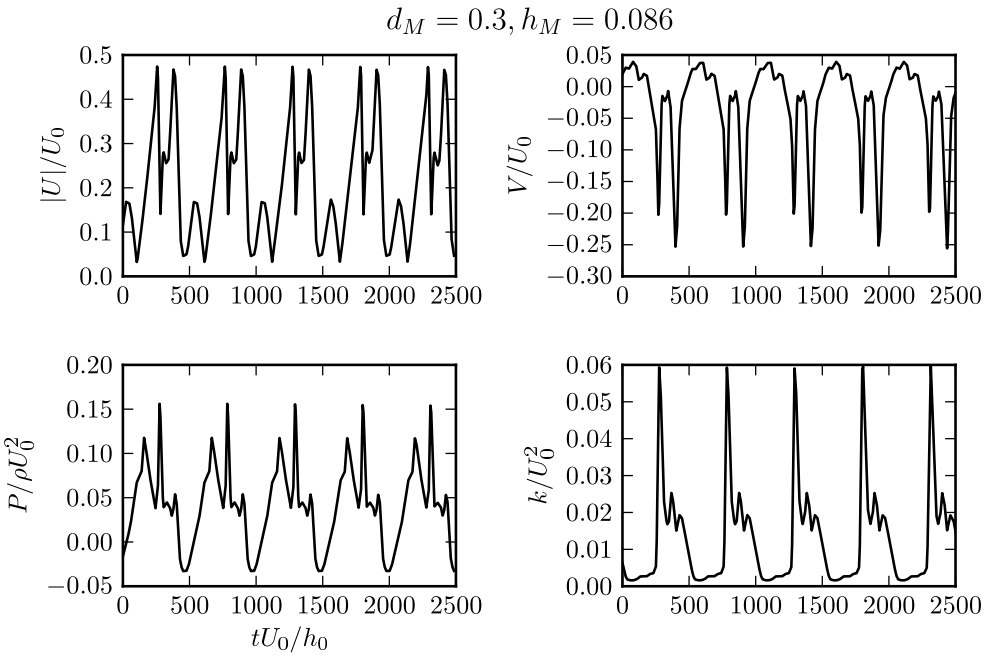

(a) Time series.

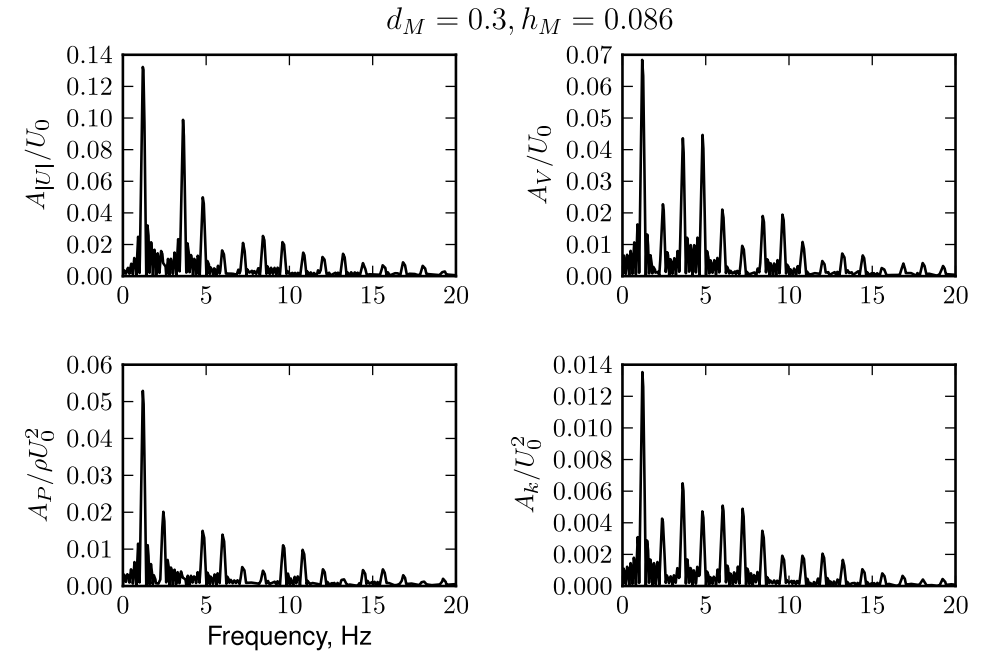

(b) Fourier transform.

Figure 6.13: Time series and frequency spectra of the variables $|\vec{U}|/U_0$, V/U_0, $P/\rho U_0^2$ and k/U_0^2 for a monitor located at $d_M = 0.3$, $h_M = 0.086$ obtained using the TCL model.

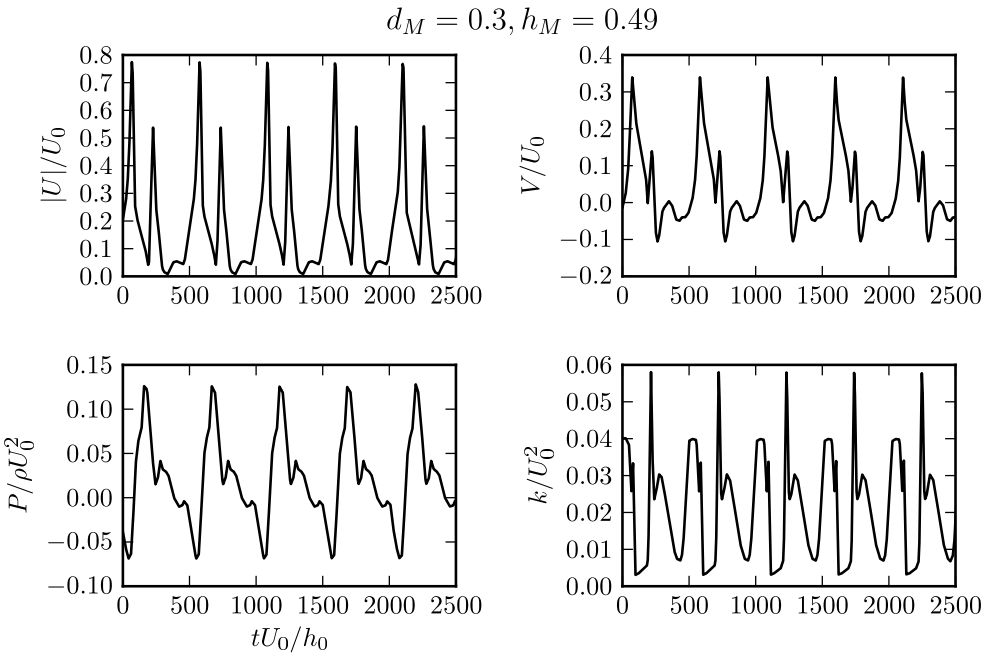

(a) Time series.

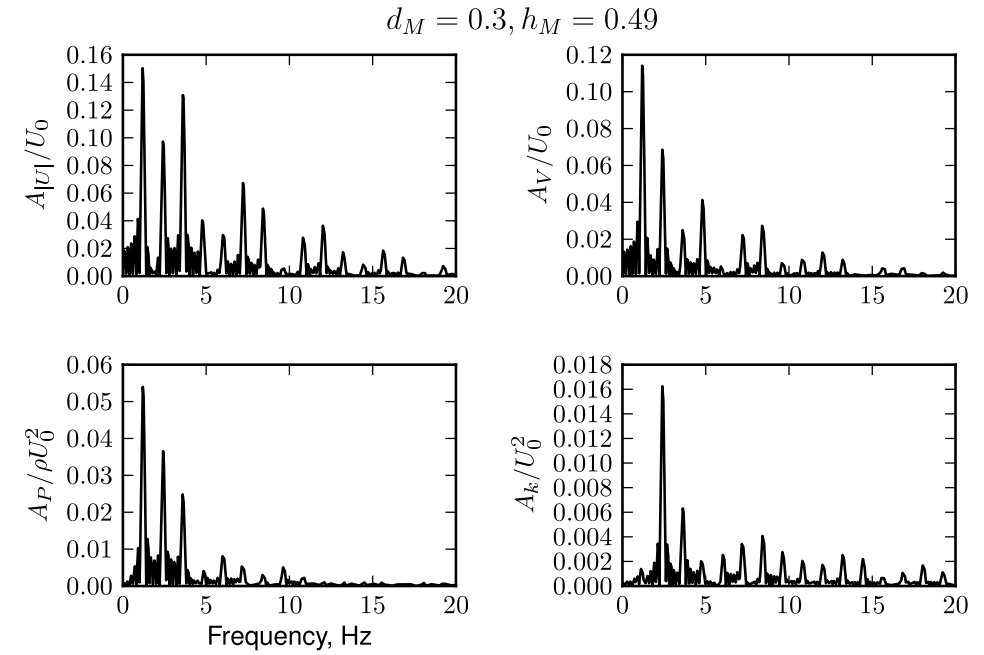

(b) Fourier transform.

Figure 6.14: Time series and frequency spectra of the variables $|\vec{U}|/U_0$, V/U_0, $P/\rho U_0^2$ and k/U_0^2 for a monitor located at $d_M = 0.3$, $h_M = 0.49$ obtained using the TCL model.

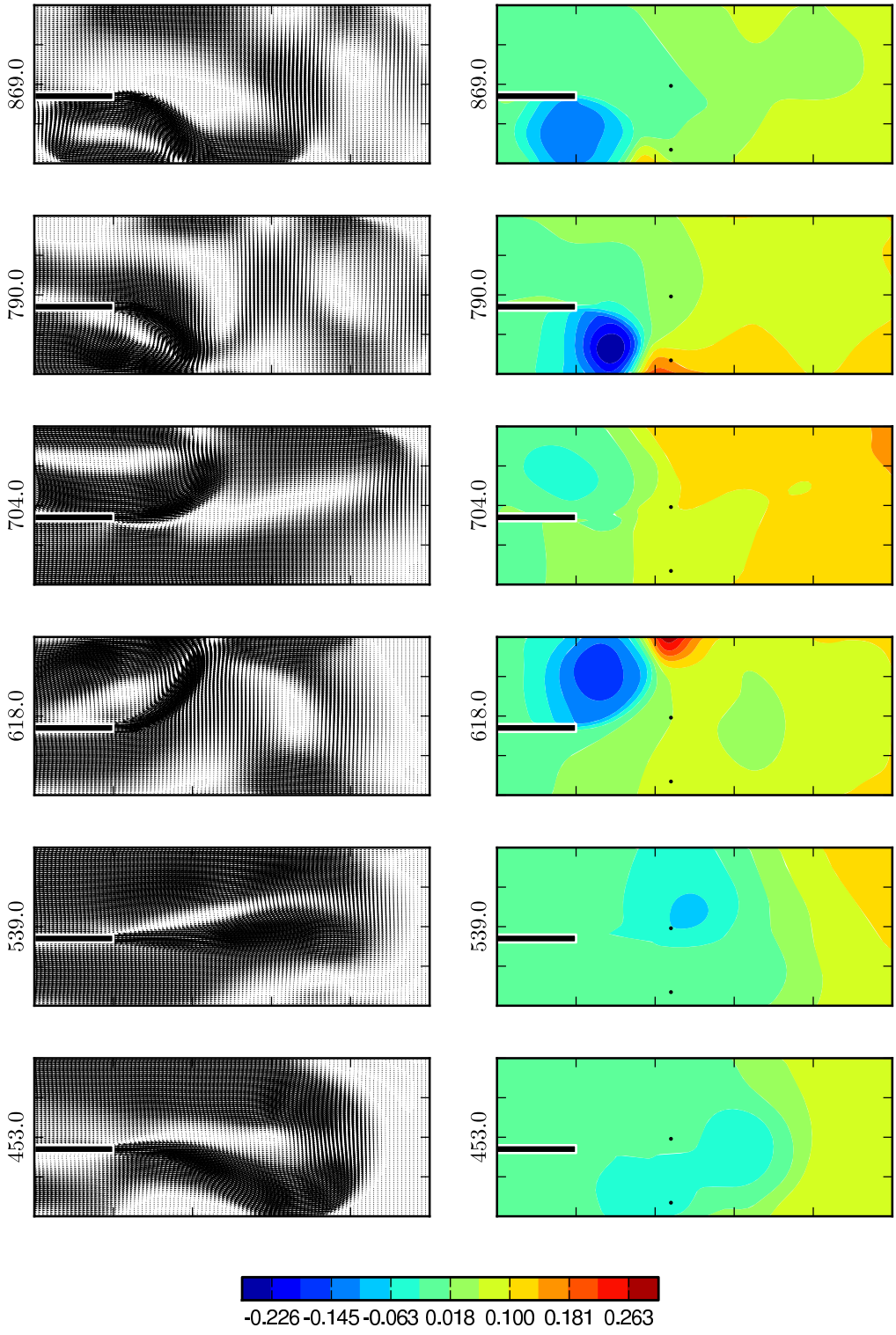

Figure 6.15: Velocity vectors and pressure contours over the dominant period of oscillation for the case $X = 0.8$, $H = 0.425$ obtained using the TCL model.

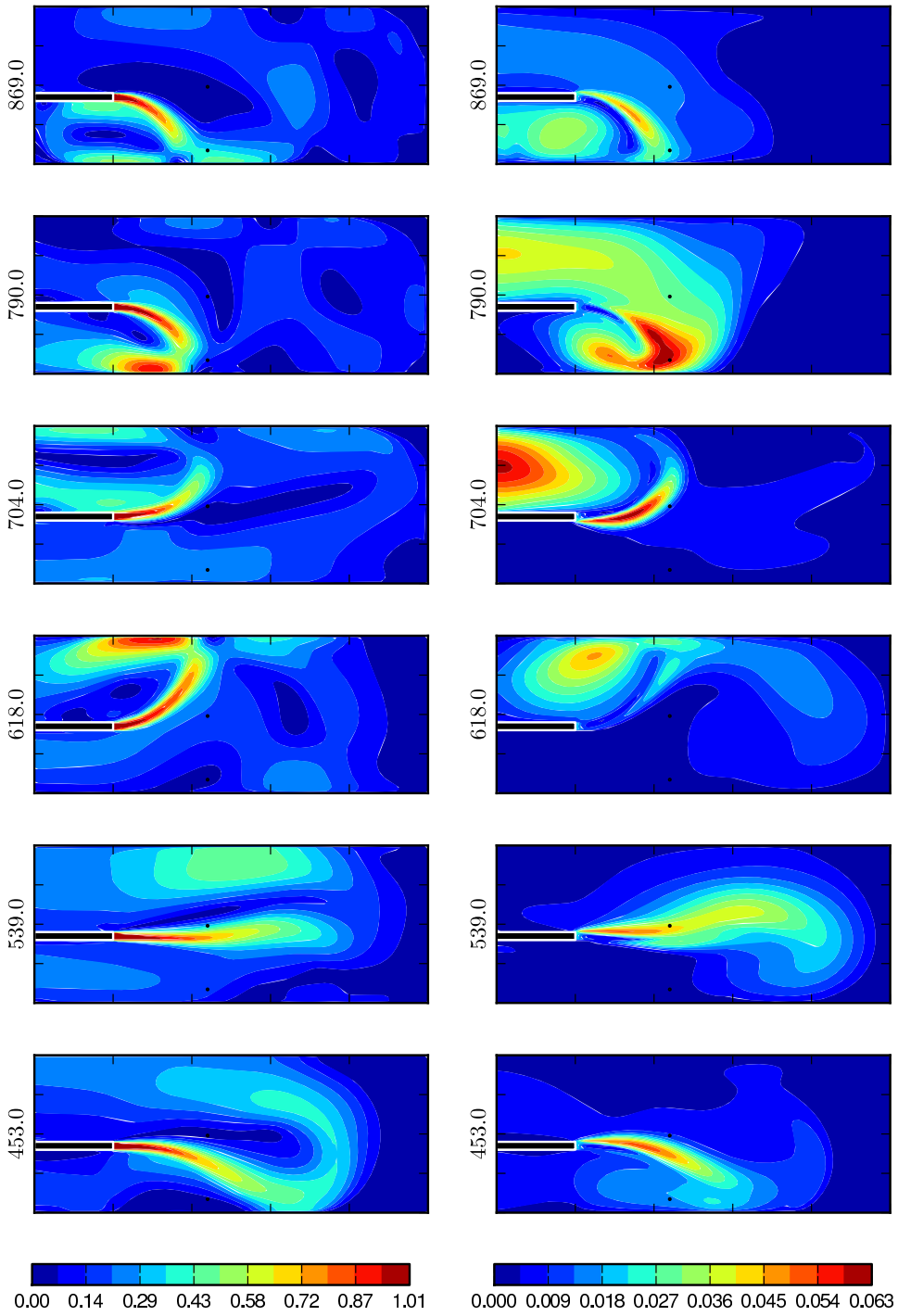

(a) Velocity magnitude (b) Turbulent kinetic energy

Figure 6.16: Contours of normalised velocity magnitude and turbulent kinetic energy over the dominant period of oscillation for the case $X = 0.8$, $H = 0.425$ obtained using the TCL model.

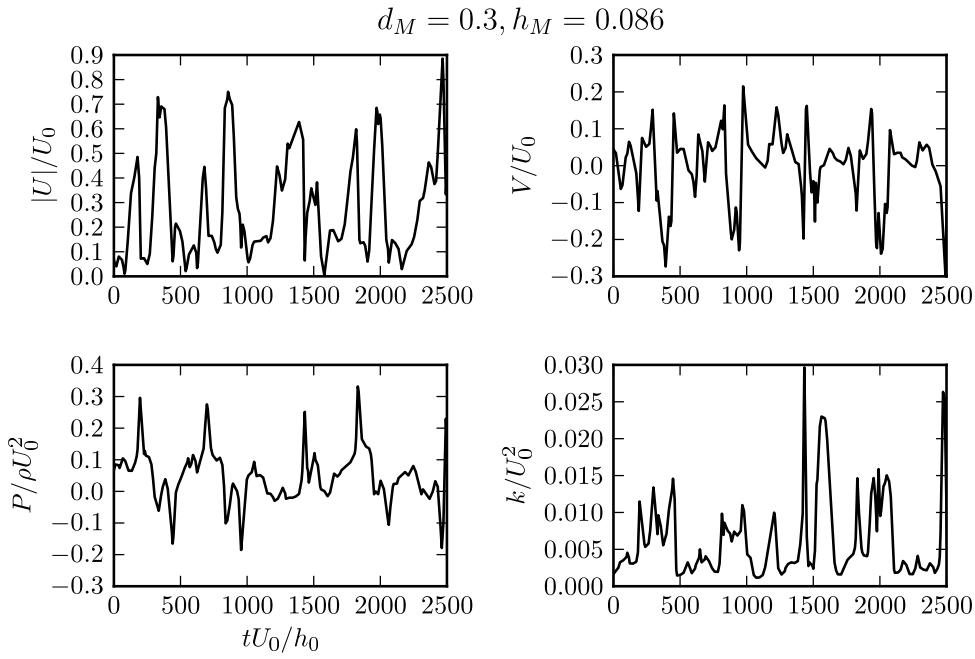

(a) Time series.

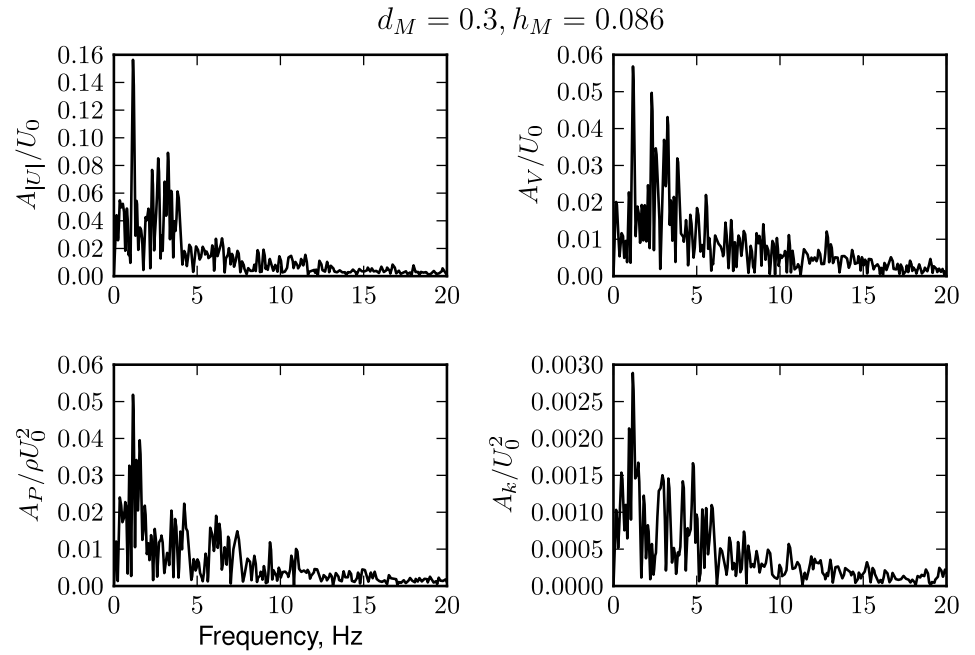

(b) Fourier transform.

Figure 6.17: Time series and frequency spectra of the variables $|\vec{U}|/U_0$, V/U_0, $P/\rho U_0^2$ and k/U_0^2 for a monitor located at $d_M = 0.3$, $h_M = 0.086$ obtained using the HJ model.

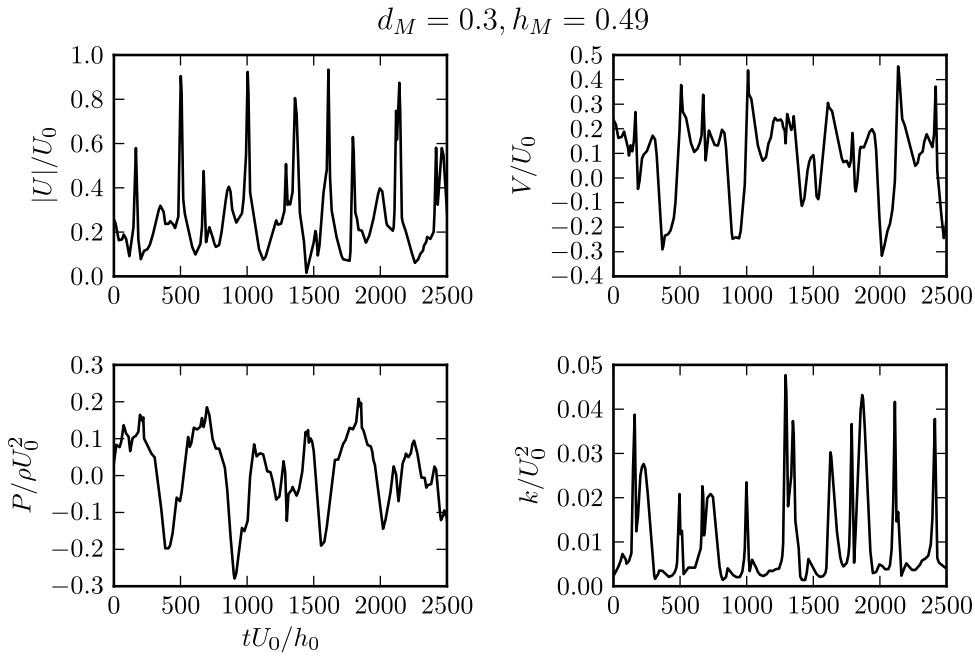

(a) Time series.

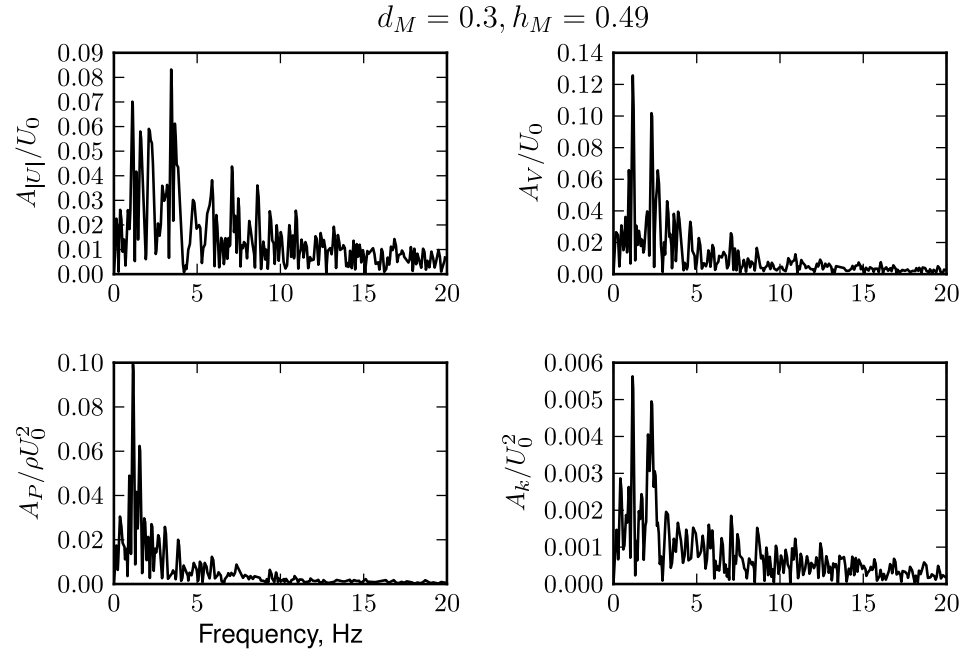

(b) Fourier transform.

Figure 6.18: Time series and frequency spectra of the variables $|\vec{U}|/U_0$, V/U_0, $P/\rho U_0^2$ and k/U_0^2 for a monitor located at $d_M = 0.3$, $h_M = 0.49$ obtained using the HJ model.

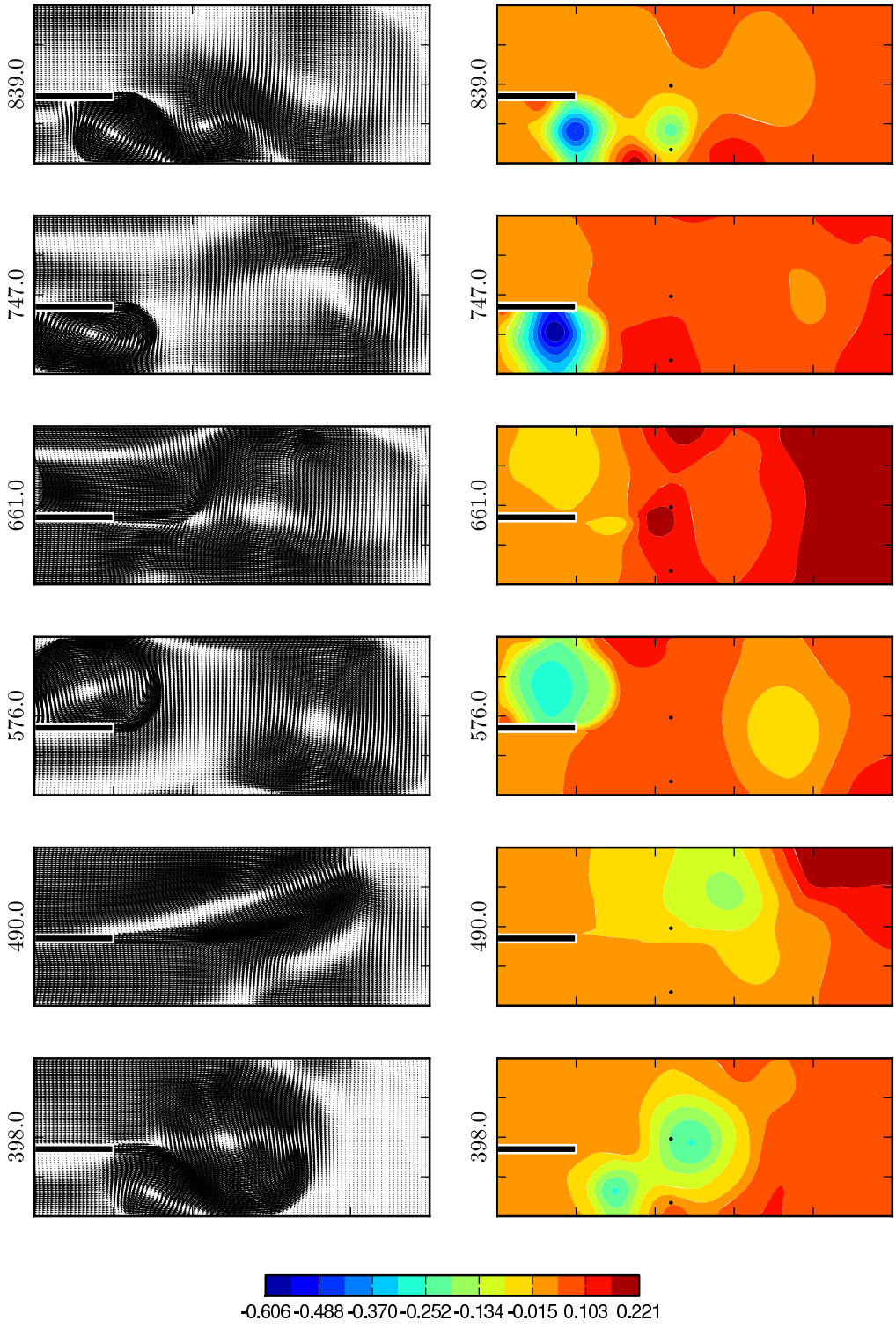

Figure 6.19: Velocity vectors and pressure contours over the dominant period of oscillation for the case $X = 0.8$, $H = 0.425$ obtained using the HJ model.

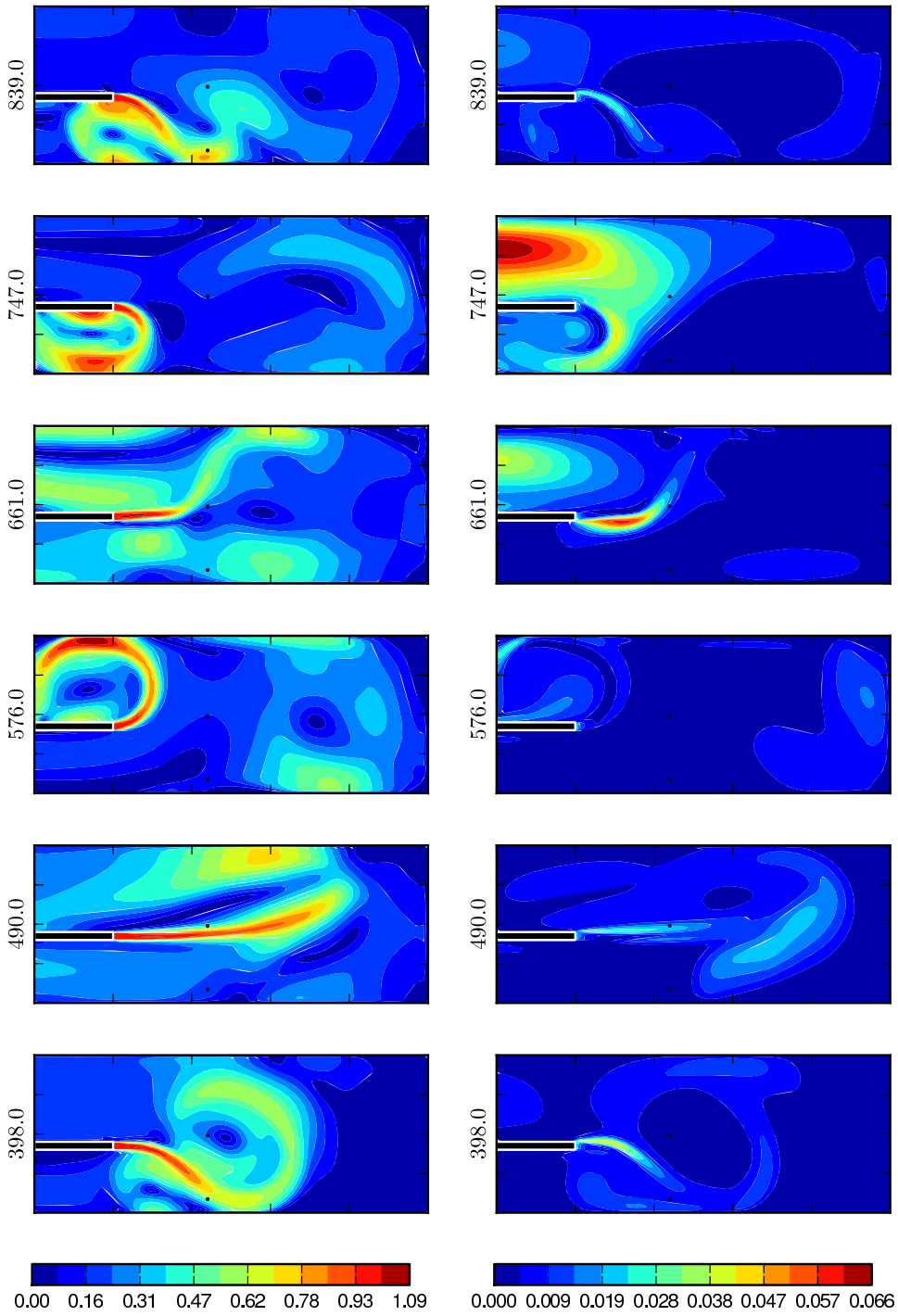

(a) Velocity magnitude (b) Turbulent kinetic energy

Figure 6.20: Contours of normalised velocity magnitude and turbulent kinetic energy over the dominant period of oscillation for the case $X = 0.8$, $H = 0.425$ obtained using the HJ model.

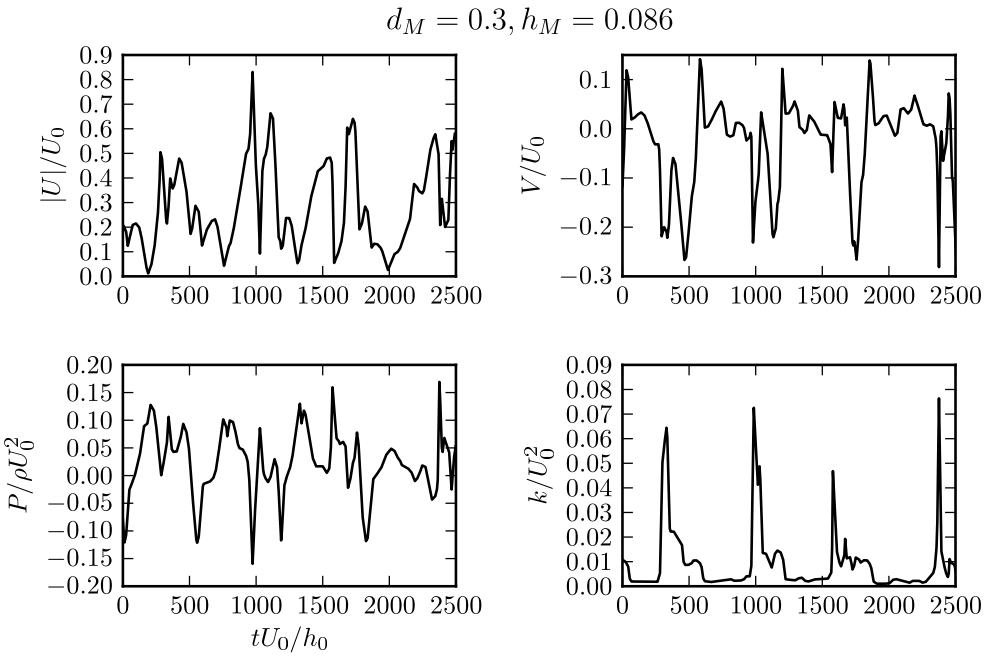

(a) Time series.

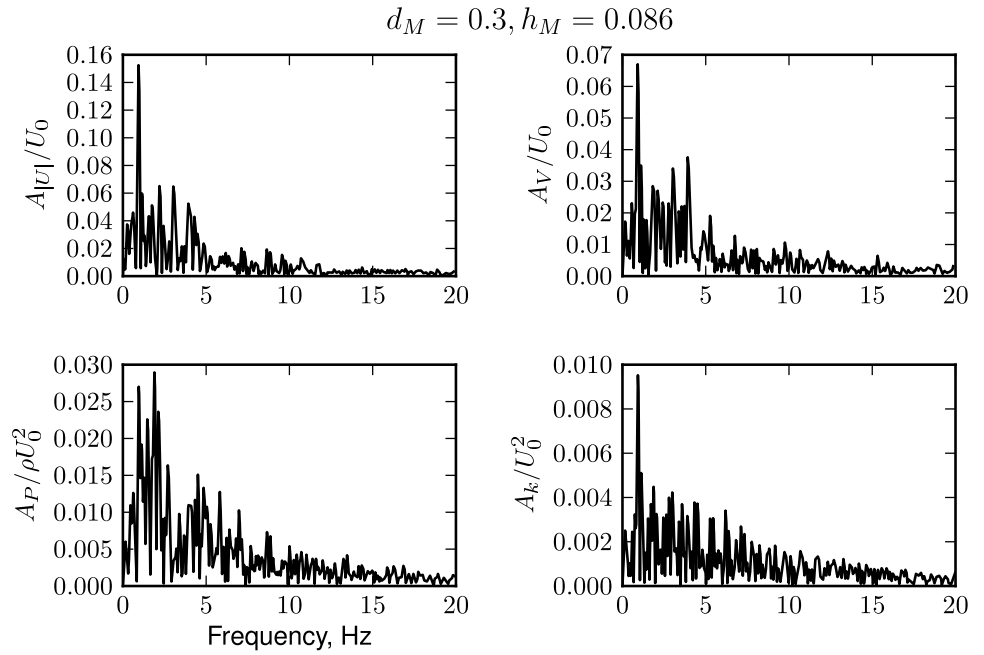

(b) Fourier transform.

Figure 6.21: Time series and frequency spectra of the variables $|\vec{U}|/U_0$, V/U_0, $P/\rho U_0^2$ and k/U_0^2 for a monitor located at $d_M = 0.3$, $h_M = 0.086$ obtained using the Shima model.

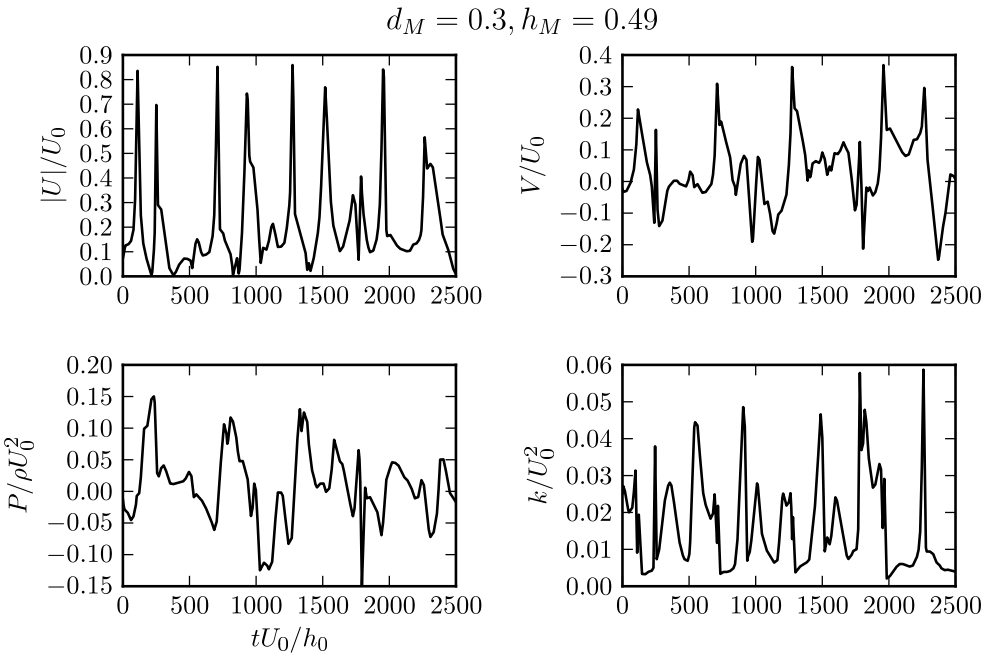

(a) Time series.

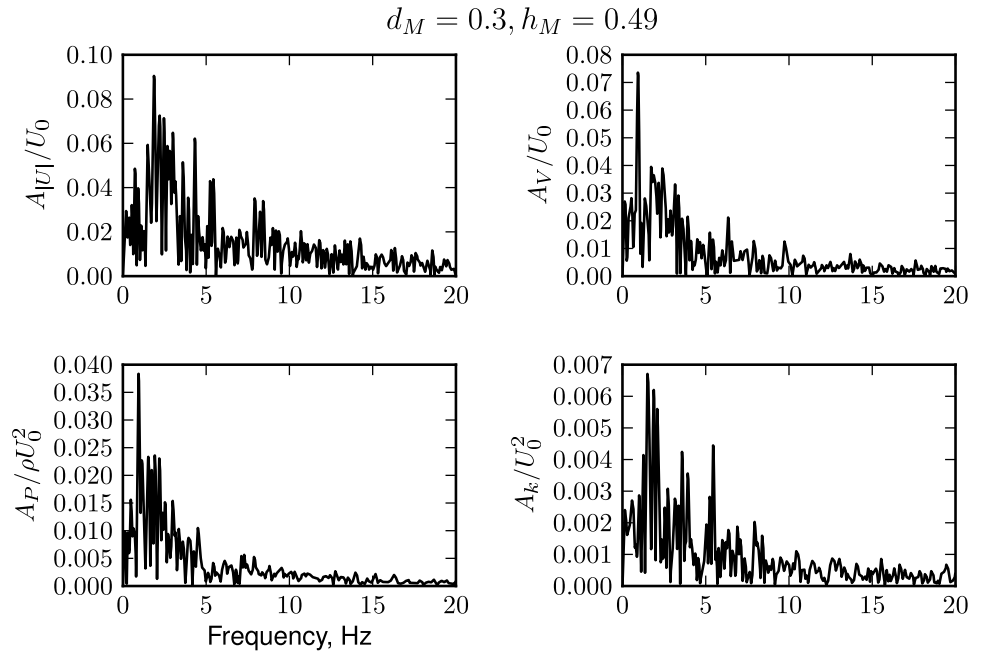

(b) Fourier transform.

Figure 6.22: Time series and frequency spectra of the variables $|\vec{U}|/U_0$, V/U_0, $P/\rho U_0^2$ and k/U_0^2 for a monitor located at $d_M = 0.3$, $h_M = 0.49$ obtained using the Shima model.

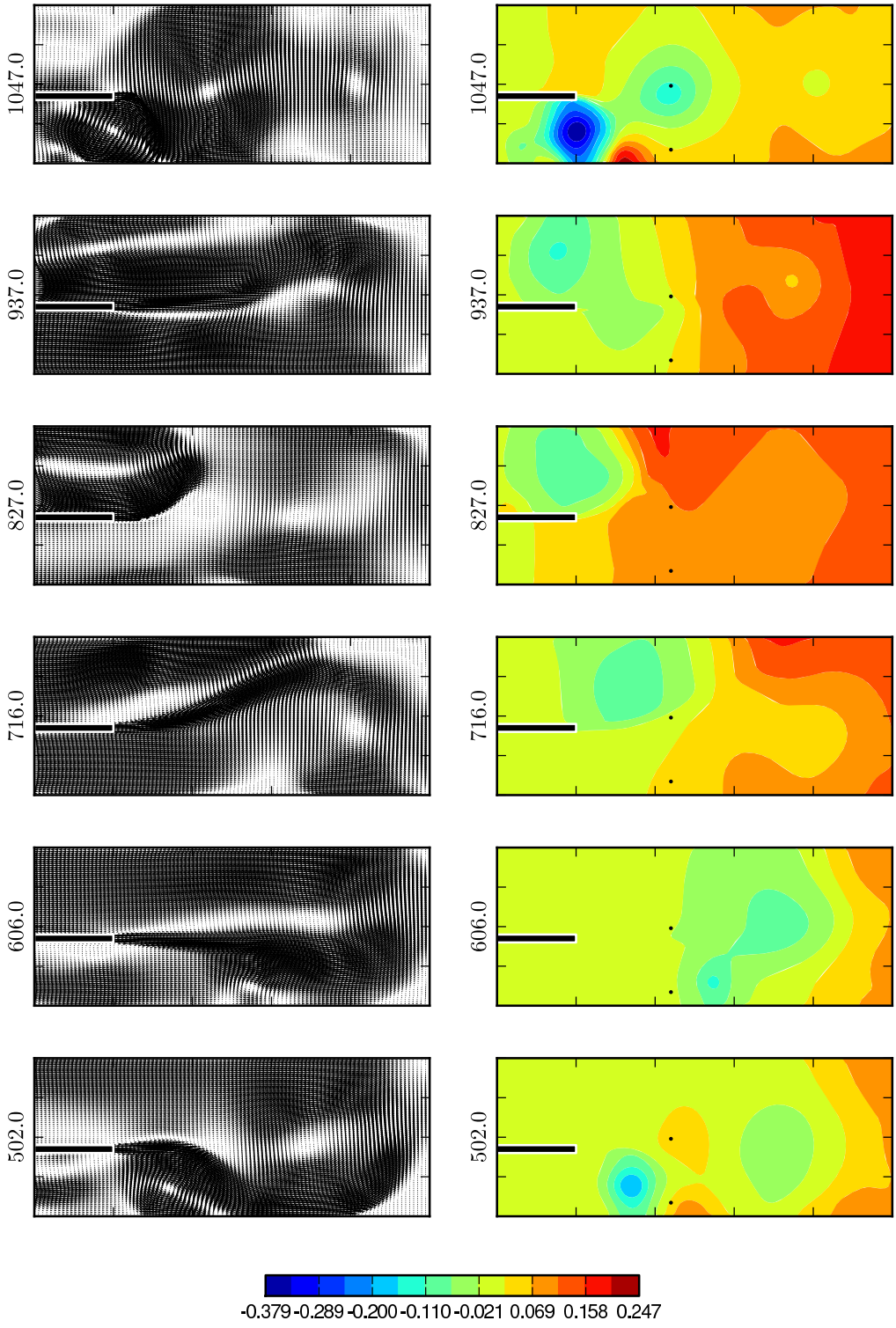

Figure 6.23: Velocity vectors and pressure contours over the dominant period of oscillation for the case $X = 0.8$, $H = 0.425$ obtained using the Shima model.

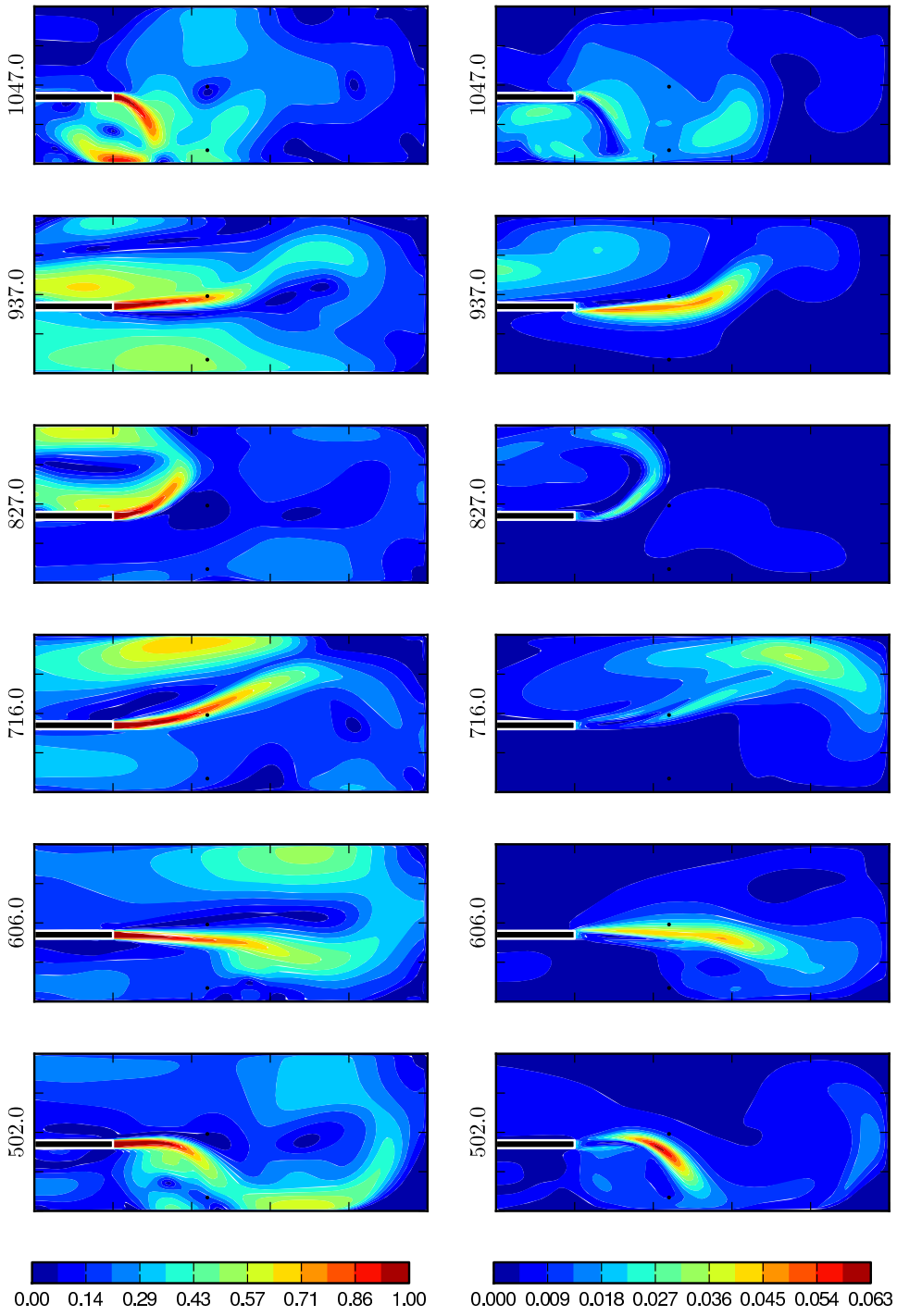

(a) Velocity magnitude (b) Turbulent kinetic energy

Figure 6.24: Contours of normalised velocity magnitude and turbulent kinetic energy over the dominant period of oscillation for the case $X = 0.8$, $H = 0.425$ obtained using the Shima model.

Chapter 7

Conclusions

A number of homogeneous turbulence problems covering various modes of mean strain and a wide range of strain rates was examined in Chapter 4. The evolution of various turbulence statistics using several RST models was presented and discussed. Somewhat different effects were observed in homogeneous shear than in irrotational strain cases, each class presenting different challenges to the models tested.

In simple shear it was generally found that models predict the correct evolution of turbulent kinetic energy k and dissipation rate ε at lower dimensionless shear rates, $Sk/\varepsilon < 4$. Despite some variation among the models in the quality of the anisotropy prediction, the more important components, a_{12} and a_{11}, were reasonably well predicted by most models. It was observed that pressure–strain-rate modelling was, in general, the more critical modelling element in homogeneous shear flows, where it was found that when the models returned the correct level of a_{12} the predicted evolution of k was generally also satisfactory. This indicates that the standard ε model equation gives roughly the correct balance of terms in these flows. This was confirmed by tests using DNS redistribution data as input to the Reynolds stress evolution equations.

A gradually decreasing trend was observed in the reference data for the long-time a_{12}, as the shear rate is increased. This trend was not captured by most models, and was reflected in an increasingly over-predicted rate of production of turbulence energy by them, which begins to be visible from the intermediate level of shear rate $Sk/\varepsilon \approx 4-5$, onwards. Since the linear pressure–strain-rate models, using constant model coefficients (such as LRR-IP and LRR-QI), were unable to replicate the variation in the long-time level of anisotropy with increasing

mean strain rate, this suggests one might need to adopt variable (strain-rate dependent) coefficients if one wishes to retain a linear tensorial expansion for ϕ_{ij}^r and reproduce the response of the Reynolds stresses to a wide range of strain rates.

At the higher shear rates tested, $Sk/\varepsilon > 16$, existing models grossly over-predict the evolution of k and ε. This is attributed mainly to the above-noted inability of the models to replicate the decay of a_{12} at high shear rates as predicted by Rapid Distortion Theory (RDT), and observed in DNS results. In addition, the normal stress anisotropies are also under-predicted by the models. With respect to the former effect, in contrast to the linear schemes, the TCL model using constant C_2, C_2' coefficients was found to have the desirable feature of a decreasing trend of long–time a_{12} with increasing shear rate. Unfortunately the low-Re, variable coefficient formulation did not retain this desired behaviour, and future work might possibly look into restoring this feature by re-associating the C_2 reduction, found by Craft (1998) to be desirable in some near-wall shear flows, with correction terms that only come into effect in regions of strong inhomogeneity. The large increase in normal stress anisotropy at high shear rates (approaching the RDT limit) is another feature that present models are unable to mimic and could therefore be addressed in future work.

In the case of homogeneous turbulence subjected to a periodic shear it was found that the models, owing to the intrinsic lag between stress and strain associated with solving an individual transport equation for each stress component, were able to return the correct qualitative trend of turbulence energy growth at low frequencies and decay at high frequencies. The critical frequency at which this change in behaviour occurs depends on the modulation of the shear stress and the applied shear, and is picked up most closely by the TCL model, although not all of the temporal variations shown by the DNS were reproduced.

In the homogeneous irrotational strain cases examined, model performance was found to be consistent over a wide range of strain rates. In these cases the Low-Re TCL model was found to return the best results. In the experimental irrotational strain cases examined (plane strain and axisymmetric contraction flows) there was evidence of an accelerated dissipation rate generation. Significant improvement was achieved through the use of an alternative P_ε model, and through a simple (though large) increase of the coefficient $C_{\varepsilon 1}$ in the conventional P_ε term. This feature would be an interesting and worthwhile subject for further study.

Possible future work could explore this trend of accelerated dissipation rate production in irrotational strain fields through additional detailed experimentation or high quality simulations. If this trend is found to be generally applicable in irrotational strains, the modifications mentioned above, or others, might be selectively applied in irrotational strains and switched off in shear dominated flows (where, as was previously discussed, the standard dissipation model and coefficient values appear to be reasonably good approximations). The additional data could contribute to the optimisation of the coefficient terms over a wider range of cases.

The problem of fully-developed channel flow subject to imposed sinusoidal pressure pulsations was examined in Chapter 5. Three frequencies were selected for study, corresponding the low, intermediate, and high frequency regimes as described in the literature. None of the models tested were able to reproduce correctly all of the observed flow features, and none returned consistently superior results in all the cases examined. A particularly challenging feature in this problem set was the partial laminarisation and re-transition that occurred cyclically at low and, to a lesser extent, intermediate frequencies.

There was a considerable degree of variation in the model predictions of mean bulk velocity, which frequently tended to be under-predicted. At intermediate and high frequencies, the time-mean bulk velocity of the LES was higher than the bulk velocity of the steady channel DNS by about 6–7%, a feature that the models did not in general seem to mimic, and which contributes to their general tendency to under-predict the time mean U_b^+.

A flow feature that was consistently well reproduced by the models over the range of frequencies examined is the fundamental mode of phase-averaged velocity modulation. Both the amplitudes and phase angles predicted by the models were in good agreement with the corresponding reference data over most of the channel height.

Because of the errors in the time-mean velocity, the phase-averaged velocity profiles were not as well reproduced as the velocity amplitude profiles (fundamental mode), and were often somewhat under-predicted.

The wall shear stress modulation returned by the LS and TCL models at the lowest frequency, $\omega^+ = 0.0016$, was in reasonable agreement with the reference data up to the re-transition phase of the cycle, where both models tended to overshoot the reference data modulation. The LS model performed better than

the TCL at this frequency. At the highest frequency, $\omega^+ = 0.04$, the wall shear stress modulation predicted by all four models was in very good agreement with the reference data. The largest variation between the models in wall shear stress modulation was observed at the intermediate frequency, $\omega^+ = 0.01$. The LS and HJ models under-predicted the amplitude of the modulation, and were out of phase with the reference data, while the TCL model once again performed poorly due to the abrupt re-transition. The Shima model in this case was in very good agreement with the LES wall shear stress modulation.

The time-mean turbulence statistics of the pulsatile flow LES generally exhibited some differences compared to a steady turbulent channel DNS at a comparable Re_τ. However, this aspect of the LES data is somewhat questionable as has been pointed out earlier. The time-mean turbulence statistics returned by the Shima model were found to be particularly sensitive to the forcing frequency. This was also true, to a lesser extent, for the HJ model. The LS and TCL models generally returned time-mean turbulence statistics that were fairly similar to their steady flow results, showing little sensitivity to the forcing frequency.

The phase-averaged turbulent kinetic energy at the low and intermediate frequencies was generally poorly predicted by the models. This appeared to be due mainly to the partial laminarisation and re-transition that occurred cyclically at these frequencies. At the lowest frequency, the Shima and HJ models could not recover from the laminarisation stage of the cycle, and a periodic turbulent solution could not be obtained using these models. The TCL model, on the other hand, suffered from excessively abrupt re-transition at the low and intermediate frequencies, which adversely affected the accuracy of its predictions. The cause of this behaviour was attributed to the low-Re_t dependencies in some of the TCL model coefficients. It is believed that considerable improvement of the TCL model's performance at the low and intermediate frequencies might be possible if this problem were corrected.

At the highest frequency examined, all four models were in much better agreement with the LES data for the phase averaged turbulent kinetic energy over most of the channel height ($y^+ > 50$). The near wall modulation of k, however, remained a difficult feature for the models to reproduce. Similar comments can be made regarding the phase-averaged Reynolds shear stress.

The ability of the TCL model, in contrast to the Shima and HJ models, to recover from the laminarisation phase of the cycle and return a turbulent periodic

solution at the lowest frequency is a desirable feature that needs to be preserved while simultaneously addressing the problem of excessively abrupt transition that adversely affects its performance. Future work in this area might take a closer look at the performance of these three RST models in predicting transition over a flat plate, as well as the present pulsatile channel cases, with the aim of making adjustments to the models for improved performance. In the case of the TCL model, it appears that there is a need reformulate the near-wall damping in some of the model coefficients to allow the model to handle the cyclic transition more gracefully.

The problem of a turbulent planar jet issuing into a dead-end enclosure has been examined in Chapter 6. Two configurations were selected for simulation: the first corresponding to a steady regime, and the second belonging to the periodic regime.

In the steady case, the general flow pattern returned by the models was qualitatively similar, with differences arising in the degree of downward deflection of the impinging jet. A lower negative pressure developing below the jet results in a larger deflection, which in turn lowers the location of the impingement point on the end wall, and increases the flow rate of the lower exiting stream relative to the upper stream. The lowest negative pressure was developed in the LS case, followed by the TCL case. This explains the difference in the flow patterns returned by the models.

The level of turbulent kinetic energy returned by the TCL and LS models was significantly higher than that returned by the HJ model. This was attributed to the larger lower stream in the LS and TCL cases, which brings the two shear layers from the lower wall stream and entrainment stream closer to each other, causing a concentration of the turbulence generated in these two shear layers.

In the unsteady case, a jet flapping motion arises, which is driven by low pressure regions that develop above and below the jet in an alternating fashion. The flapping motion is experimentally observed to be periodic for the configuration examined (Mataoui et al., 2001, 2003). However only the LS and TCL models, in this case, returned purely periodic solutions. The Shima and HJ models returned unsteady flow patterns that exhibited complex oscillations with significant cycle-to-cycle variations. Since each of the four independent Reynolds stress components is obtained from its own transport equation in RSTM's, each is free to have its own time-scale, and the potential interactions between the various

time-scales is much more complex than in eddy-viscosity models. Since the TCL model in this case is the only RSTM that correctly returns a periodic solution, it appears that, being closer to linear RSTM's, the Shima and HJ models do not return the correct interaction between processes.

The lowest dominant frequencies returned by the LS, TCL, and HJ models were relatively close to each other, having a mean value of 1.2 Hz and a standard deviation that is 2.4% of the mean. The Shima model returned a frequency that was 20% lower than the mean frequency returned by three other models. Unfortunately, differences between the reported frequencies in the reference case of Mataoui et al. (2003), and values implied by their graphs make it difficult to make a reliable comparison with the experimental data.

Possible future work might be directed towards generating more detailed data for validation and comparison. This might be through detailed experiments or high-quality LES. In addition, additional geometric configurations, covering a wider range of jet-inlet locations and the corresponding flow-regimes, might be tested using the present models to establish a better understanding of the factors driving their performance.

Taking a broad look at the results obtained in the present study, it can be said that, while no single model has consistently out-performed all other models tested, the TCL model has exhibited a number of strong points:

- In homogeneous irrotational strains it has consistently returned superior results when compared to other models tested.

- In homogeneous shear the constant coefficient version of the model was found to return improved predictions of the critical a_{12} anisotropy component, leading to improved predictions of turbulent kinetic energy production compared to other models.

- The TCL model, when compared to a number of other RSTM's tested, was found to be relatively 'robust', returning qualitatively correct results where other RSTM's were either unable to, or returned qualitatively incorrect behaviour. While numerical robustness is probably not as highly attractive as numerical accuracy, it is, nevertheless, a valuable feature in a RANS model.

Despite the above comments, a number of weakness in the present form of the

TCL model have also been identified above and some possible routes to improved performance are suggested below:

1. As noted in the discussion of homogeneous shear flows, the functional form of the more recent variable C_2 coefficient needs to be reformulated to only bring about a decrease from the original constant value of 0.55 in near–wall or strongly inhomogeneous flow regions. The effect of the current formulation (2.84) is to decrease C_2 as S^* increases. One route could be to modify this so that the reduction in C_2 occurs only above a certain threshold value of some indicator of the direction of strong inhomogeneity, such as:

$$\vec{n} = \frac{\nabla k^{1/2}}{|\nabla k^{1/2}|},$$

or the quantities d_i and d_i^A, introduced in (2.94). It might also be possible to link the decrease in C_2 to wall proximity using anisotropy invariants or the parameter A, although this may be less reliable since A can approach values associated with two-component, and even one-component, turbulence in homogeneous turbulence where there are no walls at all. It is thus recommended to employ the former approach, using gradients of a suitable turbulence statistic, which would vanish in homogeneous flows.

2. The trend of accelerated dissipation rate generation in irrotational strain fields observed in some of the experimental results requires further verification. Ideally this should be through high–quality DNS studies at higher $\mathrm{Re_t}$ and for a larger total strain than in the Lee and Reynolds (1985) database. If this trend is indeed confirmed for irrotational strains in general, one could employ suitable adjustments to the dissipation rate generation term such as the ones explored in the present study, or others, that are selectively applied in irrotational strains and switched off in shear dominated flows. One possibility for achieving this is to use factors of the form

$$\frac{S^* - \Omega^*}{S^* + \Omega^*},$$

which evaluates to zero in simple shear and unity in irrotational strains.

3. The pulsatile channel flow results suggest that there is a need to re-examine the near-wall damping in the TCL model in transitional flows with the aim

of correcting the strongly discontinuous behaviour. In this case, contrary to what has been mentioned earlier, there may be an argument for associating the near-wall damping to geometrical parameters (e.g. the wall–normal vector), rather than Re_t, the former being unaffected by the cyclic variation of turbulence statistics that is unavoidable in a periodically transitional flow. Alternatively, one can employ turbulence quantities that are less sensitive to the level of turbulence, such as the anisotropy invariants, and it may be that a careful study and tuning of the model to bypass transition on a flat plate would lead to improvements in the pulsatile channel flows.

Bibliography

Batten, P., Craft, T. J., Leschziner, M. A., Loyau, H., July 1999. Reynolds-stress-transport modelling for compressible aerodynamic applications. AIAA Journal 37 (7), 785–797.

Binder, G., Tardu, S., Blackwelder, R., Kueny, J., 1985. Large amplitude periodic oscillations in the wall region of a turbulent channel flow. In: 5^{th} Symposium on Turbulent Shear Flows. Cornell University, Ithaca, New York.

Binder, G. K., Kueny, J. L., 1981. Measurements of the periodic velocity oscillations near the wall in unsteady channel flow. In: Michel, R., Cousteix, J., Houdeville, R. (Eds.), Unsteady Turbulent Shear Flows. Springer-Verlag.

Blondeux, P., Colombini, M., 1985. Pulsatile turbulent pipe flow. In: Proc. 5^{th} Symposium on Turbulent Shear Flows. Cornell University, Ithaca, New York.

Burnel, S., Realison, J. C., Thomas, J. M., 1990. Radial distribution of the reynolds stress in a turbulent pulsating flow in a pipe. In: Rodi, W., N., G. E. (Eds.), Engineering Turbulence Modelling and Experiments. New York, pp. 419–427.

Chen, J., Meneveau, C., Katz, J., 2006. Scale interactions of turbulence subjected to a straining-relaxation-destraining cycle. Journal of Fluid Mechanics 562, 123–150.

Chieng, C. C., Launder, B. E., 1980. On the Calculation of Turbulent Heat Transport Downstream From an Abrupt Pipe Expansion. Numerical Heat Transfer, Part A: Applications 3 (2), 189–207.

Chou, P. Y., 1945. On velocity correlations and the solutions of the equations of turbulence fluctuation. Quart. Appl. Math. 3, 38–54.

Chung, M. K., Kim, S. K., 1995. A nonlinear return-to-isotropy model with reynolds number and anisotropy dependency. Physics of Fluids 7, 1425–1436.

Cotton, M. A., Craft, T. J., Guy, A. W., Launder, B. E., 2001. On modelling periodic motion with turbulence closures. Flow, Turbulence and Combustion 67, 143–158.

Cotton, M. A., Guy, A. W., Launder, B. E., 1997. Second-moment modelling of periodic and transient pipe flow. In: Proceedings of the 11^{th} Symposium on Turbulent Shear Flows. Grenoble.

Cotton, M. A., Ismael, J. O., 1991. An examination of periodic turbulent pipe flow using a low-reynolds-number k–ε turbulence model. In: Proc. 8^th Symposium on Turbulent Shear Flows. Technical University of Munich, Germany.

Craft, T., 1991. Second-moment modelling of turbulent scalar transport. Ph.D. thesis, Faculty of Technolgy, University of Manchester.

Craft, T. J., 1998. Developments in a low-reynolds-number second moment closure and its application to separating and reattaching flows. International Journal of Heat and Fluid Flow 19, 541–548.

Craft, T. J., Fu, S., Launder, B. E., Tselepidakis, D. P., 1989. Developments in modelling the turbulent second-moment pressure correlations. Tech. Rep. TFD/89/1, Dept. of Mech. Eng., UMIST.

Craft, T. J., Launder, B. E., June 1996. A reynolds stress closure designed for complex geometries. International Journal of Heat and Fluid Flow 17 (3), 245–254.

Craft, T. J., Launder, B. E., 2002. Closure modelling near the two-component limit. In: Launder, B., Sandham, N. (Eds.), Closure Strategies for Turbulent and Transitional Flows. Cambridge University Press.

Crow, S., 1968. Visco-elastic properties of fine-grained incompressible turbulence. Journal of Fluid Mechanics 33, 1–20.

Crow, S. C., 1967. Visco-elastic character of fine-grained isotropic turbulence. Physics of Fluids 10, 1587–1589.

Daly, B. J., Harlow, F. H., 1970. Transport equations in turbulence. Physics of Fluids 13, 2634–2649.

Donaldson, C. d., 1971. A progress report on an attempt to construct an invariant model of turbulent shear flows. In: Proc. AGARD Conf. on Turbulent Shear Flows. No. 1 in B. London.

Finnicum, D. S., Hanratty, T. J., 1988. Influence of imposed flow oscillations on turbulence. PhysicoChemical Hydrodynamics 10 (5/6), 585–598.

Fu, S., 1988. Computational modelling of turbulent swirling flows with second-moment closures. Ph.D. thesis, Faculty of Technology, University of Manchester.

Fu, S., Launder, B. E., Tselepidkis, D. P., 1987. Accomodating the effect of high strain rates in modelling the pressure-strain correlation. Tech. Rep. TFD/87/5, Dept. of Mech. Eng., UMIST.

Gatski, T. B., 2004. Constitutive equations for turbulent flows. Theoret. Comput. Fluid Dynamics 18, 345–369.

Gence, J. N., 1983. Homogeneous turbulence. Annual Review of Fluid Mechanics 15, 201–222.

Gibson, M. M., Launder, B. E., 1978. Ground effects on pressure fluctuations in the atmospheric boundary layer. Journal of Fluid Mechanics 86 (03), 491–511.

Guo, B., Langrish, T., Fletcher, D., August 2001. An assessment of turbulence models applied to the simulation of a two-dimensional submerged jet. Applied Mathematical Modelling 25 (8), 635–653.

Hanjalić, K., Jakirlić, S., 2002. Second-moment turbulence closure modelling. In: Launder, B., Sandham, N. (Eds.), Closure Strategies for Turbulent and Transitional Flows. Cambridge University Press.

Hanjalić, K., Launder, B. E., 1972. A reynolds stress model of turbulence and its application to thin shear flows. Journal of Fluid Mechanics 52 (4), 609–638.

Hanjalić, K., Launder, B. E., 1976. Contribution towards a reynolds-stress closure for low-reynolds number turbulence. Journal of Fluid Mechanics 74, 593–610.

Iacovides, H., Raisee, M., 1997. Computation of flow and heat transfer in 2d rib roughened passges. In: Hanjalić, K., Peeters, T. (Eds.), Proceedings of the Second International Symposium on Turbulence, Heat and Mass Transfer. Delft.

Ismael, J. O., Cotton, M. A., 1996. Calculations of wall shear stress in harmonically oscillated turbulent pipe flow using a low-reynolds-number k–ε model. Journal of Fluids Engineering 118, 189–194.

Jakirlić, S., Hanjalić, K., 1995. A second-moment closure for non-equilibrium and separating high- and low-re number flows. In: Proceedings of the 10^{th} Symposium on Turbulent Shear Flows. Vol. 3. The Pennsylvania State University, Pennsylvania, pp. 23–25–23–30.

Jakobitz, F. G., Sarkar, S., Van Atta, C. W., 1997. Direct numerical simulation of the turbulence evolutionin a uniformly sheared and stably stratified flow. Journal of Fluid Mechanics 342, 231–61.

Johansson, A. V., Hallbäck, M., 1994. Modelling of rapid pressure–strain in reynolds-stress closures. Journal of Fluid Mechanics 269, 143–168.

Kassinos, S. C., Reynolds, W. C., 1994. A structure-based model for the rapid distortion of homogeneous turbulence. Tech. Rep. TF-61, Mech. Eng. Dept., Stanford University.

Kebede, W., Launder, B. E., Younis, B. A., 1985. Large-amplitude periodic pipe flow: a second moment closure study. In: Proc. 5^{th} Symposium on Turbulent Shear Flows. Cornell University, Ithaca, New York.

Launder, B., Reece, G., Rodi, W., 1975. Progress in the development of a reynolds-stress turbulence closure. Journal of Fluid Mechanics 68 (3), 537–566.

Launder, B., Shima, N., 1989. Second-moment closure for the near-wall sublayer: development and appilication. AIAA Journal 27, 1319–1325.

Launder, B. E., Reynolds, W. C., 1983. Asymptotic near-wall stress dissipation rates in a turbulent flow. Physics of Fluids 26 (5), 1157–1158.

Launder, B. E., Sharma, B. I., 1974. Application of the energy dissipation model of turbulence to the calculation of flow near a spinning disc. Letters in Heat an Mass Transfer 1 (2), 131–138.

Lee, M. J., Kim, J., Moin, P., 1987. Turbulence structure at high shear rate. In: 6^{th} Symposium on Turbulent Sher Flows.

Lee, M. J., Kim, J., Moin, P., 1990. Structure of turbulence at high shear rate. Journal of Fluid Mechanics 216, 561–583.

Lee, M. J., Reynolds, W. C., 1985. Numerical experiments on the structure of homogeneous turbulence. Tech. Rep. TF-24, Thermosciences Division, Department of Mechanical Engineering, Stanford University.

Leschziner, M. A., Lien, F. S., 2002. Numerical aspects of applying second-moment closure to complex flows. In: Launder, B., Sandham, N. (Eds.), Closure Strategies for Turbulent and Transitional Flows. Cambridge University Press.

Lien, F. S., Leschziner, M. a., September 1994. Upstream monotonic interpolation for scalar transport with application to complex turbulent flows. International Journal for Numerical Methods in Fluids 19, 527–548.

Lindborg, E., 1995. Kinematics of homogeneous axisymmetric turblence. Journal of Fluid Mechanics 302, 179–201.

Lumley, J., 1967. Rational approach to relations between motions of differing scales in turbulent flows. Physics of Fluids 10, 1405–1408.

Lumley, J., Khajeh-Nouri, B., 1974. Computational modelling of turbulent transport. Adv. Geophys. 18Aa, 169–192.

Lumley, J. L., 1970. Toward a turbulent constitutive relation. Journal of Fluid Mechanics 41, 413–434.

Lumley, J. L., 1978. Computational modelling of turbulent flows. Adv. Appl. Mech. 18, 123–176.

Mansour, N. N., Kim, J., Moin, P., 1988. Reynolds-stress and dissipation-rate budgets in a turbulent channel flow. Journal of Fluid Mechanics 194, 15–44.

Mao, Z. X., Hanratty, T. J., 1986. Studies of the wall shear stress in a turbulent pulsating pipe flow. Journal of Fluid Mechanics 170, 545–564.

Mataoui, A., Schiestel, R., Salem, A., 2001. Flow regimes of interaction of a turbulent plane jet into a rectangular cavity: Experimental approach and numerical modelling. Flow, Turbullence and Combustion 67, 267–304.

Mataoui, A., Schiestel, R., Salem, A., 2003. Study of the oscillatory regime of a turbulent plane jet impinging in a rectangular cavity. Applied Mathematical Modelling 27, 89–114.

Matsumoto, A., Nagano, Y., Tsuji, T., 1991. Direct numerical simulation of homogeneous turbulent shear flow. In: 5^{th} Symposium on Computational Fluid Dynamics. pp. 361–364, tokyo.

Mizushina, T., Maruyama, T., Hirasawa, H., 1975. Structure of turbulence in pulsating pipe flows. Journal of Chemical Engineering of Japan 8, 210–216.

Mizushina, T., Maruyama, T., Shiozaki, Y., 1973. Pulsating turbulent flow in a tube. Journal of Chemical Engineering of Japan 6, 487–494.

Moser, R. D., Kim, J., Mansour, N. N., 1999. Direct numerical simulation of turbulent channel flow up to $\mathrm{Re}_\tau = 590$. Physics of Fluids 11, 943–945.

Naot, D., Shavit, A., Wolfshtein, M., 1972. Prediction of flow in square section ducts. Tech. Rep. 154, Mech. Eng. Dept., Technion, Haifa.

Patankar, S. V., Spalding, D. B., 1972. A calculation procedure for heat, mass and momentum transfer in three-dimensional parabolic flows. Int. J. Heat Mass Transfer 15, 1787–1972.

Pope, S. B., 2000. Turbulent flows. Cambridge University Press.

Ramaprian, B. R., Tu, S. W., 1983. Fully developed periodic turbulent pipe flow. part 2. the detailed structure of the flow. Journal of Fluid Mechanics 137, 59–81.

Reynolds, W. C., 1970. Computation of turbulent flows—state-of-the-art. Tech. Rep. MD-27, Mech. Eng. Dept., Stanford University.

Rhie, C. M., Chow, W. L., November 1983. Numerical study of the turbulent flow past an airfoil with trailing edge separation. AIAA Journal 21, 1525–1532.

Rivlin, R., 1957. The relation between the flow of non-newtonian fluids and turbulent newtonian fluids. Quart. Appl. Math. 15, 212–215.

Rogers, M., Moin, P., 1987. The structure of the vorticity field in homogeneous turbulent flows. Journal of Fluid Mechanics 176, 33–66.

Ronneberger, D., Ahrens, C. D., 1977. Wall shear stress caused by small amplitude perturbations of turbulent boundary-layer flow: an experimental investigation. Journal of Fluid Mechanics 83 (03), 433–464.

Rotta, J. C., 1951. Statistiche theorie nichthomogener turbulenz. Z. Phys. 129, 547–572.

Sarkar, S., 1995. The stabilizing effect of compressibility in turbulent shear flow. Journal of Fluid Mechanics 282, 163–186.

Schumann, U., 1977. Realizability of reynolds-stress turbulence models. Physics of Fluids 20, 721–725.

Scotti, A., Piomelli, U., May 2001. Numerical simulation of pulsating turbulent channel flow. Physics of Fluids 13 (5), 1367–1383.

Scotti, A., Piomelli, U., 2002. Turbulence models in pulsating flows. AIAA Journal 40, 537–544.

Shih, T. S., Lumley, J. L., 1985. Modelling of pressure correlation terms in reynolds-stress and scalar flux equations. Tech. Rep. FDA-85-3, Cornell University, Ithaca, N.Y.

Shima, N., 1989. Calculation of a variety of boundary layers with a second-moment closure applicable up to a wall. In: Proceedings of the 7^{th} Symposium on Turbulent Shear Flows. Stanford University.

Shima, N., 1998. Low-reynolds-number second-moment closure without wall-reflection redistribution terms. International Journal of Heat and Fluid Flow 19, 549–555.

Shir, C. C., 1973. A preliminary numerical study of atmospheric turbulent flows in the idealized planetary boundary layer. Journal of Atmospheric Science 30, 1327–1339.

Sjögren, T., Johansson, A. V., 1998. Measurement and modelling of homogeneous axisymmetric turbulence. Journal of Fluid Mechanics 347, 59–90.

Speziale, C., Sarkar, S., Gatski, T., 1991. Modelling the pressure-strain correlation of turbulence: an invariant dynamical systems approach. Journal of Fluid Mechanics 227, 245–272.

Speziale, C. G., 1985. Modelling the pressure gradient-velocity correlation of turbulence. Physics of Fluids 28, 69–71.

Speziale, C. G., 1987. Second-order closure models for rotating turbulent flows. Quarterly of Applied Mathematics 45, 721–733.

Speziale, C. G., 1991. Analytical methods for the development of reynolds-stress closures in turbulence. Annual Review of Fluid Mechanics 23, 107–157.

Tardu, S., Binder, G., Blackwelder, R. F., 1994. Turbulent channel flow with large-amplitude velocity oscillations. Journal of Fluid Mechanics 267, 109–151.

Tavoularis, S., Jimenez, J., Leuchter, O., 1997. Homogeneous flows. In: A selection of test cases for the validation of large-eddy simulations of turbulent flows. No. AR-345. AGARD, Ch. 3.

Tu, S., Ramaprian, B., 1983. Fully developed periodic turbulent pipe flow. part 1. main experimental results and comparison wiht predictions. Journal of Fluid Mechanics 137, 31–58.

van Leer, B., 1974. Towards the ultimate conservative difference scheme. ii. monotonicity and conservation combined in a second-order scheme. Journal of Computational Physics 14 (4), 361–370.

Versteeg, H. K., Malalasekera, W., 2007. An introduction to Computational Fluid Dynamics: the Finite-Volume Method, 2nd Edition. Pearson.

Yu, D., Girimaji, S., 2006. Direct numerical simulations of homogeneous turbulence subject to periodic shear. Journal of Fluid Mechanics 566, 117–151.